



HAL
open science

Model reduction for nonlinear structural problems with multiple contact interfaces

Donald Zeka

► **To cite this version:**

Donald Zeka. Model reduction for nonlinear structural problems with multiple contact interfaces. Solid mechanics [physics.class-ph]. Université Paris-Saclay, 2024. English. NNT : 2024UPAST102 . tel-04795891

HAL Id: tel-04795891

<https://theses.hal.science/tel-04795891v1>

Submitted on 21 Nov 2024

HAL is a multi-disciplinary open access archive for the deposit and dissemination of scientific research documents, whether they are published or not. The documents may come from teaching and research institutions in France or abroad, or from public or private research centers.

L'archive ouverte pluridisciplinaire **HAL**, est destinée au dépôt et à la diffusion de documents scientifiques de niveau recherche, publiés ou non, émanant des établissements d'enseignement et de recherche français ou étrangers, des laboratoires publics ou privés.

Model reduction for nonlinear structural problems with multiple contact interfaces

*Réduction de modèle pour les problèmes nonlinéaires
de structures avec interfaces de contact multiples*

Thèse de doctorat de l'université Paris-Saclay

École doctorale n° 579, Sciences Mécaniques et Énergétiques, Matériaux et
Géosciences (SMEMaG)

Spécialité de doctorat : Mécanique des solides et des structures

Graduate School : Sciences de l'ingénierie et des systèmes.

Référent : ENS Paris-Saclay

Thèse préparée dans la unité de recherche **LMPS - Laboratoire de Mécanique
Paris-Saclay (Université Paris-Saclay, CentraleSupélec, ENS Paris-Saclay, CNRS)**,
sous la direction de **Pierre-Alain GUIDAULT**, Maître de conférences,
la co-direction de **David NÉRON**, Professeur des universités,
et la co-supervision de **Martin GUITON**, Ingénieur de recherche

Thèse soutenue à Paris-Saclay, le 14 octobre 2024, par

Donald ZEKA

Composition du jury

Membres du jury avec voix délibérative

Pierre GOSSELET

Directeur de Recherche, Université de Lille

Anthony GRAVOUIL

Professeur des Universités, INSA Lyon

Pierre KERFRIDEN

Professeur des Universités, Mines Paris - PSL

Florence BERTAILS-DESCOUBES

Directrice de Recherche, INRIA Grenoble
Rhône-Alpes

Daniel RIXEN

Professeur des Universités, TU München

Président & Examineur

Rapporteur & Examineur

Rapporteur & Examineur

Examinatrice

Examineur

Titre : Réduction de modèle pour les problèmes nonlinéaires de structures avec interfaces de contact multiples

Mots clés : Contact frottant, Méthode LATIN, Méthode de décomposition de domaine, Réduction de modèle, PGD, Stratégie multiéchelle.

Résumé : Malgré les progrès continus en mécanique numérique du contact, la simulation d'une structure complexe avec de multiples interfaces de contact frottant nécessite toujours un coût de calcul élevé en raison de multiples sources de nonlinéarité : évolution du statut de contact et de frottement, dissipation par frottement, grands glissements et grandes déformations. Cela peut induire des limitations pour les applications industrielles impliquant des matériaux architecturés tels que les câbles spirales comportant de nombreux fils en contact, souvent utilisés en ingénierie offshore, ce qui a motivé ce travail. Parmi les stratégies alternatives pour réduire les coûts de calcul, une solution attractive consiste à projeter le problème d'ordre complet sur une base d'ordre réduit du problème original par diverses techniques de réduction de modèle. Cependant, leur application aux problèmes de frottement reste une question ouverte, en particulier pour les cas impliquant de grandes propagations de fronts de glissement/adhérence. La stratégie proposée repose sur le solveur nonlinéaire LATIN (LArge Time INcrement) combiné à une réduction de modèle basée sur la Proper Generalized Decomposition (PGD). La LATIN présente un traitement robuste des conditions de contact et conduit naturellement à une méthode mixte de décomposition de domaine. Par ailleurs, la formulation spatio-temporelle globale de la méthode permet d'utiliser la réduction de modèle basée sur la PGD pendant les calculs, en créant et en enrichissant à la volée des bases réduites par sous-domaine afin de mieux suivre les fronts de glissement et les phé-

nomènes de propagation. L'introduction d'une stratégie multiéchelle dans le cadre de la LATIN est cohérente avec la physique des problèmes de contact dans lesquels des phénomènes de longueurs d'onde différentes interagissent : les solutions locales aux interfaces de contact présentent des effets de gradients élevés avec une longueur d'onde courte par rapport à la longueur caractéristique de la structure. En tirant parti de ce fait, le problème grossier de la stratégie permet de capturer efficacement le comportement du problème à l'échelle de la structure, en se focalisant ensuite sur la capture des variations localisées aux interfaces de contact. Le point crucial de la thèse est que le modèle réduit doit représenter très fidèlement les informations critiques situées sur les interfaces de frottement entre les fils, qui sont cruciales pour l'évaluation de leur durée de vie en fatigue. L'objectif est de rechercher à maximiser les performances de réduction de modèle et la vitesse de convergence, tout en garantissant une évaluation précise des quantités d'interface. A cette fin, les critères de convergence pour la méthode de résolution nonlinéaire doivent assurer une bonne convergence pour les quantités locales de contact. De plus, une mise à jour appropriée des directions de recherche de la LATIN permet d'augmenter de manière significative la vitesse de convergence. Enfin, pour les problèmes très irréguliers tels que les problèmes de contact frottant, le contrôle de la qualité et de la taille des bases PGD construites progressivement le long des itérations de la LATIN est crucial pour l'efficacité de la méthode.

Title : Model reduction for nonlinear structural problems with multiple contact interfaces

Keywords : Frictional contact, LATIN method, Domain decomposition method, Model reduction, PGD, Multiscale strategy.

Abstract : Despite continuous progress in computational contact mechanics, simulating a complex structure with multiple frictional interfaces still requires a large computational cost due to multiple sources of nonlinearity : contact and friction status change, frictional dissipation, large sliding and finite deformations. This may induce limitations for industrial cases involving architected materials such as spiral strand wire ropes with many wires in contact, often used in offshore engineering, which motivated this work. Among the alternative computational strategies to reduce calculation costs, an appealing one is to project the full-order problem on a reduced-order basis of the original problem through various model reduction techniques. However, their application to frictional problems remains an open question, especially for cases involving wide propagation of sliding/sticking fronts. The proposed strategy relies on the LArge Time INcrement (LATIN) nonlinear solver combined with model reduction based on the Proper Generalized Decomposition (PGD). The LATIN presents a robust treatment of contact conditions and naturally leads to a mixed domain decomposition method. In addition, the global space-time formulation of the method allows PGD-based model reduction to be used during computations, creating and enriching on-the-fly reduced bases per substructure to better track sliding fronts and propagative phenomena. The

introduction of a multiscale strategy in the LATIN framework is consistent with the physics of contact problems, in which phenomena with different wavelengths interact : local solutions at contact interfaces presents high gradient effects with a short wavelength compared to the characteristic length of the structure. By taking advantage of this, the coarse scale problem of the strategy enables to capture efficiently the behavior of the problem at the structural level, focusing then on capturing the local contact variations at the contact interfaces. The crucial point of the thesis is that the reduced model has to represent very faithfully the critical information located on the frictional interfaces between the wires, crucial for their fatigue life evaluation. The objective is to look for maximum reduction performances and convergence speed, while guaranteeing at the same time an accurate evaluation of the interface quantities. For this purpose, convergence criteria for the nonlinear solution method must assure a good convergence for local contact quantities. Moreover, a proper updating of the LATIN search directions can significantly increase the convergence speed. Finally, for highly irregular problems such as frictional contact problems, controlling the quality and size of progressively built PGD basis along the LATIN iterations is crucial for the efficiency of the method.

Alla mia Famiglia

*Felix qui potuit rerum cognoscere causas
atque metus omnes et inexorabile fatum
subjecit pedibus strepitumque Acheruntis avari.*

Virgilio, Georgiche, libro II, v. 490–493.

Acknowledgements

I thank Pierre-Alain Guidault and David Néron for reviving a topic that has not been addressed for a long time at the LMPS, and for the trust they put in me. I thank Martin Guiton for his interest and enthusiasm in solving industrial problems with such alternative strategies. My thanks also go to Pierre Gosselet for being the president of the jury, and also the other members of the jury: Florence Bertails-Descoubes and Daniel Rixen, and more particularly Anthony Gravouil and Pierre Kerfriden who agreed to be reviewers of this thesis.

Contents

Front Matter	vi
Contents	vii
List of Figures	xi
List of Tables	xvii
List of Algorithms	xix
List of Symbols	xxi
Introduction	1
I Bibliography study and preliminary reducibility investigation	11
1 Bibliographic study	13
1 Floating Offshore Wind Turbines	16
1.1 Environment characterization	17
1.1.1 Description of the sea state	17
1.1.2 Description of the wind state	18
1.2 The floating structure	20
1.2.1 Hydrodynamic loads	21
1.2.2 Mooring system	21
2 Wire ropes	23
2.1 General description	23
2.2 Mechanical behavior	25
2.2.1 Analytical results: traction	25
2.2.2 Analytical results: bending	27
2.3 Numerical modeling	29
3 Quasi-static frictional contact problems	33
3.1 Frictional contact problem setting	33
3.2 Unilateral contact conditions	34
3.2.1 Normal contact	34
3.2.2 Tangential frictional contact	35
3.2.3 Strong formulation of the problem	38
3.2.4 Weak formulation of the problem	38
3.3 Treatment of contact constraints	40

3.3.1	Penalty method	40
3.3.2	Lagrange multipliers method	41
3.3.3	Augmented Lagrangian formulation	42
3.3.4	Nitsche method	44
3.4	Numerical strategies	45
3.4.1	Partial Dirichlet-Neumann algorithm or status method	46
3.4.2	Augmented Lagrangian and Uzawa algorithm	47
3.4.3	LATIN non-incremental method	48
4	Overview on model reduction and applications to frictional contact problems	50
4.1	Introduction to model-order reduction	50
4.2	Abstract problem	51
4.3	Proper Orthogonal Decomposition	52
4.3.1	A posteriori model reduction through Proper Orthogonal Decomposition	54
4.4	Reduced Basis Method	56
4.5	Proper Generalized Decomposition	57
4.5.1	A-priori model reduction through Galerkin-PGD	58
4.5.2	A-priori model reduction through minimal residual PGD	60
4.6	Nonlinear problems and hyperreduction	62
4.7	Model reduction in contact problems	63
5	Domain Decomposition Methods	67
5.1	Primal and dual approaches	67
5.2	Mixed domain decomposition methods	72
5.3	Domain decomposition for contact problems	73
2	Preliminary reducibility investigation	75
1	Analysis of a six layer wire rope in tension and bending	77
1.1	Global hydrodynamic FOWT model	77
1.2	Detailed local cable model	78
1.3	Contact quantities analysis	80
2	Singular Value Decomposition on the main results	84
2.1	Layer-by-layer interface reducibility investigation	86
2.2	Layer-by-layer space and time modes	88
3	Conclusions	94
II A multiscale strategy to model-order reduction for frictional contact problems		97
3	LATIN-based model reduction for frictional contact problems	99
1	Preliminary results on a simple 1D problem	101
1.1	Analysis of the solution	102
1.1.1	Load case 1: large propagation of sliding front	102

1.1.2	Load case 2: small variations of sliding front	104
1.2	Reducibility of the contact quantities	106
2	LATIN-based monoscale DDM for frictional contact problems	108
2.1	The reference problem: partitioning into substructures and interfaces	110
2.1.1	Admissibility for variables on a substructure	111
2.1.2	Interface behavior	112
2.1.3	Reformulation of the reference problem	112
2.2	Some examples of interface behaviors	113
2.3	LATIN-based iterative solver	114
2.3.1	The local stage	115
2.3.2	The linear stage	116
2.3.3	On the search directions	117
2.4	Local stage for different interface behaviors	118
2.5	Initialization and control of the convergence	121
2.6	Application on the 1D test problem	123
3	Solving linear stage problems with PGD	127
3.1	Linear stage with corrections	127
3.2	Separated representation of the unknowns during the linear stage	129
3.3	Finding a new pair of modes	130
3.4	Controlling the size and quality of the PGD basis	132
3.5	Application on the 1D test problem	134
4	Conclusions	139
4	A multiscale strategy to model-order reduction	141
1	Introduction of a multiscale strategy at the level of the interfaces	143
1.1	Definition of the macroquantities	144
1.2	Choice of the macrospace	145
1.3	Admissibility of macroquantities	146
2	The multiscale strategy within the LATIN framework	147
2.1	Microproblem on a substructure	149
2.2	The macroproblem over Ω	150
2.3	Search directions in the multiscale strategy	151
2.4	The final algorithm	151
2.5	Resolution of microproblems with PGD	152
3	Application to the 1D benchmark problem	154
4	Application to a layered structure with wide contact interfaces	156
4.1	Problem setting	156
4.2	Analysis of the solution	158
4.3	Introduction of PGD	160
4.4	Analysis of the computational cost	163
5	Conclusions	166
5	Control and improvement of the convergence	169

1	Control of the convergence of interface quantities	171
1.1	Convergence indicator based on the interface constitutive relation error	172
1.2	Limitations and modifications	175
1.3	Corroboration of the CRE convergence indicator	177
2	Improvement of the convergence of interface quantities	187
2.1	On the relevance of contact conditions on convergence rate	189
2.1.1	Contact in opening and closing	189
2.1.2	Layered structure with wide sliding propagation front	190
2.2	A strategy based on the contact status indicators	191
2.3	Consequences of a search direction in space and time	193
2.4	Application to the 1D benchmark problem	195
2.5	Application to 2D frictional contact problems	200
3	Conclusions	206
III Conclusions and perspectives		207
Appendices		219
A	Local stage for frictional contact interfaces	221
B	On the discretization of subdomain and interface quantities	225
C	Some properties of the homogenized operator	227
1	Reminder	227
2	Properties of the homogenized operator	228
D	Downsizing stage	231
E	Extended abstract in french	233
Bibliography		243

List of Figures

1	Principles of FOWTs with their mooring lines. <i>Image by Josh Bauer, NREL.</i>	1
2	3D view of a finite element model of a steel spiral strand cable of 60.4 mm diameter [Bussolati, 2019].	2
3	Example of the cross-section of a dynamic three-phase cable. <i>JDR Cables systems.</i>	3
4	General flowchart of a multiscale approach to compute fatigue damage in wire ropes [Bussolati, 2019]. In this thesis we will focus on accelerating local model simulations.	5
1.1	Example of a global hydrodynamic computation on a FOWT with the software Deeplines™ [Bussolati, 2019]. Note that the rectangular shape is a simplistic representation of an evolution of the hybrid spar-barge concept presented in [Poirette et al., 2014]. Different systems exist as illustrated in Figure 1.7.	17
1.2	Different sources of loads acting on a FOWT [Hall, 2013].	18
1.3	JONSWAP spectra for $H_s = 4\text{m}$ and $T_z = 6\text{s}$ with $\gamma = 1$ (blue) and $\gamma = 3.3$ (red) [Vorpahl et al., 2013]. S is the spectral density, representing the energy distribution of wave according to the frequency.	19
1.4	Wave Scatter Diagram for a Dutch North Sea site and a range of wind speeds between 9 m/s and 11 m/s [Vorpahl et al., 2013].	19
1.5	Power-law wind speed distribution [Bussolati, 2019].	20
1.6	Bar chart of average wind speeds fitted by a Weibull distribution [Vorpahl et al., 2013].	20
1.7	Possible FOWT designs [Hall, 2013].	21
1.8	Catenary-shaped system of mooring lines (www.abc-moorings.weebly.com).	22
1.9	Different typologies of wire ropes. (a): A spiral strand wire rope: it has layers of wires in circles around a single core wire or a grouped wire core [Judge et al., 2012]. (b): A six-strand wire rope: it is composed by strands wrapped helically. The first type is more adopted in offshore industry for permanent applications.	24
1.10	Possible contact configurations between wires in a wire rope [Lalonde et al., 2017b]. (a): Lateral line contact within layers. (b): Trellis point contact between layers.	25

1.11	Decomposition of the external traction force on a single wire [Papailiou, 1995].	27
1.12	Wire rope cross-section [Bussolati, 2019].	27
1.13	Transversal equilibrium of a curved wire element [Bussolati, 2019]	28
1.14	Moment-curvature diagram for a single layer strand in a loading-unloading cycle. Due to friction phenomena affecting bending stiffness, the behavior results hysteretic [Papailiou, 1995].	29
1.15	RVE identification in a periodic spiral strand structure [Ménard and Cartraud, 2021].	30
1.16	Solid mesh used in [Zhang and Ostoja-Starzewski, 2016] for the modeling of a single-layer rope with 7 wires.	31
1.17	Finite element model of a six-layer wire rope [Bussolati, 2019].	32
1.18	Interlayer sliding in the tension-curvature range of interest [Bussolati, 2019].	32
1.19	Frictional contact problem setting between two elastic solid bodies.	34
1.20	Coulomb frictional law for a given normal pressure F_n . (a): Frictional force threshold. (b): Frictional force flow rule.	36
1.21	Coulomb's cone representation in 2D for a given normal pressure F_n	37
1.22	Regularization of Coulomb's friction law [Wriggers and Laursen, 2006] with functions φ^i describing the smooth transition from sticking to sliding. Function φ^1 corresponds to a square root regularization, φ^2 is a hyperbolic tangent regularization and φ^3 is piece-wise linear regularization.	37
1.23	Arrangement of the snapshots.	56
2.1	Global scale model representation in Deeplines TM of the considered FOWT [Bussolati, 2019]. (a): Side view of the global model. (b): Top view of the global model representing the mooring lines numbering and their position with respect to the wind direction.	77
2.2	Wave elevation used for the global computation in [Bussolati, 2019].	79
2.3	Loadings used in [Bussolati, 2019] in the local model coming from the global computation. (a): Axial strain ε_c . (b): Curvature κ_c	79
2.4	Finite element model of the six-layer wire rope used in [Bussolati, 2019].	80
2.5	Projection of a cable layer into a 2D rectangular grid.	81
2.6	Contact status on the different layer interfaces at the minimum curvature. The blue cross stands for sticking conditions, the red circle for sliding conditions.	82
2.7	Contact status on the different layer interfaces at the maximum curvature. The blue cross stands for sticking, the red circle for sliding conditions.	83
2.8	Preload contact quantities for layer interface 3-4. (a): Normal contact forces. (b): Tangential contact forces norm. (c): Inter-wire slip norm.	83
2.9	Preload contact quantities for layer interface 4-5. (a): Normal contact forces. (b): Tangential contact forces norm. (c): Inter-wire slip norm.	84

2.10	Time evolution of contact quantities for layer interface 4-5 (in $z = 0$) at specific angular positions. (a): Normal contact forces. (b): Tangential contact forces norm. (c): Inter-wire slip norm.	85
2.11	Tangential beam directors \underline{t}_1 and \underline{t}_2 for two wires in point contact.	86
2.12	Relative approximation error for the normal contact forces between the wires of adjacent layers. (a): Global reducibility. (b): Detail on the first modes.	86
2.13	Relative approximation error for the tangential contact forces between the wires of adjacent layers. (a): Tangential beam director \underline{t}_1 . (b): Tangential beam director \underline{t}_2	87
2.14	Relative approximation error for the norm of the tangential contact forces between the wires of adjacent layers. (a): Global reducibility. (b): Detail on the first modes.	88
2.15	Relative approximation error for the inter-wire slip between the wires of adjacent layers. (a): Tangential beam director \underline{t}_1 . (b): Tangential beam director \underline{t}_2	89
2.16	Relative approximation error for the norm of inter-wire slip between the wires of adjacent layers. (a): Global reducibility. (b): Detail on the first modes.	89
2.17	First three space modes for the normal contact forces between layers 4-5. (a): Space mode 1. (b): Space mode 2. (c): Space mode 3.	90
2.18	First three time modes for the normal contact forces between layers 4-5. (a): Time mode 1. (b): Time mode 2. (c): Time mode 3.	90
2.19	First three space modes for the tangential contact forces between layers 4-5. (a): Space mode 1. (b): Space mode 2. (c): Space mode 3.	91
2.20	First three time modes for the tangential contact forces between layers 4-5. (a): Time mode 1. (b): Time mode 2. (c): Time mode 3.	91
2.21	First three space modes for the inter-wire slip between layers 4-5. (a): Space mode 1. (b): Space mode 2. (c): Space mode 3.	92
2.22	First three time modes for inter-wire slip between layers 4-5. (a): Time mode 1. (b): Time mode 2. (c): Time mode 3.	92
2.23	Plateau space modes for the inter-wire slip between layers 3-4. (a): Space mode 100. (b): Space mode 150.	93
2.24	Plateau space modes for the inter-wire slip between layers 4-5. (a): Space mode 100. (b): Space mode 180. (c): Space mode 250.	93
3.1	1D benchmark problem. (a): Graphical representation of the problem. (b): External traction force time evolution.	101
3.2	A wire from the external layer in contact with the internal layer [Bussolati, 2019]. Note that the inner wires are replaced by an homogenized beam of equivalent axial stiffness.	101
3.3	Displacement snapshots at time $t = 0$ s, $t = 0.5$ s and $t = 1$ s for load case 1.	103

3.4	Velocity snapshots at time $t = 0$ s, $t = 0.5$ s and $t = 1$ s for load case 1.	103
3.5	Frictional forces snapshots at time $t = 0$ s, $t = 0.5$ s and $t = 1$ s for load case 1.	104
3.6	SVD space modes 1, 3 and 7 of the frictional contact forces for load case 1.	104
3.7	SVD time modes 1, 3 and 7 of the frictional contact forces for load case 1.	105
3.8	Frictional forces snapshots at time $t = 0$ s, $t = 0.5$ s and $t = 1$ s for load case 2.	105
3.9	SVD space modes 1, 3 and 7 of the frictional contact forces for load case 2.	105
3.10	Relative approximation error (3.1) of the contact quantities of the 1D problem in Figure 3.1 for the two different load cases.	106
3.11	Reference structure problem being considered.	110
3.12	Decomposition of a structure in substructures and interfaces.	111
3.13	Forces and displacements acting on an interface $\Gamma_{EE'}$	113
3.14	Abstract schematic representation of an iteration of the LATIN.	115
3.15	Representation of the linear problem on a substructure with the “spring distribution” k^- on the boundary.	117
3.16	Schematic representation of the LATIN indicator η and reference error η_{ref} .	122
3.17	Space-time distribution of frictional forces along some LATIN iterations and reference solution.	124
3.18	LATIN convergence and error indicators.	125
3.19	Influence of the search direction parameter k	125
3.20	Substructured 1D problem into 5 substructures, with respective numbering.	126
3.21	Monoscale LATIN-DDM applied to the substructured 1D problem represented in Figure 3.20.	127
3.22	Convergence curves and PGD basis analysis for the LATIN-PGD(θ) strategies.	135
3.23	MAC diagrams for auxiliary space modes $\{\underline{L}_{E,k}\}$ along the iterations of the LATIN method.	137
3.24	MAC diagrams for displacement space modes $\{\underline{Z}_{E,k}\}$ along the iterations of the LATIN method.	137
3.25	MAC diagrams for contact force space modes $\{\underline{G}_{E,k}\}$ along the iterations of the LATIN method.	137
3.26	Convergence curve and PGD basis analysis for the LATIN-PGD(ζ) strategy.	138
4.1	Affine macrobasis $\{e_i^M(\underline{x})\}_{i=1,\dots,4}$ ($n_M = 4$) for an interface $\Gamma_{EE'}$	147
4.2	Monoscale and multiscale LATIN convergence indicator for different number of substructures.	154
4.3	Frictional forces distribution after 10 iterations of the full LATIN (without PGD) for the monoscale and the multiscale approach.	155
4.4	Convergence curve and PGD basis analysis for the multiscale LATIN-PGD(ζ) strategy.	156
4.5	Representation of substructures and interfaces, with numbering of the substructures and highlight of the contact interface Γ_c	157

4.6	Time evolution of prescribed external forces. Highlight of time instants A ($t = 0.5$ s) and B ($t = 1.5$ s).	157
4.7	Spatial distribution of the frictional forces and their macropart along Γ_c at time instant A.	158
4.8	Relative sliding along the contact interface Γ_c at time instants A and B.	159
4.9	LATIN indicator of the multiscale approach compared to the monoscale one for the 2D problem.	160
4.10	Convergence state of normal (in red) and tangential (in black) forces and displacements at time instant A for interface $\Gamma_{c,1-7}$ through the LATIN iterations.	161
4.11	LATIN convergence indicator of full LATIN and LATIN-PGD(ξ).	162
4.12	PGD basis size along the iterations for the LATIN-PGD(ξ) strategy.	163
4.13	Linear stage normal and tangential forces at time instant A for interface $\Gamma_{c,1-7}$ for the LATIN-PGD(ξ) strategy at two different number of iterations.	164
4.14	Computational cost of the linear stage of the LATIN-PGD(ξ), LATIN-PGD(ξ)+D and full LATIN.	164
4.15	PGD basis size of LATIN-PGD(ξ) and LATIN-PGD(ξ)+D for substructures 7 to 12.	165
5.1	Representation of the classical LATIN convergence indicator η and reference error indicator η_{ref} .	173
5.2	Graphical representation of the CRE indicator ν proposed in [Passieux, 2008]. It represents the distance between manifold $\Gamma^{[0,T]}$ and a solution belonging to $\mathbf{A}_d^{[0,T]}$.	173
5.3	2D test case with opening of frictional cracks.	176
5.4	Evolution of the indicators η and ν for the problem in Figure 5.3.	176
5.5	Evolution of the indicators η and ν for the problem in Figure 5.3 with $k = k_0$.	178
5.6	Evolution of the indicators η and ν for the problem in Figure 5.3.	178
5.7	Structure with frictional cracks in compression and bending.	179
5.8	Evolution of the indicators η and ν for the problem in Figure 5.7.	180
5.9	2D structure with a crack under mixed mode loading with numbering of subdomains and prescribed forces.	181
5.10	Reference solution at different time instants. (a): $t = 0$ s. (b): $t = 5$ s. (c): $t = 10$ s.	181
5.11	Evolution of the convergence and error indicators for the problem in Figure 5.9. (a): For $k = 0.1 k_0$. (b): For $k = k_0$. (c): For $k = 10 k_0$.	182
5.12	Contact status evolution over time for contact interfaces Γ_{2-7} and Γ_{4-9} at convergence. (a): sticking/sliding status of Γ_{2-7} . (b): contact/opening status of Γ_{4-9} .	183
5.13	Contact front evolution on interfaces Γ_{2-7} and Γ_{4-9} for the solution obtained with $k = k_0$. (a) and (b): convergence threshold $\eta_0 = 10^{-3}$. (c) and (d): convergence threshold $\nu_0 = 10^{-2}$.	184

5.14	Contact front evolution on interfaces Γ_{2-7} and Γ_{4-9} for the solution obtained with $k = 10 k_0$. (a) and (b): convergence threshold $\eta_0 = 10^{-3}$. (c) and (d): convergence threshold $\nu_0 = 10^{-2}$	185
5.15	Contact front evolution on interfaces Γ_{2-7} and Γ_{4-9} for the solution obtained with $k = 0.1 k_0$. (a) and (b): convergence threshold $\eta_0 = 10^{-3}$. (c) and (d): convergence threshold $\nu_0 = 10^{-2}$	186
5.16	Structure with frictional cracks. (a): In traction. (b): In compression.	189
5.17	LATIN indicator η and CRE indicator ν for the problem in Figure 5.3 with reference search direction $k_0 = \frac{E}{L_F} \mathbf{I}$. (a): Traction case. (b): Compression case.	190
5.18	LATIN indicator η and CRE indicator ν for the problem in Figure 4.5. (a): $k_t = k_0$. (b): $k_t = 0.1k_0$	191
5.19	Convergence indicators η_W , η_F and ν for the problem in Figure 3.1a.	195
5.20	Evolution of the indicators η_W , η_F and ν for the problem in Figure 3.1a with constant search direction k_0 and with updating at a threshold $\mathcal{I}_0 = 10^{-2}$	197
5.21	Tangential contact status and search direction at updating. (a): Tangential contact status $\mathcal{T}(\underline{x}, t)$. (b): Updated search direction $k(\underline{x}, t)$	198
5.22	Force reference error η_F with constant k_0 and with updating at different thresholds: $\mathcal{I}_0 = 10^{-1}$, $\mathcal{I}_0 = 10^{-2}$ and $\mathcal{I}_0 = 10^{-3}$	198
5.23	Force reference error η_F with constant k_0 and with updating once and twice with $\mathcal{I}_0 = 10^{-2}$ and by updating at each iteration.	199
5.24	CRE indicator ν in the cases of updating both $k^+ = k^-$ and updating only k^- with a threshold $\mathcal{I}_0 = 10^{-2}$ and relaxation parameter $\mu = 0.5$	199
5.25	CRE indicator with updating of k^+ for the problem in Figure 5.3 with two different relaxation parameters μ	201
5.26	New and old updating strategy tested on the problem in Figure 5.3.	201
5.27	Updating strategy for the problem in Figure 5.7.	202
5.28	Updating strategy for the problem in Figure 5.9.	203
5.29	Updating strategy for the problem in Figure 4.5.	204
5.30	Tangential contact status (white for sliding and black for sticking) in space and time for interface $\Gamma_{1,7}$. (a): at first update. (b): at convergence.	205
5.31	PGD basis with and without update.	205
B.1	Modification of the classical approximations of the interface forces (FE approximation of order m) and local displacements along the boundary of a substructure (FE approximation of order p): h-version and p-version [Ladevèze et al., 2002].	226

List of Tables

2.1	Number of spatial positions where contact quantities are evaluated on the different layers interfaces.	85
3.1	Used parameters for the benchmark problem.	102
3.2	Resolution of the local stage for a frictional contact interface.	121
3.3	Different LATIN-PGD strategies investigated throughout the manuscript.	134
4.1	Parameters for the two-dimensional problem.	158
5.1	Parameters of the problem in Figure 5.3.	175
5.2	Number of LATIN iterations to reach a given convergence threshold for η and ν with different values of the search direction parameter k	183

List of Algorithms

1	Uzawa algorithm	48
2	Progressive Galerkin-PGD: fixed-point scheme	59
3	Optimal Galerkin-PGD: fixed-point scheme	60
4	Parameter function update stage	60
5	Enrichment stage: new pair of PGD modes	131
6	Multiscale LATIN-DDM	153
7	Downsizing stage	231

List of Symbols

Tensor and differential calculus

First order tensors underlined : displacement field \underline{u} , position vector \underline{x} , ...

Higher order tensors in bold : small deformation tensor $\boldsymbol{\varepsilon}$,

Cauchy stress tensor $\boldsymbol{\sigma}$, Hooke's tensor \boldsymbol{K} , identity tensor \mathbf{I}_d ...

- \wedge : vector product
- \otimes : tensor product
- \cdot : simple contraction product
- $:$: double contraction product
- ∇ or $\frac{\partial}{\partial \underline{x}}$: gradient
- div : divergence
- $\boldsymbol{\varepsilon}(\underline{u})$: symmetric part of the gradient of \underline{u}
- $\dot{\underline{u}}$ or $\frac{\partial}{\partial t}$: derivative of \underline{u} with respect to time t

Algebraic notation

Vectors in bold : \mathbf{x} , ...

Matrices in double capital letters : \mathbb{A} , ...

- $\mathbb{R}^{n \times m}$: space of real matrices of size $n \times m$
- \mathbf{x}^T : transpose of \mathbf{x}
- \mathbb{A}^T : transpose of \mathbb{A}
- \mathbb{A}^{-1} : inverse of \mathbb{A}
- \mathbb{I}_d : identity matrix
- $Ker(\mathbb{A})$: kernel of \mathbb{A}
- $Im(\mathbb{A})$: image of \mathbb{A}
- $Tr(\mathbb{A})$: trace of \mathbb{A}

Topology

- \bar{A} : closure of A
 $\overset{\circ}{A}$: interior of A
 ∂A : boundary of A
 $A \setminus B$: complementary of B in A
 $mes(A)$: measure of A

Sets

- $\{x \in X \mid P\}$: subset of the $x \in X$ which verify P
 $Card(\mathbf{I})$: cardinality of the finite set \mathbf{I}
 $X \times Y$: cartesian product of the sets X and Y
 $\prod_{i \in \mathbf{I}} X_i$: cartesian product of sets $\{X_i\}_{i \in \mathbf{I}}$

Vector spaces

- $X + Y$: sum of two vector spaces X and Y
 $X \oplus Y$: direct sum of two vector spaces X and Y
 X^\perp : orthogonal of X
 $span(\{\mathbf{x}_i\}_{i \in \mathbf{I}})$: vector space spanned by the vectors $\{\mathbf{x}_i\}_{i \in \mathbf{I}}$

Applications

- $f : \begin{array}{l} X \rightarrow Y \\ x \mapsto f(x) \end{array}$: application which maps $x \in X$ to $f(x) \in Y$
 $f|_A$: restriction of $f : X \rightarrow Y$ on $A \subset X$
 $\frac{\partial f}{\partial x}(y)$ ou f'_y : gradient of $f : x \mapsto f(x)$ in y
 $f \circ g$: composite application of f and g

Functional spaces

Let O be an open set of \mathbb{R}^n , X a Banach space.

- $\| \cdot \|_X$: natural norm on X
- $\langle \cdot, \cdot \rangle_X$: natural scalar product on X
- $L^2(O; X)$: $\{u : O \rightarrow X \mid u \text{ measurable in } O \text{ and } \int_O \|u(x)\|_X^2 < \infty\}$
- $L^2(O)$: $L^2(O; \mathbb{R})$
- $H^1(O)$: Sobolev space of order 1
- $\mathcal{P}_k(O; X)$: polynomial of order k in $O \subset \mathbb{R}$ with coefficients in X
- $\mathcal{C}^k(O)$: applications k times differentiable in O

Introduction

In the context of the challenges posed by the energetic transition, the development of offshore wind power expected over the next few years is considerable: from 6.5 GW of current installed capacity to a target of 16.5 GW by 2030 [GWEC, 2023]. Among offshore structures, Floating Offshore Wind Turbines (FOWTs) offer the advantage of being installable in deeper waters, harnessing more consistent winds, and requiring less material and simpler installation processes than fixed foundation structures [GWEC, 2023]. The exploitation of FOWTs requires the development of concepts combining high-power turbines (around 22 MW on average [IEA, 2023]) with suitable mooring systems for connecting them to the seabed (Figure 1), as well as proper solutions for connecting them to the grid. Among challenges to be met for these connections, the control and prediction of mooring lines failure events as well as the optimization of loads on the power cable systems which are subject to movements of the float and currents is crucial as the loads are uncertain and highly nonlinear.



Figure 1: Principles of FOWTs with their mooring lines. *Image by Josh Bauer, NREL.*

A FOWT is essentially composed of a wind turbine mounted on a foundation, which is anchored to the seabed with mooring lines that limit its movements and rotations. This station keeping role of mooring lines ensures the operational production of the turbine and preserves the power cables and other wind turbines installed nearby. Mooring lines can be composed of chains, spiral strand steel wire ropes or, more recently, synthetic fiber ropes. Despite their large application, chains are at the origin of many failures, mostly because of out of plane bending and corrosion. Fiber ropes long term behavior for permanent mooring lines applications is still investigated [Davies et al., 2008; Sørnum et al., 2023] because of their complex nonlinear constitutive law possibly involving creep phenomena. In this context, spiral strand steel wire ropes are still providing an interesting well known solution of mooring lines for FOWTs, as illustrated by their use for the Hywind Tampen wind farm [ArcelorMittal, 2021]. An example of spiral strand steel wire rope made of steel wires, which is actually coming from a stay cable bridge but with similar architecture to that of mooring lines, is shown in Figure 2.

Despite the benefits of floating structures over fixed ones, mooring lines still remain a weak point: failures in these lines are a significant issue, leading to complex and costly maintenance and repair operations. Specifically, fatigue failures in the steel cables near socket ends are common, as these areas are subjected to complex tension and bending loads from wave motion over time, causing fretting fatigue between the steel wires [Fontaine et al., 2014]. However, their fatigue life expectancy is not clearly established, due to an approach based on these days still on empirical laws [Rossi, 2005; Maljaars and Misiak, 2021]. The mechanical response of the rope is highly dependent on the frictional contact interactions between the wires, and fatigue is largely determined by the local frictional contact conditions between two intersecting wires triggering fretting fatigue [Montalvo et al., 2023]. As these cables can undergo significant bending under the effect of float movements, geometric nonlinearities must also be taken into account.

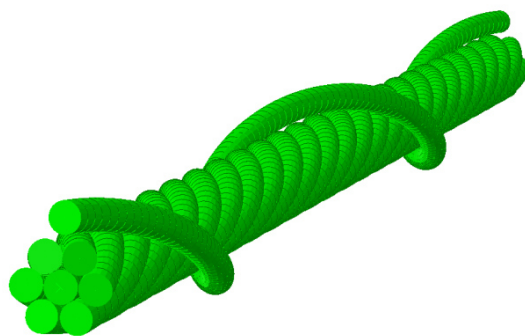


Figure 2: 3D view of a finite element model of a steel spiral strand cable of 60.4 mm diameter [Bussolati, 2019].

Another type of context for which a similar multiscale Finite Element modeling could also be of value is that of dynamic (i.e., submitted to floating foundation motion

and wave plus submarine current loading) power cables between floating wind turbines. Power cables are generally three-phase, with the three conductors being assemblies of copper or aluminium wires, wound helically around a central wire in a spiral strand (Figure 3). They are surrounded by a layer of polymeric insulation and metal foil to provide complete electrical insulation and hydraulic seal. The assembly is surrounded by sheaths and layers of metal armouring to take up the mechanical traction.

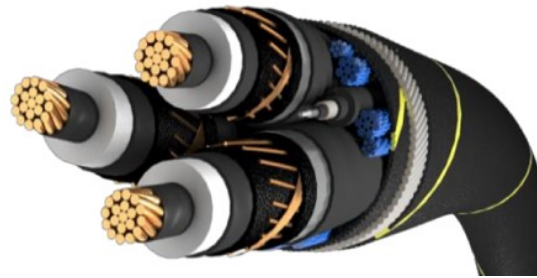


Figure 3: Example of the cross-section of a dynamic three-phase cable. *JDR Cables systems*.

In the literature, most of the work on the design of FOWT spiral strand cables concerns the optimization of the overall configuration of a cable (sections of different linear masses and floats), using hydrodynamic simulations with dedicated solvers to satisfy some limit states (extreme conditions [Poirette et al., 2017] or fatigue [Rentschler et al., 2019]). At this scale, a homogenized cable model is generally used (see for example [Leroy et al., 2017] or [Saadat and Durville, 2023]) for spiral cables based on beam or bar kinematics. The aim of this overall design, for a given environmental state, is to seek the least-cost configuration while limiting curvature and elongation, and avoiding compression.

A major limitation of these approaches is that the limit states (maximum permissible thresholds) are based on manufacturers' empirical knowledge (not necessarily representative of future floating farm conditions) and/or on experimental tests that are difficult to extrapolate. Furthermore, these approaches do not distinguish between limit states for each component of the cable. To remedy this, work has been done to propose finite element models simulating the loading on cable components, nevertheless still resorting to proper simplifications because of the high computational cost of the required simulations [Young et al., 2018; Nicholls-Lee et al., 2021].

Proposing a model on a finer scale of description, at the scale of strands, wires or components of a cable, may be necessary but leads to simulations whose calculation costs quickly become prohibitive. The complexity stems in particular from the fact that a cable's time history of tension and bending results in relative sliding between its components, driven by contact and friction phenomena. This makes it particularly difficult to establish design laws based on simplified experimental tests for this type of conditions (unlike in the case of pure tension). This difficulty is likely to result in failure rates which exceed the expected limits. Replacing these empirical laws with multiscale

modelling, enriched by the physics describing the behavior of each component of the cable is necessary, at least to increase the level of understanding of the essential mechanisms that need to be taken into account for the design of such structures. A hydrodynamic calculation on the global scale of the cable can be used to identify critical traction and bending zones. It is then possible to make use of a local model on a smaller scale, on the scale of components, strands, and wires for a section of a metric length cable section. However, a numerical local model able to properly estimate what happens inside a wire rope subjected to tension and bending, balancing accuracy and computational costs, still lacks in the industry.

A step forward in this direction was made in [Bussolati, 2019; Bussolati et al., 2019; Guidault et al., 2019; Bussolati et al., 2020; Guidault et al., 2021], where a finite element model of this case study has been developed to efficiently simulate the loading on part of a mooring line of a FOWT for a given sea state (Figure 2). It was shown that, by assuming small sliding and large rotations between the wires of the rope (modeled by beams), the proposed model makes it possible to predict the mechanics of the wires with a reduced computational cost by comparison with a contact and friction algorithm in large sliding (see also [Guiton et al., 2022] for a comparison of this model to large sliding ones in reproducing an experimental test).

The goal in [Bussolati, 2019] was to build a tool, represented in the flowchart in Figure 4, which takes into account tension and bending and predicts the fatigue damage along each mooring line, considering local stress variations linked to the contact interactions between the wires. However, the use of this model in an industrial setting, taking into account the very large number of loading cases representing the different wind and sea conditions over a period of several years, requires the use of alternative, efficient and robust numerical strategies. In this perspective, the use of model reduction techniques to further reduce the computation time of this type of problem may be an interesting solution.

Over the years, Reduced-Order Models (ROM) have proven themselves as reliable tools in reducing computational complexity in the context of linear and nonlinear problems, and consist in constructing a reduced order basis (ROB) in which the partial differential equations of the problem are projected [Chinesta et al., 2011; Hesthaven et al., 2016]. These methods allow a saving in computation time of several orders of magnitude, especially when the dimension of the problem is large, in space, time or parameters. Nevertheless, the application of model reduction for structural problems involving a large number of evolving frictional contact interactions and providing output on contact and friction quantities with ensured accuracy remains a largely open question [Giacoma et al., 2015; Balajewicz et al., 2016; Fauque et al., 2018; Cardoso et al., 2018; Benaceur et al., 2020].

ROM methods can be distinguished by the way in which the ROB is constructed. A first family of techniques, named *a posteriori* methods, involves a training phase, called offline phase, where the full-order problem is solved for some particular time instants or parameter values, generating the so-called snapshots. Snapshots are then used to

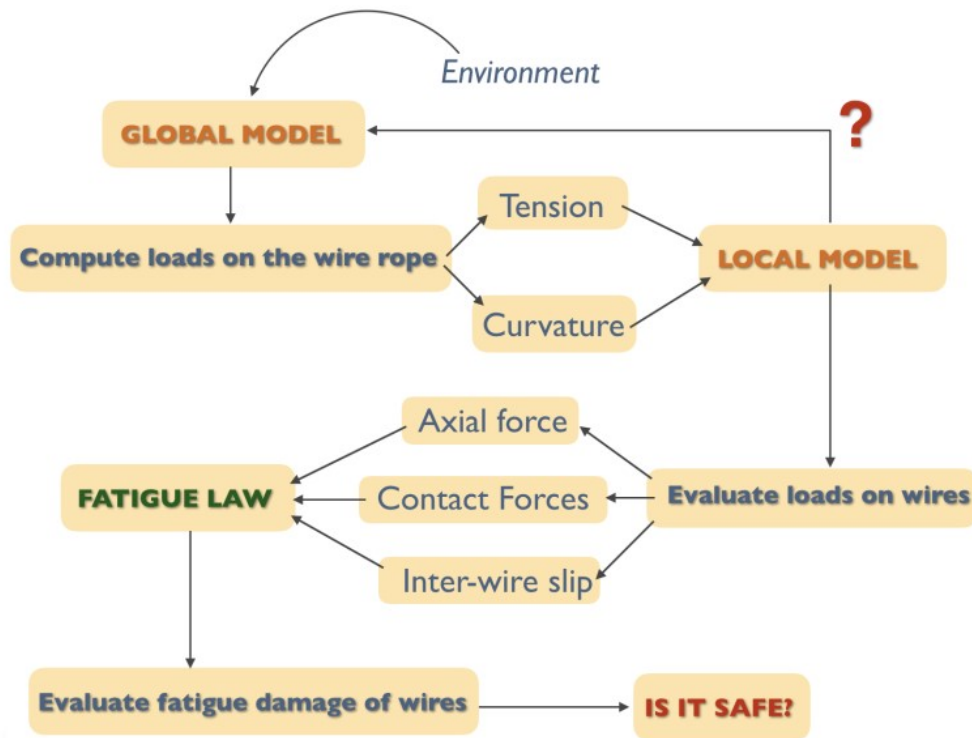


Figure 4: General flowchart of a multiscale approach to compute fatigue damage in wire ropes [Bussolati, 2019]. In this thesis we will focus on accelerating local model simulations.

create a ROB on which to project the full-order equations and obtain a reduced-order model. The most classical way to obtain a ROB from a given set of snapshots is the Proper Orthogonal Decomposition (POD) [Chatterjee, 2000]. Nevertheless, the quality of the ROM is strongly affected by the representativeness of the ROB, especially for highly nonlinear problems. A second family of ROM techniques consists in seeking the solution of the targeted problem in the span of a consistent ROB progressively built by a dedicated algorithm during the solving stage. This represents the a priori model reduction methods, where no offline training phase is required. To this family belongs the Proper Generalized Decomposition (PGD) [Nouy, 2010; Chinesta et al., 2011].

A predetermined ROB may not easily and efficiently capture non-regular and propagating multiscale phenomena that occur at contact interfaces: sliding, sticking and separation zones being difficult to follow. For this reason, an a priori approach based on the PGD [Nouy, 2010] may represent a more efficient way to tackle frictional contact problems through a reduced-order model that allows the ROB to be enriched during computations to account for the evolution of frictional contact conditions.

Furthermore, strand cables present a structured geometry and naturally exhibit a multiscale behavior. On a macroscale, their behaviour depends on tension and bending variations associated with environmental loads, generally varying around mean values

(they are represented by Gaussian processes in offshore dedicated multiphysics softwares like Deeplines WindTM [DeepLines, Principia] or OpenFAST [OpenFAST, NREL]). This behavior is characterized by a distribution of loads with gradients according to the layer of wires (e.g., increase of contact pressure from outer layer to the central wire) and according to the relative location with respect to the bending axis (sliding maximum at the bending axis and decreasing towards the outer and inner-arc locations). At the microscale, the behavior depends on the friction phenomena between the wires making up the cable. A multiscale computational strategy of the DDM type will be therefore examined in order to further improve performances. We will be interested in particular in the mixed DDM [Ladevèze and Nouy, 2003; Ladevèze et al., 2007; Ladevèze et al., 2010] based on the LATIN method [Ladevèze, 1999].

The LATIN presents a robust treatment of contact conditions, sharing similarities with augmented Lagrangian approaches [Simo and Laursen, 1992], and naturally leads to a mixed DDM. In addition, the global space-time formulation of the method allows PGD-based model reduction to be used during computations, creating and adapting (i.e., adding or retrieving some modes) on-the-fly reduced bases per substructure to better track sliding fronts and propagative phenomena. The introduction of a multiscale strategy in the LATIN framework is consistent with the physics of contact problems, in which phenomena with different wavelengths interact: local solutions at contact interfaces presents high gradient effects with a short wavelength compared to the characteristic length of the structure [Giacoma et al., 2014; Guidault et al., 2023]. By taking advantage of this, the coarse scale problem of the strategy enables to capture efficiently the behavior of the problem at the structural level, focusing then on capturing the local contact variations at the contact interfaces.

The aim of this thesis is to propose an approach to model reduction appropriate to this type of problem, reducing computation time as much as possible while faithfully representing the useful characteristic information. The crucial point of the thesis is that the reduced model will have to represent very faithfully the critical information located on the frictional interfaces between the wires because, apart from particular environmental conditions such as corrosion, the fatigue of strand cables is largely determined by the fretting fatigue between the wires [Montalvo, 2023; Montalvo et al., 2023].

The development of model reduction and DDM tools is generally very intrusive and requires the use of a relatively “open” calculation code. Recent developments in industrial contexts include model reduction based on the LATIN-PGD technique for nonlinear problems implemented in Simcenter SAMCEF software of Siemens [Scanff et al., 2022], or the LATIN-based mixed DDM implemented in *Code_Aster* of EDF R&D [Oumaziz et al., 2017; Oumaziz et al., 2018]. Here, we will work and develop on SCoFiEIDD (Structure Computation with Finite Elements and Domain Decomposition), an in-house MATLAB code, with the feasibility of the approach that will be illustrated through 2D simplifications of different layers of a metric segment of anchor cable in

frictional contact with each other.

To exemplify the feasibility of the method, the first step will be to verify the possibility of reducing the solution of a tension and bending calculation on a metric cable section with the developed model described in [Bussolati, 2019; Bussolati et al., 2019; Guidault et al., 2019; Bussolati et al., 2020; Guidault et al., 2021], for a given sea state. For this local calculation on a cable section, the imposed tension and curvature histories are obtained from a global calculation on a floating wind structure carried out in a previous work at LMPS in collaboration with IFP Energies nouvelles [Bussolati, 2019]. An a posteriori SVD analysis of the local calculation solution at different time steps will enable to assess its ability to be reduced. Moreover, the possibility of separating space and time scales, which can be exploited during the model reduction approach, will be investigated.

A second step, which constitutes the core of the thesis, will be devoted to development of a PGD approach to this model, exploiting the separation in space domain through DDM. We'll be looking for maximum reduction performances and convergence speed, with a multiscale computational strategy of the DDM type adapted to contact, while guaranteeing at the same time an accurate evaluation of interface quantities.

Within the target application on FOWTs, several scientific challenges arise. First of all convergence criteria for the nonlinear solution method must assure a good convergence for local contact quantities: a global convergence criterion does not ensure local convergence of the interface quantities, which are crucial for fretting fatigue life prediction. Moreover, the LATIN convergence rate for contact problems strongly depends on search directions, and updating search directions is a challenging issue [Sun et al., 2008]. Another issue concerns the efficient treatment and accurate representation of the multiscale content for contact interface quantities. Moreover, for highly irregular problems such as frictional contact problems, controlling the quality and size of progressively built PGD basis along the LATIN iterations is crucial for the efficiency of the method.

Manuscript outline

The manuscript is organized in five chapters.

- In **Chapter 1**, we present a bibliographic study in the fields involved in this study. We start with a description of FOWTs and the characterization of the main environmental actions to which they are subjected to, as in fact they represent the ultimate motivation of the thesis. We then focus on the mechanics of spiral strand cables, reporting some analytical results available in the literature as well as the most common computational methods to model them, and their current limitations. This first part of the literature review is also important to understand the subsequent **Chapter 2**, as well as the remaining chapters where we make use of simplified models inspired by the mechanics of wire ropes. Then we deal

with frictional contact problems, with the various formulations and numeric methods commonly adopted to tackle them. Afterwards we give an overview on model reduction techniques and the main strategies to deal with frictional contact problems and their current limitations. Finally, we talk about domain decomposition methods for structural problems.

- In **Chapter 2**, we perform a preliminary SVD analysis on the results from [Bus-solati, 2019] on a six-layer strand cable portion subject to oscillating tensile and bending loads around a preloaded state. It consists of an a posteriori separability analysis to check the potential reducibility of this kind of problem and the suitability to the methods that we will use. The SVD is employed to analyze the reducibility of the most significant quantities in the model, such as inter-wire slip and normal and tangential forces between the different layers. The results are very encouraging as these problems result to display a very good potential for reducibility.
- In **Chapter 3** we introduce the strategy based on the LATIN to solve frictional contact problems and introduce PGD-based model reduction. Prior to introducing the strategy, a simple but representative one-dimensional frictional problem, inspired by the mechanics of a single wire of the spiral strand cable, and its reference solution are presented, which will later serve as basis for an explanation of the features of the method. Thereafter, the LATIN method, in its monoscale DDM version, is introduced and is then applied to the test problem. The strengths of the method are highlighted, as well as some specific points related to frictional contact problems that require further improvements. The introduction of PGD in the LATIN scheme is then detailed and applied to the test problem, with focus on properly controlling the PGD basis size and quality along the iterations.
- In **Chapter 4**, we present the multiscale strategy to model reduction for frictional contact problems. Multiscale aspects are introduced at the interface level by exploiting a separation of scales between macroquantities and microquantities. Then the introduction of PGD in the multiscale framework is described. The most important features of the approach are shown comprehensively on the one-dimensional frictional benchmark problem, emphasizing the possibility to create reduced bases of different size between subdomains with the coarse scale problem of the multiscale strategy which well captures the first structural modes. Then, its robustness and effectiveness are tested on a layered structure with wide frictional contact interfaces subjected to more complex loadings, representative of the considered application. Here we focus on how to exploit the multiscale strategy to get the maximum reduction in terms of computational cost while ensuring accurate representation of interface quantities.
- In **Chapter 5**, we propose some contributions to the strategy concerning some crucial aspects for the final application, that is the control of the error on the

interface quantities along the iterations of the LATIN nonlinear solver and the improvement of the convergence rate for microscopic interface contact quantities, which are driven by the search directions of the LATIN. In particular, a convergence indicator independent from the search directions is investigated. The effectiveness of this criterion to stop the LATIN iterations in order to obtain a solution of desired quality, independently from the adopted search direction, is shown on different frictional contact problems displaying complex and different contact status conditions. Then, a strategy for updating on-the-fly the search directions is proposed, taking advantage of the peculiarity of the LATIN solver to provide a global space-time view of the solution at each iteration, in order to speed up the convergence of the local microquantities at the interface level.

Part I

**Bibliography study and preliminary
reducibility investigation**

Chapter 1

Bibliographic study

This first chapter is devoted to a bibliographical study of the main topics of the thesis. It starts with a brief introduction to Floating Offshore Wind Turbines and how the different loads to which they are subject to are characterized. Then, an overview of the mechanics of wire ropes is given, reporting some important analytical results and the main numerical techniques used for their modeling. An important part is then devoted to frictional contact problems and model reduction techniques. The main strategies used to tackle frictional contact problems are reported, with a short introduction to the LATIN method and similarities it shares with more classical methods. Regarding model reduction, a panoramic of a posteriori and a priori techniques is given, followed by some specific cases for contact problems. Finally, a summary on domain decomposition methods in structural mechanics is provided, with a brief introduction the mixed strategy based on the LATIN method.

Contents

1	Floating Offshore Wind Turbines	16
1.1	Environment characterization	17
1.1.1	Description of the sea state	17
1.1.2	Description of the wind state	18
1.2	The floating structure	20
1.2.1	Hydrodynamic loads	21
1.2.2	Mooring system	21
2	Wire ropes	23

2.1	General description	23
2.2	Mechanical behavior	25
2.2.1	Analytical results: traction	25
2.2.2	Analytical results: bending	27
2.3	Numerical modeling	29
3	Quasi-static frictional contact problems	33
3.1	Frictional contact problem setting	33
3.2	Unilateral contact conditions	34
3.2.1	Normal contact	34
3.2.2	Tangential frictional contact	35
3.2.3	Strong formulation of the problem	38
3.2.4	Weak formulation of the problem	38
3.3	Treatment of contact constraints	40
3.3.1	Penalty method	40
3.3.2	Lagrange multipliers method	41
3.3.3	Augmented Lagrangian formulation	42
3.3.4	Nitsche method	44
3.4	Numerical strategies	45
3.4.1	Partial Dirichlet-Neumann algorithm or status method	46
3.4.2	Augmented Lagrangian and Uzawa algorithm	47
3.4.3	LATIN non-incremental method	48
4	Overview on model reduction and applications to frictional contact problems	50
4.1	Introduction to model-order reduction	50
4.2	Abstract problem	51
4.3	Proper Orthogonal Decomposition	52
4.3.1	A posteriori model reduction through Proper Orthogonal Decomposition	54
4.4	Reduced Basis Method	56
4.5	Proper Generalized Decomposition	57
4.5.1	A-priori model reduction through Galerkin-PGD	58
4.5.2	A-priori model reduction through minimal residual PGD	60
4.6	Nonlinear problems and hyperreduction	62
4.7	Model reduction in contact problems	63

5	Domain Decomposition Methods	67
5.1	Primal and dual approaches	67
5.2	Mixed domain decomposition methods	72
5.3	Domain decomposition for contact problems	73

1 Floating Offshore Wind Turbines

Floating Offshore Wind Turbines (FOWTs) are special structures consisting of a turbine, a tower, a floating platform anchored to the seabed with mooring lines, and a system of power cables to connect them to the grid. The design of a FOWT presents numerous challenges, as it requires :

- evaluating the impact of sea waves on the floater and the influence of water on the motion of the mooring lines through hydrodynamic calculations;
- estimating the effects of wind on the turbine and the tower using aerodynamic calculations;
- implementing control strategies, particularly for blade orientation and generator torque, to ensure structural safety and optimize energy production;
- solving a highly nonlinear structural dynamics problem.

Additionally, the stochastic nature of environmental loads introduces significant uncertainties in the analysis outcomes, compounded by other uncertainty sources such as material properties, model parameters and approximations, and actual installation configurations [Vorpahl et al., 2013; Bailey et al., 2014].

In Figure 1.1 is shown an example of a global hydrodynamic model of a FOWT structure consisting of the floater and the mooring lines [Bussolati, 2019]. Such an analysis requires the characterization of the wave loads and the modeling of the mooring lines, which are often represented by simple beam elements, and consequently require a homogenized constitutive behavior [Cartraud and Messager, 2006; Saadat and Durville, 2023] which is somehow representative of the behavior of a real wire rope.

This type of calculation allows the extraction of tension and curvature histories on the mooring lines for a given environmental load, going on to determine the most critical areas. The procedure is repeated for thousands of different most possible environmental loads, and provides the time series of tension and curvature used as input to determine the mean expectation of fatigue life endurance of the mooring lines based only on tension and curvature histories. However, **the fatigue life of wire ropes when subjected to bending is highly influenced by the relative succession of microsliding that occurs due to frictional phenomena resulting in fretting fatigue, which requires calculation on a more detailed wire rope model** [Raof, 1992; Montalvo et al., 2023].

In [Bussolati, 2019], a *top-down* approach has been followed, i.e., the information of the global model (tension and curvature) is used as boundary conditions for the local model. Indeed, it has been seen that the results of the local model do not appreciably influence the global behavior due to the slenderness of the wire ropes, which justifies this approach.

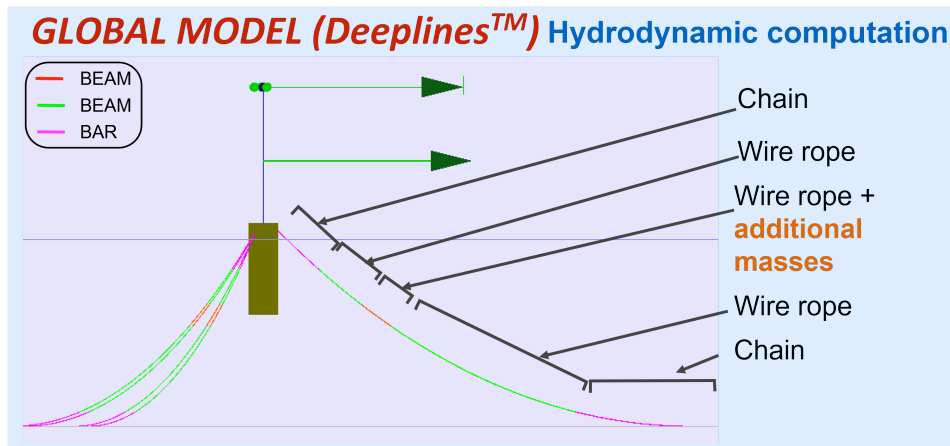


Figure 1.1: Example of a global hydrodynamic computation on a FOWT with the software Deeplines™ [Bussolati, 2019]. Note that the rectangular shape is a simplistic representation of an evolution of the hybrid spar-barge concept presented in [Poirette et al., 2014]. Different systems exist as illustrated in Figure 1.7.

1.1 Environment characterization

The main mechanical loads on a FOWT at a given site derive from the actions of the wind on the tower and the turbine and the actions of the sea on the floating structure and mooring lines (Figure 1.2). These loadings have in fact a random behavior and a statistical distribution of them can be made so as to have a prediction of the possible environmental states that can occur during the lifespan of the turbine.

1.1.1 Description of the sea state

The description of the state of the sea consists in measuring the elevation of the sea surface at a fixed position over time. This leads to a random series of data that in fact cannot be described by a single periodic wave. In spite of this, it is still possible to describe the energy state of this data series through a spectrum in the frequency domain.

A time scale separation in this spectrum can be exploited with a stationary duration which is generally of 3h (e.g., [Labeyrie, 1990]). Consequently, offshore engineering distinguishes short-term statistics (i.e., the wave elevation during a given 3h duration) and long term statistics (i.e., pluriannual). The latter is given by the joint probability of a small number of parameters of an idealized spectrum function.

The JONSWAP (Joint North Sea Wave Project) spectrum, originally defined for the North Seas and later adapted for offshore applications, is one of the most widely used in that context. In such a spectrum, the input parameters are the significant wave height H_s and the mean zero-crossing period T_z . The significant wave height H_s is

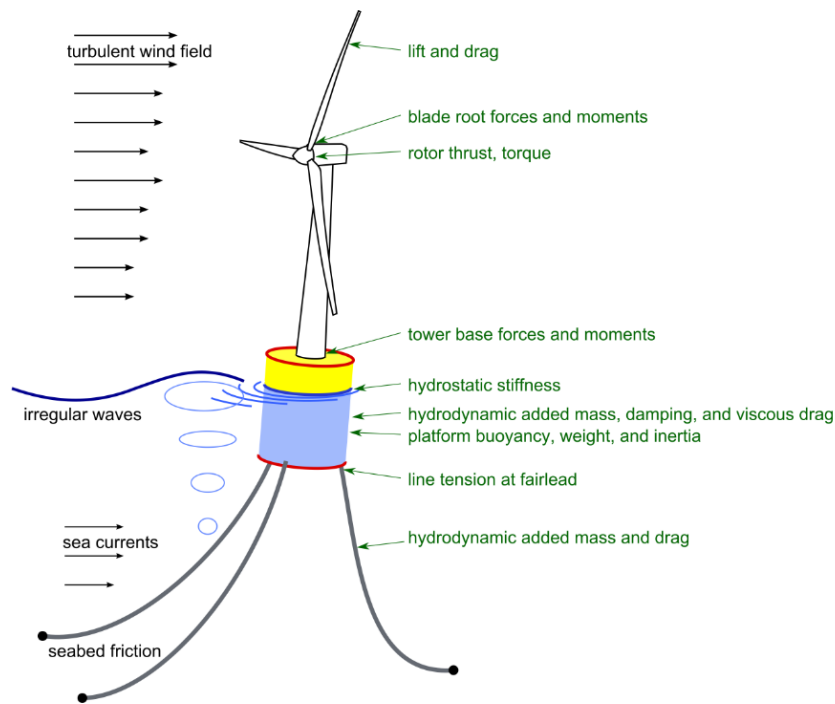


Figure 1.2: Different sources of loads acting on a FOWT [Hall, 2013].

defined as the mean height of the third highest wave in a sea state, while the mean zero-crossing period T_z represents the average period between two zero-crossing waves with positive slope in an irregular sea state, and can be determined directly by the time series. In the JONSWAP spectrum, a peak-shape parameter γ is usually used and, for a given spectrum and data T_z and H_s , the peak period T_p of the spectrum, i.e., the period associated with the highest energy in the spectrum (the spectral peak) can be derived (Figure 1.3).

To simulate a FOWT during its entire design lifetime (about 20 years for instance to estimate the fatigue life), long-term wave statistics can be used. A common approach to describe these statistics consists in making use of Wave Scatter Diagrams (WSD), which are diagrams that give the discretized joint probability of pairs of H_s and T_p in a two dimensional matrix for a range of wind speeds (Figure 1.4).

1.1.2 Description of the wind state

For the wind state, similar considerations to the sea state characterization can be made. Wind speed is generally measured at different height locations of a met mast and can be represented by a stationary process with a stationary duration of 10 minutes. The turbulence box is generated from input parameters that are composed of :

- the 10 minutes time-averaged wind speed at a given height;

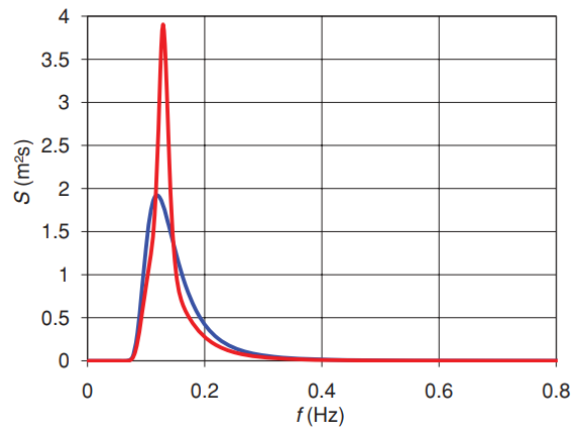


Figure 1.3: JONSWAP spectra for $H_s = 4\text{m}$ and $T_z = 6\text{s}$ with $\gamma = 1$ (blue) and $\gamma = 3.3$ (red) [Vorpahl et al., 2013]. S is the spectral density, representing the energy distribution of wave according to the frequency.

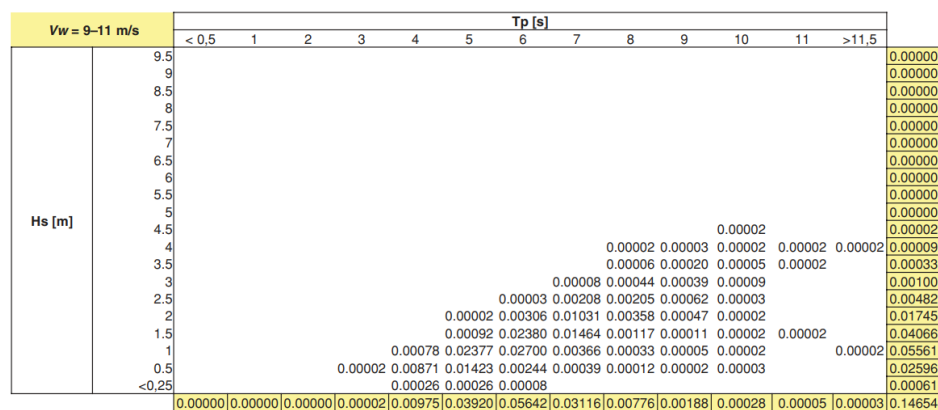


Figure 1.4: Wave Scatter Diagram for a Dutch North Sea site and a range of wind speeds between 9 m/s and 11 m/s [Vorpahl et al., 2013].

- the standard deviation representing the turbulence;
- a vertical profile with either power-law or log-normal function (Figure 1.5);
- parameters of a spectrum like Mann or Kaimal one accounting for the spatial correlation [Dimitrov et al., 2017; Rinker, 2018].

For long-term statistics, the probability of a given 10 minutes time-averaged wind speed is usually fitted by a Weibull distribution (Figure 1.6).

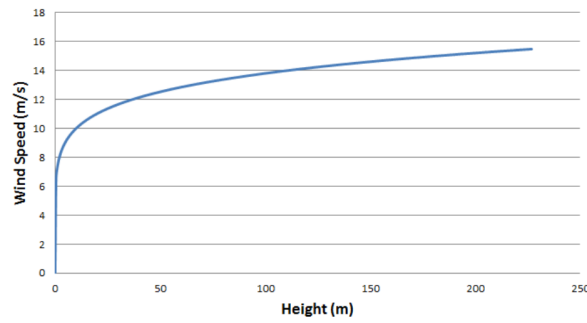


Figure 1.5: Power-law wind speed distribution [Bussolati, 2019].

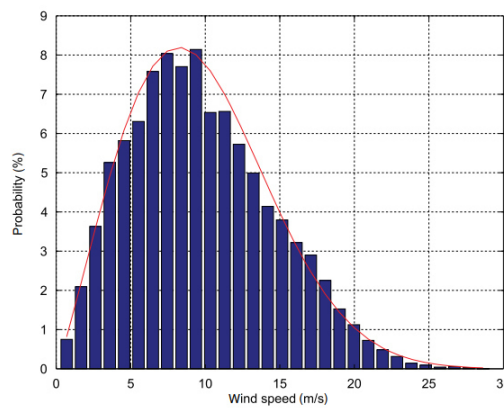


Figure 1.6: Bar chart of average wind speeds fitted by a Weibull distribution [Vorpahl et al., 2013].

1.2 The floating structure

The floating structure of FOWTs comprises the floater, the tower and the turbine, and it is subjected to the effects of waves on the floater and wind on the tower and turbine. The main design typologies for the floating structures of FOWTs are illustrated in Figure 1.7. The whole floating structure is often considered as a rigid body, since deformations in the platform are negligible if compared to its gross motion. Hence, its degrees of freedom are the six associated to rigid body motions.

From a wind turbine design perspective, using a floating platform instead of a fixed foundation introduces significant new motions. Among these, pitch of the floater is the most problematic for a turbine. This pitch can be easily excited by both wave loading and wind thrust, generating additional bending moments in the tower and blades, which are two of the most critical structural loads. To limit the bending moments under extreme loading and optimize electrical production under operational conditions, control strategies have also been developed [Guillemin et al., 2016].

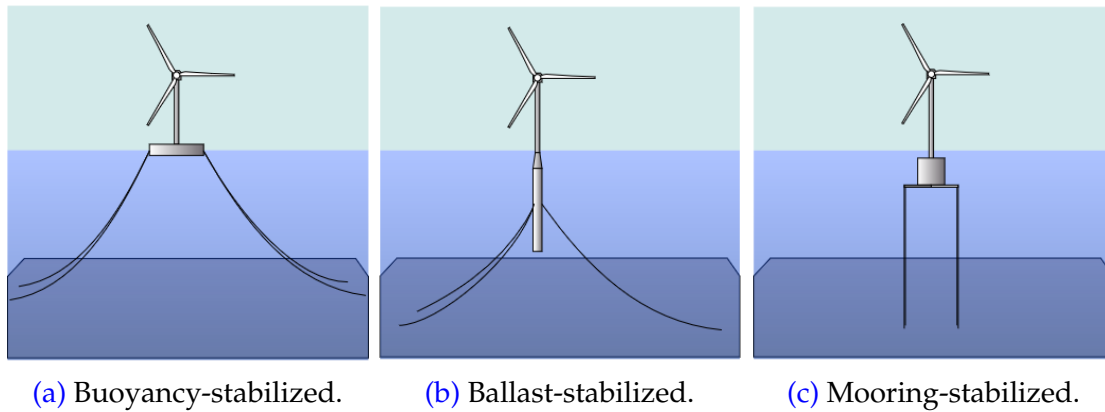


Figure 1.7: Possible FOWT designs [Hall, 2013].

1.2.1 Hydrodynamic loads

The main hydrodynamic loadings on a floating platform arise from buoyancy, waves, and the platform's own motion in the water. Hydrodynamic loadings are considered as the superposition of three loading sources, namely *hydrostatics*, *diffraction* and *radiation*.

- Hydrostatic forces arise from the static restoring force resulting from buoyancy when the platform is displaced from its equilibrium position or orientation along any of its degrees of freedom. This force can be calculated by determining the magnitude and centroid of the water volume displaced by the platform.
- Diffraction loads are exerted on the platform by incident waves, often calculated without considering the platform's motion. This is commonly known as the diffraction problem, as it deals with the forces caused by waves diffracting around the platform. For platforms that are very small relative to the waves wavelength, the wave excitation forces can be calculated based on the undisturbed wave kinematics alone due to minimal wave scattering or diffraction.
- Radiation loads on the platform result from its motion in the water, which generates waves that radiate outward. In an inviscid approximation, the forces that result from radiation can be split in two components: added mass, which accounts for the mass of water that is accelerated by the floater, and wave-radiation damping, proportional to the velocity of the floater, whose power is equal to the power radiated away in the generated waves. These waves influence the pressure field around the body, impacting its motion.

1.2.2 Mooring system

The mooring lines serve to anchor the floater to the seabed, reducing the loads on the floating structure by minimizing its motions. This helps to prevent excessive displacements, preserving the power cables, protecting other wind turbines, and ensuring

suitable operational conditions.

Mooring lines can be made of chains, synthetic cables, or more often wire ropes. Mooring lines made of wire ropes are usually composed of different segments. Chains are used in the upper part that connects to the floater to facilitate tensioning, and on the part that rests on the seabed to resist abrasion. Additional masses are also usually positioned on each mooring line, to limit the floater movements and keep the lines in tension.

Mooring lines can generally be classified into two categories, based on their shape:

- *tension legs*, which are kept in tension by the buoyancy of the floater (Figure 1.7c);
- *catenary*, which consist of long lines that sit on the seabed before reaching the anchor thanks to the heavy chains resting on the seafloor (Figure 1.8).

The catenary-shaped mooring lines are usually more adopted. The advantage of this setup over tension legs is the use of cheaper anchors, as they are subjected to lower magnitude forces due to the longer length of the mooring lines. Most of the restoring forces in a catenary system are generated by the weight of the lines themselves. Moreover, a mooring line is designed in order to have a minimal tension, consequently each mooring line is subjected to complex tension-bending loadings around a preloaded state.

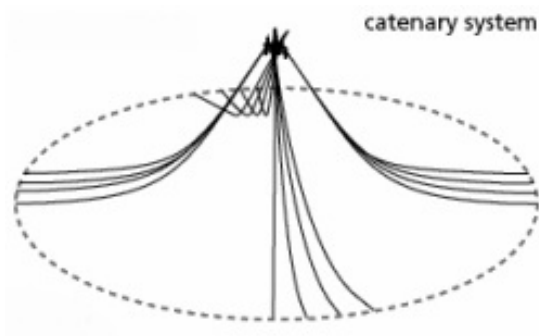


Figure 1.8: Catenary-shaped system of mooring lines (www.abc-moorings.weebly.com).

2 Wire ropes

In this section, first a brief introduction to the wire ropes geometry and mechanics will be presented, with some analytical results to better understand their behavior under traction and bending loads, which are the ones occurring during the life service of offshore wind turbines. For more details on this part one can refer to [Bussolati, 2019]. Subsequently, the main wire rope modeling techniques adopted in the literature are briefly recalled.

2.1 General description

Wire ropes used for offshore wind turbine mooring lines consist of a complex assembly of steel wires. These wires are produced through a wire drawing process, which aims to increase the wire's ultimate tensile strength and reduce its ductility. The particular manufacturing process also yields residual stresses on the wire, in particular in such a manner that compression residual stresses are present on the wire surface in order to contain fatigue cracks during their initiation process [Vannes et al., 1973; Smallwood, 1990].

Wire ropes can be wrapped together in various configurations (Figure 1.9), resulting in two main categories of wire ropes: spiral strands (Figure 1.9a) and stranded ropes (Figure 1.9b). A **spiral strand wire rope consists of layers of helical wires wrapped around a single core wire** or a grouped wire core. In contrast, a stranded wire rope typically has six or eight strands, or groups of wires, helically wrapped around either an empty core or another single strand. The wires within a strand form double helices, meaning each wire is a helix around another helix. In the offshore oil industry, spiral strands are more often used for permanent applications due to their superior resistance compared to stranded wire ropes, which are typically more used for temporary applications, such as during the drilling phase. Additionally, spiral strand ropes allow for easier extrusion of a polymeric sheath over them, providing a barrier to seawater.

The helical shape provides an essential combination of high axial strength and stiffness with high bending flexibility [de Jong, 2015]. The lay angles (i.e., the angle the wires of each layer make with their axis of revolution) in a specific wire rope architecture are selected to minimize the length disparities between wires and, ideally, to reduce tension-torsion coupling caused by the helical arrangement. Additionally, spiral strands are engineered to restrict the lateral spacing between wires within the same layer. The geometric condition of lateral contact in the unloaded configuration is defined as follows [Knapp, 1979]:

$$\sqrt{1 + \frac{\tan^2\left(\frac{\pi}{2} - \frac{\pi}{n_i}\right)}{\cos^2\alpha_i}} = \frac{R_i}{r_i}, \quad (1.1)$$

where r_i , R_i , n_i and α_i are respectively the wire radius, the layer radius, the number of wires and the lay angle associated to the layer i .

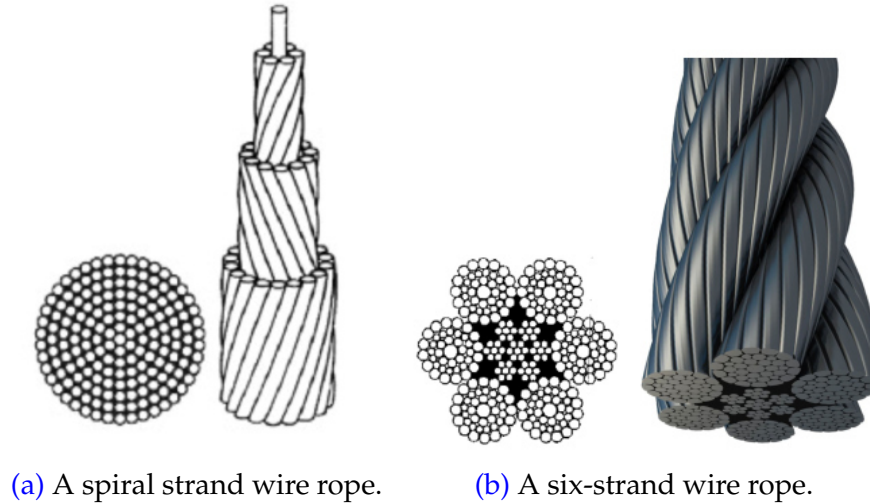


Figure 1.9: Different typologies of wire ropes. (a): A spiral strand wire rope: it has layers of wires in circles around a single core wire or a grouped wire core [Judge et al., 2012]. (b): A six-strand wire rope: it is composed by strands wrapped helically. The first type is more adopted in offshore industry for permanent applications.

The contact conditions that take place between the wires of wire ropes are crucial for understanding the fatigue phenomena that occur during their service life. The contact area acts as a stress concentration zone promoting crack nucleation. Therefore, the fatigue life prediction with contact decreases by several factors compared to the endurance limit determined by purely uniaxial tests [Siegert, 1997; Montalvo, 2023; Montalvo et al., 2023]. Experimental observations confirm in fact that crack initiation begins at the inter-wire contact zones [Giglio and Manes, 2003].

In a wire rope, two types of inter-wire contacts can be identified, as illustrated in Figure 1.10:

- *line contact*: occurs within a given layer between adjacent wires, and between the wires in the first layer and the central core wire. It can be regarded as the line contact between parallel cylinders. This type of contact influences the overall axial, torsional, and free bending stiffness, and the contact area is rectangular (Figure 1.10a).
- *trellis contact*: occurs between two adjacent layers, where respective wires cross at an oblique angle, creating a localized point contact rather than a line contact. Due to its localized nature, the contact stresses are much higher than those in line contacts within a layer. Trellis contacts are the most involved in fatigue phenomena, and the contact area in this case is elliptical (Figure 1.10b).

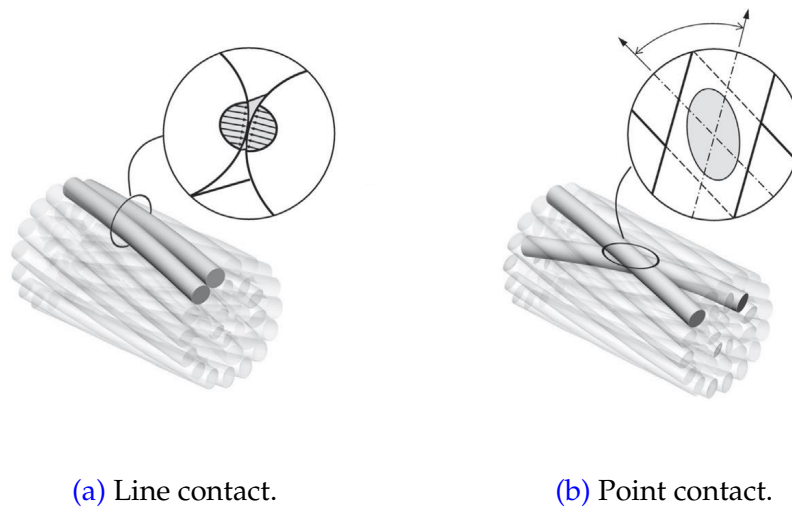


Figure 1.10: Possible contact configurations between wires in a wire rope [Lalonde et al., 2017b]. (a): Lateral line contact within layers. (b): Trellis point contact between layers.

2.2 Mechanical behavior

In the literature, analytical models for stranded ropes are limited and typically address axial loading scenarios (tension and torsion without bending) assuming either no friction [Xiang et al., 2015] or perfect adhesion [Usabiaga and Pagalday, 2008]. On the contrary, analytical models for spiral strands are more developed and include bending effects and finite friction as well. There are in this category two primary approaches:

- *semi-continuous models*, where each layer is treated as an orthotropic cylinder [Hobbs and Raouf, 1983; Jolicoeur and Cardou, 1996];
- *thin rod models*, where individual wires are considered separately [Papailiou, 1995; Hong et al., 2005].

Here, we consider the second category of models (thin rod models), since they provide direct insights into the behavior of individual wires, which are easier to interpret and utilize.

2.2.1 Analytical results: traction

Let us start by considering the behavior of the rope when subjected to traction loads. Traction loading is crucial for the considered wire ropes application, since they are required at first instance to bear tension loads. Moreover, wire ropes for mooring applications are usually pretensioned, so that they always work in tension, as a compression stress state may lead to buckling phenomena.

Let us consider an axial force T_{rope} applied to the wire rope. The axial force induces a uniform elongation $\varepsilon_c = \frac{\Delta L}{L}$ on the rope axis and, because of the particular helical geometry of the rope, torsion phenomena arise which try to “unwind” the rope and make the wires rotate by a quantity $\Delta\theta$ around its central axis:

$$T_{\text{rope}} = (EA)_{\text{rope}} \frac{\Delta L}{L} + K_{\theta} \frac{\Delta\theta}{L} = (EA)_{\text{rope}} \varepsilon_c + K_{\theta} \tau_c, \quad (1.2)$$

where $(EA)_{\text{rope}}$ represents the axial stiffness of the rope and K_{θ} the torsional stiffness. The total traction force applied on the wire rope can be considered as uniformly distributed on each wire:

$$\sum_{n=1}^{N_{\text{wires}}} S_n = T_{\text{rope}}, \quad (1.3)$$

with S_n being the component of the traction force on every wire in the direction of the rope axis (see [Figure 1.11](#)).

Therefore, by assuming the following hypotheses [[Papailiou, 1995](#)]:

- the change in the lay angle caused by the tensile load is negligible;
- radial contraction of wires cross sections, arising from Poisson effect and contact pressure, is neglected;
- the torsion τ_c of the rope cross section is neglected;
- shear forces acting on the wires are negligible compared with the tensile force;
- the wires are in line contact condition with the layer underneath (this is true only for the first layer in contact with the core wire);

we can state that in each layer i of the wire rope, every wire is subjected to the same tensile force T_i ([Figure 1.11](#)) given by

$$T_i = \frac{S_i}{\cos \alpha_i}, \quad (1.4)$$

with α_i being the lay angle of the wires. The transverse component U_i prevents the rope to unwind.

Since wires in adjacent layers are in contact with each other, a uniformly extended wire rope will experience no longitudinal slippage, though interwire slippage may occur within each layer. However, actual contact conditions between layers, such as trellis contacts, lead to microslips between adjacent layers during tension [[Paradis and Légeron, 2011](#)] which are responsible for the hysteretic behavior observed in tension tests [[Huang and Vinogradov, 1996](#)]. More refined models take into account also the influence of the radial contraction [[Costello, 2012](#)] and the lateral contact [[Siegert, 1997](#)].

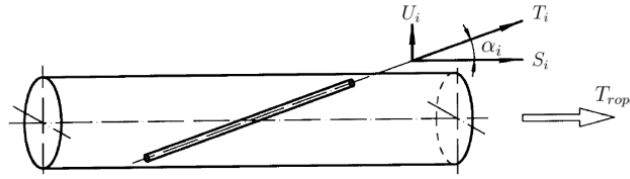


Figure 1.11: Decomposition of the external traction force on a single wire [Papailiou, 1995].

2.2.2 Analytical results: bending

Let us consider the case where the rope, in addition to a tensile load, is also submitted to a uniform bending curvature κ_c . When bending occurs, one can express the position of the helical wire at a given section by means of the angle θ in the cross-section of the rope (Figure 1.12), with $\theta = 0$ and $\theta = \pi$ corresponding to the bending axis, $\theta = \pi/2$ being the outer arc (top sector), and $\theta = -\pi/2$ being the inner arc (bottom sector).

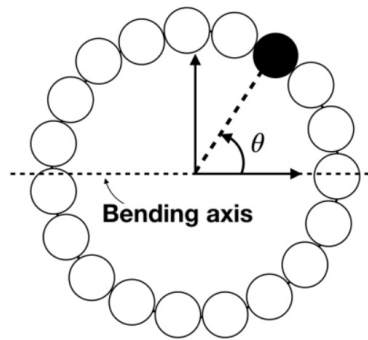


Figure 1.12: Wire rope cross-section [Bussolati, 2019].

During bending, two different types of loadings occur on a helical wire: wire elongation and wire bending around its own transverse axis. Concerning wire elongation, one can distinguish between two limit situations [Papailiou, 1995]:

- when the curvature is sufficiently low, wires are in stick state and the rope behaves as a Euler-Bernoulli beam, since sections remain plane in the deformed configuration;
- once the rope curvature reaches a certain threshold, the helical wires are in complete slip state.

Since the wires in the wire rope are curved, the equilibrium of the wire implies contact pressures p_i between each wire belonging to layer i and the wires belonging to layer $i - 1$ which can be obtained, for example, by considering line contact pressures. By

performing the equilibrium equation of an infinitesimal wire element (Figure 1.13), one obtains:

$$p_i = \frac{T_i}{\rho_i}, \quad (1.5)$$

that is a line contact pressure proportional to the traction force, with ρ_i being the curvature radius of the helical geometry of the wire. It should also be noted that the total pressure acting on the wires of a given layer is the sum of the pressure induced by all the outer layers, that is to say the normal contact pressure increases from the outer to the inner layers. Actually, given the geometry of the wire rope, contact between wires of adjacent layers does not occur along lines but along contact points. In this case, the expression for the normal contact force at a given contact point is given by [Papailiou, 1995]:

$$P_i = 2T_i \sin \alpha_i \sin\left(\frac{\Delta\theta_i}{2}\right), \quad (1.6)$$

with $\Delta\theta_i = \frac{2\pi}{b_i}$ and b_i being the number of contact points between layer i and layer $i - 1$ per lay length. Even in this case, one obtains a contact interaction proportional to the external traction force.

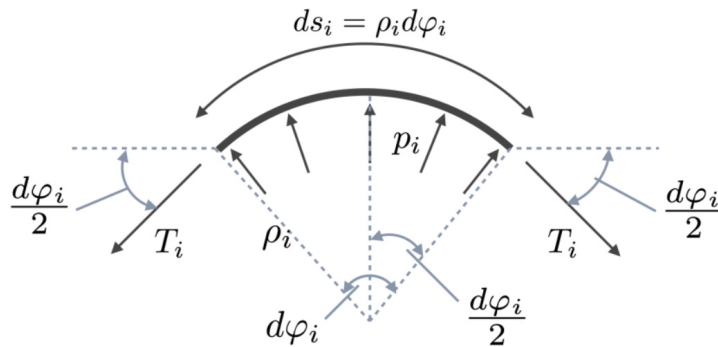


Figure 1.13: Transversal equilibrium of a curved wire element [Bussolati, 2019]

Due to friction, the moment-curvature relation of a wire rope is nonlinear. Initially, all wires are in stick state and the cross sections remain plane, with the wire rope following beam kinematics. Under these conditions, the bending stiffness is maximum. **Slippage in a layer starts in the proximity of the neutral axis. The first layer to slip is the most external one, since the contact pressure involved is the lowest one.** For the internal layers the contribution of the external ones increases the contact pressure and consequently higher friction forces can take place. By considering the simplified approach proposed by [Papailiou, 1995], which considers that each layer suddenly slips when a certain level of curvature is attained, the bending diagram takes therefore a multilinear shape. The change between the two situations (total sticking/total slip) affects the bending stiffness of the rope: when the slip state of the wires is triggered,

the bending stiffness of the rope decreases, as it can be seen in the idealized diagram of Figure 1.14 for a loading-unloading cycle. A more accurate modeling is proposed in [Houle-Paradis, 2012], where shear effects and micro-slipping are also taken into account at the inter-layer wire contact interfaces, as opposed to only considering a stick-slip system.

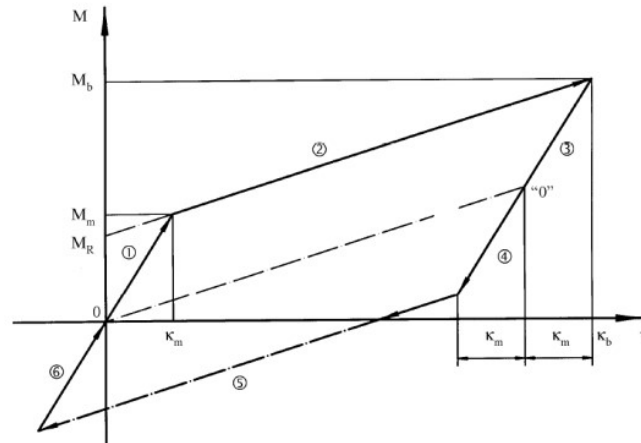


Figure 1.14: Moment-curvature diagram for a single layer strand in a loading-unloading cycle. Due to friction phenomena affecting bending stiffness, the behavior results hysteretic [Papailiou, 1995].

2.3 Numerical modeling

The analytical models mentioned previously are indeed useful, and for some specific load cases can give rather accurate results. However, in real case structures, some adopted hypotheses may be too strong to be considered acceptable. For this reason, efforts have been made also to characterize the behavior of wire ropes with numerical models.

Numerical models for wire ropes can be first categorized by the scale at which they want to model the behavior of the wire ropes. We can distinguish therefore a first category of models, the global scale models, whose purpose is to predict the global nonlinear bending-curvature behavior and/or the axial-torsional coupling of the rope, by appropriately modeling the frictional phenomena which take place at the level of the individual wires. This is done often by means of computational homogenization techniques [Geers et al., 2010]. The other category consists in full-scale models, where the wire rope is modeled at the level of the single wires, whose aim is to accurately predict local contact phenomena occurring between each wire. The wire modeling in this case can be distinguished between solid elements and beam elements.

■ Computational homogenization techniques

The computational homogenization of beam-like structures has been addressed in several works [Buannic and Cartraud, 2001; Boso et al., 2005; Cartraud and Messenger, 2006; Treysede and Cartraud, 2022; Xing et al., 2022; Saadat and Durville, 2023]. In the context of cables, in the computational homogenization framework, the spiral strand as a whole represents the heterogeneous medium to be homogenized. After homogenization, the spiral strand is represented at the macroscale as a single beam, and a periodic portion of the spiral strand is the RVE (Figure 1.15). Among others, in [Ménard and Cartraud, 2021], the asymptotic homogenization approach from [Cartraud and Messenger, 2006] was extended to homogenize contact nonlinearities, being able to capture the nonlinear bending behaviour stemming from the stick-slip transition. More recently, [Saadat and Durville, 2023] proposed a mixed stress-strain FE^2 homogenization technique [Feyel and Chaboche, 2000] to identify the nonlinear constitutive behavior of homogenized beam elements able to reproduce the hysteretic bending response of spiral strands (Figure 1.14). When dealing with strands with many layers however it is difficult to identify a periodic RVE if the different layers have different lay angles. For this reason other approaches consider to model each layer by an orthotropic cylinder whose mechanical properties are chosen to match the behavior of its corresponding layer of wires [Jolicoeur and Cardou, 1996].

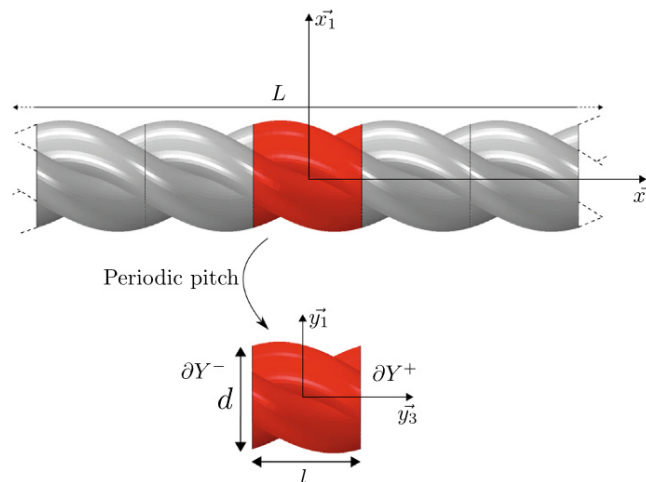


Figure 1.15: RVE identification in a periodic spiral strand structure [Ménard and Cartraud, 2021].

■ Solid elements

In [Kmet et al., 2013], the authors make use of Abaqus®/Explicit to model the wires of a multilayer spiral strand with linear brick elements, with reduced integration and hourglass control, to predict the three-dimensional stress state in the wires when

the rope is bent over a rigid support. The same model is also adopted in [Stanova et al., 2011] to simulate a pure tension test. Linear brick elements were also used to determine the evolution of the bending stiffness in a single-layer strand [Zhang and Ostoja-Starzewski, 2016] (Figure 1.16). In [Judge et al., 2012], the authors used 3D elasto-plastic finite elements to model a multilayer spiral strand, implemented in the commercial software LS-DYNA.

The use of such models in circumstances when the loadings are long and complex is computationally very costly, due to the very high number of degrees of freedom and the complex contact conditions, which render the simulations not affordable in terms of computational time. Employing a numerical model that minimizes computational cost as much as possible is crucial.

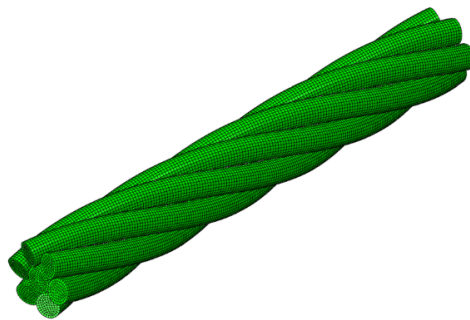


Figure 1.16: Solid mesh used in [Zhang and Ostoja-Starzewski, 2016] for the modeling of a single-layer rope with 7 wires.

■ Beam elements

Given the slender structure of the wires that compose the wire ropes, the kinematics at the scale of the wires can well be represented a beam elements. Such modeling is in good agreement with those obtained by solid models as well as with experimental results [Lalonde et al., 2017a].

Frictionless contact in large sliding between non-parallel beams with circular section was originally proposed in [Wriggers and Zavarise, 1997], extended to frictional contact with return mapping in [Zavarise and Wriggers, 2000] and to contact square cross-section beams in [Litewka and Wriggers, 2002]. Other contributions are distinguished by their ability to deal with the case of punctual or linear contact between beams, to take into account non-circular beam sections, to take into account friction or not, and on the contact detection [Konyukhov and Schweizerhof, 2010; Durville, 2012; Neto et al., 2016, 2017; Weeger et al., 2017; Meier et al., 2017; Meier et al., 2018].

Regarding specific applications to wire rope modeling, in [Lalonde et al., 2017b] the authors used ANSYS software to model each wire of a multilayer electrical conductor

with beam elements, handling contact with edge-to-edge contact elements. The model was then used to compute the fatigue damage caused by wind-induced vibration (free bending fatigue) on an electrical conductor made of aluminum and steel wires [Lalonde et al., 2017a]. Indentation at trellis contact positions was observed and, to better model this phenomenon, an anisotropic friction law was adopted. Evidence of such phenomena are however not reported for steel wires. Although the calculation cost is reduced due to the decrease in the size of the problem compared to a solid model, it remains however prohibitive to conduct fatigue calculations, as the contact detection step in large sliding still remains expensive.

In [Bussolati, 2019], by taking advantage of the fact that in the operating conditions to which wire ropes for mooring line applications are subjected to, a small inter-wire slip is encountered (Figure 1.18), it is proposed to model a six-layer wire rope (Figure 1.17) by mean of beam elements and with a new beam-to-beam contact element in small sliding and large rotations and with a penalty formulation [Bussolati et al., 2019; Guidault et al., 2019; Bussolati et al., 2020; Guidault et al., 2021]. The small sliding conditions enables to assume that the contact coupling is fixed, therefore no resources are consumed in the contact search phase, reducing calculation times considerably with respect to a large sliding beam-to-beam contact algorithm [Guiton et al., 2022]. The model is being extended to a Lagrange multiplier formulation [Ammar et al., 2023].

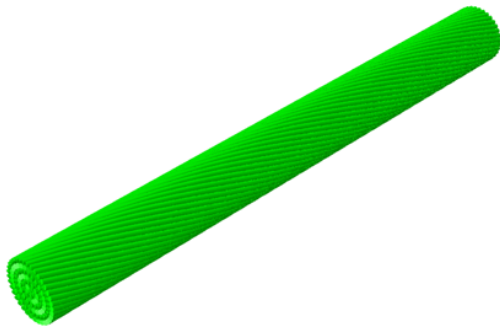


Figure 1.17: Finite element model of a six-layer wire rope [Bussolati, 2019].

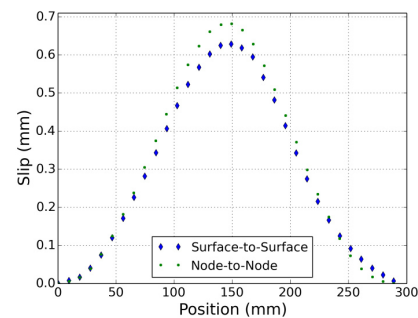


Figure 1.18: Interlayer sliding in the tension-curvature range of interest [Bussolati, 2019].

3 Quasi-static frictional contact problems

Contact, from a mechanical perspective, refers to any type of interaction between separate bodies that come in touch through a contact interface. Boundary value problems involving contact are critically important in engineering structures, and represent one of the most difficult nonlinear problems to deal with, mathematically as well as numerically. The rapid improvement of computer technology and numerical methods allows today the modeling of complex mechanical contact problems, nevertheless still most standard finite element softwares struggle to solve contact problems, especially those involving friction, with robust algorithms. Therefore, developing efficient and accurate methods for computational contact mechanics remains still a significant challenge.

Pioneering works on contact mechanics can be traced back to Hertz [Hertz, 1882] on the solution for frictionless contact between two ellipsoidal bodies. A first mathematical treatment of the contact problem, without friction, was posed by Signorini [Signorini, 1959], with Fichera's proof of the existence and uniqueness of the arising variational inequalities [Fichera, 1963, 1964; Fichera, 1973; Kinderlehrer and Stampacchia, 2000]. A major breakthrough in this field was represented by [Duvaut, 1972; Duvaut and Lions, 1976], where variational inequalities arising from frictional contact problems and issues involving large deformations were examined.

Computational contact mechanics problems present several challenges, from geometry discretization and contact detection to the numerical implementation of a numerical algorithm. A wide and detailed overview on the topic can be found in [Wriggers and Laursen, 2006; Yastrebov, 2011]. Here, we limit ourselves to the algorithmic part, going briefly to present the most important aspects of a contact problem with friction and the various strategies that can be used to solve it.

3.1 Frictional contact problem setting

Let us consider two elastic solid bodies Ω_E and $\Omega_{E'}$ in possible contact with each other along the contact interface $\Gamma_c = \Gamma_E = \Gamma_{E'}$. The union $\Omega = \Omega_E \cup \Omega_{E'}$ of the two bodies is subjected to body forces \underline{f}_d acting on Ω with prescribed displacement boundary conditions \underline{U}_d on $\partial_1\Omega = \partial_1\Omega_E \cup \partial_1\Omega_{E'}$ and prescribed tractions \underline{F}_d on $\partial_2\Omega = \partial_2\Omega_E \cup \partial_2\Omega_{E'}$ (Figure 1.19). A linear elastic behavior of the materials is assessed (small perturbations, homogeneous-isotropic linear-elastic material, small slidings) and a quasi-static regime is assumed.

Let \underline{u} be the displacement field and σ be the Cauchy stress. The trace of the displacement field \underline{u} on the contact interfaces Γ_E and $\Gamma_{E'}$, namely $\underline{W}_E = \underline{u}|_{\Gamma_E}$ and $\underline{W}_{E'} = \underline{u}|_{\Gamma_{E'}}$

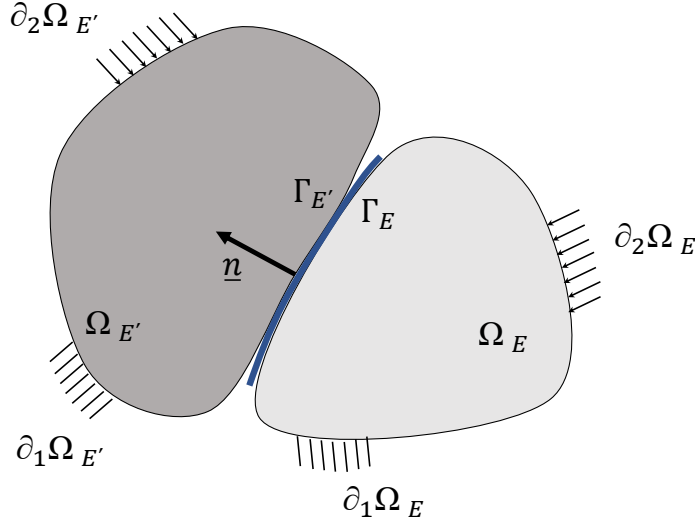


Figure 1.19: Frictional contact problem setting between two elastic solid bodies.

can be decomposed along the normal and tangential direction to Γ_c :

$$\underline{W}_E = \mathbf{P}_n \underline{W}_E + \mathbf{P}_t \underline{W}_E \quad \text{and} \quad \underline{W}_{E'} = \mathbf{P}_n \underline{W}_{E'} + \mathbf{P}_t \underline{W}_{E'}, \quad (1.7)$$

with $\mathbf{P}_n = \underline{n} \otimes \underline{n}$ being the normal projector to the interface, \underline{n} being the outward normal of Γ_c from Ω_E to $\Omega_{E'}$, and $\mathbf{P}_t = \mathbf{I}_d - \underline{n} \otimes \underline{n}$ is the tangential projector on the interface. Similarly, on the contact interface, the body Ω_E (resp. $\Omega_{E'}$) is subject to equilibrated contact forces \underline{F}_E (resp. $\underline{F}_{E'}$) from the body $\Omega_{E'}$ (resp. Ω_E), which can be decomposed as follows:

$$\underline{F}_E = \mathbf{P}_n \underline{F}_E + \mathbf{P}_t \underline{F}_E \quad \text{and} \quad \underline{F}_{E'} = \mathbf{P}_n \underline{F}_{E'} + \mathbf{P}_t \underline{F}_{E'}, \quad (1.8)$$

where $\mathbf{P}_n \underline{F}_E$ are normal contact forces and $\mathbf{P}_t \underline{F}_E$ are the tangential frictional forces.

We define $g_n = \underline{n} \cdot (\underline{W}_{E'} - \underline{W}_E) + g_0$ the relative normal displacement gap at the contact interface, with g_0 being an initial gap, and $\dot{g}_t = \mathbf{P}_t (\dot{\underline{W}}_{E'} - \dot{\underline{W}}_E)$ the relative sliding velocity at the contact interface. To simplify the notation for the following, we define $F_n = \underline{n} \cdot \underline{F}_E$ and $\underline{F}_t = \mathbf{P}_t \underline{F}_E$.

3.2 Unilateral contact conditions

Normal and tangential contact behaviors are ruled by pertinent contact conditions.

3.2.1 Normal contact

Normal contact conditions correspond to the so-called *Signorini conditions* [Signorini, 1959]. They consist in requiring the two bodies, when in contact, to not penetrate each other. Moreover, when contact occurs, the normal contact force has to be negative. A

complementary conditions is then introduced to take into account both the case of contact and separation:

Definition 1.1 (Signorini conditions). *At the contact interface Γ_c , the following conditions hold for the normal contact:*

- non penetration condition: $g_n \geq 0$;
- compressive contact pressure: $F_n \leq 0$;
- complementarity condition: $F_n g_n = 0$.

3.2.2 Tangential frictional contact

For the tangential behavior constitutive law, we consider the classical Coulomb's friction law [Coulomb, 1821]. In the simplest case, the friction law states that the tangential stress on the contact interface depends on the normal contact pressure and its direction is given by the relative sliding, that is:

$$\underline{E}_t = \underline{E}_t(F_n, \underline{s}). \quad (1.9)$$

In the previous constitutive definition, \underline{s} is a unitary vector in the tangential plane of the contact interface, which determines the direction of relative sliding:

$$\underline{s} = \begin{cases} \frac{\dot{\underline{g}}_t}{\|\dot{\underline{g}}_t\|}, & \text{if } \|\dot{\underline{g}}_t\| > 0; \\ \underline{0}, & \text{if } \|\dot{\underline{g}}_t\| = 0. \end{cases} \quad (1.10)$$

The relative motion on the contact interface is bounded by the frictional stress, that is, there is no relative sliding if the tangential stress is smaller than a threshold:

$$\|\underline{E}_t\| < f|F_n|, \quad (1.11)$$

with f being the friction coefficient (Figure 1.20a). Once the threshold is reached, the tangential stress assumes the value $f|F_n|$ and “flows” along the direction given by \underline{s} (Figure 1.20b):

$$\underline{E}_t = f|F_n| \frac{\dot{\underline{g}}_t}{\|\dot{\underline{g}}_t\|}. \quad (1.12)$$

The previous two conditions are complemented by an additional condition distinguishing between sticking and slipping (or sliding) conditions:

$$\|\underline{s}\| \left\| \|\dot{\underline{g}}_t\| \underline{E}_t - f|F_n| \dot{\underline{g}}_t \right\| = 0. \quad (1.13)$$

The Coulomb frictional conditions are then summarized as follows:

Definition 1.2 (Coulomb frictional conditions). At the contact interface Γ_c , the following conditions hold for the tangential contact:

- sliding threshold: $\|\underline{E}_t\| - f|F_n| \leq 0$;
- flow rule: $\|\underline{\dot{g}}_t\| \|\underline{E}_t - f|F_n| \underline{\dot{g}}_t = \underline{0}$;
- complementarity condition: $\|\underline{s}\| \left\| \|\underline{\dot{g}}_t\| \|\underline{E}_t - f|F_n| \underline{\dot{g}}_t \right\| = 0$.

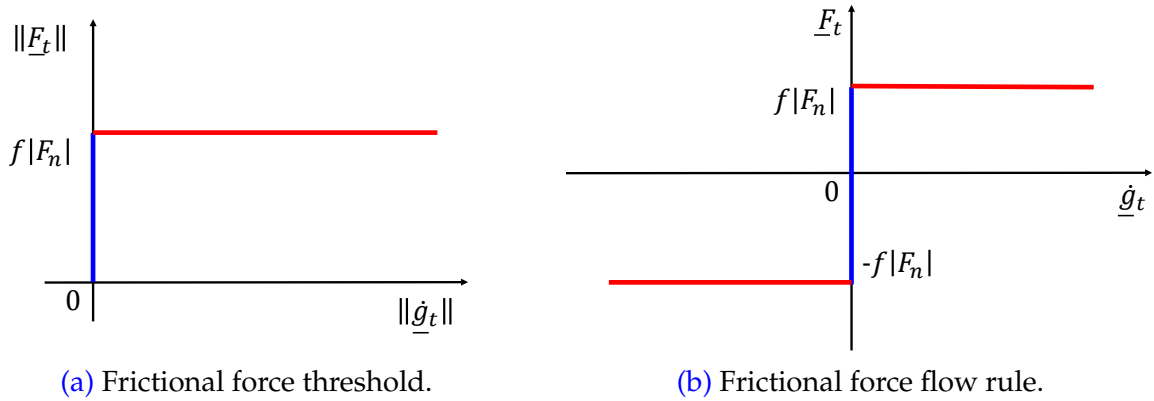


Figure 1.20: Coulomb frictional law for a given normal pressure F_n . (a): Frictional force threshold. (b): Frictional force flow rule.

The possible admissible contact states with friction can be represented through the so-called “Coulomb’s cone” (Figure 1.21), an open set determined by:

$$\mathcal{C}(F_n) = \{\|\underline{E}_t\| < f|F_n|\}. \quad (1.14)$$

Any possible contact state fulfilling frictional conditions corresponds to a unique point either in the interior of the cone:

$$\underline{E}_t \in \mathcal{C}(F_n), \quad (1.15)$$

or on its closure:

$$\underline{E}_t \in \partial\mathcal{C}(F_n). \quad (1.16)$$

Any stress state in the interior of Coulomb’s cone does not result in relative tangential sliding. On the contrary, relative sliding implies that the actual stress state is situated at the boundary of Coulomb’s cone.

The expressions for adhesion and sliding conditions given by Coulomb’s law are non-differentiable at the onset of sliding. This can lead to difficulties for conventional solution techniques. Regularized models have been proposed [Oden and Pires, 1984;

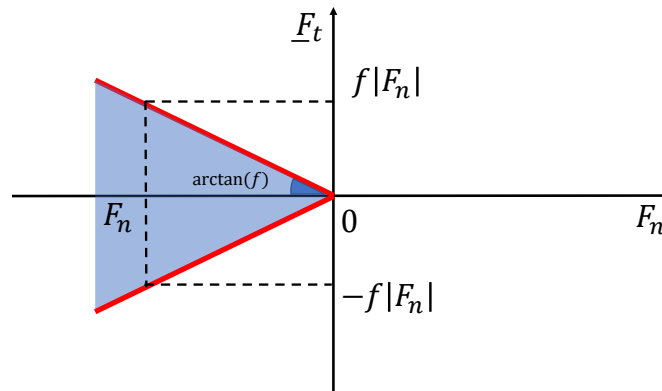


Figure 1.21: Coulomb's cone representation in 2D for a given normal pressure F_n .

Raous, 1999], based on a functional form which yields a smooth transition from stick to slip conditions (Figure 1.22). Regularization leads to simpler and more robust numerical implementations, however they may lack in describing accurately the stick-slip transitions.

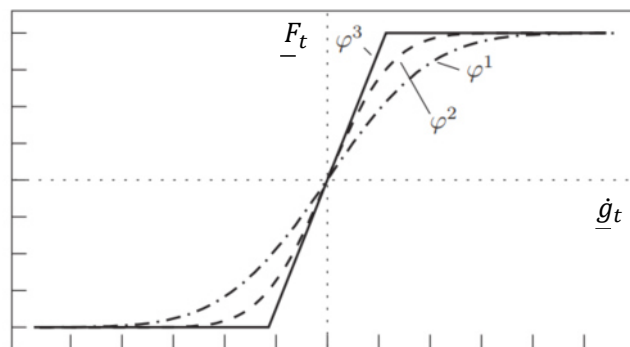


Figure 1.22: Regularization of Coulomb's friction law [Wriggers and Laursen, 2006] with functions φ^i describing the smooth transition from sticking to sliding. Function φ^1 corresponds to a square root regularization, φ^2 is a hyperbolic tangent regularization and φ^3 is piece-wise linear regularization.

The described formulation of friction phenomena shares strong similarities with plasticity theory [Curnier, 1984; Wriggers, 1987; Giannakopoulos, 1989; De Saxcé and Feng, 1998; De Saxcé and Bousshine, 1998]. In the case of frictional contact the flow rule is non-associated, since there is no irreversible slip in the normal direction. The principle of maximum dissipation is inapplicable in this case, except when the contact pressure is constant. A more detailed treatment of the analogies between associated/non-associated plasticity and friction phenomena can be found in [Michalowski, 1978].

The formulation of elasto-plastic constitutive relations in frictional contact mechanics is driven by two main reasons. The first one is that such a modeling enables to

regularize and generalize Coulomb's law, as in general one can assume softening as well as hardening for the frictional constitutive behavior [Wriggers and Laursen, 2006]. The other one comes from experimental observations on metallic surfaces [Anand, 1993], which suggest the use of elasto-plastic relations splitting the tangential motion into a elastic or adhesive (stick) part and a plastic or slip part. Another analogy can be made with variational formulations of linear elastic fracture mechanics [Salvadori and Carini, 2011].

3.2.3 Strong formulation of the problem

Having defined the normal and tangential contact conditions of the problem, we can therefore define the formulation of the frictional contact problem:

Problem 1.1 (*contact between two elastic bodies*). Find the displacement field \underline{u} and the Cauchy's stress field σ satisfying:

– kinematic admissibility:

$$\underline{u} \in \mathcal{U}, \text{ with } \mathcal{U} = \{\underline{u} \in \mathcal{H}^1(\Omega) : \underline{u}|_{\partial_1\Omega} = \underline{U}_d\}; \quad (1.17)$$

– static admissibility:

$$\begin{cases} \sigma \cdot \underline{n} = \underline{F}_d \text{ on } \partial_2\Omega, \\ \sigma \cdot \underline{n} = \underline{F}_E = -\underline{F}_{E'} \text{ on } \Gamma_c, \\ \operatorname{div}\sigma + \underline{f}_d = \underline{0} \text{ on } \Omega; \end{cases} \quad (1.18)$$

– constitutive relation:

$$\sigma = \mathbf{K} : \varepsilon \text{ on } \Omega, \quad (1.19)$$

with \mathbf{K} being the Hookean tensor and $\varepsilon = \frac{1}{2}(\nabla\underline{u} + \nabla\underline{u}^T)$ the small strain tensor;

– Signorini conditions ([Definition 1.1](#));

– Coulomb's frictional law ([Definition 1.2](#)).

3.2.4 Weak formulation of the problem

In order to define a weak formulation of the contact problem, let \mathcal{U}_0 be the space of kinematically admissible displacements variations to zero in $\partial_1\Omega$. We define the following closed convex subsets of \mathcal{U} and \mathcal{U}_0 for the kinematic admissibility of contact conditions:

$$\mathcal{U}_{ad} = \{\underline{u} \in \mathcal{U} : g_n \geq 0 \text{ on } \Gamma_c\}, \quad \mathcal{U}_{ad,0} = \{\delta\underline{u} \in \mathcal{U}_0 : \delta g_n \geq 0 \text{ on } \Gamma_c\}. \quad (1.20)$$

Let us first consider the frictionless contact problem. The corresponding weak form is a variational inequality [Duvaut, 1972; Kinderlehrer and Stampacchia, 2000]:

Problem 1.2 (*weak form of the frictionless contact problem*). Find $\underline{u} \in \mathcal{U}_{ad}$ such that, $\forall \delta \underline{u} \in \mathcal{U}_{ad,0}$,

$$\int_{\Omega} \boldsymbol{\varepsilon}(\underline{u}) : \mathbf{K} : \boldsymbol{\varepsilon}(\delta \underline{u}) d\Omega \geq \int_{\Omega} \underline{f}_d \cdot \delta \underline{u} d\Omega + \int_{\partial_2 \Omega} \underline{E}_d \cdot \delta \underline{u} dS. \quad (1.21)$$

The existence and unicity of the solution of the previous problem are ensured [Fichera, 1973; Kikuchi and Oden, 1988]. Since in absence of friction, the problem is purely elastic, it can equivalently be rewritten as a minimization problem for the total energy $\Pi(\underline{u})$ of the bodies:

Problem 1.3 (*weak form as a minimization of energy*). Find $\underline{u} \in \mathcal{U}_{ad}$ such that, $\forall \delta \underline{u} \in \mathcal{U}_{ad,0}$,

$$\Pi(\underline{u}) \leq \Pi(\underline{u} + \delta \underline{u}), \quad (1.22)$$

with

$$\Pi(\underline{u}) = \frac{1}{2} \int_{\Omega} \boldsymbol{\varepsilon}(\underline{u}) : \mathbf{K} : \boldsymbol{\varepsilon}(\underline{u}) dV - \int_{\Omega} \underline{f}_d \cdot \underline{u} dV - \int_{\partial_2 \Omega} \underline{E}_d \cdot \underline{u} dS. \quad (1.23)$$

In presence of friction, the problem becomes non-conservative and the solution is path-dependent, for this reason the problem is generally treated by an incremental approach. Let $\underline{g}_t = \dot{\underline{g}}_t dt$ be the tangential sliding, the variational formulation of the contact problem with friction is defined as follows [Duvaut, 1972]:

Problem 1.4 (*weak form for the frictional contact problem*). Find $\underline{u} \in \mathcal{U}_{ad}$ such that, $\forall \delta \underline{u} \in \mathcal{U}_{ad,0}$,

$$\int_{\Omega} \boldsymbol{\varepsilon}(\underline{u}) : \mathbf{K} : \boldsymbol{\varepsilon}(\delta \underline{u}) d\Omega + \int_{\Gamma_c^\bullet} f |F_n(\underline{u})| \|\delta \underline{g}_t\| dS \geq \int_{\Omega} \underline{f}_d \cdot \delta \underline{u} d\Omega + \int_{\partial_2 \Omega} \underline{E}_d \cdot \delta \underline{u} dS. \quad (1.24)$$

with $\int_{\Gamma_c^\bullet} f |F_n(\underline{u})| \|\delta \underline{g}_t\| dS$ being the virtual work of the frictional contact forces, and Γ_c^\bullet being the part of Γ_c where sliding occurs.

This problem is more complex compared to the frictionless case because of the non-differentiable contribution of the frictional forces. The existence and uniqueness of the solution has not been proven except for a regularized form of the problem and a small frictional coefficient [Duvaut, 1980].

3.3 Treatment of contact constraints

The introduction of contact conditions, with and without friction, leads to problems formulated in terms of variational inequalities. The variational inequality is often transformed, after deleting the contact kinematic conditions and introducing dual conditions and dual variables, into more standard variational equations, which are easier to introduce in a finite element framework and do not require totally new minimization techniques. Among the most popular and widely used methods in contact mechanics are those inspired from optimization theory: penalty method, Lagrangian multipliers, or augmented Lagrangian multipliers [Wriggers and Laursen, 2006].

3.3.1 Penalty method

The penalty method is one of the most widely used approaches for constrained problems. It consists in penalizing the constraint function leading to an unconstrained problem. Although, in case of contact problems, the non-exact verification of the contact condition leads to unphysical penetrations between the contacting bodies and elastic slip even in stick state conditions.

■ Frictionless case

The method consists in considering the contact interface as an elastic structural interface with positive finite stiffness k_n [Kikuchi and Oden, 1988], with contact pressure defined as a continuous function of the penetration:

$$F_n(g_n) = \begin{cases} 0, & g_n > 0; \\ k_n g_n, & g_n \leq 0. \end{cases} \quad (1.25)$$

Therefore, the contact condition is strictly fulfilled for non-negative gaps. However, according to the relation between contact pressure and the gap function, real contact appears only for negative gaps, i.e., only if a penetration takes place. With the penalty method contact forces are computed from the violation of the penetration condition. The exact solution can be obtained within the limit $k_n \rightarrow +\infty$, however this leads to ill-conditioning of the involved matrices and compromises must be made affecting the accuracy of the solution.

■ Frictional case

In the frictional case, the constraint appears only when we are in a stick state, in fact in that state we have a condition on the relative sliding to be zero. In that case, an indeterminate tangential reaction force arises to fulfill such a condition. Therefore, similarly to the normal contact, in the tangential plane a positive finite stiffness k_t is

introduced to penalize the sticking condition:

$$\underline{F}_t = \begin{cases} k_t \underline{g}_t, & \|\underline{g}_t\| < \frac{f|F_n|}{k_t}; \\ f|F_n| \frac{\dot{\underline{g}}_t}{\|\dot{\underline{g}}_t\|}, & \|\underline{g}_t\| \geq \frac{f|F_n|}{k_t}. \end{cases} \quad (1.26)$$

It is evident therefore that in this case, even in stick conditions, there is some sliding. This condition is called “slip-in-stick” condition, and represents an elastic sliding at the contact interface [Wriggers and Laursen, 2006; Yastrebov, 2011]. From a physical point of view, the slip-in-stick represents elastic deformations within the contact interface, and should vanish when the load is removed. There is therefore a direct analogy with elasto-plastic theory of deformation: the deformation inside the yield surface (the Coulomb’s cone in case of frictional contact) results in elastic deformation, whereas reaching the yield surface leads to plastic flow.

3.3.2 Lagrange multipliers method

The most common approach to solve constrained problems is the one based on the use of the Lagrange multipliers. The contact problem can be replaced by the search of a stationary point (precisely saddle point) of a specifically constructed Lagrangian functional.

■ Frictionless case

The Lagrangian is obtained from the energy functional $\Pi(\underline{u})$ to which is added a term involving dual variables, the Lagrange multipliers λ_n , which coincide in fact with the contact forces:

$$\mathcal{L}(\underline{u}, \lambda_n) = \Pi(\underline{u}) + \int_{\Gamma_c} \lambda_n g_n dS. \quad (1.27)$$

The stationary condition corresponds to the following condition on the variation of the Lagrangian:

$$\delta \mathcal{L}(\underline{u}, \lambda_n) = \delta \Pi(\underline{u}) + \int_{\Gamma_c} g_n \delta \lambda_n + \lambda_n \delta g_n dS = 0. \quad (1.28)$$

The variation of the energy of the system is equivalent to the variational principle of virtual work, so the last equality can be rewritten in an extended form as:

Problem 1.5 (Lagrangian formulation of the frictionless contact problem). Find $\underline{u} \in \mathcal{U}$ and $\lambda_n \leq 0$ such that, $\forall \delta \underline{u} \in \mathcal{U}_0$ and $\forall \delta \lambda_n \leq 0$,

$$\int_{\Omega} \boldsymbol{\varepsilon}(\underline{u}) : \mathbf{K} : \boldsymbol{\varepsilon}(\delta \underline{u}) d\Omega + \int_{\Gamma_c} g_n \delta \lambda_n + \lambda_n \delta g_n dS = \int_{\Omega} \underline{f}_d \cdot \delta \underline{u} d\Omega + \int_{\partial_2 \Omega} \underline{F}_d \cdot \delta \underline{u} dS.$$

The constraint $\lambda_n \leq 0$ has still to be fulfilled, that is why the Lagrange multiplier method does not convert a minimization problem with inequality constraints to a fully unconstrained one. For a more rigorous formulation of Lagrange multiplier method for contact problems the reader is referred to [Kikuchi and Oden, 1988].

■ Frictional case

In the frictional case, a Lagrange multiplier $\underline{\lambda}_t$ is introduced in the tangential direction to take into account the constraint on the relative sliding, and corresponds to the frictional reaction force:

$$\underline{\dot{g}}_t = \underline{0}, \quad \text{if } \|\underline{\lambda}_t\| < f|\lambda_n|.$$

When sliding occurs, the tangential stress is simply given by the flow rule:

$$\underline{\lambda}_t = f|\lambda_n| \frac{\underline{\dot{g}}_t}{\|\underline{\dot{g}}_t\|}.$$

In this case, the variational formulation becomes:

Problem 1.6 (Lagrangian formulation of the frictional contact problem). Find $\underline{u} \in \mathcal{U}$, $\underline{\lambda}_t$ and $\lambda_n \leq 0$ such that, $\forall \delta \underline{u} \in \mathcal{U}_0$, $\forall \delta \underline{\lambda}_t$, and $\forall \delta \lambda_n \leq 0$,

$$\int_{\Omega} \boldsymbol{\varepsilon}(\underline{u}) : \mathbf{K} : \boldsymbol{\varepsilon}(\delta \underline{u}) d\Omega + \int_{\Gamma_c^*} g_n \delta \lambda_n + \lambda_n \delta g_n + \underline{g}_t \cdot \delta \underline{\lambda}_t + \underline{\lambda}_t \cdot \delta \underline{g}_t dS +$$

$$\int_{\Gamma_c^\bullet} g_n \delta \lambda_n + \lambda_n \delta g_n + \underline{\lambda}_t \cdot \delta \underline{g}_t dS = \int_{\Omega} \underline{f}_d \cdot \delta \underline{u} d\Omega + \int_{\partial_2 \Omega} \underline{F}_d \cdot \delta \underline{u} dS,$$

where Γ_c^\bullet and Γ_c^* are the parts of Γ_c where slip and stick conditions occur, respectively.

The Lagrange multipliers method leads to an exact verification of the contact conditions and the contact forces. Although the contact forces (i.e., the Lagrange multipliers) are introduced as additional unknowns to the problem. It is to be noted that this leads to an increase of the size of the problem to be solved, especially when multiple contact interfaces are present.

3.3.3 Augmented Lagrangian formulation

Augmented Lagrangian formulations are a class of algorithms widely used to solve constrained optimization problems. The formulation consists in the Lagrangian multipliers formulation augmented by an augmentation (or penalty) term [Fortin and Glowinski, 2000], and provides an unconstrained minimization problem with a smooth functional, which is a great advantage from a numerical point of view. The augmented Lagrangian formulation has been considered extensively within the context

of incompressibility constraints [Glowinski and Le Tallec, 1984], frictionless contact [Wriggers et al., 1985; Kikuchi and Oden, 1988] and large displacement contact problems including friction [Alart and Curnier, 1991; Simo and Laursen, 1992; Pietrzak and Curnier, 1999].

■ Frictionless case

In the frictionless case, the following augmented Lagrange functional is introduced for the normal contact constraint [Pietrzak and Curnier, 1999]:

$$\Pi_n^{AL} = \begin{cases} \int_{\Gamma_c} (\lambda_n g_n + \frac{k_n}{2} g_n^2) dS, & \hat{\lambda}_n \leq 0; \\ \int_{\Gamma_c} -\frac{1}{2k_n} |\lambda_n|^2 dS, & \hat{\lambda}_n > 0. \end{cases} \quad (1.29)$$

where the quantity $\hat{\lambda}_n = \lambda_n + k_n g_n$ is the *augmented Lagrangian multiplier* of the problem. The variation of the previous potential leads to:

$$\delta \Pi_n^{AL} = \begin{cases} \int_{\Gamma_c} (\hat{\lambda}_n \delta g_n + \delta \lambda_n g_n) dS, & \hat{\lambda}_n \leq 0; \\ \int_{\Gamma_c} -\frac{1}{k_n} \lambda_n \delta \lambda_n dS, & \hat{\lambda}_n > 0. \end{cases} \quad (1.30)$$

The structure of this functional is such that it holds not only for $\lambda_n \leq 0$, but also for $\lambda_n > 0$ when the contact is open. It represents a mixture of the augmented Lagrangian formulation with the perturbed Lagrangian method [Oden, 1981; Simo et al., 1985].

■ Frictional case

In the frictional case, an augmented Lagrangian multiplier of frictional forces can be similarly introduced as $\hat{\lambda}_t = \lambda_t + k_t \underline{g}_t$. The following functional is then defined in the state of contact ($\hat{\lambda}_n \leq 0$) [Pietrzak and Curnier, 1999]:

$$\Pi_t^{AL} = \begin{cases} \int_{\Gamma_c} (\lambda_t \cdot \underline{g}_t + \frac{k_t}{2} \underline{g}_t \cdot \underline{g}_t) dS, & \|\hat{\lambda}_t\| \leq f |\hat{\lambda}_n|; \\ \int_{\Gamma_c} -\frac{1}{2k_t} (\|\lambda_t\|^2 - 2f \hat{\lambda}_n \|\lambda_t\| + (f \hat{\lambda}_n)^2) dS, & \|\hat{\lambda}_t\| > f |\hat{\lambda}_n|. \end{cases} \quad (1.31)$$

And, in the case of opening ($\hat{\lambda}_n > 0$):

$$\Pi_t^{AL} = \int_{\Gamma_c} -\frac{1}{2k_t} \|\lambda_t\|^2 dS \quad \forall \hat{\lambda}_t. \quad (1.32)$$

The variation of the previous functionals in the case of closed contact leads to:

$$\delta\Pi_t^{AL} = \begin{cases} \int_{\Gamma_c} (\hat{\lambda}_t \cdot \delta \underline{g}_t + \delta \underline{\lambda}_t \cdot \underline{g}_t) dS, & \|\hat{\lambda}_t\| \leq f|\hat{\lambda}_n|; \\ \int_{\Gamma_c} (f|\lambda_n| \frac{\hat{\lambda}_t}{\|\hat{\lambda}_t\|} \cdot \delta \underline{g}_t - \frac{1}{k_t} [\lambda_t - f|\lambda_n| \frac{\hat{\lambda}_t}{\|\hat{\lambda}_t\|}] \cdot \delta \underline{\lambda}_t) dS, & \|\hat{\lambda}_t\| > f|\hat{\lambda}_n|. \end{cases} \quad (1.33)$$

And, in the case of opening:

$$\delta\Pi_t^{AL} = \int_{\Gamma_c} -\frac{1}{k_t} \lambda_t \cdot \delta \underline{\lambda}_t dS \quad \forall \hat{\lambda}_t. \quad (1.34)$$

The search for the exact Lagrange multipliers λ_n and $\underline{\lambda}_t$ is an iterative process consisting in different augmentation stages. The commonly adopted approach consists in an Uzawa-like double-loop algorithm where the augmentations are performed in the outer loop and convergence of the nonlinear problem (with a fixed Lagrange multiplier given by the outer loop) is reached in the inner loop [Glowinski and Le Tallec, 1984; Bertsekas, 1988; Simo and Laursen, 1992]. In particular, with the Uzawa algorithm, the Lagrange multipliers do not count as additional unknowns in the problem (as opposed to the Lagrange multiplier method), since they are kept constant in the inner loop and updated in the outer loop. Therefore, the penalty parameters k_n and k_t do not affect the conditioning of the problem, nor the accuracy at convergence. This iteration procedure usually increases the required number of iterations, but yields a very simple and robust algorithm [Wriggers et al., 1985; Laursen and Simo, 1993; Zavarise et al., 1995].

This formulation combines the strengths of both the classical Lagrange multipliers and the penalty method, i.e., decreases the ill-conditioning of the governing equations, guarantees the exact satisfaction of the constraints with finite penalties, and especially guarantees robustness of the problem, that is it generally converges. **However, the augmentation parameters affect the convergence rate of the problem, with optimal values that depend on the specific problem and are not known a priori** [Sun et al., 2008].

3.3.4 Nitsche method

Another formulation which can be applied to enforce the contact constraints was derived by Nitsche [Nitsche, 1971; Wriggers and Zavarise, 2008]. See [Becker and Hansbo, 1999] for its application to domain decomposition with non-matching grids, to large deformation problems [Mlika et al., 2017; Mlika, 2018], or thermomechanical contact problems [Seitz et al., 2019].

It is based on a different concept in which, instead of the Lagrange multipliers, contact forces are computed from the stress field of the bodies. The Nitsche functional to take into account frictionless contact conditions is the following:

$$\Pi_n^N = - \int_{\Gamma_c} \frac{1}{2} (F_n^E + F_n^{E'}) g_n dS + \frac{1}{2} \int_{\Gamma_c} k_n g_n^2 dS. \quad (1.35)$$

The variation of the Nitsche functional leads to:

$$\delta\Pi_n^N = - \int_{\Gamma_c} \frac{1}{2} (\delta F_n^E + \delta F_n^{E'}) g_n dS - \frac{1}{2} (F_n^E + F_n^{E'}) \delta g_n dS + \int_{\Gamma_c} k_n g_n \delta g_n dS. \quad (1.36)$$

The method consists in expressing the contact forces and their variations in terms of the displacement field of each body in contact. In the case of linear elasticity they are:

$$\begin{aligned} F_n^j &= \underline{n}^j \cdot \boldsymbol{\sigma}(\underline{u}^j) \cdot \underline{n}^j = \underline{n}^j \cdot (\mathbf{K} : \boldsymbol{\varepsilon}(\underline{u}^j)) \cdot \underline{n}^j, \\ \delta F_n^j &= \underline{n}^j \cdot \boldsymbol{\sigma}(\delta \underline{u}^j) \cdot \underline{n}^j = \underline{n}^j \cdot (\mathbf{K} : \boldsymbol{\varepsilon}(\delta \underline{u}^j)) \cdot \underline{n}^j, \end{aligned} \quad (1.37)$$

for $j = E, E'$.

The Nitsche method yields a formulation which only depends upon the primary displacement variables and, in contrast to the Lagrange multiplier method, one does not need to introduce additional variables. Similar considerations can be done for the frictional stick case. In the nonlinear case the Nitsche method becomes more complex, since the variations of the tractions depend upon the type of constitutive equations used to model the solid. They are thus more difficult to compute than the variations of the Lagrange multipliers.

3.4 Numerical strategies

In this section, we briefly examine some algorithms crucial for handling contact problems. Generally, we can differentiate between global algorithms, which are required to determine the correct number of active constraint equations and to solve the global equilibrium problem, and local algorithms, which are needed to integrate frictional constitutive equations at the interface.

Regarding local algorithms, an evolution equation for the tangential sliding has to be solved. Early methods consist in “trial-and-error” algorithms [Curnier et al., 1992], or based on mathematical programming approach [Klarbring, 1986]. Another interesting method involves recasting the frictional laws in terms of non-associated plasticity [Fredriksson, 1976; Michalowski, 1978], with the application of return mapping schemes to frictional problems [Wriggers, 1987; Giannakopoulos, 1989]. This approach enables the development of algorithmic tangent matrices, necessary for achieving quadratic convergence within Newton-type iterative schemes. However, due to the non-associativity of the frictional slip, these matrices are non-symmetrical. Similarly, the bi-potential method [De Saxcé and Feng, 1998] provides a powerful tool to model dissipative constitutive laws (such as Coulomb friction laws) and enables to write the contact conditions in a compact form and to uncover an implicit normality rule structure. In particular, the complete contact law can be rewritten as a projection equation onto Coulomb’s cone. See [Joli and Feng, 2008] for an application of the bi-potential method with Newton algorithm, or [Feng, 1995; Feng et al., 2003] with Uzawa algorithm.

The range of global algorithms for constraint optimization is vast. These include simplex methods, active set strategies, sequential quadratic programming, penalty, Lagrangian and augmented Lagrangian techniques. Since contact problems result in a nonlinear system, these techniques are often coupled with a Newton nonlinear solver or nonlinear Gauss-Seidel method [Jourdan et al., 1998]. However, the non-differentiability of the contact laws complicates the direct application of Newton methods. This has inspired the use of generalized and/or non-smooth Newton methods [Curnier and Alart, 1988; Pang, 1990; Alart and Curnier, 1991; Alart, 1997; Christensen, 2002; Bertails-Descoubes et al., 2011; Renard, 2013; Seitz et al., 2015].

In a dynamic context, these strategies are still valid but special attention must be devoted to the choice of time integration schemes in order to guarantee numerical stability during the resolution of nonlinear problem. The interested reader may refer to the following papers for more details and pertinent literature review in different contexts: [Visseque et al., 2013; Li et al., 2018; Di Stasio et al., 2021; Barboteu et al., 2023; Barboteu et al., 2024].

3.4.1 Partial Dirichlet-Neumann algorithm or status method

The status method is one of the easiest methods to deal with contact conditions and to implement. The main idea is to replace the geometrical constraints due to normal and frictional contact by partial Dirichlet-Neumann boundary conditions in an iterative manner based on the status of the nodes. This method operates at two iterative levels:

- at the lower level, the interface nodes are iteratively updated based on previous calculations. For instance, if interpenetration is detected, a Dirichlet condition is imposed to ensure continuity of movement;
- at the global level, mechanical calculations are iteratively updated with the Dirichlet and Neumann conditions from the previous level.

To handle normal contact conditions, two node statuses are defined: contact or detachment. For each interface node, a test is performed to check if the status needs to be maintained or changed. Regarding tangential contact, a test is carried out on the tangential reaction on these nodes: if the reaction remains within the Coulomb's cone, the nodes are considered adherent. If the tangential reaction exceeds the cone, the nodes are considered to be sliding. In adhesion, complete Dirichlet conditions are imposed to ensure continuity of displacement at the interface. In the case of sliding; the normal contact condition is managed by a partial Dirichlet condition along the interface normal, imposing MPC-type (Multi Point Constraint) conditions [Abel and Shephard, 1979]. Tangential sliding conditions are addressed through a partial Neumann condition, imposing a reaction at the Coulomb's cone boundary.

Such a strategy is however very sensitive to contact status switches and may lead to instabilities. Moreover, the Dirichlet conditions that change with each iteration lead to continually factorize the stiffness matrix, which can be a costly operation.

3.4.2 Augmented Lagrangian and Uzawa algorithm

As explained previously, a combination of the penalty and the Lagrange multiplier methods leads to augmented Lagrangian methods, which try to combine the merits of both approaches. Here we consider the frictionless problem. A discretized formulation of the frictionless augmented Lagrangian (1.29) yields:

$$\mathcal{L}^{AL}(\mathbf{u}) = \Pi(\mathbf{u}) + \boldsymbol{\Lambda}^T \mathbf{G}^c(\mathbf{u}) + \frac{k_n}{2} \mathbf{G}^c(\mathbf{u})^T \mathbf{G}^c(\mathbf{u}) - \frac{1}{2k_n} \boldsymbol{\lambda}^T \boldsymbol{\lambda}, \quad (1.38)$$

where $\boldsymbol{\Lambda}$ and \mathbf{G}^c contain respectively the force contributions and kinematic constraints related to the nodes in contact, and $\boldsymbol{\lambda}$ is related to the nodes in opening, which ensures differentiability of the functional. Its variation with respect to displacements and Lagrange multipliers yields the nonlinear equation system:

$$\begin{aligned} \mathbf{G}(\mathbf{u}) + \boldsymbol{\Lambda}^T \mathbf{C}^c + k_n \mathbf{C}^c(\mathbf{u})^T \mathbf{G}^c(\mathbf{u}) &= \mathbf{0} \\ \mathbf{G}^c(\mathbf{u}) &= \mathbf{0} \\ -\frac{1}{k_n} \boldsymbol{\lambda} &= \mathbf{0}. \end{aligned} \quad (1.39)$$

In the previous equations, $\mathbf{G}(\mathbf{u})$ stems from the linearization of $\Pi(\mathbf{u})$ and $\mathbf{C}^c(\mathbf{u})$ from the linearization of $\mathbf{G}^c(\mathbf{u})$. By employing Newton's method to solve (1.39), leads to the following incremental equation system at the state $(\mathbf{u}_i, \boldsymbol{\Lambda}_i)$:

$$\begin{bmatrix} \mathbf{K}_t + k_n \mathbf{C}^{cT} \mathbf{C}^c & \mathbf{C}^{cT} & \mathbf{0} \\ \mathbf{C}^c & \mathbf{0} & \mathbf{0} \\ \mathbf{0} & \mathbf{0} & -1/k_n \mathbf{I}_d \end{bmatrix}_i \begin{Bmatrix} \Delta \mathbf{u} \\ \Delta \boldsymbol{\Lambda} \\ \Delta \boldsymbol{\lambda} \end{Bmatrix}_{i+1} = - \begin{Bmatrix} \widehat{\mathbf{G}} \\ \mathbf{G}^c \\ -1/k_n \boldsymbol{\lambda} \end{Bmatrix}_i, \quad (1.40)$$

where $\widehat{\mathbf{G}}$ represents the residual of \mathbf{G} after linearization.

The previous linear system involves the direct computation of both displacements and Lagrange multipliers. When the strategy is used in combination with an Uzawa algorithm, the Lagrange multipliers are supposed fixed, that is only the variation with respect to the displacements is computed. In such a way, only the equations pertaining to the displacements are solved, while the Lagrange multipliers are updated in an outer loop. By performing the variation with respect to the displacements, and keeping fixed the Lagrange multipliers $\overline{\boldsymbol{\Lambda}}$, we get:

$$\mathbf{G}^{UA}(\mathbf{u}, \overline{\boldsymbol{\Lambda}}) = \mathbf{G}(\mathbf{u}) + \overline{\boldsymbol{\Lambda}}^T \mathbf{G}^c + k_n \mathbf{G}^c(\mathbf{u})^T \mathbf{G}^c(\mathbf{u}) = \mathbf{0}. \quad (1.41)$$

For a known fixed Lagrange multiplier $\overline{\boldsymbol{\Lambda}}$, Newton's method is used to solve the nonlinear problem (1.41). This results, after linearization, in the equation system at the state $(\mathbf{u}_i, \overline{\boldsymbol{\Lambda}})$:

$$\left[\mathbf{K}_t(\mathbf{u}_i, \overline{\boldsymbol{\Lambda}}) + k_n \mathbf{C}^c(\mathbf{u}_i)^T \mathbf{C}^c(\mathbf{u}_i) \right] \Delta \mathbf{u}_{i+1} = -\widehat{\mathbf{G}}(\mathbf{u}_i, \overline{\boldsymbol{\Lambda}}). \quad (1.42)$$

After convergence of the Newton scheme, Lagrange multipliers are update in the outer loop:

$$\overline{\boldsymbol{\Lambda}}_{k+1} = \overline{\boldsymbol{\Lambda}}_k + k_n g_n(\mathbf{u}_{i+1}). \quad (1.43)$$

The schematic Uzawa strategy is shown in [Algorithm 1](#).

Algorithm 1: Uzawa algorithm

```

Initialize:  $\mathbf{u}_0 = \mathbf{0}, \bar{\Lambda}_0 = \mathbf{0}$ 
for  $k=1, \dots, \text{convergence}$  do
  for  $i=1, \dots, \text{convergence}$  do
    - solve  $\mathbf{G}(\mathbf{u}_i, \bar{\Lambda}_k) = \mathbf{0}$ 
    - check convergence  $\|\mathbf{G}(\mathbf{u}_i)\| \leq \text{TOL}$ 
  - perform augmentations  $\bar{\Lambda}_k = \bar{\Lambda}_{k-1} + k_n g_n(\mathbf{u}_i)$ 
  - check convergence:  $\|g_n(\mathbf{u}_i)\| \leq \text{TOL}$ 

```

3.4.3 LATIN non-incremental method

The strategies presented beforehand implicitly refer to an incremental approach to solve the frictional contact problem, consisting in making converge the problem at a given time step t_j , knowing the converged solution from the previous time step t_{j-1} , up to the final time T . A different resolution method consist in making use of a non-incremental approach. In a non-incremental approach, all time steps are swept at each iteration and each non-incremental iteration ends on a space-time approximation of the solution.

The LATIN method, introduced in [Ladevèze, 1999], is a general strategy for dealing with nonlinear evolution problems and belongs to the family of non-incremental solvers. The main idea of the LATIN is to separate the difficulties of a given problem. For many classes of problems this consists in avoiding the simultaneity of the global character of the problem and its local nonlinear behavior, which leads to a partitioning of the underlying equations into two manifolds: one pertaining to the local and possibly nonlinear equations, while the other one is related to the linear and possibly global equations. The search for the solution is based on a two search alternating direction algorithm, which shares similarities with ADMM (Alternating Direction Methods of Multipliers) methods [Glowinski and Le Tallec, 1989, 1990; Glowinski, 2015]. At each iteration, a solution on the whole space and time domain of the problem is alternately built in each of the two manifolds. When applied to frictional contact problems, the LATIN method separates the internal equations belonging to the substructures from the contact conditions that occur at the contact interfaces. In addition, the two-search direction alternate algorithm of the LATIN shares similar features with augmented Lagrangian formulations combined with Uzawa-like algorithms [Fortin and Glowinski, 2000; Simo and Laursen, 1992], which makes it a strongly robust strategy for dealing with contact problems, ensuring an exact satisfaction of contact conditions at convergence.

To briefly explain the strategy, let us go back to **Problem 1.1**. Let $\mathbf{A}_d^{[0,T]}$ be the manifold of solutions satisfying kinematic admissibility (1.17), static admissibility (1.18) and the constitutive relation (1.19) (which here represents a linear elasticity behavior),

and let $\Gamma^{[0,T]}$ be the manifold of solutions satisfying Signorini conditions ([Definition 1.1](#)) and Coulomb's frictional law ([Definition 1.2](#)) in all the time domain $[0, T]$. The LATIN method for solving [Problem 1.1](#) consists in iterating successively between manifolds $\mathbf{A}_d^{[0,T]}$, a phase which is called *linear stage*, and $\Gamma^{[0,T]}$, named *local stage*, by following two alternating search direction equations \mathbf{E}^+ and \mathbf{E}^- introduced to iterate in a fixed-point manner between the two manifolds and to close the problem. Starting from an initial admissible solution \mathbf{s}_0 , at convergence the exact solution $\mathbf{s}_{\text{exact}}$ is reached at the intersection between the two manifolds:

$$\mathbf{s}_0 \Rightarrow \dots \Rightarrow \mathbf{s}_n \in \mathbf{A}_d^{[0,T]} \xrightarrow[\mathbf{E}^+]{\text{local stage}} \hat{\mathbf{s}}_{n+1/2} \in \Gamma^{[0,T]} \xrightarrow[\mathbf{E}^-]{\text{linear stage}} \mathbf{s}_{n+1} \in \mathbf{A}_d^{[0,T]} \Rightarrow \dots \Rightarrow \mathbf{s}_{\text{exact}}$$

Moreover, the LATIN naturally leads to a mixed DDM strategy [[Champaney et al., 1999](#); [Oumaziz et al., 2017](#)], where interface variables are constituted by the interface displacements (primal unknowns) and contact forces (dual unknowns). The introduction of a coarse problem (reduced interface problem) to endow the DDM with the scalability property is also possible [[Ladevèze and Dureisseix, 2000](#); [Ladevèze and Nouy, 2003](#)]. However, the most attractive feature of the method lies in its non-incremental nature in space-time. In such a way, it is possible to make use of on-the-fly model reduction based on the separation of variables, such as PGD [[Nouy, 2010](#)], even for nonlinear problems [[Ladevèze et al., 2010](#)]. The strategy, applied to frictional contact problems, will be detailed in the second part of this manuscript.

4 Overview on model reduction and applications to frictional contact problems

This section deals with model reduction, both a posteriori and a priori strategies. The main model reduction techniques in the literature are introduced concisely. In order to be uniform in notation and without losing generality, the techniques are introduced on an abstract parameter-dependent boundary value problem. Thereafter are reported the applications of these techniques specifically for contact problems, with or without friction, highlighting strong and weak points and focusing on the benefits that a multiscale approach can bring to model reduction of frictional contact problems.

4.1 Introduction to model-order reduction

In the last decades, reduced-order modeling (ROM) techniques have been developed to reduce computational costs of linear and nonlinear computational problems with negligible losses in terms of accuracy of the solution. These methods allow for a simplified representation of the evolution of physical systems employing a very reduced number of DOFs. They consist in performing the resolution into a reduced subspaces, or “reduced-order basis” (ROB), of the original problem such that it captures the most dominant aspects of the original one, guaranteeing, at the same time, an acceptable accuracy. Among these methods, model reduction methods based on separation of variables (of space and time, or other parameters) are the most commonly adopted since they allow for a simplified representation of the field functions and allow to project the original problem onto a reduced subspace.

A good approximation of the solution of a given problem sought by model-order reduction can be assumed on the condition that the set of precomputed solutions is appropriate in the sense that its Kolmogorov n -width converges to zero as n goes to infinity:

Definition 1.3 (Kolmogorov n -width). Let Z be an Hilbert linear space, X be a subset of Z , and Z_n a generic n -dimensional subspace of Z . The deviation of X from Z_n is:

$$E(X; Z_n) = \sup_{u \in X} \inf_{v_n \in Z_n} \|u - v_n\|_Z. \quad (1.44)$$

The Kolmogorov n -width of X in Z is defined as:

$$d_n(X; Z) = \inf_{Z_n} E(X; Z_n) = \inf_{Z_n} \sup_{u \in X} \inf_{v_n \in Z_n} \|u - v_n\|_Z. \quad (1.45)$$

Basically, the n -width measures the extent to which X may be approximated by a n -dimensional subspace of Z .

These classes of methods can be distinguished by the way in which the ROB is constructed. A first family of techniques, called *a-posteriori* methods, involves a learning phase, called off-line stage where the full-order problem is solved for some values of the parameters, generating the so-called snapshots, which then are used to create a reduced-order basis to project the equations and obtain a reduced-order model. The most classical way to obtain a ROB from a given set of snapshots is the Proper Orthogonal Decomposition (POD). The POD extracts the most relevant modes from the snapshots, and these modes are then used to create a pertinent ROB. The strong point of the method consists in the fact that the number of relevant POD modes is much lower than the scale of the full-order problem, however the quality of the reduced model is strongly affected by the pertinence of the ROB. Another way to obtain a ROB is the Reduced Basis method, which improves the procedure for the selection of the appropriate snapshots.

Another path consists in seeking the solution of the targeted problem in the span of a consistent ROB, progressively built by dedicated algorithm during the solving stage. This represents the *a-priori* model reduction methods, where no off-line learning stage is required. To this family belongs the Proper Generalized Decomposition (PGD).

In the following, some of these techniques are described and illustrated on an abstract boundary value problem where, for the sake of generality, the time dependency is replaced by a general parameter dependency with respect to a parameter μ .

4.2 Abstract problem

Let us consider a bounded regular domain Ω included in \mathbb{R}^3 and a parameter domain \mathcal{D} . Let \underline{u} be a function defined on \mathcal{D} with values on a Hilbert space \mathcal{V} , solution of the following parameter-dependent boundary value problem expressed in an abstract weak sense:

Problem 1.7. $\forall \mu \in \mathcal{D}$, find $\underline{u} \in \mathcal{V}$ such that, $\forall \underline{v} \in \mathcal{V}$,

$$a(\underline{u}, \underline{v}; \mu) = l(\underline{v}; \mu), \quad (1.46)$$

with $l(\bullet; \mu)$ a linear form on \mathcal{V} and $a(\bullet, \bullet; \mu)$ a continuous symmetric bilinear form on \mathcal{V} .

By performing a semi-discretization in space on an approximated finite-dimensional space $\mathcal{V}_n \subset \mathcal{V}$ of dimension n , and by identifying $\underline{v} \in \mathcal{V}_n$ by a vector $\mathbf{v} = (v_1, \dots, v_n)^T \in \mathbb{R}^n$, the following discretized system has to be solved for every $\mu \in \mathcal{D}$:

$$\mathbb{A}(\mu)\mathbf{u} = \mathbf{l}(\mu). \quad (1.47)$$

That is, a $n \times n$ linear system depending on a parameter μ for which we are interested to compute the solution, at a computational cost of $\mathcal{O}(n^3)$. It is easy to understand how, if n is very large, the solution of Eq.(1.47) for a large number of parameter values becomes unfeasible.

For this purpose, model-order reduction techniques aim at reducing the computational complexity of such kind of problems. In order to analyse the features of these techniques, let us introduce the following functional space:

$$\mathcal{L}^2(\mathcal{D}; \mathcal{V}) := \{\underline{u} : \mathcal{D} \mapsto \mathcal{V}; \int_{\mathcal{D}} \|\underline{u}\|_{\mathcal{V}}^2 d\mu < \infty\}, \quad (1.48)$$

with $\|\underline{u}\|_{\mathcal{V}}$ being a norm on \mathcal{V} . By denoting $\mathcal{P} = \mathcal{L}^2(\mathcal{D}; \mathbb{R}) := \mathcal{L}^2(\mathcal{D})$ and identifying the space $\mathcal{L}^2(\mathcal{D}; \mathcal{V})$ with the tensor product space $\mathcal{V} \otimes \mathcal{P}$, we are interested in finding $\underline{u}(\underline{x}; \mu) \in \mathcal{V} \otimes \mathcal{P}$ solution of the following space-parameter weak boundary value problem:

Problem 1.8. Find $\underline{u} \in \mathcal{V} \otimes \mathcal{P}$ such that, $\forall \underline{v} \in \mathcal{V} \otimes \mathcal{P}$,

$$A(\underline{u}, \underline{v}) = L(\underline{v}), \quad (1.49)$$

with $A(\underline{u}, \underline{v}) = \int_{\mathcal{D}} a(\underline{u}, \underline{v}; \mu) d\mu$ and $L(\underline{v}) = \int_{\mathcal{D}} l(\underline{v}; \mu) d\mu$.

4.3 Proper Orthogonal Decomposition

An introduction to the Proper Orthogonal Decomposition, whose origins date back to the Eigenvalue Decomposition introduced by Beltrami [Beltrami, 1873] and its generalization, the Singular Value Decomposition (SVD) introduced by Jordan [Jordan, 1874], can be found in [Chatterjee, 2000].

Let us suppose that the solution $\underline{u}(\underline{x}; \mu) \in \mathcal{V} \otimes \mathcal{P}$ of **Problem 1.8** is known, the Proper Orthogonal Decomposition consists in searching for a separated representation \underline{u}_M of \underline{u} in space and parameters such it is the optimal one with respect to some particular norm. The separated representation is in the form:

$$\underline{u}_M = \sum_{k=1}^M \underline{\Phi}_k(\underline{x}) \lambda_k(\mu), \quad (\underline{\Phi}_k, \lambda_k) \in \mathcal{V} \times \mathcal{P}, \quad (1.50)$$

with $\underline{\Phi}_k$ functions of the space variables, called space modes or space functions, and λ_k functions of the parameter, defined as parameter modes or functions. The previous separated representation is defined as the one which minimizes the distance to the solution \underline{u} with respect to a given norm on $\mathcal{V} \otimes \mathcal{P}$, i.e.,

$$\|\underline{u} - \underline{u}_M\|^2 = \min_{\substack{\{\underline{\Phi}_k\}_{k=1}^M \in (\mathcal{V})^M \\ \{\lambda_k\}_{k=1}^M \in (\mathcal{P})^M}} \left\| \underline{u} - \sum_{k=1}^M \underline{\Phi}_k(\underline{x}) \lambda_k(\mu) \right\|^2. \quad (1.51)$$

A classical choice for the norm consists in introducing a natural norm on $\mathcal{V} \otimes \mathcal{P}$ defined by

$$\|\underline{u}\|^2 = \int_{\mathcal{D}} \|\underline{u}\|_{\mathcal{V}}^2 d\mu, \quad (1.52)$$

and, by denoting with $\langle \cdot, \cdot \rangle_{\mathcal{V}}$ the inner product associated with $\|\cdot\|_{\mathcal{V}}$, one can define an inner product on $\mathcal{V} \otimes \mathcal{P}$ associated with $\|\cdot\|$ as:

$$\langle \langle \underline{u}, \underline{v} \rangle \rangle = \int_{\mathcal{D}} \langle \underline{u}, \underline{v} \rangle_{\mathcal{V}} d\mu. \quad (1.53)$$

It can be shown that the inner product $\langle \langle \cdot, \cdot \rangle \rangle$ holds the following separation property :

$$\langle \langle \underline{\Phi}\lambda, \underline{\Phi}^*\lambda^* \rangle \rangle = \langle \underline{\Phi}, \underline{\Phi}^* \rangle_{\mathcal{V}} \langle \lambda, \lambda^* \rangle_{\mathcal{P}}, \quad \forall \underline{\Phi}, \underline{\Phi}^* \in \mathcal{V}, \forall \lambda, \lambda^* \in \mathcal{P}, \quad (1.54)$$

with $\langle \lambda, \lambda^* \rangle_{\mathcal{P}} = \int_{\mathcal{D}} \lambda \lambda^* d\mu$ being the natural inner product in $\mathcal{L}^2(\mathcal{D})$. Under these circumstances, the POD problem 1.51 is equivalent to finding the M eigenvectors associated to the M largest eigenvalues of the following eigenproblem:

$$\mathbf{R}(\underline{\Phi}) = \sigma \underline{\Phi}, \quad (1.55)$$

with $\mathbf{R} : \mathcal{V} \mapsto \mathcal{V}$ being a symmetric positive linear operator, called spatial correlation operator or POD operator, defined as:

$$\langle \mathbf{R}(\underline{\Phi}), \underline{\Phi}^* \rangle_{\mathcal{V}} = \langle \langle \underline{\Phi}^*, \underline{u} \rangle_{\mathcal{V}} \langle \underline{u}, \underline{\Phi} \rangle_{\mathcal{V}} \rangle_{\mathcal{P}} \quad \forall \underline{\Phi}^*. \quad (1.56)$$

By denoting with $\{\underline{\Phi}_k\}_{k \geq 1}$ an orthogonal set of eigenfunctions of \mathbf{R} , and by sorting the eigenpairs $(\underline{\Phi}_k, \sigma_k) \in \mathcal{V} \times \mathbb{R}^+$ in an increasing order of the eigenvalues, i.e., $(\sigma_1 \geq \sigma_2 \geq \dots \geq 0)$, then the optimal orthogonal separated representation \underline{u}_M of order M for \underline{u} can be obtained, with

$$\lambda_k(\mu) = \frac{\langle \underline{\Phi}_k, \underline{u} \rangle_{\mathcal{V}}}{\|\underline{\Phi}_k\|_{\mathcal{V}}^2}, \quad (1.57)$$

and the approximation error which verifies:

$$\|\underline{u} - \underline{u}_M\|^2 = \|\underline{u}\|^2 - \sum_{k=1}^M \sigma_k \xrightarrow{M \rightarrow \infty} 0. \quad (1.58)$$

Remark 1.1. *The optimal separated representation can be equivalently reformulated as an eigenproblem on λ , as follows:*

$$\mathbf{G}(\lambda) = \sigma \lambda, \quad (1.59)$$

where \mathbf{G} represents the complementary POD operator, defined as

$$\langle \mathbf{G}(\lambda), \lambda^* \rangle_{\mathcal{P}} = \langle \langle \lambda^*, \underline{u} \rangle_{\mathcal{P}} \langle \underline{u}, \lambda \rangle_{\mathcal{P}} \rangle_{\mathcal{V}}, \quad \forall \lambda^*. \quad (1.60)$$

Similarly, from the eigenvectors λ_k of \mathbf{G} , one can find the space functions as:

$$\underline{\Phi}_k(\underline{x}) = \frac{\langle \lambda_k, \underline{u} \rangle_{\mathcal{P}}}{\|\lambda_k\|_{\mathcal{P}}^2}. \quad (1.61)$$

It can be shown that eigenproblems (1.55) and (1.59) are equivalent, that is to say if $(\underline{\Phi}_k, \sigma_k) \in \mathcal{V} \times \mathbb{R}^+$ is an eigenpair of (1.55), then $(\lambda_k, \sigma_k) \in \mathcal{V} \times \mathbb{R}^+$, with λ_k given by (1.57), is an eigenpair of (1.59) and vice versa.

Remark 1.2. A natural choice for $\langle \cdot, \cdot \rangle_{\mathcal{V}}$ and $\langle \cdot, \cdot \rangle_{\mathcal{P}}$ is the inner product in \mathcal{L}^2 . The energy norm associated to the bilinear form a is also often used.

4.3.1 A posteriori model reduction through Proper Orthogonal Decomposition

POD is a useful tool for data compression/analysis and reduced-order modeling in different domains, such as stochastic analysis of experimental or numerical data, acoustics, image treatment, dynamical systems, CFD, etc. [Chatterjee, 2000; Atwell and King, 2001; Kerschen et al., 2005; Zimmermann, 2013]. In order to perform classical POD, an approximation of \underline{u} has to be known in order to perform the a posteriori analysis. In a parametrized problem, the usual way to proceed is to choose a sample of size p of the parameter domain $\mathcal{D}_p \subset \mathcal{D}$ and to solve the full-order problem for all the parameters in \mathcal{D}_p . For each parametric problem solved, through the POD procedure a reduced-order basis of space functions is extracted and added to a global reduced-order basis. Then the reduced-order basis is used to project the equations of the full-order problem onto a reduced subspace.

■ Galerkin projection on a spatial reduced-order basis

Let us suppose that a global reduced-order basis in space $\{\underline{\Phi}_k\}_{k=1}^M$ has been extracted by solving the parametric problem for p different parameters in \mathcal{D} , that is, a low-dimensional subspace $\mathcal{V}_M = \text{span}\{\underline{\Phi}_k\}_{k=1}^M \subset \mathcal{V}$ has been constructed, with $M \leq p$. A posteriori model reduction with POD consists in a Galerkin projection of the original problem onto the low-dimensional subset \mathcal{V}_M , that is to find $\underline{u}_M \in \mathcal{V}_M \otimes \mathcal{P}$ such that,

$$A(\underline{u}_M, \underline{v}_M) = L(\underline{v}_M), \quad \forall \underline{v}_M \in \mathcal{V}_M \otimes \mathcal{P}. \quad (1.62)$$

Eq. (1.62) consists in a parameter-weak formulation of the following system of M equations:

$$\sum_{j=1}^M a(\underline{\Phi}_j, \underline{\Phi}_i; \mu) \lambda_j(\mu) = l(\underline{\Phi}_i; \mu), \quad i \in \{1, \dots, M\}, \quad (1.63)$$

where the unknowns are the parameter functions $\{\lambda_k\}_{k=1}^M$. The previous problem can then be used to solve the problem for different values of the parameter with a reduced computational cost. In a discretized version, Eq. (1.63) consists in solving the following linear system:

$$[\Phi_M^T \mathbb{A}(\mu) \Phi_M] \Lambda_M = \Phi_M^T \mathbf{l}(\mu), \quad (1.64)$$

where $\Phi_M = \{\Phi_k\}_{1 \leq k \leq M}$ represents the collection of the space functions and $\Lambda_M = \{\lambda_k\}_{1 \leq k \leq M}$ the collection of the parameter functions. $\mathbb{A}_M(\mu) = \Phi_M^T \mathbb{A}(\mu) \Phi_M \in \mathbb{R}^{M \times M}$ represents the reduced-order discrete operator of the problem, now of size $(M \times M)$, projection of the full operator \mathbb{A} onto the reduced-order basis, while $\mathbf{l}_M(\mu) = \Phi_M^T \mathbf{l}(\mu) \in \mathbb{R}^M$ represents the projection of the linear operator onto the reduced-order basis. Now, in the reduced subspace, for every parameter one has to solve a $M \times M$ linear system, with $M \ll n$.

Remark 1.3. *If the operator \mathbb{A} is parameter-independent or with an affine dependence on μ , the projection onto the reduced-order basis can be done once and for all in the offline stage. Instead, when it depends on μ in a non-affine manner, the projection onto the reduced-order basis has to be computed each time for every parameter where we want to solve the problems, and it can be computationally costly as it scales with the size of the original problem n , thus reducing the performances of model-order reduction [Greppl et al., 2007; Capaldo et al., 2017].*

Remark 1.4. *Another point of view consists in constructing a low-dimensional subspace $\mathcal{P}_M = \text{span}\{\lambda_k\}_{k=1}^M \subset \mathcal{P}$ by means of POD applied to the problem for the p different parameter values, and then looking for the Galerkin approximation $\underline{u}_M \in \mathcal{V} \otimes \mathcal{P}_M$ defined by:*

$$A(\underline{u}_M, \underline{v}_M) = L(\underline{v}_M), \quad \forall \underline{v}_M \in \mathcal{V} \otimes \mathcal{P}_M. \quad (1.65)$$

This time, Eq. (1.65) leads to solve a set of M equations for the M space functions $\{\Phi_k\}_{k=1}^M$. However this approach, for large scale applications, leads to higher computational costs compared to the approach based on projecting onto a basis of space functions.

■ POD in the discretized format

The application of the POD for model-order reduction of boundary value problems requires the preliminary computation of a suitable reduced-order basis. This reduced-order basis can be computed by performing a POD of the solution of the full-order problem for a sample of p parameter values in $\mathcal{D}_p \subset \mathcal{D}$. These solutions are called snapshots of the problem, and can be arranged in a matrix \mathbb{A} of size $n \times p$, as in Figure 1.23.

By making use of an \mathcal{L}^2 norm on both \mathcal{V} and \mathcal{P} , applying POD to such an arrangement of vectors $\mathbf{u}(\mu_i) \in \mathbb{R}^n$ leads to solve the following eigenvalue problem for the

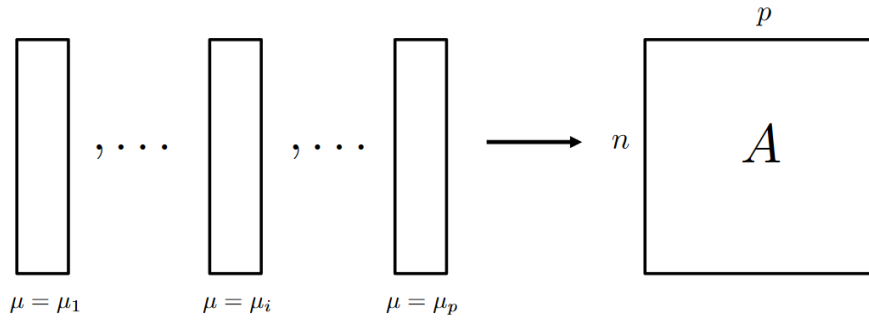


Figure 1.23: Arrangement of the snapshots.

covariance matrix $\mathbf{C} = \mathbb{A}^T \mathbb{A}$ in order to find the spatial basis:

$$\mathbf{C} \Phi_i = \alpha_i \Phi_i. \quad (1.66)$$

In this discretized format, and by making use of a proper norm, POD is also equivalently known as Principal Component Analysis (PCA), Karhunen-Loeve Decomposition (KLD) or Singular Value Decomposition (SVD) [Wu et al., 2003].

We also give a brief explanation of the SVD, a concept we will need later throughout the manuscript. The SVD is a factorization of a real or complex rectangular matrix, introduced first in [Beltrami, 1873] for real matrices, and extended later to complex matrices in [Eckart and Young, 1936]. The SVD factorization has the following form:

$$\mathbb{A} = \mathbb{V} \Sigma \mathbb{U}^T, \quad (1.67)$$

where \mathbb{V} is the $n \times n$ matrix of the orthonormal space vectors \mathbf{V}_k , \mathbb{U} is the $p \times p$ matrix of the orthonormal parametric vectors \mathbf{U}_k , and Σ is a $n \times p$ diagonal matrix whose non-zero entries $\min(n, p)$ are the singular values $\sigma_k > 0$ of the matrix. The singular values are the square roots of the eigenvalues of the covariance matrix $\mathbf{C} = \mathbb{A}^T \mathbb{A}$. Singular values are ordered in Σ in a decreasing manner, and their magnitude indicates the relevance that the respective mode has in representing \mathbb{A} . The faster the singular values decrease, the more \mathbb{A} is approximable with a reduced number of modes:

$$\mathbb{A} \approx \mathbb{A}_M = \sum_{k=1}^M \mathbf{V}_k \sigma_k \mathbf{U}_k^T. \quad (1.68)$$

4.4 Reduced Basis Method

For the Galerkin-POD, the quality of the solution obtained in the reduced subspace is affected by the quality of the computed ROB. In particular, for problems which have strong variations in boundary conditions or strong dynamic evolutions the number of necessary snapshots to have a suitable reduced-order basis can increase so much that the technique becomes unsuitable [Glüsmann and Kreuzer, 2009]. For this reason,

the Reduced Basis method [Maday, 2006; Rozza et al., 2008; Quarteroni et al., 2015; Hesthaven et al., 2016] improves the procedure for the selection of the appropriate snapshots in order to obtain a relevant ROB, although it will not necessarily give a basis with a smaller dimension.

Similarly to the POD, the Reduced Basis method belongs to the separated variables model reduction techniques, and the idea behind consists in approximating the solution $\underline{u}(\underline{x}; \mu)$ of a parameter-dependent problem by a linear combination of preliminary computed solutions $\underline{u}(\underline{x}; \mu_i)$ corresponding to properly chosen parameters that maximize an a posteriori error estimator [Veroy and Patera, 2005; Rozza, 2011]. The main difference of the Reduced Basis method with respect to the POD lays in the construction of the ROB. In the Reduced Basis method the snapshots are constructed at specific parameter values selected by a greedy algorithm:

$$\begin{aligned} \mu_1 &= \arg \sup_{\mu \in \mathcal{D}} \|\underline{u}(\underline{x}; \mu)\|_{\mathcal{V}}, \\ &\vdots \\ \mu_{i+1} &= \arg \sup_{\mu \in \mathcal{D}} \|\underline{u}(\underline{x}; \mu) - \Pi_i \underline{u}(\underline{x}; \mu)\|_{\mathcal{V}}, \end{aligned} \tag{1.69}$$

with Π_i being an orthonormal projection onto $\Phi_i = \text{span}\{\underline{u}(\underline{x}, \mu_k)\}$, $k = 1, \dots, i$. That is, a greedy algorithm that looks for the best M parameters where to evaluate the full problem.

■ A posteriori model reduction with Reduced Basis method

The procedure to solve [Problem 1.8](#) by the Galerkin Reduced Basis method is similar to the Galerkin-POD one. During the offline phase, the full-order model is first solved for some relevant parameter values μ_i obtained by the greedy algorithm described previously. These are the snapshots of the solution, and a ROB is obtained simply by collecting the snapshot solutions $\Phi_i = \underline{u}(\underline{x}, \mu_i)$ and performing an orthonormalization in order to improve the conditioning of the reduced-order problem. The main difference with POD-based model reduction relies on the fact that, thanks to the greedy algorithm, the computed snapshots do not need to be compressed in order to extract a relevant reduced-order basis, instead the snapshots themselves are used as reduced-order basis.

4.5 Proper Generalized Decomposition

Other techniques do not involve preliminary costly simulations in order to construct a reduced-order basis. They progressively build, by online dedicated algorithms, a pertinent ROB during the resolution of the same problem.

The Proper Generalized Decomposition (PGD) is a recent model-order reduction technique that can be intended as a generalization of the POD, that is orthogonality

between the modes of a compressed representation of a function is not strictly required, and when it is verified it coincides with the POD. Here we will focus directly on the application of the PGD to the solution of boundary value problems. PGD is based on the separation of variables and operates a priori, that is, one looks directly for a low-dimensional separated representation of the solution of a problem, without going through the computation of snapshots. Its origins can be traced back to the “radial loading approximation” introduced as a feature of the LATIN method to reduce memory requirements [Ladevèze, 1999]. It has since become a stand-alone technique applicable to the resolution of various boundary value problems [Nouy, 2010; Chinesta et al., 2011]: from parametric problems [Chinesta et al., 2010], real-time simulations [Niroomandi et al., 2013], inverse problems [González et al., 2012] to stochastic problems [Nouy, 2009]. Strict bounds on global error in the PGD context can be found in [Ladevèze and Chamoin, 2011].

4.5.1 A-priori model reduction through Galerkin-PGD

Here, we introduce the classical definition of PGD based on Galerkin orthogonality criteria, applied to the parametric abstract [Problem 1.8](#).

■ Progressive PGD

Let us assume that a $M - 1$ order decomposition $\underline{u}_{M-1}(x; \mu)$ of \underline{u} in the form of [Eq. \(1.50\)](#) is already known. One looks for the decomposition of order M by searching for a new couple $(\underline{\Phi}_M, \lambda_M) \in \mathcal{V} \times \mathcal{P}$ through Galerkin orthogonality with respect to the test function $\underline{v} = \underline{\Phi}_M^* \lambda_M + \underline{\Phi}_M \lambda_M^*$, as follows:

$$A(\underline{u}_{M-1} + \underline{\Phi}_M \lambda_M, \underline{\Phi}_M^* \lambda_M + \underline{\Phi}_M \lambda_M^*) = L(\underline{\Phi}_M^* \lambda_M + \underline{\Phi}_M \lambda_M^*), \quad \forall (\underline{\Phi}_M^*, \lambda_M^*) \in \mathcal{V} \times \mathcal{P}. \quad (1.70)$$

Given the linearity of operators A and L , $\underline{\Phi}_M$ and λ_M satisfy [Eq. \(1.70\)](#) if and only if they satisfy the following two problems:

$$A(\underline{u}_{M-1} + \underline{\Phi}_M \lambda_M, \underline{\Phi}_M^* \lambda_M) = L(\underline{\Phi}_M^* \lambda_M), \quad \forall \underline{\Phi}_M^* \in \mathcal{V}, \quad (1.71)$$

$$A(\underline{u}_{M-1} + \underline{\Phi}_M \lambda_M, \underline{\Phi}_M \lambda_M^*) = L(\underline{\Phi}_M \lambda_M^*), \quad \forall \lambda_M^* \in \mathcal{P}. \quad (1.72)$$

[Eq. \(1.71\)](#) is an application $S_M : \mathcal{P} \mapsto \mathcal{V}$ which maps $\lambda_M \in \mathcal{P}$ into $\underline{\Phi}_M = S_M(\lambda_M) \in \mathcal{V}$. Conversely, [Eq. \(1.72\)](#) is an application $P_M : \mathcal{V} \mapsto \mathcal{P}$ which maps $\underline{\Phi}_M \in \mathcal{V}$ into $\lambda_M = P_M(\underline{\Phi}_M) \in \mathcal{P}$. The resolution technique of the previous problem can be performed with a fixed-point type iterative process that alternatively solves $\underline{\Phi}_M = S_M(\lambda_M)$, assuming known λ_M (from the previous iteration) and then solves $\lambda_M = P_M(\underline{\Phi}_M)$, as shown in [Algorithm 5](#). This approach is named progressive Galerkin-PGD, since modes are computed progressively and added to the separated representation of \underline{u} until a good convergence of the solution is obtained.

Algorithm 2: Progressive Galerkin-PGD: fixed-point scheme

```

Initialize  $\lambda_M = 1$ ;
while non convergence do
  - compute  $\underline{\Phi}_M = S_M(\lambda_M)$ ;
  - compute  $\lambda_M = P_M(\underline{\Phi}_M)$ ;
  - check convergence;
Set  $\underline{u}_M = \underline{u}_{M-1} + \underline{\Phi}_M \lambda_M$ 

```

However, this approach leads to a separated representation that is not always optimal, that is it may require a large number of modes to obtain a given level of accuracy.

■ Optimal Galerkin-PGD

A more general approach consists in finding the M spatial functions $\Phi_M = \{\Phi_i\}_{1 \leq i \leq M}$ and the M parameter functions $\Lambda_M = \{\lambda_i\}_{1 \leq i \leq M}$ simultaneously. Let $P : (\mathcal{V})^M \mapsto (\mathcal{P})^M$ be the application which maps the set of space functions Φ_M onto the set of parameter functions $\Lambda_M = P(\Phi_M)$, defined by:

$$A(\Phi_M \cdot \Lambda_M, \Phi_M \cdot \Lambda_M^*) = L(\Phi_M \cdot \Lambda_M^*), \quad \forall \Lambda_M^* \in (\mathcal{P})^M, \quad (1.73)$$

with $\Phi_M \cdot \Lambda_M = \sum_{k=1}^M \Phi_k \lambda_k$. Let also $S : (\mathcal{P})^M \mapsto (\mathcal{V})^M$ be instead the application which maps the set of parameter functions Λ_M onto the set of space functions $\Phi_M = S(\Lambda_M)$:

$$A(\Phi_M \cdot \Lambda_M, \Phi_M^* \cdot \Lambda_M) = L(\Phi_M^* \cdot \Lambda_M), \quad \forall \Phi_M^* \in (\mathcal{V})^M. \quad (1.74)$$

The optimal couple (Φ_M, Λ_M) is thus the one that satisfies both of the previous equations, and the computation of this couple can be performed with a fixed-point type algorithm analogous to the one used in the definition of the progressive-PGD ([Algorithm 3](#)). However, this approach leads to algebraic systems M times bigger than the ones obtained with a progressive search of the decomposition, and thus to prohibitive calculation costs as soon as the number of PGD functions overpasses a given number, as also M is not known a priori for a given accuracy.

■ Approximation of the optimal Galerkin-PGD

In the context of parameter-dependent PDEs, the application of the map P is relatively cheap since it corresponds to a set of equations for the scalar parameter modes obtained with the formulation of the original problem on a reduced-order basis of space functions. The application of the map S , instead, is more costly since it involves the solution of a set of coupled parameter-independent PDEs for the vectorial space modes (formulation of the original problem on a reduced-order basis of parameter functions).

Algorithm 3: Optimal Galerkin-PGD: fixed-point scheme

```

Initialize  $\Lambda_M = \mathbf{I}$ ;
while non convergence do
  | - compute  $\Phi_M = S(\Lambda_M)$ ;
  | - compute  $\Lambda_M = P(\Phi_M)$ ;
  | - check convergence;
end
Set  $\underline{u}_M = \Phi_M \cdot \Lambda_M$ 

```

For this reason, the optimal Galerkin PGD strategy, consisting in searching simultaneously for the M couples of the decomposition should be avoided. Making use of the progressive PGD, and introducing a simple additional stage to [Algorithm 5](#), makes it possible to significantly improve the quality of the progressive PGD. The additional stage consists in introducing the application of P in order to update the whole set of parameter functions Λ_M after each construction of a new couple of functions (Φ_M, λ_M) . This cheap updating stage for the parameter functions, described in [Algorithm 4](#), can significantly improve the quality of the progressive PGD decomposition [[Nouy, 2010](#)].

Algorithm 4: Parameter function update stage

```

- perform Algorithm 5 and find  $\Phi_M$ ;
- compute  $\Lambda_M = P(\Phi_M)$ ;
- set  $\underline{u}_M = \Phi_M \cdot \Lambda_M$ 

```

4.5.2 A-priori model reduction through minimal residual PGD

The PGD strategy based on Galerkin orthogonality is easy to implement but generally may present convergence issues. Another way for formulating the PGD is to use a minimum residual formulation, which is generally more robust than Galerkin-PGD in the sense that monotonous convergence in the residual norm can be proved, although convergence may be slower [[Ladevèze and Nouy, 2003](#); [Nouy, 2010](#)]. The minimal residual formulation for [Problem 1.8](#) consists in defining the PGD approximation as a problem of minimization of its residual $\mathcal{R}(\underline{u})$, defined as follows:

$$\langle \langle \underline{v}, \mathcal{R}(\underline{u}) \rangle \rangle := L(\underline{v}) - A(\underline{u}, \underline{v}) = \langle \langle \underline{v}, \mathcal{L} - \mathcal{A}(\underline{u}) \rangle \rangle, \quad \forall \underline{v} \in \mathcal{V} \otimes \mathcal{P}, \quad (1.75)$$

with $\mathcal{L} \in \mathcal{V} \otimes \mathcal{P}$ and $\mathcal{A} : \mathcal{V} \otimes \mathcal{P} \mapsto \mathcal{V} \otimes \mathcal{P}$ defined by using Riesz representations on the Hilbert space $\mathcal{V} \otimes \mathcal{P}$. Still a progressive search for the PGD couples is considered, that is a $M - 1$ order approximation \underline{u}_{M-1} is supposed to be known, and one looks for a new couple (Φ_M, λ_M) defined as follows:

Problem 1.9 (progressive minimal residual PGD). Find $(\underline{\Phi}_M, \lambda_M) \in \mathcal{V} \times \mathcal{P}$ such that,

$$(\underline{\Phi}_M, \lambda_M) = \arg \min_{(\underline{\Phi}_M, \bar{\lambda}_M) \in \mathcal{V} \times \mathcal{P}} \|\mathcal{R}(\underline{u}_{M-1} + \underline{\Phi}_M \bar{\lambda}_M)\|^2. \quad (1.76)$$

That is to say,

$$(\underline{\Phi}_M, \lambda_M) = \arg \min_{(\underline{\Phi}_M, \bar{\lambda}_M) \in \mathcal{V} \times \mathcal{P}} \frac{1}{2} \langle \mathcal{A}(\underline{\Phi}_M \bar{\lambda}_M), \mathcal{A}(\underline{\Phi}_M \bar{\lambda}_M) \rangle - \langle \mathcal{R}(\underline{u}_{M-1}), \mathcal{A}(\underline{\Phi}_M \bar{\lambda}_M) \rangle. \quad (1.77)$$

Stationarity conditions for Eq. (1.77) lead to the following problem:

$$\forall (\underline{\Phi}_M^*, \lambda_M^*) \in \mathcal{V} \times \mathcal{P},$$

$$\langle \mathcal{A}(\underline{\Phi}_M \lambda_M), \mathcal{A}(\underline{\Phi}_M^* \lambda_M + \underline{\Phi}_M \lambda_M^*) \rangle = \langle \mathcal{R}(\underline{u}_{M-1}), \mathcal{A}(\underline{\Phi}_M^* \lambda_M + \underline{\Phi}_M \lambda_M^*) \rangle. \quad (1.78)$$

Similarly to the Galerking-PGD, even in this case one has to solve iteratively the following two problems:

- $\underline{\Phi}_M = S_M(\lambda_M) \in \mathcal{V}$ defined by:

$$\langle \mathcal{A}(\underline{\Phi}_M \lambda_M), \mathcal{A}(\underline{\Phi}_M^* \lambda_M) \rangle = \langle \mathcal{R}(\underline{u}_{M-1}), \mathcal{A}(\underline{\Phi}_M^* \lambda_M) \rangle, \quad \forall \underline{\Phi}_M^* \in \mathcal{V}; \quad (1.79)$$

- $\lambda_M = P_M(\underline{\Phi}_M) \in \mathcal{P}$ defined by:

$$\langle \mathcal{A}(\underline{\Phi}_M \lambda_M), \mathcal{A}(\underline{\Phi}_M \lambda_M^*) \rangle = \langle \mathcal{R}(\underline{u}_{M-1}), \mathcal{A}(\underline{\Phi}_M \lambda_M^*) \rangle, \quad \forall \lambda_M^* \in \mathcal{P}. \quad (1.80)$$

The verification of the previous equations consist in a pseudo-eigenproblem $G_M(\underline{\Phi}_M) = \sigma_M \underline{\Phi}_M$ for the operator $G_M = S_M \circ P_M$. It can be proven that this method has a monotonic convergence in the residual norm, i.e.,

$$\|\mathcal{R}(\underline{u}_M)\|^2 = \|\mathcal{R}(\underline{u}_{M-1})\|^2 - \sigma_M(\underline{\Phi}_M), \quad (1.81)$$

but the resulting decomposition may present very poor convergence properties with respect to usual solution norm $\|\underline{u} - \underline{u}_M\|$. A suitable residual norm may improve this convergence rate, however, the construction of a suitable norm is not straightforward and the use of optimal norms may induce additional computational issues. The best approach to use for the construction of the PGD modes depends on the problem we are willing to solve, and the interested reader can refer to [Nouy, 2010] for a detailed overview of different approaches for different boundary value problems.

4.6 Nonlinear problems and hyperreduction

Model-order reduction is particularly suitable for linear problems, in fact when operator a in [Problem 1.7](#) is linear and independent from μ (or with an affine dependency on μ), its projection onto a reduced basis, as in [Eq. \(1.63\)](#), can be done once and for all offline and can be then factorized and used for the solution of the problem at different parameter values. When we have to deal with nonlinear problems, the solution needs to be coupled with linearization techniques that generate a series of different linear problems that need to construct a new reduced-order model. This means that one has to evaluate the nonlinear terms, integrate them over the entire domain and then project them on the ROB, with a computational complexity that scales with the size of the original problem.

In order to exemplify this, let us consider the following nonlinear reference problem: find $\underline{u} \in \mathcal{V} \otimes \mathcal{P}$ such that $\forall \underline{v} \in \mathcal{V} \otimes \mathcal{P}$,

$$A(\underline{u}, \underline{v}) + G(\underline{u}, \underline{v}) = L(\underline{v}), \quad (1.82)$$

with G being a nonlinear form on \underline{u} and \underline{v} obtained with the integration of a nonlinear function $g(\underline{u}; \mu)$. The most used technique to solve nonlinear problems is the Newton-Raphson method, an incremental iterative solver which at every iteration requires to solve a linear problem. Let us consider a given ROB of space functions $\Phi_M = \{\Phi_i\}_{1 \leq i \leq M}$, we search for an approximate solution $\underline{u}_M = \sum \Phi_i \lambda_i$, and by considering Φ_j as a test function. In the incremental step the following linear system for $\Lambda = \{\lambda_i\}_{1 \leq i \leq M}$ is obtained [[Capaldo et al., 2017](#)]:

$$\sum_i \left[A(\Phi_i, \Phi_j) + \int_{\Omega} \Phi_i \frac{\partial g}{\partial \underline{u}}(\underline{u}^{(n)}; \mu) \Phi_j \right] \lambda_i = -\mathcal{R}(\underline{u}^{(n)}; \mu, \Phi_j), \quad (1.83)$$

where the residual \mathcal{R} now takes into account also the nonlinear term G . The linear term $A(\Phi_i, \Phi_j)$ does not depend on the current value of the iterated solution $\underline{u}^{(n)}$ and, if it does not depend on the parameter μ , it can be computed once and for all, provided that the ROB does not change. However, the nonlinear term $\frac{\partial g}{\partial \underline{u}}(\underline{u}^{(n)}; \mu)$ and the residual $\mathcal{R}(\underline{u}^{(n)}; \mu)$ depend nonlinearly on $\underline{u}^{(n)}$ and also on μ , and have to be computed at each iteration anyway.

It can be shown [[Capaldo et al., 2017](#)] that the evaluation of the nonlinear terms in the reduced framework scales with the dimension of the original high-dimensional problem, and thus represents a bottleneck for the application of model reduction in nonlinear problems. In order to overcome this obstacle, several approaches have been proposed, indicated as *hyperreduction methods*.

For model reduction techniques based on a learning stage (POD-Galerkin or Reduced Basis methods for instance), the Empirical Interpolation Method (EIM) is probably one of the most popular. It has been developed in particular for linear elliptic

problems with non-affine parameter dependence [Barrault et al., 2004] as well as for nonlinear elliptic and parabolic problems [Grepl et al., 2007]. It consists in approximating the nonlinear function $g(\underline{u}; \mu)$ with interpolating functions evaluated at some “magic points” computed offline by a greedy selection. Several variants can be found in the literature, for example the Best Interpolation Point Method [Nguyen and Peraire, 2008] or the Discrete EIM (DEIM) [Chaturantabut and Sorensen, 2010; Tiso and Rixen, 2013]. Another family of techniques for nonlinear problems is the one based on the a priori Hyper-Reduction [Ryckelynck, 2005]. Reduced Integration Domain (RID) techniques are also used, they consist in selecting few elements of the mesh to perform the local integration of the nonlinear terms [Fauque et al., 2018].

In [Capaldo et al., 2017], a new approximation technique, called Reference Point Method (RPM), is proposed in the context of PGD-based model reduction. The RPM is similar to the EIM, however it does not interpolate the nonlinear function. It is rather an approximation technique of the integrals involved in the Galerkin projection similarly to quadrature techniques in classical finite element methods, and is more efficient in contexts where the ROB changes quite often, as in PGD-based model reduction.

4.7 Model reduction in contact problems

The application of model reduction to contact mechanics problems is challenging, since a reduced-order basis may not easily and efficiently capture non-regular and propagating phenomena that occur at the contact interface: sliding, sticking and separation zones being difficult to represent. The difficulty associated to efficiently capture propagating phenomena with a separated format can be exemplified in [Allier et al., 2015], where a one dimensional transient thermal problem with a moving thermal load poses major issues to classical PGD approaches. Even though not strictly related to contact problems, this example is illustrative on how the sliding front of a contact problem may be difficult to capture with a reduced-order basis.

Mainly we can distinguish between a posteriori methods, applied on parametric contact problems where a large amount of contact analyses must be carried out by varying an appropriate parameter which may be, for example, the coefficient of friction or the position of a rigid obstacle, and a priori methods, based essentially on the PGD combined with the LATIN solver.

■ A posteriori methods

With regard to a posteriori methods, in [Balajewicz et al., 2016], the authors consider a parametric contact problem (body in contact with a parametrized obstacle) without friction formulated with the method of Lagrange multipliers, and propose a strategy based on the POD of different snapshots of the problem to build a reduced-order basis for both the displacement field \underline{u} and the contact forces $\underline{\lambda}$ (i.e., the Lagrange multipliers). The construction of a ROB for the Lagrange multipliers requires it to be a positive basis. For this purpose, the authors operate a non-negative matrix factorization (NNMF) of

the snapshots, which is the positive counterpart of the SVD [Lee and Seung, 1999]. The iterative greedy approach for sampling the parameter domain during the training of the ROM is equipped with an error indicator of reasonable offline computational complexity. The computational complexity of the resulting iterative sampling and ROB construction procedure is dominated, however, by the cost of a high number of high-dimensional simulations equal to the number of parameter samplings.

In [Benaceur et al., 2020] a similar approach is applied in the context of the Reduced Basis method for frictionless parametric contact problems with nonlinear constraints (which can be the case, for example, of a frictionless contact problem in large displacements) combined with the Empirical Interpolation Method to deal with the nonlinear constraints. The authors construct the ROB for the Lagrange multipliers by means of a cone-projected greedy algorithm that conserves the non-negativity of the basis. In [Niakh et al., 2023], a recent extension of the previous work, the authors propose an algorithm that guarantees inf-sup stability [Brezzi, 1974] of the generated reduced problem.

Still with the Reduced Basis method, the same authors consider model reduction for parameterized contact problems (in this case with and without friction) formulated with Nitsche's method [Niakh et al., 2024]. The strategy presents considerable benefits compared to mixed (primal-dual) approaches. In fact, since Nitsche's method is a primal method that does not require the introduction of additional Lagrange multipliers, there is no need to guarantee inf-sup stability. In addition, the need to construct a ROB for the Lagrange multipliers, which present low reducibility [Kollepara et al., 2023], is avoided.

In [Fauque et al., 2018], the authors propose an hyperreduction method based on a reduced integration domain (RID) for frictionless contact problems formulated with Lagrange multipliers. The potential contact zone is reduced through the reduced mesh involved in the hyperreduced equations. In contrast to previous work on mixed formulations, which choose to project the dual variable, i.e., the Lagrange multipliers, onto a dual ROB, the authors treat the contact forces on the full-order model restricted to the RID in order to obtain a better quality of the contact forces and contact constraints. Due to non-projection on a dual ROB, the ROM checks all the contact conditions of the FOM in the RID.

A similar idea has also been developed in [Ballani et al., 2018], for parametrized frictional contact problems with augmented Lagrangian formulation. In practice, in order to be more accurate on the interface contact quantities, the authors exploit a "linear-nonlinear domain decomposition" to develop a hybrid formulation: a Reduced Basis approximation is performed on the part of the domain associated to linear elastic behavior (i.e., far from the contact interface), and a full-order model is adopted at the local nonlinear contact interface. The method is particularly efficient when the contact interface is really small compared to the whole structure. For numerous and large contact interfaces, the method loses considerable efficiency.

A different approach, even though it does not necessarily correspond to model-order reduction, is adopted in [Cardoso et al., 2018]. The authors take advantage

of similarities between the mechanical fields around the contact edges in cylindrical contact configurations under fretting conditions and crack tips functions in linear elastic fracture mechanics. POD modes are used to generate enrichment functions in an X-FEM (eXtended Finite Element Method [Moës et al., 1999]) environment and to compute the stiffness matrix which depends on the location of the contact edge.

For general contact problems however, the contact front or the position of sticking/s-sliding front is not known in advance, which makes these techniques not appropriate in our situation, with this knowledge being not available.

■ A priori LATIN-PGD strategy

The a posteriori methods discussed previously present a significant gain in computational time in the online phase, however the offline phase is still too expensive. Moreover, the approaches are directed to parameterized problems. In our case we are dealing with a large variety of possible external loads that are not parameterized but results from a statistical description of external environmental loads. Taking a subset of the possible external environmental loads and performing full scale simulations on a detailed wire rope model remains infeasible. Moreover, such problems present large sliding fronts propagating across vast frictional contact interfaces. The a posteriori methods described above do not investigate this class of problems.

However, some interesting points can be made that motivate the use of an a priori multiscale approach based on DDM. In [Fauque et al., 2018] it is made clear that being accurate on the frictional contact interface is a challenging task. They propose to overcome this problem by avoiding creating a reduced basis for the forces (the most difficult to reduce) but going to represent them at full scale in appropriate parts of the contact interface. This is a choice that in practice motivates the use of a DDM approach for model reduction of contact problems. DDM naturally allows different regions of the body to be separated, freely allowing one to choose where to be most accurate with the reduced model. Same thing can be said about [Ballani et al., 2018]. Here DDM is much more obvious. The authors choose to use a reduced model for the “global” part of the problem, and a full scale approach in the contact interface.

These ideas are completely natural in the LATIN-based DDM approach. LATIN naturally presents the concept of contact interface in a physically meaningful way. In addition, **the coarse scale problem of the multiscale approach is natural and itself acts as a coarse reduced model** that is able to effectively capture the behavior of areas “far away” from the contact interfaces. Then, the reduced-order model on the contact interfaces is created locally on the interfaces themselves, different for each subdomain, allowing for better accuracy in the contact zones.

Applied to different contexts (viscoelasticity, homogenization, delamination in composites...etc) [Ladevèze and Nouy, 2003; Nouy and Ladevèze, 2004; Ladevèze et al., 2007; Ladevèze et al., 2010; Caignot et al., 2010], the multiscale LATIN-based mixed DDM with PGD makes it possible to take into account also frictional contact interactions. In previous works, however, rather short frictional cracks had a more

or less limiting effect on the global scale, surrounded by other material nonlinearities. It has never been investigated to what extent a multiscale approach, in particular one based on domain decomposition, may be helpful in efficiently solving frictional contact problems with a model reduction approach, and what are the benefits of combining a multiscale strategy with PGD.

A first application of the strategy with PGD specifically to frictional contact problems can be found in [Giacoma et al., 2015], even though in the monoscale version. The most critical point to consider for frictional contact problems with PGD is that frictional problems present a low reducibility, thus a lot of modes are usually required. Moreover, given the high irregularity of frictional problems, a lot of useless PGD modes may be generated decreasing the efficiency of the approach. In this direction in [Giacoma et al., 2016] it is proposed a downsizing algorithm to sort the reduced basis.

As mentioned before, the coarse scale problem of LATIN itself acts as a coarse reduced model. In this spirit, the same authors in [Giacoma et al., 2014] make use of the classical LATIN method (monoscale without PGD) and use it in combination with a multigrid model that acts as a coarse reduced model or coarse scale problem, which can capture the global behavior of the structure, and later the LATIN method is used to capture more local effects. At each iteration, the LATIN method is used at the fine scale, then cheap coarse corrections are computed to enrich the fine-scale solution thanks to the ROB previously computed. It is, however, still an a posteriori approach, which does not make use of PGD, but builds the coarse ROB offline through SVD on different snapshots.

In DDM based on LATIN, however, the introduction of a coarse problem is natural and does not require the precomputation of snapshots, combined with a strong mechanical sense.

5 Domain Decomposition Methods

Domain decomposition methods (DDM) are numerical strategies for the treatment of large-scale problems which consist in partitioning a given problem into many smaller sub-problems defined on appropriate subdomains so as to treat their resolution more efficiently. DDM can be categorized in two classes: approaches with overlapping subdomains [Schwarz, 1869] and approaches without overlapping, which are the most used nowadays thanks also to their easier implementation. Among these methods, three types of approaches exist: primal methods, dual methods and mixed methods. For a detailed overview on non-overlapping primal and dual methods one can refer to [Gosselet and Rey, 2006; Magoules and Rixen, 2007].

Regarding primal and dual methods, two main classes can be distinguished: the Finite Element Tearing and Interconnecting (FETI) method [Farhat and Roux, 1991; Farhat et al., 1993; Farhat, 1994] and the Balanced Domain Decomposition method (BDD) [Le Tallec et al., 1991; Mandel, 1993; Mandel and Brezina, 1996]. The BDD method consists in choosing the displacement field at the interface between two subdomains as main unknown (primal approach) while the FETI method consists in working with the interface force field (dual approach). Originally FETI could not handle floating substructures, that is substructures without enough Dirichlet boundary conditions, while the BDD had no such a problem but manifested loss of scalability as the number of subdomain increases. In order to deal with these problems, the rigid body modes of the subdomains can be introduced in the resolution stage as a “coarse scale problem” so as to make the primal and dual methods able to handle floating subdomains and decompositions without loss of scalability. In practice, the coarse problem enables non-neighboring subdomains to interact without requiring the transmission of data through intermediate subdomains. It then enables to spread global information on the whole structure scale giving to DDM a multiscale aspect.

Mixed DDM strategies also include those based on the LATIN method [Ladevèze, 1999]. The mixed nature of the strategy enables one to deal with different interfaces characterized by complex constitutive behaviors with a single resolution method. When the LATIN-based mixed DDM is not equipped with a coarse scale problem, we refer to it as a monoscale DDM [Ladevèze, 1999; Champaney et al., 1999; Oumaziz et al., 2017]. A multiscale version of the LATIN-based mixed DDM, in which a coarse scale problem is introduced, was firstly described in [Ladevèze et al., 2001].

Here, we will briefly introduce the primal, dual and mixed approaches for domain decomposition, largely inspired by [Gosselet and Rey, 2006]. Then we will present some techniques to handle contact problems with DDM.

5.1 Primal and dual approaches

Primal and dual approaches are essentially based based on Schur’s complement [Schur, 1917; Gosselet and Rey, 2006]. The starting point consists in partitioning a

given structure Ω into substructures $\Omega_E \subset \Omega$. Each substructure interacts with the neighboring substructures through static and kinematic interface quantities.

Let us consider, in the discretized case, the linear equilibrium problem for the whole structure: $\mathbf{K}U = F$. The local equilibrium of each substructure Ω_E can be written as:

$$\mathbf{K}^E U^E = \lambda^E + F^E, \quad (1.84)$$

where λ^E is the interface force acting on Ω_E due to the neighboring substructures, defined on the boundary $\partial\Omega_E$, and F^E are external forces acting on Ω_E . Interface forces between substructures have to be equilibrated, that is:

$$\sum_E \mathbf{A}^E \mathbf{t}^E \lambda^E = 0, \quad (1.85)$$

and displacements at the interfaces have to be continuous:

$$\sum_E \mathbf{B}^E \mathbf{t}^E U^E = 0. \quad (1.86)$$

In the previous equations \mathbf{t}^E is a boolean trace operator, \mathbf{A}^E is an operator accounting for the sum of interface quantities, and the \mathbf{B}^E operator accounts for difference at the interfaces. DDM based on Schur complement consider to solve the problem by condensing the local problems (1.84) of the subdomains on the interfaces. For this purpose, if X^E is a vector defined on Ω_E , we define $X_b^E = \mathbf{t}^E X^E$ the trace of X^E on $\partial\Omega_E$ and $X_i^E = (\mathbf{I}_d - \mathbf{t}^E)X^E$ the restriction of X^E on the interior of Ω_E .

■ Finite Element Tearing and Interconnecting

As mentioned before the FETI method [Farhat and Roux, 1991; Farhat et al., 1994] prioritizes the dual quantities λ^E at the interfaces, and systematically ensures their equilibrium conditions by considering a single autoequilibrated Lagrange multiplier at the interface $\lambda_b = \mathbf{B}^{E^T} \lambda^E$. The resolution strategy of the global problem consists in injecting the local problems (1.84), condensed on the interfaces, into the interface kinematic admissibility equation (1.86). Concerning the local problems per subdomain (1.84), they involve only Neumann boundary conditions and therefore they are not invertible. What is usually done is to resort to a generalized inverse \mathbf{K}^{E+} such that:

$$\forall X \in \text{Im}(\mathbf{K}^E), \quad \mathbf{K}^E \mathbf{K}^{E+} X = X. \quad (1.87)$$

One can thus solve (1.84):

$$U^E = \mathbf{K}^{E+} (\lambda^E + F^E) + \mathbf{R}^E \alpha^E, \quad (1.88)$$

where α^E represents the rigid body modes of Ω_E and \mathbf{R}^E is the kernel of \mathbf{K}^{E+} , together with the conditions that $\lambda^E + F^E$ does not excite the kernel of \mathbf{K}^{E+} :

$$\mathbf{R}^{E^T} (\lambda^E + F^E) = 0. \quad (1.89)$$

The local equilibrium of Ω_E (1.88) is then condensed on the boundary $\partial\Omega_E$ by introducing the dual Schur complement \mathbf{S}_d^E of Ω_E :

$$U_b^E = \mathbf{S}_d^E \lambda_b^E + U_c^E + \mathbf{R}_b^E \alpha^E, \quad (1.90)$$

$$\text{with } \begin{cases} \mathbf{S}_d^E = \mathbf{t}^E \mathbf{K}^{E+} \mathbf{t}^{E^T} \\ U_c^E = \mathbf{t}^E \mathbf{K}^{E+} F^E \\ \mathbf{R}_b^E = \mathbf{t}^E \mathbf{R}^E \end{cases}$$

The previous condensed equilibrium equations return the interface displacements at the boundary which have to satisfy the kinematic admissibility (1.86) and auto-equilibrium (1.89), and leads to the following global condensed problem to be solved:

$$\begin{pmatrix} \mathbf{S}_d & \mathbf{G} \\ \mathbf{G}^T & 0 \end{pmatrix} \begin{pmatrix} \lambda_b \\ \alpha \end{pmatrix} = \begin{pmatrix} -F \\ -e \end{pmatrix}$$

$$\text{with } \begin{cases} \mathbf{S}_d = \sum_E \mathbf{B}^E \mathbf{S}_d^E \mathbf{B}^{E^T} \\ \mathbf{G} = \begin{pmatrix} \dots & \mathbf{B}^E \mathbf{R}_b^E & \dots \end{pmatrix} \\ F = \sum_E \mathbf{B}^E U_c^E \\ e = \begin{pmatrix} \dots & F_b^E \mathbf{B}^E \mathbf{R}_b^E & \dots \end{pmatrix} \end{cases} \quad (1.91)$$

This global problem would require to compute and exchange a lot of local operators per subdomain, which can be costly. Moreover the system bandwidth can be important since Dual Schur complements are generally full matrices and concern all subdomain interface degrees of freedom. Making use of a direct solver is consequently not a good idea and an iterative solver is preferable, such as a preconditioned conjugate gradient algorithm.

Knowledge of good preconditioners can speed up the convergence of the algorithm. The classical preconditioner adopted is $\tilde{\mathbf{S}}_d^{-1}$, called the Dirichlet preconditioner, that is the weighted assembly of the local primal Schur complements \mathbf{S}_p^E :

$$\tilde{\mathbf{S}}_d^{-1} = \sum_E \tilde{\mathbf{B}}^E \mathbf{S}_p^E \tilde{\mathbf{B}}^{E^T}, \quad (1.92)$$

with $\tilde{\mathbf{B}}^E$ a weighted assembly operator [Rixen and Farhat, 1999]. The admissibility condition for interface forces can be handled efficiently by a projection operation. The interface reactions are sought in the form :

$$\lambda_b = \lambda_0 + \mathbf{P} \lambda^*, \quad \text{with } \begin{cases} \mathbf{G}^T \lambda_0 = -e \\ \mathbf{G} \mathbf{P} = 0 \end{cases} \quad (1.93)$$

These conditions are satisfied by choosing the initialization λ_0 and the projector \mathbf{P} such that :

$$\begin{aligned}\lambda_0 &= -\mathbf{G}(\mathbf{G}^T\mathbf{G})^{-1}\mathbf{e}, \\ \mathbf{P} &= \mathbf{I} - \mathbf{G}(\mathbf{G}^T\mathbf{G})^{-1}\mathbf{G}^T.\end{aligned}\tag{1.94}$$

The initialization λ_0 is the assembly of a combination of the resultants and moments of the interface reactions of each substructure in equilibrium with the resultants and moments of the imposed external loads, which represents the coarse scale problem for FETI. The part of the solution λ^* calculated during the iterations of the conjugate gradient is sought in the complementary space of λ_0 . Therefore one can identify two scales: a coarse scale part with a long length of variation of the interface quantities, and the complementary part with a shorter length of variation which is sought iteratively during iterations of the conjugate gradient. The projection operation thus ensures the scalability of the method.

Other versions of the FETI method include:

- FETI-2: the FETI-2 method [Farhat et al., 1998, 1998; Mandel et al., 1999] incorporates additional constraints into the coarse problem in order to handle thin and shell structures, as well as dynamic applications [Farhat et al., 1995], more efficiently.
- FETI-DP: a dual-primal version of the FETI method [Farhat et al., 2000b; Farhat et al., 2001; Mandel and Tezaur, 2001; Klawonn and Rheinbach, 2006]. Dirichlet conditions at the “corner” nodes are also taken into account at each iteration of the conjugate gradient, thus eliminating the need to determining the solution belonging to the kernel of the Schur complement. The system becomes invertible and the calculation of the generalized inverse is avoided.
- Hybrid FETI-DP: when a large number of subdomains is present, the coarse scale problem can become costly. In Hybrid FETI-DP methods [Klawonn and Rheinbach, 2010; Řiha et al., 2016; Řiha et al., 2017] a three-level approach is used, with the subdomains grouped into clusters which are used to solve the coarse problem.
- T-FETI: Total FETI methods treat the Dirichlet boundary conditions using Lagrange multipliers [Dostál et al., 2006; Kozubek et al., 2013].

■ Balancing Domain Decomposition method

The BDD primal method [Mandel, 1993; Le Tallec, 1994] is similar to the dual method and its efficiency is comparable to that of FETI. BDD consist in enforcing the displacement continuity at the interfaces and by writing a single interface displacement vector $U_b = \mathbf{A}^{E^T} U_b^E$. By renumbering the nodes with interior and boundary quantities, the local equilibrium of a subdomain (1.84) can be rewritten as:

$$\begin{pmatrix} \mathbf{K}_{ii}^E & \mathbf{K}_{ib}^E \\ \mathbf{K}_{bi}^E & \mathbf{K}_{bb}^E \end{pmatrix} \begin{pmatrix} U_i^E \\ U_b^E \end{pmatrix} = \begin{pmatrix} F_i^E \\ F_b^E + \lambda^E \end{pmatrix}\tag{1.95}$$

This problem can then be condensed on the boundary thanks to the primal Schur complement \mathbf{S}_p^E of the substructure Ω_E , such that:

$$\mathbf{S}_p^E U_b^E = \lambda^E + F_c^E, \quad (1.96)$$

$$\text{with } \begin{cases} \mathbf{S}_p^E = \mathbf{K}_{bb}^E - \mathbf{K}_{bi}^E \mathbf{K}_{ii}^{E-1} \mathbf{K}_{ib}^E \\ F_c^E = F_b^E - \mathbf{K}_{bi}^E \mathbf{K}_{ii}^{E-1} F_i^E \end{cases}$$

The global equilibrium problem to be solved therefore becomes:

$$\mathbf{S}_p U_b = F_c, \quad (1.97)$$

$$\text{with } \begin{cases} \mathbf{S}_p = \sum_E \mathbf{A}^E \mathbf{S}_p^E \mathbf{A}^{E^T} \\ F_c = \sum_E \mathbf{A}^E F_c^E \end{cases}$$

As with the FETI method, the use of a conjugate gradient to solve the interface problem requires the use of a good preconditioner and a projector, in order to rapidly transmit the information with a long variation length during iterations. The introduction of the projector in the primal domain decomposition method is associated with the iterative solution of the interface problem using the Neumann preconditioner:

$$\tilde{\mathbf{S}}_p^{-1} = \sum_E \tilde{\mathbf{A}}^E \mathbf{S}_d^E \tilde{\mathbf{A}}^{E^T}, \quad (1.98)$$

with $\tilde{\mathbf{A}}^E$ a weighted assembly operator. Evaluating $\tilde{\mathbf{S}}_p^{-1}$ consists in solving Neumann problems on each substructure. It is then necessary to ensure that the residual $r_p = F_c - \mathbf{S}_p U_b$ is self-balancing, that is:

$$\mathbf{G}_p^T r_p = 0, \quad \text{with } \mathbf{G}_p = \left(\dots \tilde{\mathbf{A}}^E \mathbf{R}_b^E \dots \right). \quad (1.99)$$

This constraint is classically dealt with by looking for the solution in the form:

$$U_b = U_0 + \mathbf{P} U_b^*, \quad (1.100)$$

with

$$\begin{aligned} U_0 &= \mathbf{G}_p (\mathbf{G}_p^T \mathbf{S}_p \mathbf{G}_p)^{-1} \mathbf{G}_p^T F_c, \\ \mathbf{P} &= \mathbf{I} - \mathbf{G}_p (\mathbf{G}_p^T \mathbf{S}_p \mathbf{G}_p)^{-1} \mathbf{G}_p^T \mathbf{S}_p. \end{aligned} \quad (1.101)$$

It is possible also to include additional kinematic conditions relating to the interface nodes for the preconditioner: for example, imposing continuity of displacements for the corner nodes. This leads to the BDDC method, primal version of the FETI-DP [Mandel and Sousedik, 2007; Mandel et al., 2012].

5.2 Mixed domain decomposition methods

Mixed domain decomposition methods involve searching for a combination of displacements and interface forces [Farhat et al., 2000a]. The kinematic and static admissibility equations are coupled by introducing a new interface variable $\mu_b^E = \lambda^E + \mathbf{k}^E U_b^E$. The condensed local problem of each substructure becomes:

$$\left(\mathbf{S}_p + \mathbf{k}^E \right) U_b = \mu_b^E + F_c^E. \quad (1.102)$$

In practice, the introduction of \mathbf{k}^E parameters regularize the local problems for floating or partially floating substructures, however they also have a strong influence on the convergence of the method. As it is posed, the interface problem can be solved iteratively without preconditioning. Finally, as the local problems are well posed, the coarse problem required for fast transmission of long-wavelength effects during the iterations of the iterative solver must be artificially introduced.

■ LATIN-based mixed DDM

The mixed domain decomposition method based on the LATIN method [Ladevèze, 1999] decomposes the structure into substructures separated by interfaces, with substructures and interfaces having their own variables and equations. One of the originalities of this approach is that the interfaces are endowed with a stronger physical sense and it is possible to attribute them their own complex constitutive behavior in terms of both primal and dual variables, thus the mixed nature of the approach.

Unlike the mixed approach described previously, the mixed interface variables arise naturally when the interface problem is solved using the LATIN solution algorithm. In the LATIN the condensed system is iteratively solved by an alternating direction method of multipliers (ADMM), which is similar to Uzawa-like algorithms. This alternating direction iterative scheme is naturally introduced in the LATIN method. The LATIN process is described here in a simplified way. In the next chapters the strategy will be presented rigorously in detail.

We assume that the behavior of the substructures is linear elastic, with nonlinearities concentrated at the interfaces, and that the discretizations of the substructure and interface fields are compatible. An iteration of the LATIN algorithm applied to the solution of the substructured problem consists of two steps:

- *A global stage.* A stage consisting on solving independent problems per substructure in parallel. To this end, an artificial interface stiffness operator \mathbf{k}^E is introduced, linking the primal and dual fields of the interfaces of the substructure Ω_E to those from the previous iteration:

$$\lambda_{b_n}^E + \mathbf{k}^E U_{b_n}^E = \lambda_{b_{n-1/2}}^E + \mathbf{k}^E U_{b_{n-1/2}}^E. \quad (1.103)$$

The condensed local equilibrium problem of each substructure can then be solved locally by injecting the previous equation in such a way as to eliminate interface force unknowns:

$$\left(\mathbf{s}_p + \mathbf{k}^E \right) U_{b_n}^E = F_c^E + \lambda_{b_{n-1/2}}^E + \mathbf{k}^E U_{b_{n-1/2}}^E. \quad (1.104)$$

- *A local stage.* A stage on the interface fields where the local behavior, possibly nonlinear, is solved locally on each interface:

$$\mathbf{b}_{EE'}(U_{b_{n-1/2}}^E, U_{b_{n-1/2}}^{E'}, \lambda_{b_{n-1/2}}^E, \lambda_{b_{n-1/2}}^{E'}) = 0, \quad (1.105)$$

where $\mathbf{b}_{EE'}$ represents the constitutive behavior of the interface between subdomains Ω_E and $\Omega_{E'}$.

The coarse scale problem in the LATIN is obtained by imposing the continuity of an average of interface fields between adjacent substructures, and by calculating and assembling an homogenized behavior operator of the substructures in the sense of these quantities. The averages of the interface fields, called macroscopic quantities, are the long-variation parts of the solution. The complementary microscopic quantities are instead related to local variations.

The strategy is very versatile and adapted to many different fields. Structures with high material heterogeneity [Ladevèze et al., 2001; Loiseau, 2001], for fatigue cracking calculations with integration of XFEM [Guidault et al., 2007; Guidault et al., 2008], damage in laminated composites [Violeau, 2007], debonding in laminates [Kerfriden, 2008; Kerfriden et al., 2009; Saavedra et al., 2012], and more recently for magnetostatic simulations [Ruda, 2023; Ruda et al., 2024]. Space-time approximations of the solution can be used to efficiently solve problems posed over a large time interval and requiring fine temporal discretizations [Ladevèze and Nouy, 2002; Nouy, 2003; Nouy and Ladevèze, 2004; Passieux, 2008; Passieux et al., 2010]. A third scale (super macroscale) can be introduced to solve efficiently the coarse scale problem when the number of subdomains becomes large [Loiseau, 2001; Ladevèze and Nouy, 2002; Nouy, 2003; Kerfriden, 2008; Kerfriden et al., 2009].

5.3 Domain decomposition for contact problems

Domain decomposition strategies can also be applied to efficiently solve large contact problems. In the case of contact problems, the concept of interface is naturally present which leads to decomposing the structure so that the decomposition interfaces coincide with the contact interfaces. In the case of contact interfaces, however, the continuity of displacements is not verified, which makes primal methods unsuitable for this purpose. For this reason, dual FETI and mixed LATIN-based approaches are generally better suited for this type of problems. For an overview on the topic one may refer to [Dostál et al., 2016].

A solution to frictionless contact problems based on the FETI method, named FETI-C, was introduced in [Dureisseix and Farhat, 2001] with scalability properties based on an active set strategy wherein a coarse contact system was integrated to guide the iterative prediction of the active contact zone.

In [Avery et al., 2004; Avery and Farhat, 2009] a FETI-DP method is introduced for solving iteratively frictionless contact problems, named FETI-DPC, featuring a nonlinear Krylov-type acceleration scheme. Numerical scalability is achieved with respect to both the problem size and the number of subdomains.

Several works from Dostál and coworkers [Dostál and Schöberl, 2002; Dostál and Horák, 2003, 2004, 2004; Dostál et al., 2009; Dostál et al., 2010; Dostál et al., 2012] combine the FETI method with results from bounded constrained quadratic programming developing optimal algorithms for solving constrained variational inequalities.

In a recent work, [Yin et al., 2024] propose to integrate the FETI method into the B-differentiable equations (BDEs) method [Pang, 1990] for the analysis of 3D elastic frictional contact problem with small deformations. The governing equations consisting of the contact equations, interface continuity equations and equilibrium equations for each subdomain are formulated with the BDEs.

However, it is not necessary that the contact interfaces coincide with the subdomain interfaces, they can also be located within the subdomains. In this way, for example, it is possible also to make use of a primal approach as in [Barbotteu et al., 2001], where the authors partition a structure with multiple contact interfaces by treating the physical contact interfaces inside the subdomains. The strategy is solved with a Newton-Schur algorithm, that is at each linearization of a generalized Newton algorithm, the linearized problem is solved with a primal Schur complement method.

Domain decomposition has also been applied successfully to non-smooth contact dynamics [Moreau, 1999], see for example [Visseque et al., 2013] for a FETI-based approach and [Alart et al., 2012] for combining the advantages of nonlinear Gauss-Seidel solvers and the LATIN.

Mixed DDM, such as the one based on the LATIN, allows to tackle frictional contact problems in an easy and straightforward manner without any ad-hoc modification to the LATIN algorithm. The conditions of contact with friction are verified in the local stage in an exact manner through simple contact indicator functions [Champaney, 1996]. The monoscale approach was first introduced to efficiently handle large assemblies with friction and joints [Champaney, 1996; Champaney et al., 1997; Champaney et al., 1999]. The introduction of multiscale aspects ensures scalability of the method [Ladevèze et al., 2002]. Recently a non-intrusive version of the LATIN-based DDM for contact problems has been proposed in the monoscale case [Oumaziz et al., 2017] and in the multiscale one [Oumaziz et al., 2018].

Chapter 2

Preliminary reducibility investigation and scale separability on a cable section in tension and bending

In this Chapter, we analyze the possibility of reducing the solution of a tension and bending calculation on a metric cable section with the developed model described in [Bussolati, 2019] (see also [Bussolati et al., 2019; Guidault et al., 2019; Bussolati et al., 2020; Guidault et al., 2021]), for a given sea state. For this local calculation the imposed tension and curvature histories are obtained from a global calculation on a floating wind structure carried out in a previous work at LMPS in collaboration with IFP Energies nouvelles. We first go on to investigate how the quantities of interest behave over time, i.e., inter-wire slip and normal and tangential contact forces between the different layers of the cable, as well as how the contact status evolves over time through the different layers. Then, an a posteriori SVD analysis of the local calculation solution at different time steps will enable to assess its ability to be reduced. Moreover, the possibility of separating space and time scales, which can be exploited during the model reduction approach, is investigated.

Contents

1	Analysis of a six layer wire rope in tension and bending	77
1.1	Global hydrodynamic FOWT model	77
1.2	Detailed local cable model	78
1.3	Contact quantities analysis	80

- 2 Singular Value Decomposition on the main results 84**
- 2.1 Layer-by-layer interface reducibility investigation 86
- 2.2 Layer-by-layer space and time modes 88
- 3 Conclusions 94**

1 Analysis of a six layer wire rope in tension and bending

In this section, we first go on to describe the global hydrodynamic model used in [Bussolati, 2019]. A global hydrodynamic simulation for a given wave elevation time history has allowed to assess which areas of the mooring lines are the most critical in terms of traction and curvature. Here, having access to the text files of the local model results from Abaqus/Standard, we analyze how the different contact quantities and the contact status evolve over time on the different layers of the wire rope.

1.1 Global hydrodynamic FOWT model

In [Bussolati, 2019], a global model of a FOWT (Figure 2.1) has been adopted to obtain the mechanical state of a whole mooring line for a particular sea state to which the FOWT may be subjected to during its lifespan. In particular, an extreme sea state with a significant wave height $H_s = 8.75$ m and peak period $T_p = 16.5$ s (see Section 1.1.1 in Chapter 1 for their definition), represented in Figure 2.2, has been adopted and the resulting global model has been implemented in the dedicated hydrodynamic software DeepLinesTM. For a more in-depth analysis one can refer to Chapter 5 in [Bussolati, 2019].

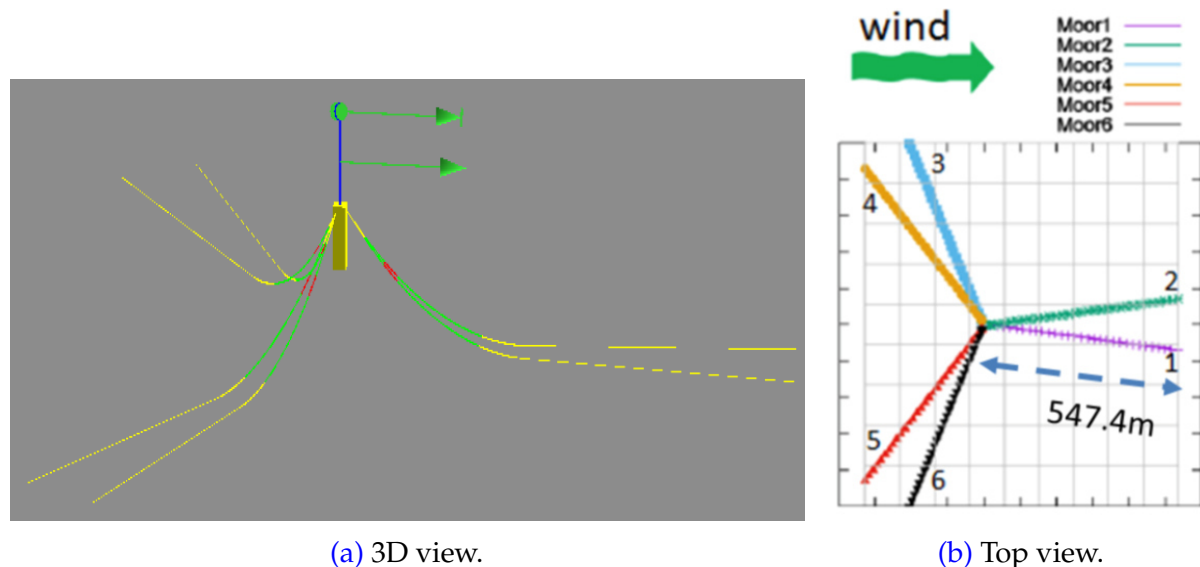


Figure 2.1: Global scale model representation in DeepLinesTM of the considered FOWT [Bussolati, 2019]. (a): Side view of the global model. (b): Top view of the global model representing the mooring lines numbering and their position with respect to the wind direction.

A generic case study of a cylinder-like shape floater, equipped with a redundant mooring system of six catenary mooring lines and supporting a downsized version

of the NREL 5 MW wind turbine [Jonkman et al., 2009] to a 3.6 MW wind turbine has been considered. The considered sea depth is uniform and equal to 100 m. The mooring lines are catenary-shaped and attached to the floater in three pairs. The pair of lines are equally spaced from each other and each line has a total length of 572 m. Each mooring line is composed of three parts, with chains at the extremities and spiral strand ropes in between (in yellow and green respectively in Figure 2.1a). Wire ropes are modeled by beam elements, whose formulation takes into account large rotations and displacements [Fargues, 1995], as well as torsional stiffness and shear deformability. However, axial, bending and torsional behavior are fully uncoupled, which is not realistic for wire ropes. Chains have no bending stiffness and have been modeled by bar elements. An additional mass of 2 tons is distributed on a part of each mooring line in order to limit the floater movements and to keep the lines in tension [Lopez-Olocco et al., 2022] (in red in Figure 2.1a). The modeling of contact between mooring line and seabed is based on a penalty method and no friction is assumed [Fontaine et al., 2002].

From the results of the hydrodynamic computation of the global model in Figure 2.1 subjected to the sea state in Figure 2.2, the position at 79 m from the top along the mooring line 1 (see Figure 2.1b) was identified as the most critical in terms of bending stresses. Tension and curvature histories from this position have then been used for a local wire model computation. For this purpose, a top-down approach was followed, which means that the results from the global model are not appreciably dependent on what happens locally on the wire rope. It was shown in fact in [Bussolati, 2019] that a nonlinear bending behavior in order to account for frictional phenomena (as the one in Figure 1.14), representative of the wire rope for a given tension, does not present great influence on the tension and curvature time series at a given critical location. This is mainly due to the fact that wire ropes are very slender structures with relatively low bending stiffness, which does not affect the overall behavior of the mooring system considerably.

1.2 Detailed local cable model

Once the position at $s = 79$ m along the mooring line 1 has been identified as the most critical, axial strain ε_c and curvature κ_c histories in that position coming from the global computation (represented in Figure 2.3) have been used as input loadings for a detailed local model of a portion of the wire rope. One should notice that axial strain and curvature time histories are in anti-phase and characterized by non-zero initial values due to a preload of initial tensioning ε_0 and an initial curvature κ_0 . Moreover, as opposed to the wave elevation history represented in Figure 2.2, which takes place in a time interval of 1000 s, the first 50 s of the axial strain and curvature histories are filtered since they are used to set up the initial loadings.

The considered steel wire rope profile of the local model consists in six layers helically wound around a central core wire. **The layers have alternate lay angle directions and are composed of 5, 11, 17, 23, 29 and 35 wires respectively from the**

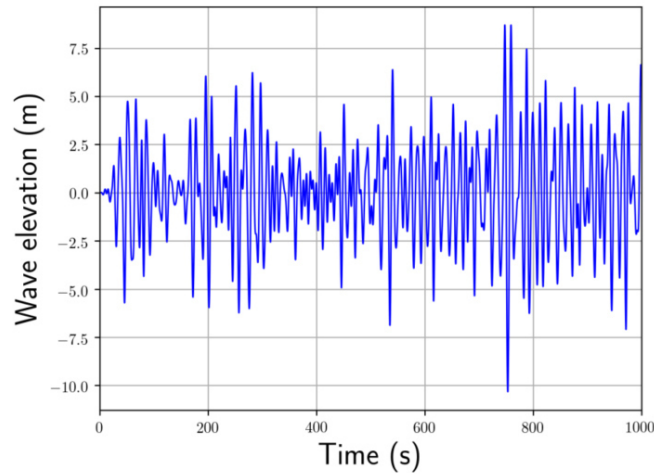
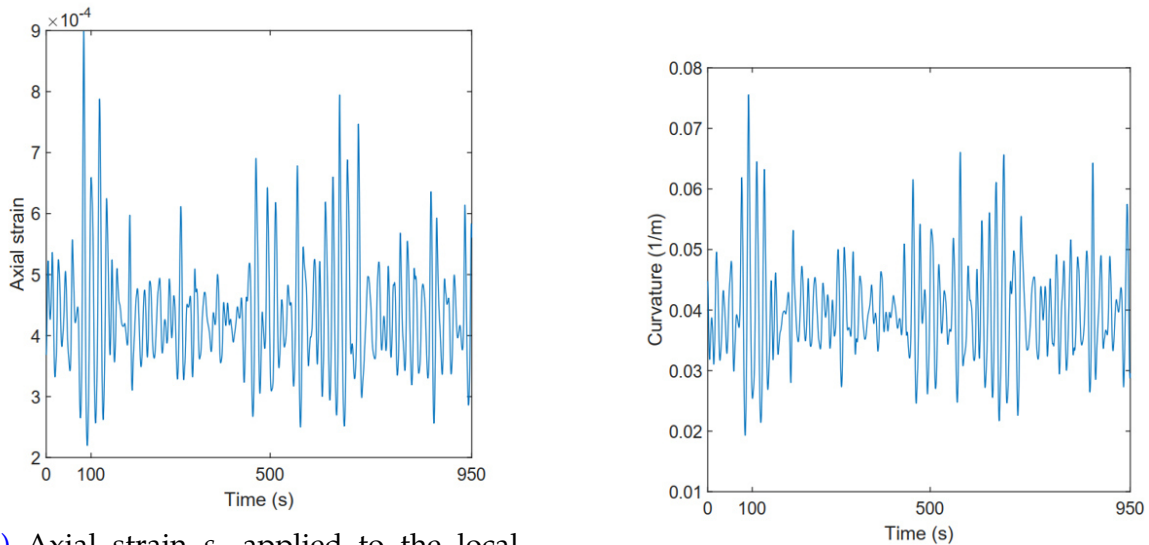


Figure 2.2: Wave elevation used for the global computation in [Bussolati, 2019].



(a) Axial strain ε_c applied to the local model.

(b) Curvature κ_c applied to the local model.

Figure 2.3: Loadings used in [Bussolati, 2019] in the local model coming from the global computation. (a): Axial strain ε_c . (b): Curvature κ_c .

inner layer (layer 1) to the outer layer (layer 6), as in Figure 2.4.

In [Bussolati, 2019], each wire has been modeled with beam elements, and a novel USER element corresponding to beam-to-beam penalty contact formulation, assuming small sliding but large rotations between the wires, has been proposed and adopted for the contact interactions between the wires [Bussolati et al., 2020]. The diameter of the wire rope is 60.4 mm and the model length is set to the longest pitch which is that of the external layer, i.e., about 580 mm. For the steel, it was assumed a linear elastic behavior, with Young modulus $E = 210$ GPa and Poisson ratio $\nu = 0.3$. The friction

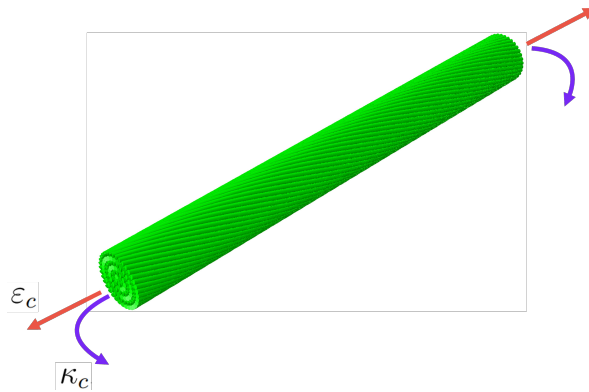


Figure 2.4: Finite element model of the six-layer wire rope used in [Bussolati, 2019].

coefficient has been set to 0.12, which is the typical value for steel wire ropes after the application of grease acting as a lubricant [Raouf and Hobbs, 1988]. Boundary conditions simulating the continuity of the wire rope at the end cross-sections were applied (see [Bussolati et al., 2019] for more details about these particular boundary conditions).

For fretting fatigue the sliding magnitude has a huge effect on the fatigue life expectancy of these structures, with an important decrease between $15 \mu\text{m}$ and $150 \mu\text{m}$ [Montalvo et al., 2023]. It is therefore important for the reduced model to accurately represent interface contact quantities.

1.3 Contact quantities analysis

A detailed description of the results coming from the local model is available in [Bussolati, 2019; Bussolati et al., 2020]. Here, we limit ourselves to a brief description of the most interesting results for our study. The following results for the contact quantities are represented by mapping each layer on a rectangular grid along the axial longitudinal position z on the rope (here between -50 mm and 50 mm with respect to the centre of the model) and the angular position θ on the cross-section with respect to the bending axis (as shown in Figure 2.5).

Remark 2.1. *The results shown from here onwards were obtained by analyzing the Abaqus output files made available by [Bussolati, 2019]. The results we show here are not present in [Bussolati, 2019], but they are the result of an independent study.*

An important role in the wire rope's analysis is played by the contact status between the different layers, which provides meaningful information on the rope solicitation levels. Figure 2.6 represents the contact status snapshot for the different layers interfaces when the minimum curvature occurs. All the contact interfaces remain in sticking conditions, except for the last one between layers 5 and 6 where a large sliding zone is

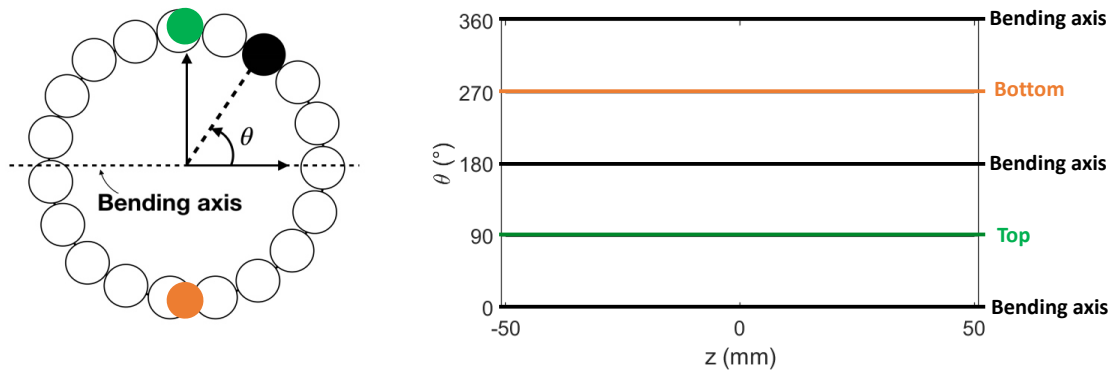


Figure 2.5: Projection of a cable layer into a 2D rectangular grid.

present. **Sticking zones are localized in the top and bottom sectors at 90° and 270° respectively, while sliding propagates from the bending axis, that is 0° , 180° and 360°** (see [Section 2.2](#) in [Chapter 1](#) and [[Papailiou, 1995](#)]). One should notice that the contact point distributions is increasing from the inner to the outer interfaces. This is both due to an increase of wire numbers per layer but also to an increase of the helix pitch in the outermost layers.

In [Figure 2.7](#) is shown the contact status snapshot when the maximum curvature occurs. Almost total sliding conditions occur in layer interfaces 4-5 and 5-6. A large sliding zone is also present at interface 3-4 as well as a small amount that occurs more internally, at interface 2-3. As seen before, sticking zones are localized in the top and bottom angular sectors, while sliding propagates from the bending axis. In general, **one can say that the most critical layers from the point of view of variable contact conditions are the outermost layers**. Indeed, in the outermost layers, the normal contact forces are lower, as also the bending effects due to curvature are more pronounced.

The contact quantities due to the preloads ε_0 and κ_0 (normal contact forces, norm of the tangential contact forces and norm of the inter-wire slip) for interface 3-4 and interface 4-5 are shown respectively in [Figure 2.8](#) and [Figure 2.9](#). Although the data are defined only at the pointwise contact points between the wires belonging to different layers, the discrete data has been interpolated in space variable on the same grid as the contact status shown before to facilitate the visualization and interpretation of the results.

With regard to normal contact forces, one can notice that for each layer interface the results have no significant difference by changing the angular position with respect to the bending axis. Normal forces display some periodicity along the angular position, with no particular dependence on the bending axis position. Normal contact forces also are higher when moving from the external to the internal layers (see [Section 2.2](#) in [Chapter 1](#) and [[Papailiou, 1995](#)]), since the external layers exert a pressure on the internal ones. Tangential contact forces, instead, show a larger dependency with respect

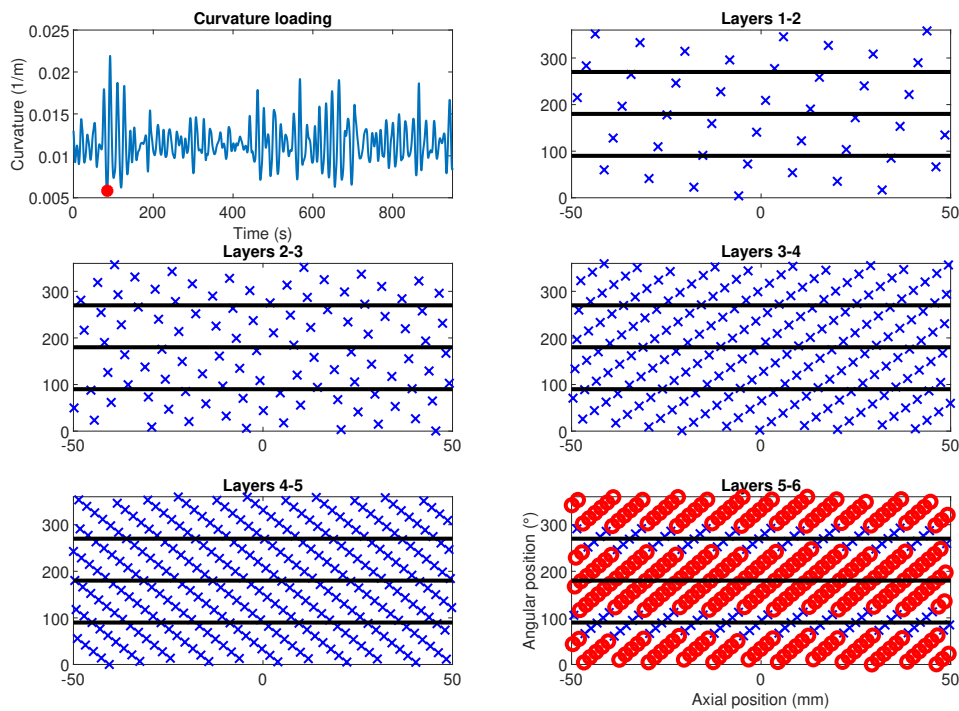


Figure 2.6: Contact status on the different layer interfaces at the minimum curvature. The blue cross stands for sticking conditions, the red circle for sliding conditions.

to the angular position due to the different sliding-sticking conditions that occur in the different angular positions of the section. At higher normal forces correspond higher tangential forces as well. Regarding the inter-wire slip, as expected from the previous contact status analysis, the locations where the largest amount of sliding occurs belong to the bending axis, while the top and bottom sectors (90° and 270°) are the ones with the highest grip.

1. Analysis of a six layer wire rope in tension and bending

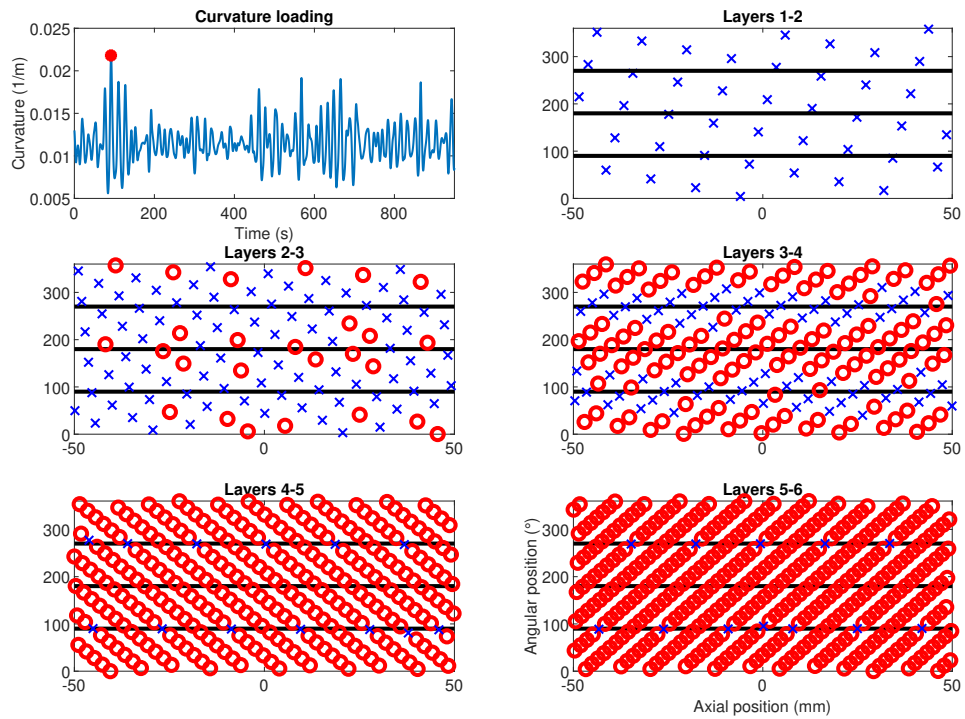


Figure 2.7: Contact status on the different layer interfaces at the maximum curvature. The blue cross stands for sticking, the red circle for sliding conditions.

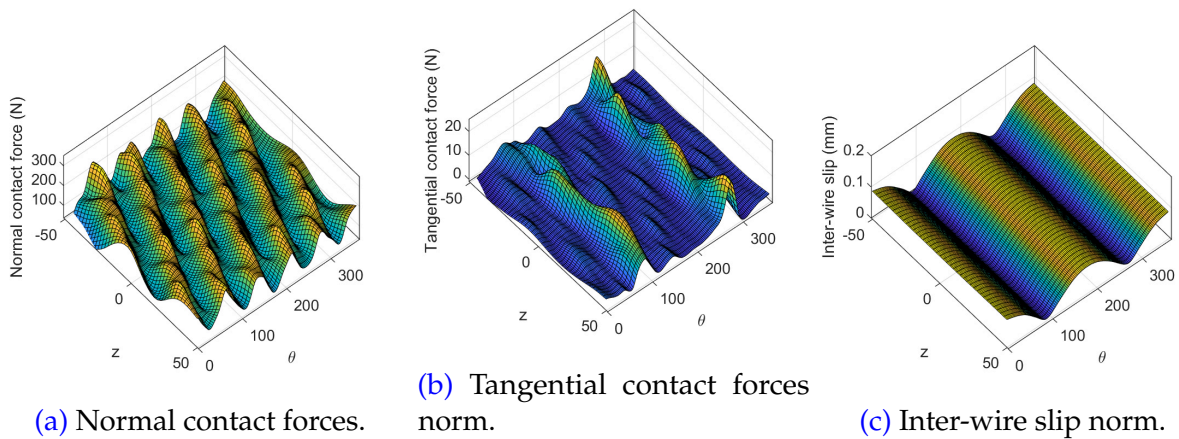


Figure 2.8: Preload contact quantities for layer interface 3-4. (a): Normal contact forces. (b): Tangential contact forces norm. (c): Inter-wire slip norm.

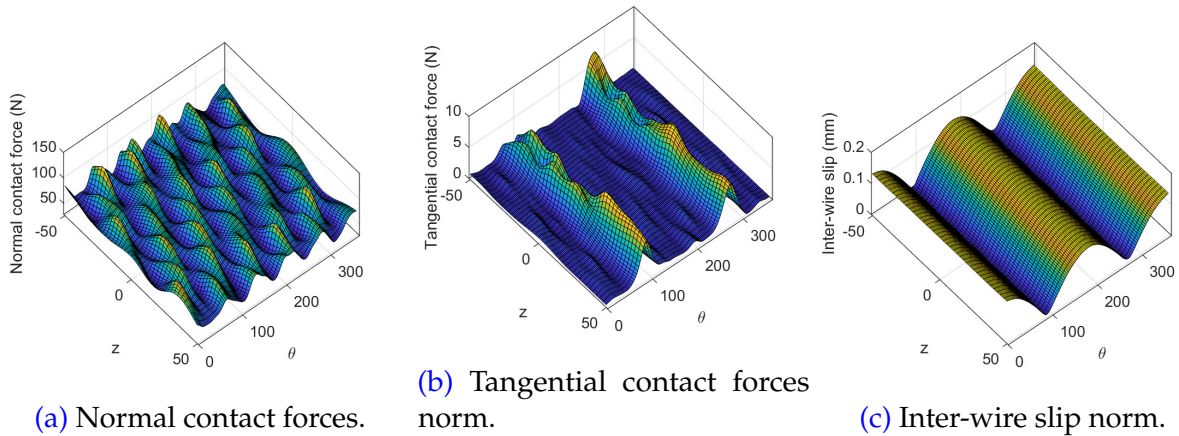


Figure 2.9: Preload contact quantities for layer interface 4-5. (a): Normal contact forces. (b): Tangential contact forces norm. (c): Inter-wire slip norm.

Figure 2.10 shows the evolution in time of the contact quantities for layer interfaces 4-5 evaluated at the center of the wire axis ($z = 0$) and at different angular positions, namely the bending axis, the top angular sector and the bottom one (see Figure 2.5). It results that the most critical quantities belong to the bending axis angular position. This applies especially to tangential contact forces and inter-wire slip. One can notice that tangential contact forces and inter-wire slip at the bending axis exhibit a pronounced change in behavior around time $t \approx 100$ s, when the peak curvature occurs. In particular, the inter-wire slip reaches a stabilized state after a sudden shift in the sliding. This shift in the sliding occurs for all the layer interfaces, except for the most internal one which in fact is always in sticking conditions (Figure 2.6 and Figure 2.7), and presents an increasing magnitude moving from the internal to the external layers.

2 Singular Value Decomposition on the main results

In this section, SVD is performed to study the reducibility of the contact quantities involved in the study of wire ropes: normal and tangential contact forces and the inter-wire slip between wires of adjacent layers (see Section 4.3.1 in Chapter 1 for the definition of SVD). The relative approximation error committed in approximating the desired quantities with M modes is defined as:

$$err = \frac{\|\mathbb{A} - \mathbb{A}_M\|_F}{\|\mathbb{A}\|_F}, \quad (2.1)$$

where $\|\bullet\|_F$ stands for the Frobenius norm. The snapshot matrix $\mathbb{A}^{N_x \times N_t}$ collects the quantities of interest along the N_x spatial positions (depending on the layers) and N_t load steps (or time steps) of the analysis ($N_t = 1401$ load steps considered in [Bussolati, 2019]). Finally $\mathbb{A}_M^{N_x \times N_t}$ represents the SVD approximation of \mathbb{A} with M modes.

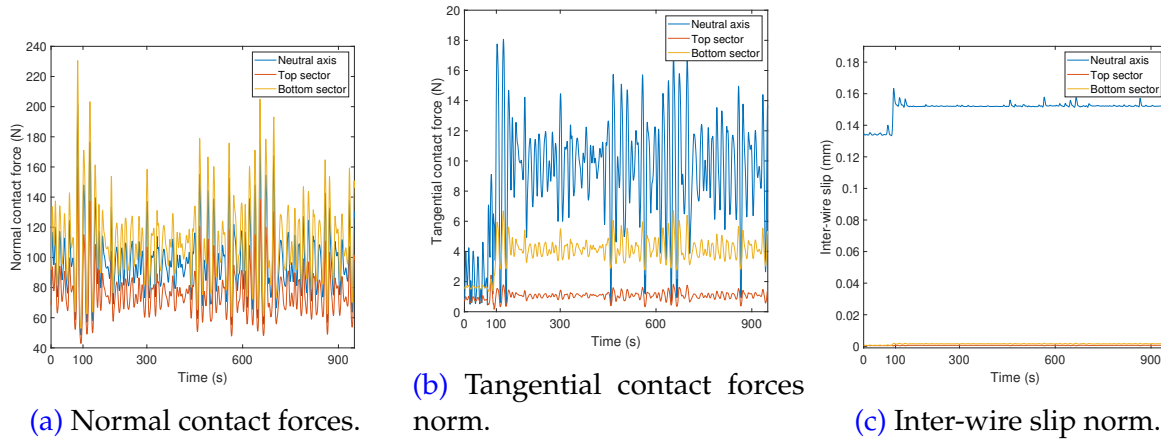


Figure 2.10: Time evolution of contact quantities for layer interface 4-5 (in $z = 0$) at specific angular positions. (a): Normal contact forces. (b): Tangential contact forces norm. (c): Inter-wire slip norm.

In [Table 5.2](#) is shown the number of rows N_x of the snapshot matrix \mathbb{A} for the different layers of the wire rope model and the different quantities that were analyzed. One should notice that the outer layers, having a higher number of wires as also a longer helix pitch, present an overall higher number of rows N_x of spatial quantities in their corresponding snapshot matrix, as it can be seen in [Figure 2.6](#) and [Figure 2.7](#) for inter-layer contact quantities.

Contact quantities	
Layer interface 1-2	$N_x = 42$
Layer interface 2-3	$N_x = 112$
Layer interface 3-4	$N_x = 195$
Layer interface 4-5	$N_x = 286$
Layer interface 5-6	$N_x = 375$

Table 2.1: Number of spatial positions where contact quantities are evaluated on the different layers interfaces.

Tangential contact forces and inter-wire slip between two contacting wires are defined on the two directions \underline{t}_1 and \underline{t}_2 tangent to the respective wires of adjacent layers in point contact, as shown in [Figure 2.11](#). Since these directions are not orthogonal to each other, in order to have a better understanding of the reducibility of the involved quantities, the reducibility of the norm of the above quantities, which does not depend on the directions considered, was also analyzed.

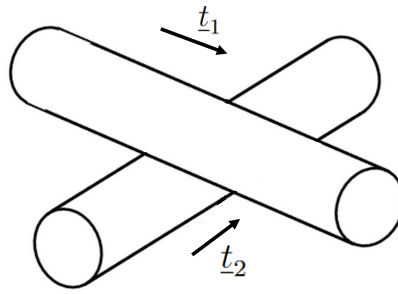


Figure 2.11: Tangential beam directors t_1 and t_2 for two wires in point contact.

2.1 Layer-by-layer interface reducibility investigation

Figure 2.12 shows the approximation error of the normal contact forces for the different layer interfaces. With 10 modes, accuracy levels between 10^{-3} and 10^{-4} can be reached for every interface. The error evolution does not show an appreciable difference by moving from one interface to another. In fact, even though the mean value of the normal contact forces increases moving from the outer layers to the inner ones, their variation around this mean value is proportional to the external traction and curvature and results to be independent from the sticking-sliding conditions that may occur at a given layer interface.

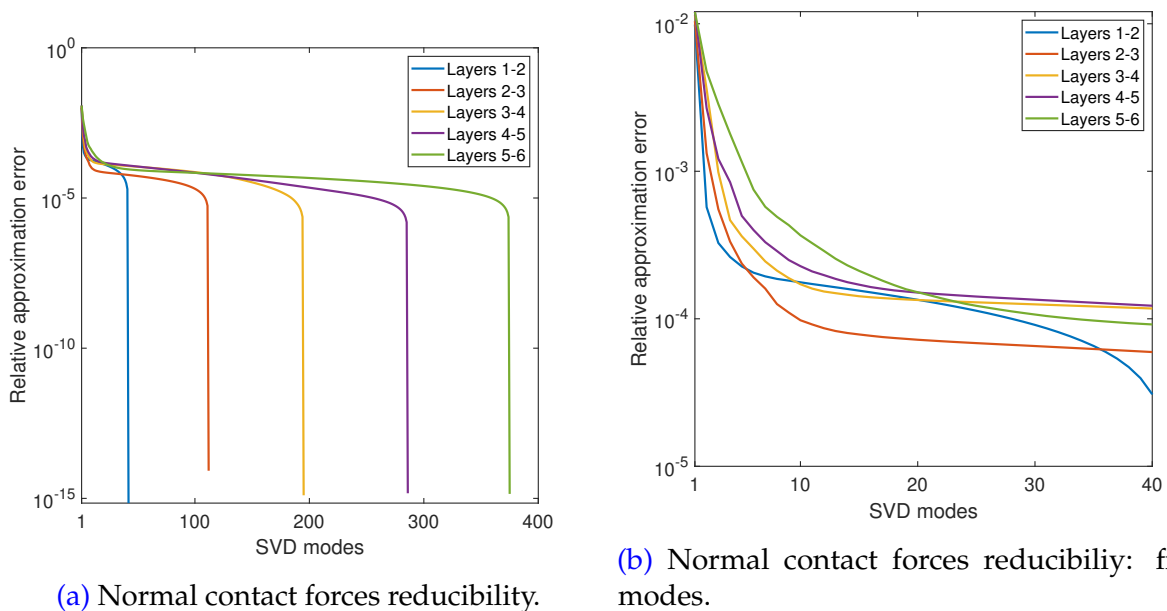
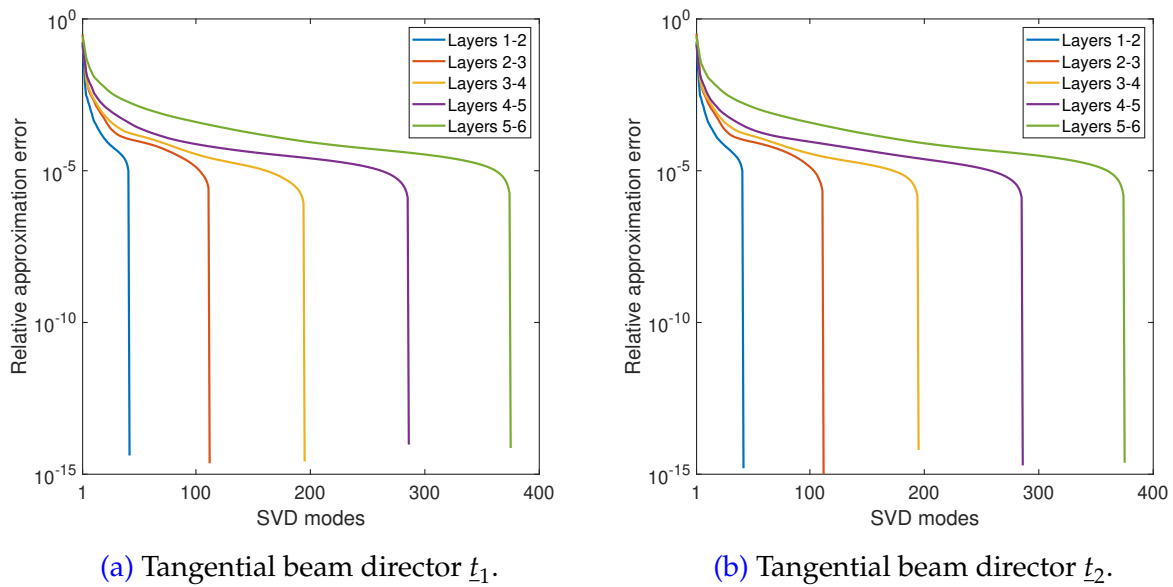


Figure 2.12: Relative approximation error for the normal contact forces between the wires of adjacent layers. (a): Global reducibility. (b): Detail on the first modes.

Figure 2.13 shows the approximation error for the tangential contact forces between

the different layer interfaces along the two tangential beam directors. For the tangential contact forces, a wider dependency of the reducibility with respect to the layer interfaces is observed, if compared to normal contact forces. Inner layers, where a higher value of the normal contact forces occurs, as well as a lower slip, present better reducibility compared to the outer ones, where different and more variable sticking and sliding conditions occur over time, making it more challenging to capture the tangential contact interactions. Nevertheless, no appreciable difference can be observed for the reducibility of the tangential contact forces in the two considered beam directors. Compared to normal contact forces, **tangential forces present a more challenging reducibility due to their highly non-smooth nature depending on the sticking-sliding conditions that occur in time and space**. The error on the tangential forces norm is represented in [Figure 2.14](#), and the trend remains indistinguishable from those in the respective tangential beam directors ([Figure 2.13](#)).



[Figure 2.13](#): Relative approximation error for the tangential contact forces between the wires of adjacent layers. (a): Tangential beam director \underline{t}_1 . (b): Tangential beam director \underline{t}_2 .

As for tangential contact forces, in [Figure 2.15](#) is represented the approximation error for the inter-wire slip between the different layers along the two tangential beam directors. Similarly to tangential contact forces, inner layers present a better reducibility than the outer ones. This is because of the reasons explained previously: in the external layer interfaces the contact status conditions are more variable (see [Figure 2.6](#) and [Figure 2.7](#)), and the amount of sliding is higher compared to the internal ones. In particular, the two outermost layer interfaces display an odd behavior compared to the other layers. The innermost layers have the error plateauing around the value of 10^{-5} after about 50 modes. The last two contact interfaces between layers 4-5 and 5-6, on

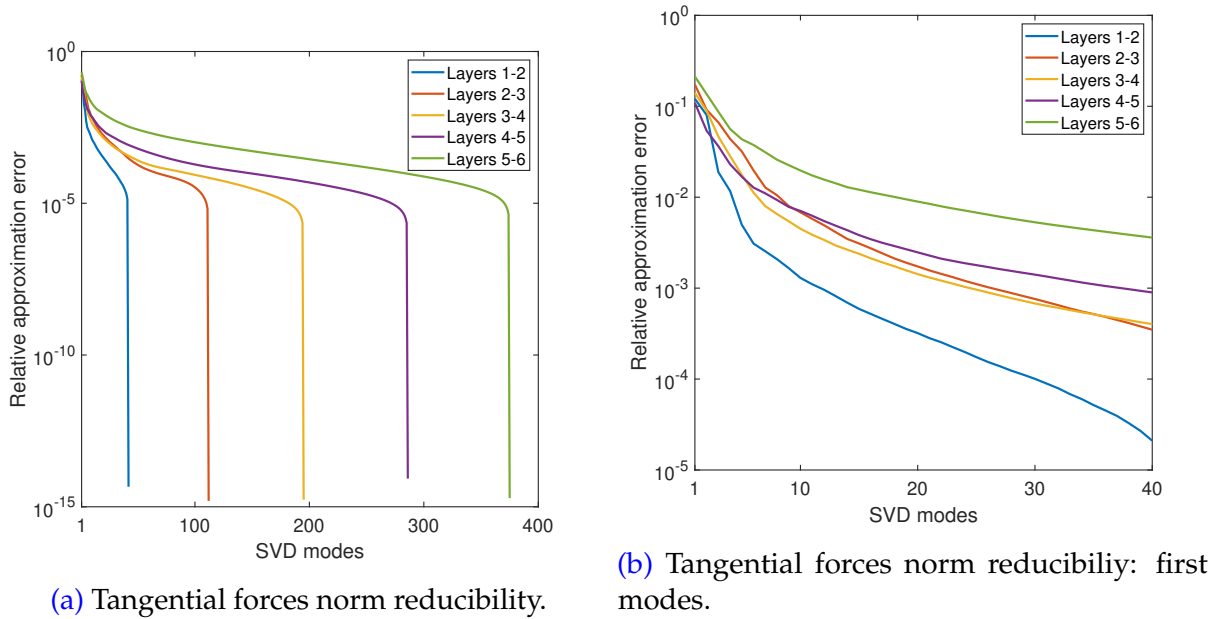


Figure 2.14: Relative approximation error for the norm of the tangential contact forces between the wires of adjacent layers. (a): Global reducibility. (b): Detail on the first modes.

the other hand, present a first long plateau after a few modes that settles around an error of 10^{-3} , and then a second plateau that settles on an error of about 10^{-6} . For the inner layer interfaces, mostly in sticking state, a very low approximation error can be reached with few modes. However for the two outermost layer interfaces, subjected to large sliding fronts across the whole layer interface, an accurate representation requires more modes to accurately track the sliding front, which is critical for fretting fatigue life expectancy [Montalvo, 2023; Montalvo et al., 2023].

Similarly, no significant difference between the two beam directions can be appreciated. The error for the inter-wire slip norm is represented in Figure 2.16, and the trend remains indistinguishable from those in the respective tangential beam directors (Figure 2.15).

2.2 Layer-by-layer space and time modes

Here, some space and time modes for the different interface contact quantities are analyzed, in order to interpret their previously described behavior.

In Figure 2.17 are represented the first three spatial modes (obtained from the SVD, thus orthonormalized with respect to each other) for the normal contact forces at layer interface 4-5 (we choose to show this layer interface because it presents variable contact conditions and also allows comparison with layer interface 3-4 to analyze the behavior

2. Singular Value Decomposition on the main results

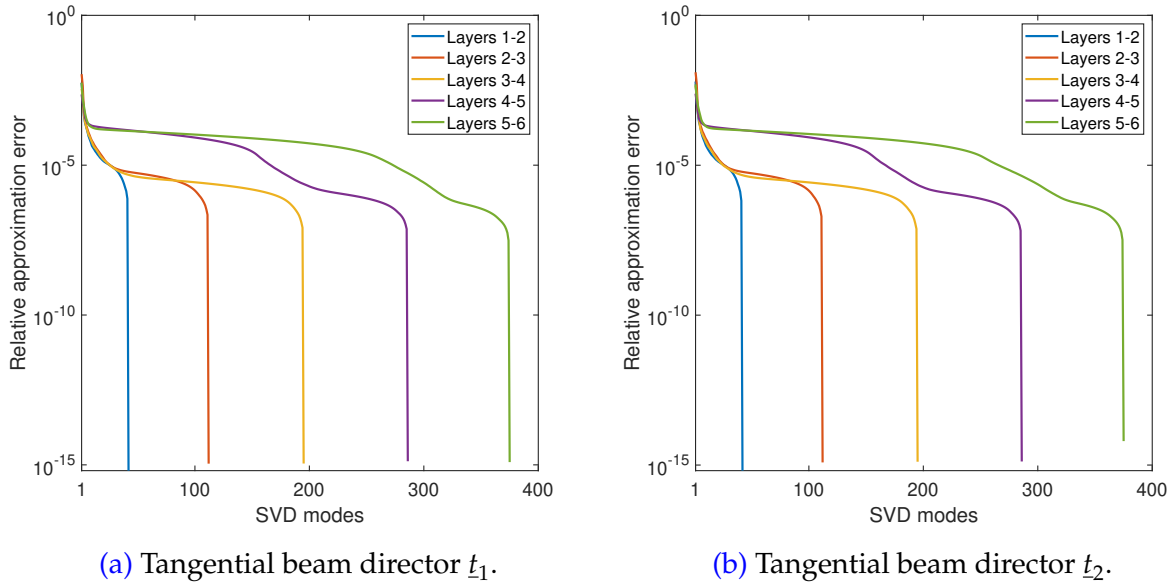


Figure 2.15: Relative approximation error for the inter-wire slip between the wires of adjacent layers. (a): Tangential beam director t_1 . (b): Tangential beam director t_2 .

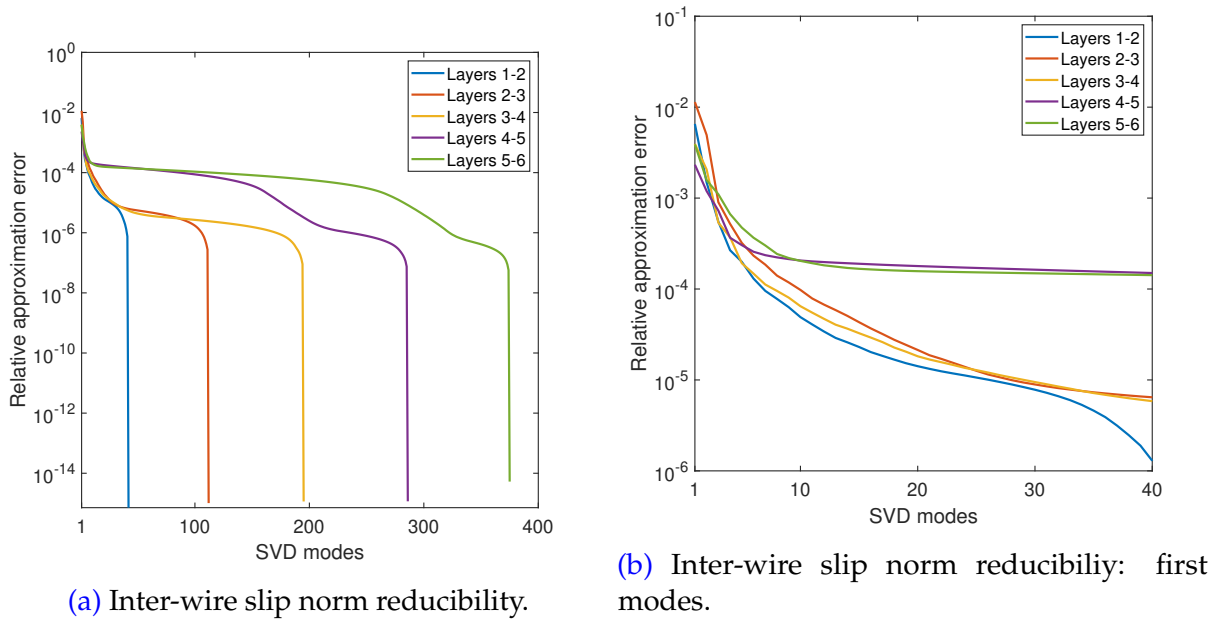


Figure 2.16: Relative approximation error for the norm of inter-wire slip between the wires of adjacent layers. (a): Global reducibility. (b): Detail on the first modes.

switch shown in Figure 2.16). The first mode, the most energetic one, displays a similar behavior to the snapshot shown in Figure 2.9. The second mode, on the other hand, evidently represents a mode due to the curvature loading as it can be seen by the fact

that it differs from the upside and downside position with respect to the bending axis. Subsequent modes bring localized correction.

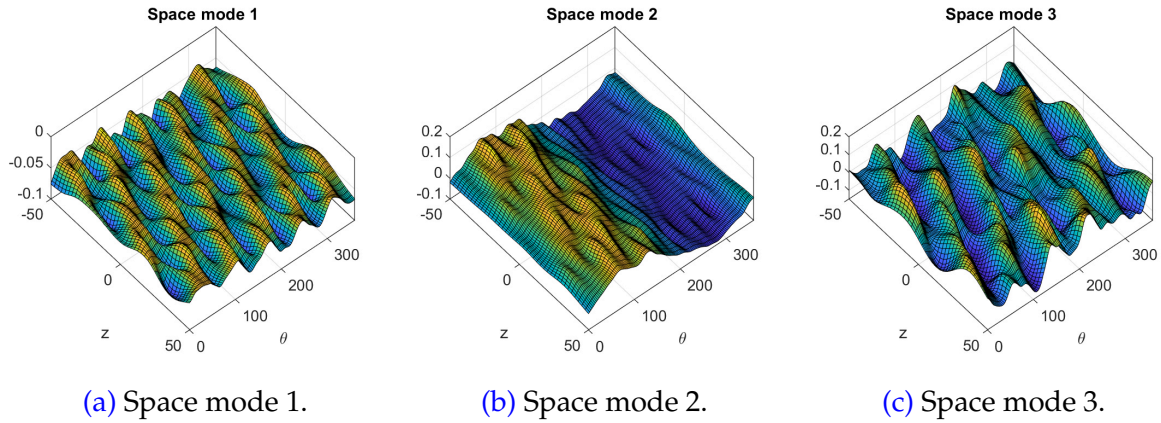


Figure 2.17: First three space modes for the normal contact forces between layers 4-5. (a): Space mode 1. (b): Space mode 2. (c): Space mode 3.

The corresponding first three time modes (orthonormalized) for normal contact forces between layers 4-5 are shown in Figure 2.18. It can be seen that from the second mode onward, both spatial and temporal modes exhibit a shape that oscillates around zero. This turns out to be true for spatial modes, as well as for temporal modes after the time value of $t \approx 100$ s. This fact can reasonably be related to the trend of the wire rope behavior seen before, which reaches a stabilized state around this time value.

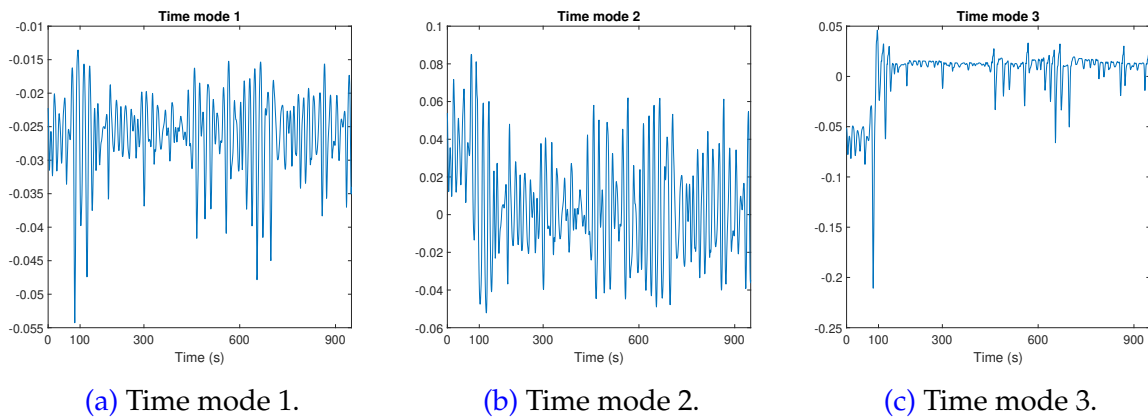


Figure 2.18: First three time modes for the normal contact forces between layers 4-5. (a): Time mode 1. (b): Time mode 2. (c): Time mode 3.

Figure 2.19 represents the first three spatial modes for the tangential contact forces between layers 4-5. If compared to the spatial modes of normal contact forces in Figure 2.17, one can notice that in this case the modes exhibit a more pronounced dependence on the position relative to the bending axis. The corresponding time modes

are shown in Figure 2.20. As for normal contact forces, after the second mode, the spatial modes oscillate around zero while time modes reach this state after $t \approx 100$ s (see Figure 2.20b and Figure 2.20c).

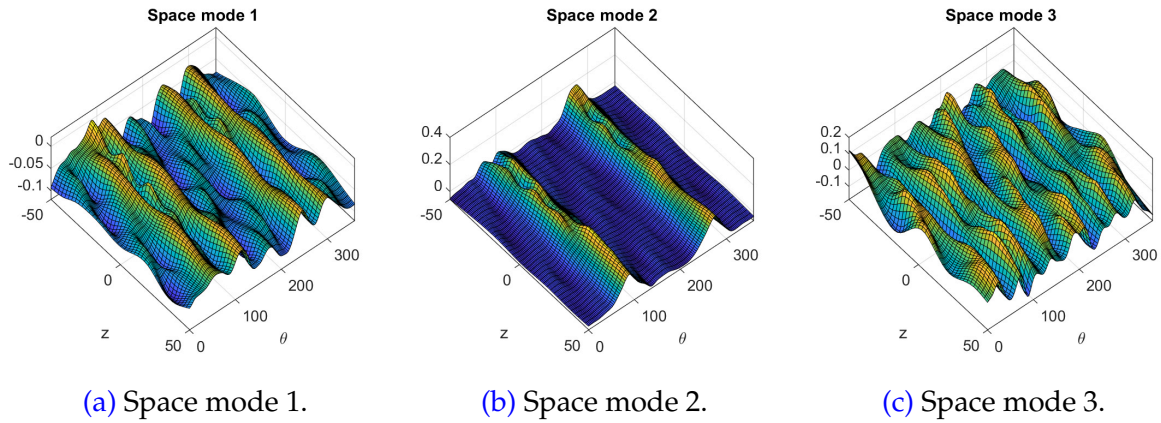


Figure 2.19: First three space modes for the tangential contact forces between layers 4-5. (a): Space mode 1. (b): Space mode 2. (c): Space mode 3.

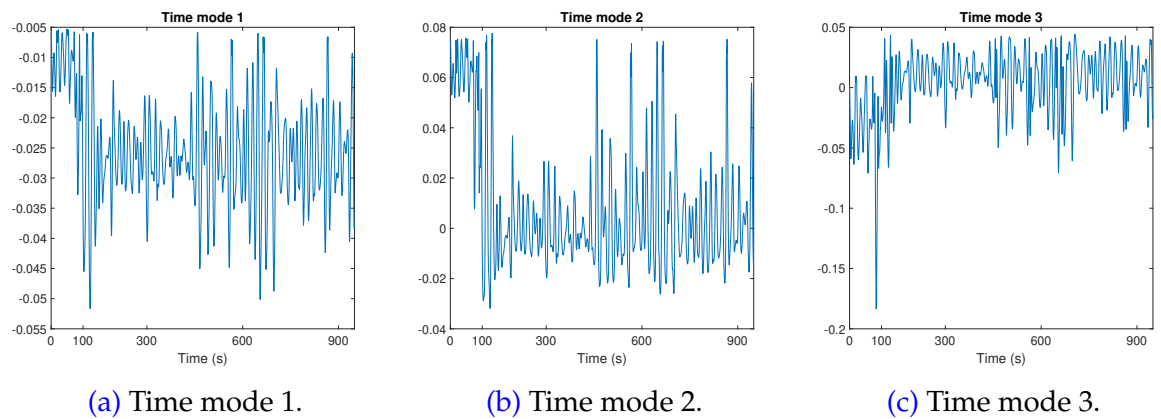
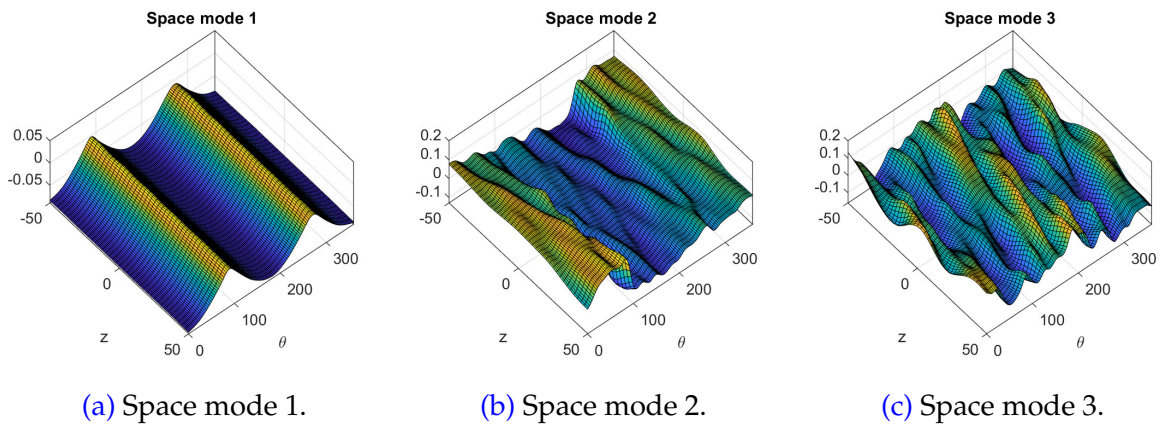
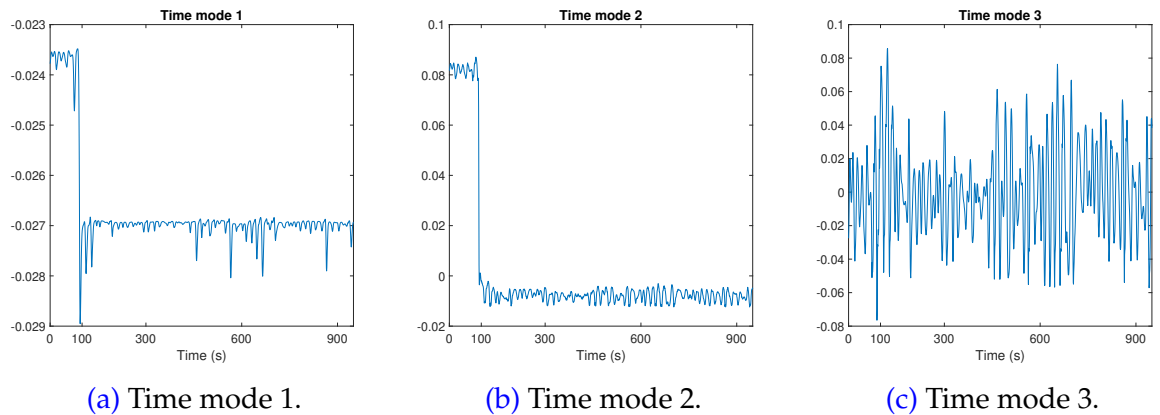


Figure 2.20: First three time modes for the tangential contact forces between layers 4-5. (a): Time mode 1. (b): Time mode 2. (c): Time mode 3.

The first three spatial modes for the inter-wire slip between layers 4-5 are shown in [Figure 2.21](#). The first mode captures a global behavior similar to the snapshot in [Figure 2.9](#) and, as for tangential contact forces, space modes show a remarked dependence on the sliding and sticking zones. The corresponding time modes, represented in [Figure 2.22](#), display a quite different behavior if compared to the normal and tangential forces. In fact the first time modes capture the shift in sliding that occurs at $t \approx 100$ s, while the subsequent time modes bring more localized corrections. Even in this case, from the second time mode and onward, the modes oscillate around zero.



[Figure 2.21](#): First three space modes for the inter-wire slip between layers 4-5. (a): Space mode 1. (b): Space mode 2. (c): Space mode 3.



[Figure 2.22](#): First three time modes for inter-wire slip between layers 4-5. (a): Time mode 1. (b): Time mode 2. (c): Time mode 3.

Another interesting point to analyze is the shift in the SVD approximation error behavior of the inter-wire slip between the interfaces of layers 3-4 and below and that of layers 4-5 and above seen in [Figure 2.16](#).

In [Figure 2.23](#) are represented two space modes for the inter-wire slip between layers 3-4 located in the plateau zone, and in [Figure 2.24](#) are shown three space modes for the inter-wire slip between layers 4-5 located in the two different plateau zones. The two space modes of layers 3-4 in [Figure 2.23](#) result indistinguishable from each other and show no signs of dependence on sliding and sticking zones, as in fact sliding-sticking transitions in layers 3-4 are very limited. The plateau modes of layers 4-5 in [Figure 2.24](#) instead show a more peculiar behavior. Space mode 100, which belongs to the the first plateau, as it can be noticed, brings localized corrections in the angular sections around the bending axis, where sliding conditions propagate. Space mode 180 belongs in the transition zone between the two plateaus and, as it can be noticed, the corrections are localized in the sticking regions, i.e., the top and bottom angular sectors. This trend continues then until the second plateau as it can be seen from the space mode 250.

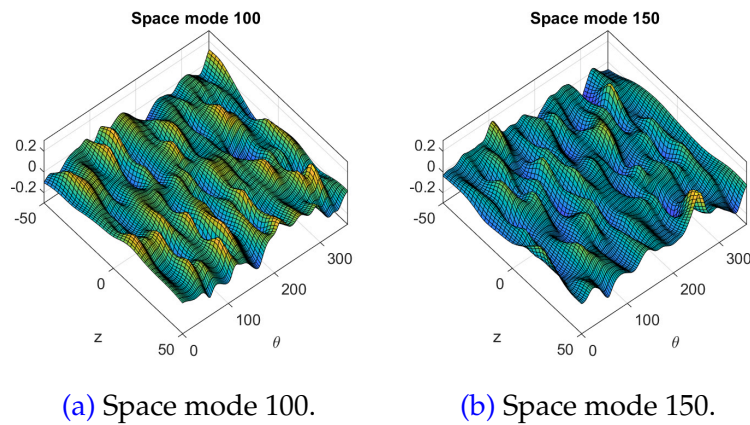


[Figure 2.23](#): Plateau space modes for the inter-wire slip between layers 3-4. (a): Space mode 100. (b): Space mode 150.

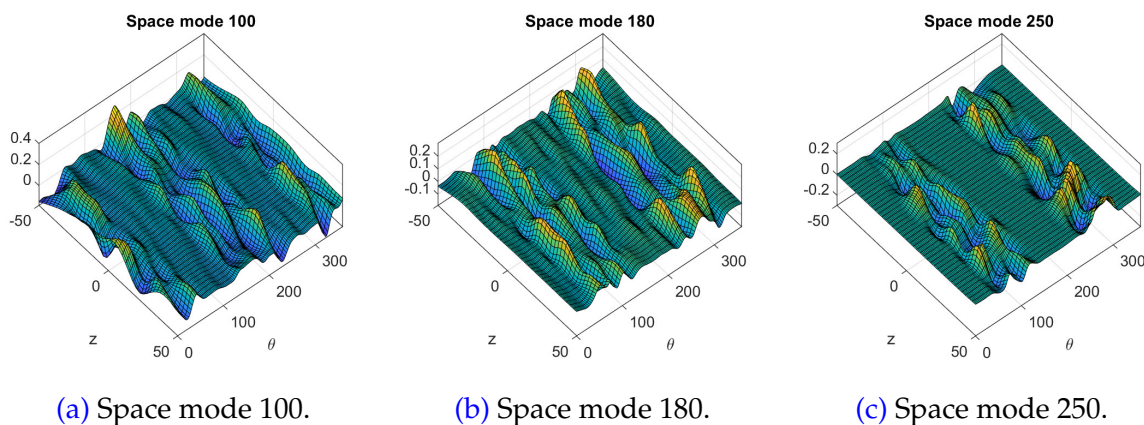


[Figure 2.24](#): Plateau space modes for the inter-wire slip between layers 4-5. (a): Space mode 100. (b): Space mode 180. (c): Space mode 250.

This difference in behavior is most likely due to the fact that in the outermost layers almost complete sliding conditions occur (as shown in [Figure 2.7](#)), as opposed to the inner layers, and in general are subject to more severe sliding-sticking transitions along time. These transitions arise and propagate in the neighbourhoods of the bending axis and, since they constitute the major contribution to the amount of sliding, they represent the areas that are corrected first by the SVD modes. The long first plateau of layers 4-5 in [Figure 2.16](#) is most likely a zone where the SVD modes seek to correct the strong discontinuity in sliding that occurs at maximum curvature (see [Figure 2.10](#)). Since this is a sudden discontinuity, and very localized, the error committed in approximating it decreases very slowly. Once the sliding zones around the bending axis have come to convergence in the first plateau, the sticking zones of the top and down sectors with respect to the bending axis are rapidly sent to convergence in the transition zone between the plateaus.

3 Conclusions

In this Chapter, first of all a brief description of the global and local analyses performed in [[Bussolati, 2019](#)] on a fine local model of a FOWT was presented. The global analysis, performed on DeepLinesTM, consists of an hydrodynamic computation on an entire FOWT structure equipped with 6 mooring lines under the action of a critical sea state. Then, after identifying the most critical bending zone in the mooring lines, a local FEM analysis was performed in [[Bussolati, 2019](#)] on a detailed model of a wire rope portion subjected to the traction and curvature time histories of the critical zone obtained from the global model.

We investigated and briefly presented the most important results of the local model, along with an analysis of the contact status complexity between the different layer interfaces. **Mainly, sliding conditions occur in the areas around the bending axis, with mostly sticking conditions in the areas around the top and bottom angular sectors.** In particular, what emerges is that the outermost layers display more critical and complex frictional contact conditions, subjected to large sliding fronts which can propagate throughout the whole layer interface. This point is crucial, since it significantly can affect the convergence and reducibility of the contact problem. Therefore, a robust and efficient strategy for solving the contact problem is required.

Subsequently, we performed an SVD of the main results obtained from the local model (normal and tangential contact forces, inter-wire slip) in order to investigate the reducibility of the particular problem. SVD was performed layer-by-layer, so as to thoroughly understand how layer dependency affects reducibility. **In general, the analyzed quantities show a good potential for reducibility,** mainly due to the particular loads acting on the structure, which consist of oscillations around a pre-

loaded state. In particular, the **reducibility presents a dependency on the layer, with the more internal layer presenting better reducibility, as opposed to the outermost ones** [Guidault et al., 2023; Zeka et al., 2023]. Normal contact forces show the best trend in terms of reducibility, while tangential contact forces result more difficult to represent in a reduced-order framework, as also display a large dependency on the layers interface. Regarding inter-wire slip, for the inner layer interfaces, mostly in sticking state, a very low approximation error can be reached with few modes. However for the two outermost layer interfaces, subjected to large sliding fronts across the whole layer interface, an accurate representation requires more modes to accurately track the sliding front, which is critical for fretting fatigue life expectancy.

Some space and time modes for layers 4-5 were then investigated and related to the behavior of the different contact quantities. Space modes display a multiscale nature in which the first modes capture a macro behavior of different quantities, mainly related to preload, while the following modes bring more localized corrections due to the variable loading and local frictional phenomena mainly around the bending axis [Guidault et al., 2023]. The time modes, on the other hand, highlight the shift in behavior that occurs around $t \approx 100$ s following maximum curvature.

This analysis is interesting since it allows to understand how these kind of structures behave and what are the most critical aspect to take care of for in order to propose a suitable model reduction strategy. In particular, the results suggest the adoption of a model reduction strategy that takes into account the structured geometry of layered cables, as well as the dependency of contact quantities on the different layers and on the angular position, in order to be more accurate when needed in the most critical zones.

By following these suggestions, in the second part of this manuscript a pertinent model reduction strategy appropriate to this type of problem, and coupled with a robust nonlinear solver, will be introduced.

Part II

**A multiscale strategy to
model-order reduction for frictional
contact problems**

Chapter 3

LATIN-based mixed DDM to model reduction for frictional contact problems

This chapter presents the proposed strategy for dealing with evolutionary frictional contact problems with model reduction, and represents the first part of the article [Zeka et al., 2024a]. The proposed strategy relies on the LATIN nonlinear solver combined with a priori model reduction based on the PGD. The chapter begins with the analysis of a simple frictional contact benchmark problem, intended as a simplified representation of the mechanics of a wire within a rope. This problem will then serve as a benchmark to test the features and limitations of the proposed strategy. Thereafter the LATIN method for frictional contact problems via domain decomposition is presented in detail. Finally, the introduction of PGD in the LATIN scheme is discussed, focusing on the control of quality and size of the reduced base along the iterations of the nonlinear solver.

Contents

1	Preliminary results on a simple 1D problem	101
1.1	Analysis of the solution	102
1.1.1	Load case 1: large propagation of sliding front	102
1.1.2	Load case 2: small variations of sliding front	104
1.2	Reducibility of the contact quantities	106
2	LATIN-based monoscale DDM for frictional contact problems	108

2.1	The reference problem: partitioning into substructures and interfaces	110
2.1.1	Admissibility for variables on a substructure	111
2.1.2	Interface behavior	112
2.1.3	Reformulation of the reference problem	112
2.2	Some examples of interface behaviors	113
2.3	LATIN-based iterative solver	114
2.3.1	The local stage	115
2.3.2	The linear stage	116
2.3.3	On the search directions	117
2.4	Local stage for different interface behaviors	118
2.5	Initialization and control of the convergence	121
2.6	Application on the 1D test problem	123
3	Solving linear stage problems with PGD	127
3.1	Linear stage with corrections	127
3.2	Separated representation of the unknowns during the linear stage	129
3.3	Finding a new pair of modes	130
3.4	Controlling the size and quality of the PGD basis	132
3.5	Application on the 1D test problem	134
4	Conclusions	139

1 Preliminary results on a simple 1D problem

In this section, before introducing the adopted strategy to model-order reduction for frictional contact problems, is investigated the reducibility of the displacements, velocities and frictional forces of a one-dimensional frictional contact benchmark problem [Zeka et al., 2022]. The problem consists of a clamped bar subjected to a time-dependent traction loading $F_d(t)$ on the free side. The bar is in contact with a frictional interface along its entire length by means of a normal pressure $p(t)$ acting on it (Figure 3.1a). In practice, it is assumed that the bar is always in contact with the frictional surface due to the pressure p considered to be constant.

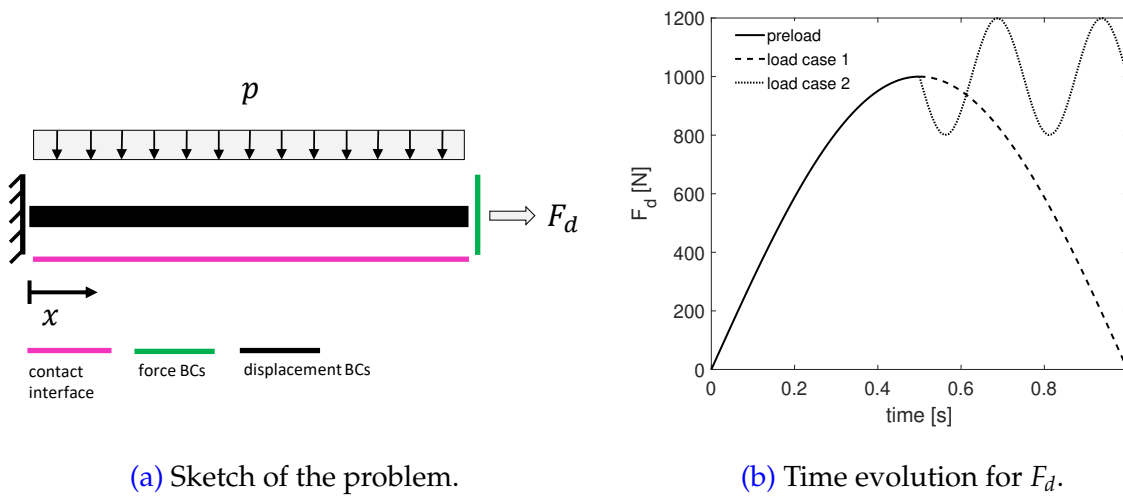


Figure 3.1: 1D benchmark problem. (a): Graphical representation of the problem. (b): External traction force time evolution.

The considered benchmark problem can be seen as representative of the mechanics of a single steel wire from a part of a mooring line composed of a wire rope (Figure 3.2, see also Figure 1.13 in Chapter 1).

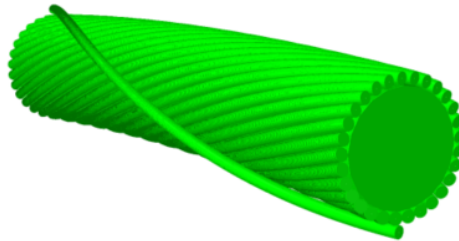


Figure 3.2: A wire from the external layer in contact with the internal layer [Bussolati, 2019]. Note that the inner wires are replaced by an homogenized beam of equivalent axial stiffness.

In fact the rope is subjected to external loadings from the sea state and, because of the helical geometry of the rope, traction and bending phenomena cause pressure loads between the different layers of wires which slide with respect to each other resulting in frictional contact phenomena.

Concerning the traction force acting on the bar, two different load cases are considered (represented in [Figure 3.1b](#)). Both of them start from a preloading stage where the value of 1000 N is reached. The load case 1 consists in fully unloading the bar after the preloading, while the load case 2 consists in performing some small-amplitude oscillations around this preloaded state. The first load case should put us in a more critical condition, since one has to deal in fact with a larger propagation of sliding front which is more challenging to track with respect to the second load case. The parameters adopted for the problem are shown in [Table 3.1](#). The problem, after a finite element discretization in space and time, has been solved with the LATIN method (of which the details will be given in the next section of this chapter). Continuous linear shape functions have been used for substructure displacement field and piecewise constant shape functions for interface quantities (see [Appendix B](#) on the discretization of subdomain and interface quantities). A converged solution (high number of iterations) was taken as a reference solution and analyzed in the following section. Obviously, any more conventional nonlinear solver could have been used for this purpose.

Parameters of the 1D problem	
Young modulus, E	210 GPa
bar cross section, S	3.14 mm ²
bar length, L	1 m
number of DOFs, N_x	50
number of time steps, N_t	100
time interval, $[0, T]$	$[0, 1 \text{ s}]$
friction coefficient, f	0.3
pressure load, p	5000 N/m

[Table 3.1](#): Used parameters for the benchmark problem.

1.1 Analysis of the solution

1.1.1 Load case 1: large propagation of sliding front

In [Figure 3.3](#), [Figure 3.4](#) and [Figure 3.5](#) are shown, respectively, some snapshots of the reference solution of the problem for the displacement, velocity and frictional contact forces distributions for the load case 1. In dark gray is highlighted the areas where sliding occurs, while in the white areas there are sticking conditions. From [Figure 3.3](#) and [Figure 3.4](#) one can notice that the sliding front propagates as the traction force increases, from $t = 0 \text{ s}$ to $t = 0.5 \text{ s}$ during the preloading stage. A portion of the

bar, the one closer to the clamped end ($x/L = 0$), remains always in sticking conditions. During the unloading part another sliding front propagates from the free end of the bar ($x/L = 1$) until the traction force becomes zero. At the end, because of the presence of friction, the bar does not get back to its original undeformed position but remains in a sticking deformed state. [Figure 3.5](#), displaying some snapshots of the frictional contact forces, is in agreement with what has been said about displacements and velocities. In the sticking zone, near the clamped end, the frictional forces are zero, whereas in the sliding zone, during loading, they are equal in absolute value to the Coulomb friction threshold $f_p = 1500$ N. In the unloading phase, a new sliding front propagates located in the zone where the friction forces change sign.

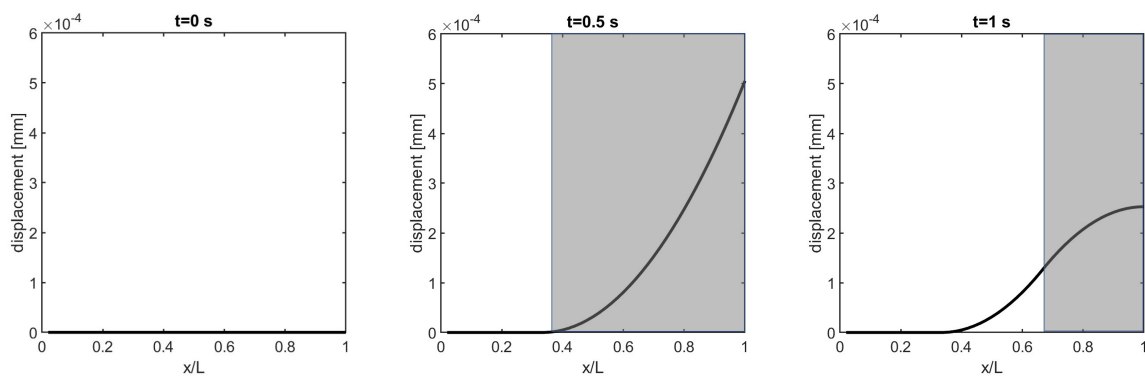


[Figure 3.3](#): Displacement snapshots at time $t = 0$ s, $t = 0.5$ s and $t = 1$ s for load case 1.

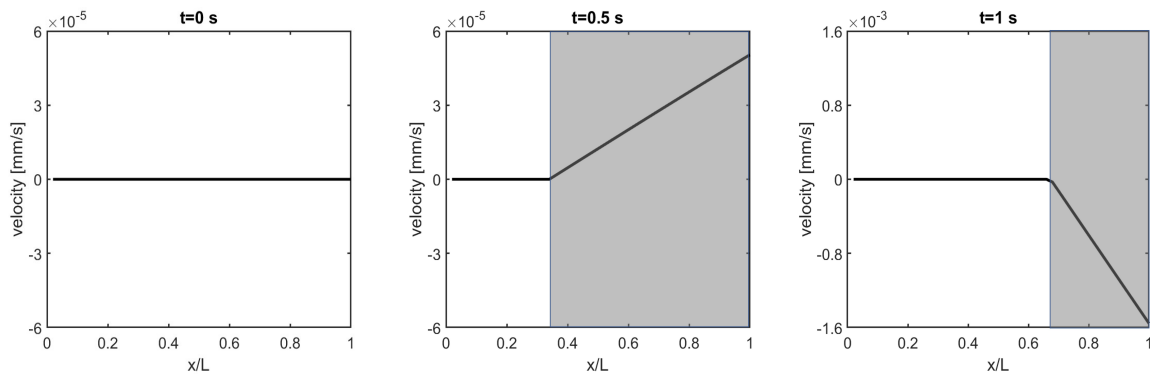


[Figure 3.4](#): Velocity snapshots at time $t = 0$ s, $t = 0.5$ s and $t = 1$ s for load case 1.

After obtaining the reference solution for displacements, velocities and frictional forces, an a posteriori SVD analysis can be performed to exemplify the reducibility of the space-time solution (see [Section 4.3.1](#) in [Chapter 1](#) for the definition of SVD). A few space modes for frictional forces are given in [Figure 3.6](#), and the corresponding time modes are shown in [Figure 3.7](#). First modes depict a generally global scale of the solution. One can see that the space modes clearly separate the sticking zone (in white)

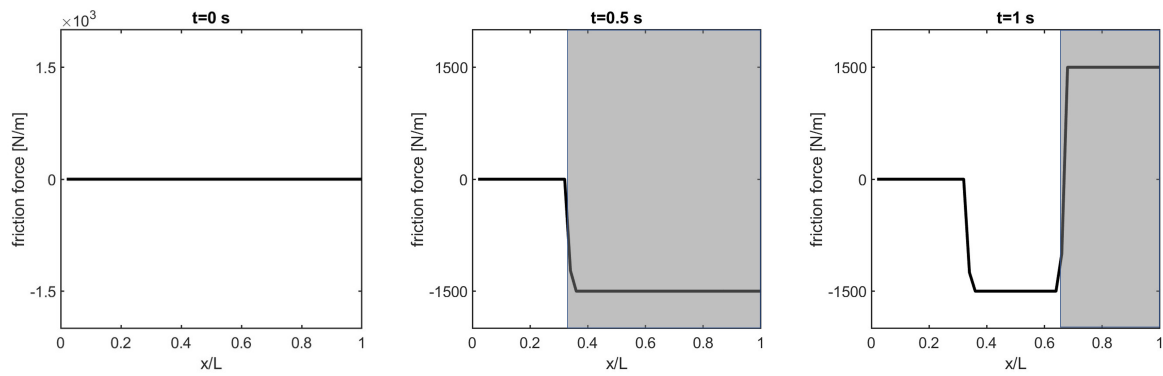


Figure 3.5: Frictional forces snapshots at time $t = 0$ s, $t = 0.5$ s and $t = 1$ s for load case 1.

from the ones where sliding occurs (light gray for sticking-sliding transition and dark gray for mainly sliding). Subsequent space modes still emphasize this distinction as also bring localized corrections to the sliding zones. Similar considerations can be made for the time modes. The first time mode depicts a global proportionality to the external traction loading, while subsequent modes bring localized corrections at specific time instants.

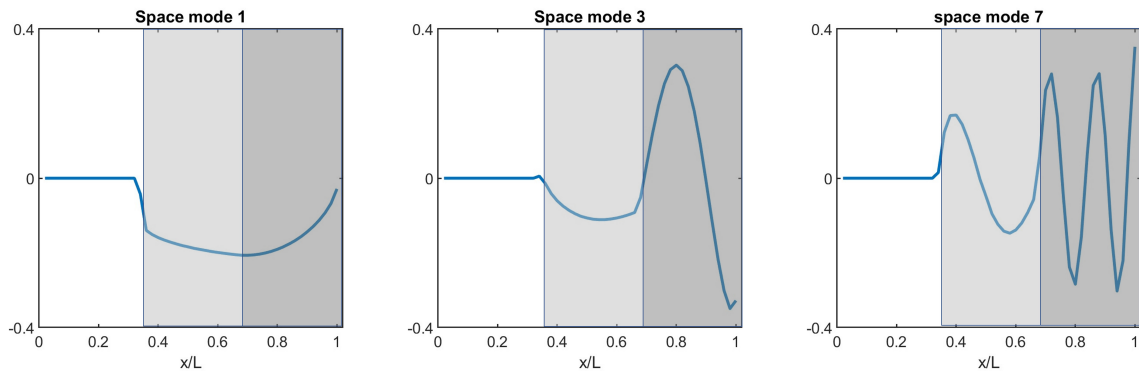


Figure 3.6: SVD space modes 1, 3 and 7 of the frictional contact forces for load case 1.

1.1.2 Load case 2: small variations of sliding front

Regarding load case 2, the main differences lie in the second part of the loading, the first being the same. As it can be seen from Figure 3.8, where some snapshots of the contact forces in the second part of the loading are shown, the sliding region due to the oscillating load is extremely localized in the neighborhood part where the load is applied. The sliding front presents a much smaller propagation amplitude compared to load case 1. By looking at some spatial modes in Figure 3.9, this is reflected in a larger localization of modes in the region where local sliding occurs.

1. Preliminary results on a simple 1D problem

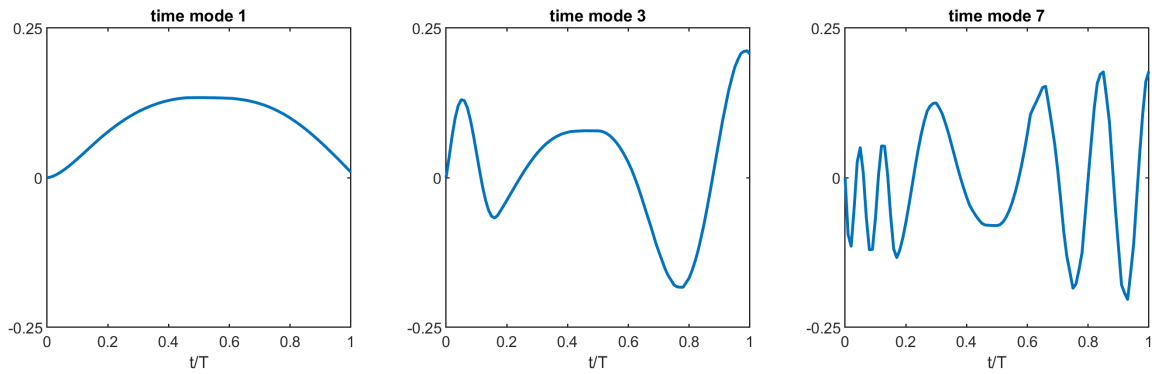


Figure 3.7: SVD time modes 1, 3 and 7 of the frictional contact forces for load case 1.

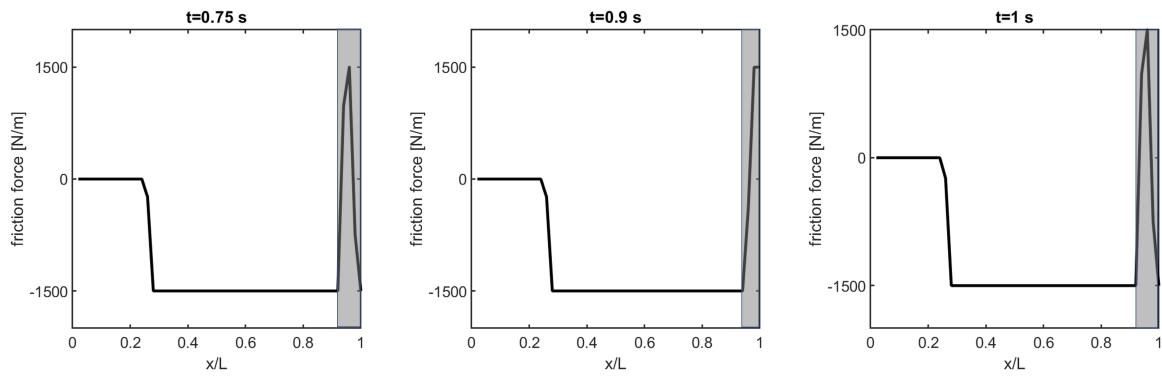


Figure 3.8: Frictional forces snapshots at time $t = 0$ s, $t = 0.5$ s and $t = 1$ s for load case 2.

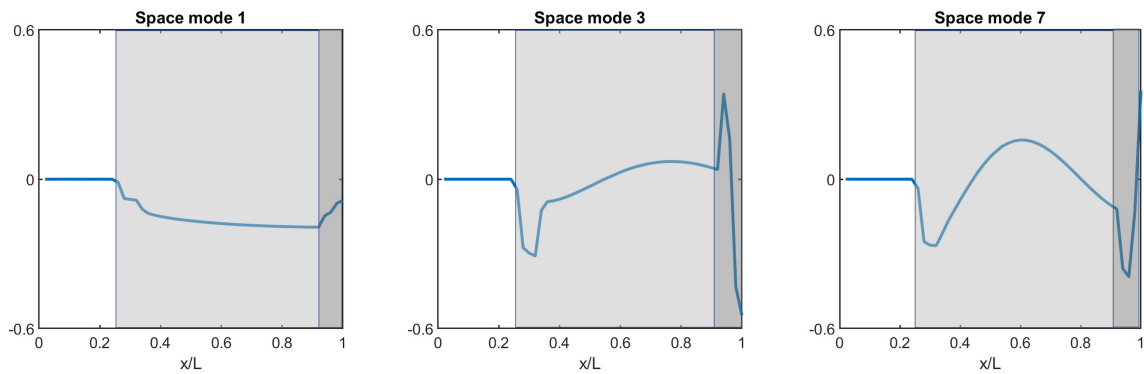


Figure 3.9: SVD space modes 1, 3 and 7 of the frictional contact forces for load case 2.

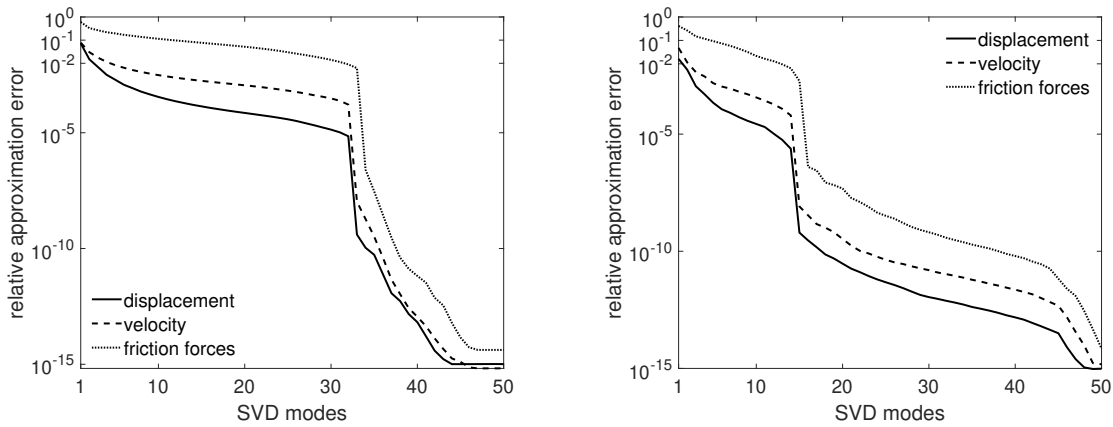
1.2 Reducibility of the contact quantities

In Figure 3.10 is shown the SVD relative approximation error

$$err = \frac{\|\mathbb{A} - \mathbb{A}_p\|_F}{\|\mathbb{A}\|_F} \quad (3.1)$$

between the original field and a truncated SVD of order p for displacements, velocities and frictional forces for the two considered load cases in Figure 3.1b. The snapshot matrix $\mathbb{A}^{N_x \times N_t}$ collects the quantities of interest along the N_x spatial positions and N_t time steps, with \mathbb{A}_p which represents the SVD approximation of \mathbb{A} with p modes, and $\|\bullet\|_F$ stands for the Frobenius norm.

In both cases, **displacements present a better reducibility compared to frictional contact forces and velocities. Frictional contact forces, due to their highly non-smooth nature, present a very low reducibility**, in agreement with similar results in [Giacoma et al., 2015; Guidault et al., 2023] as well as in Chapter 2. For the first load case (Figure 3.10a), the reducibility for frictional forces is quite critical. Being a propagation problem with a large sliding front, frictional forces need a large basis to reach a good accuracy (relative approximation error (3.1) below 10^{-4}). For the second load case the reducibility of the problem strongly improves, especially for frictional forces, as in fact the **small-amplitude oscillations cause smaller variations in contact conditions**.



(a) SVD of load case 1.

(b) SVD of load case 2.

Figure 3.10: Relative approximation error (3.1) of the contact quantities of the 1D problem in Figure 3.1 for the two different load cases.

In particular, the two load cases we have considered create comparable contact and reducibility conditions to the outermost layers of the cable section analyzed in Chapter 2 where the front propagates over the whole layer interface (load case 1), and the innermost layers whose front remains located around the bending axis (load case 2). Propagation problems are known for their low reducibility and capturing their behavior

with a ROB is challenging, even for ROBs enriched on-the-fly as in PGD [Allier et al., 2015; Nouy, 2010]. Clearly, for particular applications where one deals with loads such as the second load case, or problems where the contact interface is small relative to the overall structure of the problem and/or a few contact interfaces are present, this can help to start with a good potential reducibility.

As seen in the above example and in [Chapter 2](#), when wide contact interfaces are present, different regions subjected to different sticking and sliding conditions can be encountered (but also open/closed contact conditions). This suggests the **separation of these different regions a priori and the application of the model reduction strategy separately, ideally in each zone, through a DDM approach**. Therefore, the different potential reducibility of the different subregions is exploited and the computational time can further be improved thanks to the parallelization given by the DDM. Another aspect to consider is the presence of multiscale aspects in the solution of contact problems. As highlighted in [Giacoma et al., 2015], global modes on a structural level and localized modes on the contact interfaces are present and the introduction of **multiscale aspects may effectively improve the handling of similar problems**.

In the following, we will put ourselves in the condition of the first load case, considered as more critical since it is less reducible due to important sliding front propagation, and we will analyze how the proposed approach behaves in the case of a problem with low reducibility.

2 LATIN-based monoscale DDM for frictional contact problems

Incremental methods for solving a nonlinear problem (e.g., Newton-Raphson, quasi-Newton, modified Newton methods) consist in making converge the problem at a given time instant t , knowing the converged solution from the previous time instant $t - \Delta t$, up to the final time T . On the contrary, in non-incremental methods, all time steps are swept at each iteration and each non-incremental iteration ends on a space-time approximation of the solution. The LATIN method, introduced in [Ladevèze, 1985; Ladevèze, 1999], is a general strategy for dealing with nonlinear evolution problems and belongs to the family of non-incremental solvers.

The LATIN, as firstly introduced, is based on three principles:

- *Principle P1.* Partitioning of the underlying equations into two manifolds: a manifold $\Gamma^{[0,T]}$ pertaining to the local and possibly nonlinear equations, and a manifold $\mathbf{A}_d^{[0,T]}$ related to the linear and possibly global equations.
- *Principle P2.* Search for the solution based on a two search alternating direction algorithm, which shares similarities with ADMM (Alternating Direction Methods of Multipliers) methods [Glowinski and Le Tallec, 1989, 1990; Glowinski, 2015]. At each iteration, a solution on the whole space and time domain of the problem is alternately built in each of the two manifolds in a fixed-point like manner.
- *Principle P3.* Use of an adapted representation of the iterate in reduced or compact form, such as a representation in separate space and time variables through PGD. This third point is not mandatory in the strategy, however for large scale evolution problems with a high number of time steps it is crucial for for solution/iterate storage issues and the efficiency of the method.

A non-exhaustive list of applications of the strategy includes small-strain elasto-plasticity and visco-plasticity [Boisse, 1987; Cognard, 1989; Relun et al., 2013], geometric nonlinearities due to large displacements [Boucard, 1996], cyclic damage computation [Bhattacharyya et al., 2018a; Bhattacharyya et al., 2018b] and more recently also stochastic problems [Zheng et al., 2024]. Multi-physics problems can also be tackled by the LATIN strategy [Dureisseix et al., 2003; Néron, 2004; Wurtzer et al., 2024] by separating the different physics from each other in order to simplify the resolution of the problem. For a recent overview on the different applications of the LATIN method one may refer to [Scanff et al., 2021].

The LATIN, in particular, allows for an efficient treatment of DDM, where subdomains and interfaces are considered separately. The subdomain/interface distinction makes it easy to introduce specific interface behaviors, such as interplies for composites [Kerfriden et al., 2009; Saavedra et al., 2012] or contact for assemblies [Champaney et al., 1999].

Initially introduced in the monoscale version without any coarse scale problem, the first works on the multiscale version (in space) can be traced back to [Ladevèze and Dureisseix, 2000; Ladevèze et al., 2001; Loiseau, 2001], with also the introduction of a third super macroscale to efficiently solve the coarse scale problem [Loiseau, 2001]. An extension of the multiscale approach in time was performed in [Ladevèze and Nouy, 2003; Nouy, 2003] in the context of highly heterogeneous structures, where a new formulation of the coarse scale problem with a Lagrange multiplier is introduced as well as PGD in the multiscale approach [Nouy and Ladevèze, 2004]. Subsequent works on the LATIN-based multiscale DDM strategy mainly refer to this framework, with applications in different fields, as explained in [Section 5.2](#) of [Chapter 1](#)

Among other things, **the LATIN is also a robust solver for frictional contact problems**. When applied to frictional contact problems, the LATIN method separates the internal equations belonging to the substructures from the contact conditions that occur at the contact interfaces. For this reason, it naturally leads to a mixed DDM where interface variables are constituted by the interface displacements or velocities (primal unknowns) and contact forces (dual unknowns). In addition, the two-search direction alternate algorithm of the LATIN shares similar features with augmented Lagrangian formulations combined with Uzawa-like algorithms [Fortin and Glowinski, 2000; Simo and Laursen, 1992], which makes it a strongly robust strategy for dealing with frictional contact problems ensuring an exact satisfaction of contact conditions at convergence.

Applications of the LATIN method specifically for frictional contact problems can be found in [Champaney et al., 1999; Ribeaucourt et al., 2007; Pierres et al., 2010; Oumaziz et al., 2017; Cardoso et al., 2018; Cardoso, 2019] for the monoscale strategy, or in [Ladevèze et al., 2002; Oumaziz, 2017; Oumaziz et al., 2018] for the multiscale one. Recent works on frictional contact problems couple the LATIN solver with cutFEM [Claus and Kerfriden, 2018] (Cut Finite Element Method [Hansbo and Hansbo, 2002]) or IGA [Lapina et al., 2024](IsoGeometric Analysis [Hughes et al., 2005]).

The LATIN strategy with PGD makes it possible to take into account also frictional contact interactions. However, in previous works, rather short frictional cracks had a more or less limiting effect on the global scale, surrounded by other material nonlinearities. A first application of the strategy with PGD specifically to frictional contact problems can be found in [Giacoma et al., 2015], even though without coarse scale problem. The most critical point to consider for frictional contact problems with PGD is that frictional problems present a low reducibility, consequently a large number of PGD modes is usually required to represent the solution. Moreover, given the high irregularity of frictional problems, a lot of useless PGD modes may be generated throughout

the iterations of the solution strategy decreasing the efficiency of the approach. To avoid such limitations, [Giacoma et al., 2015; Giacoma et al., 2016] proposed a sorting and downsizing algorithm to efficiently sort the reduced basis throughout the LATIN iterations.

In fact, the strategy with PGD has not extensively been considered in the case of frictional contact problems with large and multiple contact interfaces, where the contact conditions have an important effect at the global scale. We are interested to investigate to what extent a multiscale approach, in particular one based on DDM, may be helpful in efficiently solving frictional contact problems with a model reduction approach and what are the benefits and limits of combining a multiscale strategy with PGD [Zeka et al., 2024a; Zeka et al., 2024d; Zeka et al., 2024b, 2024c].

2.1 The reference problem: partitioning into substructures and interfaces

We consider, assuming small perturbations and isothermal quasi-static state, the equilibrium of a linear elastic structure occupying the space domain Ω on the time interval $[0, T]$ being studied (Figure 3.11). The structure being subjected to body forces \underline{f}_d and imposed loads \underline{F}_d on a part $\partial_2\Omega$ of the boundary $\partial\Omega$ and, on the complementary part $\partial_1\Omega$, displacements \underline{U}_d are prescribed. Internal or external frictional contact interfaces are present and designated with Γ_c . All quantities marked “d” are known data.

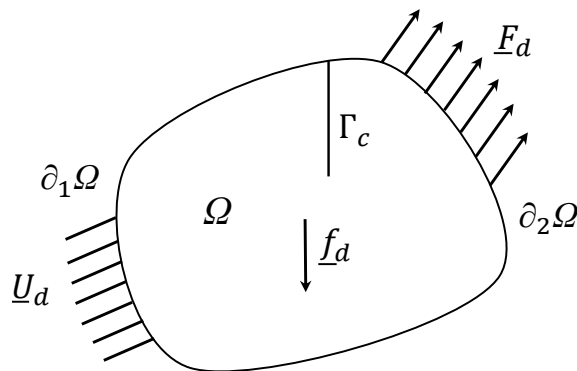


Figure 3.11: Reference structure problem being considered.

The basic idea of the mixed DDM strategy consists in **describing the structure as an assembly of simple components: substructures and interfaces** [Ladevèze, 1999], where each substructure has its own variables and equations.

A substructure Ω_E , with $E \in \mathbf{E}$ and \mathbf{E} being the set of substructures (Figure 3.12), is subjected to the action of its environment, that is the set of neighboring substructures

of Ω_E , defined by a force field \underline{F}_E and a displacement field \underline{W}_E acting on its boundary $\partial\Omega_E$ (Figure 3.13).

Concerning the neighboring substructures of Ω_E , since we will not make distinction between internal interfaces and external interfaces corresponding to boundary conditions, we can consider in these cases that the structure is linked to a structure Ω_{E_1} whose boundary contains $\partial_1\Omega$ and a structure Ω_{E_2} whose boundary contains $\partial_2\Omega$. We can then introduce the set $\mathbf{V}_E = \{E' \in \{\mathbf{E}, E_1, E_2\} \mid \text{mes}(\partial\Omega_E \cap \partial\Omega_{E'}) \neq 0\}$ of the neighboring substructures of Ω_E in a broader sense.

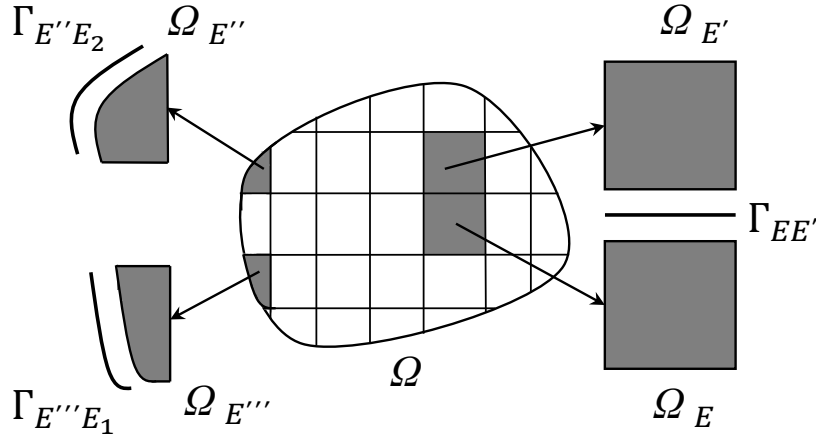


Figure 3.12: Decomposition of a structure in substructures and interfaces.

2.1.1 Admissibility for variables on a substructure

The displacement and the Cauchy stress fields within a substructure Ω_E are denoted with \underline{u}_E and σ_E , and they belong respectively to spaces $\mathcal{U}_E^{[0,T]}$ and $\mathcal{S}_E^{[0,T]}$ defined on Ω_E . Here, a space $\square^{[0,T]}$ with superscript $[0, T]$ designates the space of functions defined on $[0, T]$ which take values in \square . An interface $\Gamma_{EE'}$ between two substructures Ω_E and $\Omega_{E'}$ transfers both the displacement and the force fields $(\underline{W}_{EE'}, \underline{W}_{E'E})$ and $(\underline{F}_{EE'}, \underline{F}_{E'E})$ restricted to $\Gamma_{EE'}$, which belong respectively to spaces $\mathcal{W}_{EE'}^{[0,T]}$ and $\mathcal{F}_{EE'}^{[0,T]}$ defined on $\Gamma_{EE'}$. The previous spaces, extended to the set of neighboring interfaces of Ω_E , result in spaces $\mathcal{W}_E^{[0,T]}$ and $\mathcal{F}_E^{[0,T]}$:

$$\mathcal{W}_E^{[0,T]} = \prod_{E' \in \mathbf{V}_E} \mathcal{W}_{EE'}^{[0,T]} \quad \text{and} \quad \mathcal{F}_E^{[0,T]} = \prod_{E' \in \mathbf{V}_E} \mathcal{F}_{EE'}^{[0,T]}. \quad (3.2)$$

Extended to all substructures, this partitioning leads to the definition of the spaces $\mathcal{W}^{[0,T]}$ and $\mathcal{F}^{[0,T]}$. We denote with $\mathbf{E}_E^{[0,T]} = \mathcal{U}_E^{[0,T]} \times \mathcal{W}_E^{[0,T]}$ and $\mathbf{F}_E^{[0,T]} = \mathcal{S}_E^{[0,T]} \times \mathcal{F}_E^{[0,T]}$, as well as $\mathbf{S}_E^{[0,T]} = \mathbf{E}_E^{[0,T]} \times \mathbf{F}_E^{[0,T]}$. Therefore, one can define the admissibility of a

solution $\mathbf{s}_E = (\underline{u}_E, \underline{W}_E, \sigma_E, \underline{F}_E) \in \mathbf{S}_E^{[0,T]}$ which completely describes the state within a substructure:

Definition 3.1 (E-admissibility). A solution $\mathbf{s}_E = (\underline{u}_E, \underline{W}_E, \sigma_E, \underline{F}_E) \in \mathbf{S}_E^{[0,T]}$ is said to be E-admissible, that is $\mathbf{s}_E \in \mathbf{S}_{E,ad}^{[0,T]}$, if it verifies:

– the kinematic admissibility: $(\underline{u}_E, \underline{W}_E) \in \mathbf{E}_{E,ad}^{[0,T]} \mid \exists \underline{u}_E \in \mathcal{U}_E^{[0,T]}$ such that $\underline{u}_E|_{\partial\Omega_E} = \underline{W}_E$,

– the static admissibility: $(\sigma_E, \underline{F}_E) \in \mathbf{F}_{E,ad}^{[0,T]} \mid \forall (\underline{u}^*, \underline{W}^*) \in \mathbf{E}_{E,ad}^{[0,T]}$,

$$\int_{\Omega_E \times [0,T]} \sigma_E : \varepsilon(\underline{u}^*) d\Omega dt = \int_{\Omega_E \times [0,T]} \underline{f}_d \cdot \underline{u}^* d\Omega dt + \int_{\partial\Omega_E \times [0,T]} \underline{F}_E \cdot \underline{W}^* dS dt,$$

– the constitutive relation: $\sigma_E = \mathbf{K} : \varepsilon(\underline{u}_E)$, with \mathbf{K} being the Hookean tensor and $\varepsilon(\underline{u}_E)$ the small strain tensor.

2.1.2 Interface behavior

An interface $\Gamma_{EE'}$ between two substructures Ω_E and $\Omega_{E'}$ is driven by a constitutive law between the force fields $(\underline{F}_{EE'}, \underline{F}_{E'E})$ and the displacement fields $(\underline{W}_{EE'}, \underline{W}_{E'E})$ restricted on $\Gamma_{EE'}$. To lighten the notation, in the following when we refer to the force and displacement fields restricted on $\Gamma_{EE'}$ we refer to them simply as $(\underline{F}_E, \underline{F}_{E'})$ and $(\underline{W}_E, \underline{W}_{E'})$ as in [Figure 3.13](#).

The constitutive behavior at the different interfaces depends on the type of interface behavior which is to be modeled, and is expressed as a constitutive law which can be formally written as:

$$\mathbf{b}_{EE'}(\underline{F}_E, \underline{W}_E, \underline{F}_{E'}, \underline{W}_{E'}) = \mathbf{0}, \quad \forall (x, t) \in \Gamma_{EE'} \times [0, T]. \quad (3.3)$$

The interface constitutive behavior operator $\mathbf{b}_{EE'}$ describes in an abstract form the mechanical behavior of the interface. For example, for a perfect interface this condition corresponds to the continuity of the displacements across the interface, $\underline{W}_E - \underline{W}_{E'} = \underline{0}$, and the equilibrium of the interface forces $\underline{F}_E + \underline{F}_{E'} = \underline{0}$. Boundary conditions in displacements and forces are also taken into account through a specific interface behavior (interfaces $\Gamma_{E''E_1}$ and $\Gamma_{E''E_2}$ in [Figure 3.12](#) respectively).

2.1.3 Reformulation of the reference problem

The reference problem in [Figure 3.11](#), after the partitioning in substructures and interfaces, can be reformulated as follows:

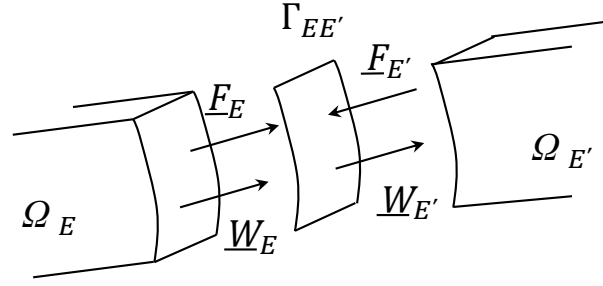


Figure 3.13: Forces and displacements acting on an interface $\Gamma_{EE'}$.

Problem 3.1 (reference substructured problem). Find $\mathbf{s}_{\text{exact}} = \{\mathbf{s}_E\}_{E \in \mathbf{E}}$, with $\mathbf{s}_E = (\underline{u}_E, \underline{W}_E, \sigma_E, \underline{F}_E) \in \mathbf{S}_E^{[0,T]}$, verifying:

- the E -admissibility of \mathbf{s}_E , $\forall E \in \mathbf{E}$, that is $\mathbf{s}_E \in \mathbf{S}_{E,\text{ad}}^{[0,T]}$ (**Definition 3.1**);
- the constitutive behavior of the interfaces (3.3).

Note that two types of formulations for the primal unknowns can be found in the literature: the formulation in velocity and the formulation in displacement. The velocity formulation is usually adopted in the context of material nonlinearities, where constitutive relations are expressed in a rate formulation (see [Nouy and Ladevèze, 2004; Passieux et al., 2010]), while the displacement formulation is usually more adopted in the context of linear elastic behaviour of the substructures [Giacoma et al., 2015; Cardoso et al., 2018; Cardoso, 2019], as in the case discussed herein.

2.2 Some examples of interface behaviors

The behaviors described here are written locally at each point of an interface $\Gamma_{EE'}$, $E \in \mathbf{E}, E' \in \mathbf{V}_E$.

■ Boundary conditions

Boundary conditions can be taken into account through a specific interface behavior:

$$\begin{aligned} \underline{W}_E &= \underline{U}_d \quad \text{on} \quad \Gamma_{E,E_1} = \partial\Omega_E \cap \partial_1\Omega, \\ \underline{F}_E &= \underline{F}_d \quad \text{on} \quad \Gamma_{E,E_2} = \partial\Omega_E \cap \partial_2\Omega. \end{aligned} \tag{3.4}$$

■ Perfect interfaces

For a perfect interface $\Gamma_{EE'}$, displacement continuity and interface force equilibrium have to be verified:

$$\begin{aligned} \underline{W}_E - \underline{W}_{E'} &= \underline{0}, \\ \underline{F}_E + \underline{F}_{E'} &= \underline{0}. \end{aligned} \quad (3.5)$$

■ Frictional contact interfaces

At a contact interface $\Gamma_{EE'}$ between substructure Ω_E and $\Omega_{E'}$, Signorini non penetration conditions for the normal contact and Coulomb's law for the tangential frictional behavior have to be satisfied, as well as the interface force equilibrium.

For the normal contact, the following conditions have to be verified (see [Definition 1.1](#)):

- *non-penetration condition*: $\underline{n} \cdot (\underline{W}_{E'} - \underline{W}_E) + g_0 \geq 0$;
- *compressive contact force*: $\underline{n} \cdot \underline{F}_E \leq 0$;
- *complementarity condition*: $(\underline{n} \cdot (\underline{W}_{E'} - \underline{W}_E) + g_0)(\underline{n} \cdot \underline{F}_E) = 0$.

with g_0 being the initial normal gap and \underline{n} the outward normal from E to E' .

For the tangential contact instead, the following conditions hold (see [Definition 1.2](#)):

- *sticking*: $\|\mathbf{P}_t \underline{F}_E\| < f |\underline{n} \cdot \underline{F}_E|$ and $\mathbf{P}_t (\dot{\underline{W}}_{E'} - \dot{\underline{W}}_E) = \underline{0}$;
- *sliding*: $\|\mathbf{P}_t \underline{F}_E\| = f |\underline{n} \cdot \underline{F}_E|$ and $\mathbf{P}_t (\dot{\underline{W}}_{E'} - \dot{\underline{W}}_E) = \rho \mathbf{P}_t \underline{F}_E$, with $\rho \geq 0$.

with f being the friction coefficient and $\mathbf{P}_t = \mathbf{I}_d - \underline{n} \otimes \underline{n}$ the tangential projector on the interface.

2.3 LATIN-based iterative solver

With reference to the substructured [Problem 3.1](#), let us denote with $\mathbf{A}_d^{[0,T]}$ the manifold of linear elastic solutions \mathbf{s} satisfying the E -admissibility ([Definition 3.1](#)), and refer with $\Gamma^{[0,T]}$ to the manifold of solutions $\hat{\mathbf{s}}$ satisfying the constitutive behavior at the interfaces (3.3). The LATIN method for solving [Problem 3.1](#) consists in iterating successively between manifold $\mathbf{A}_d^{[0,T]}$, a phase which is called *linear stage*, and $\Gamma^{[0,T]}$, named *local stage*, by following two alternating search directions \mathbf{E}^+ and \mathbf{E}^- introduced to iterate in a fixed-point manner between the two manifolds and to close the problem (see [Figure 3.14](#)). Starting from an initial admissible solution $\mathbf{s}_0 \in \mathbf{A}_d^{[0,T]}$, at convergence the exact solution $\mathbf{s}_{\text{exact}} \in \mathbf{A}_d^{[0,T]} \cap \Gamma^{[0,T]}$ is reached at the intersection between the two manifolds:

$$\mathbf{s}_0 \Rightarrow \dots \Rightarrow \mathbf{s}_n \in \mathbf{A}_d^{[0,T]} \xrightarrow[\mathbf{E}^+]{\text{local stage}} \hat{\mathbf{s}}_{n+1/2} \in \Gamma^{[0,T]} \xrightarrow[\mathbf{E}^-]{\text{linear stage}} \mathbf{s}_{n+1} \in \mathbf{A}_d^{[0,T]} \Rightarrow \dots \Rightarrow \mathbf{s}_{\text{exact}}$$

iteration $n+1$

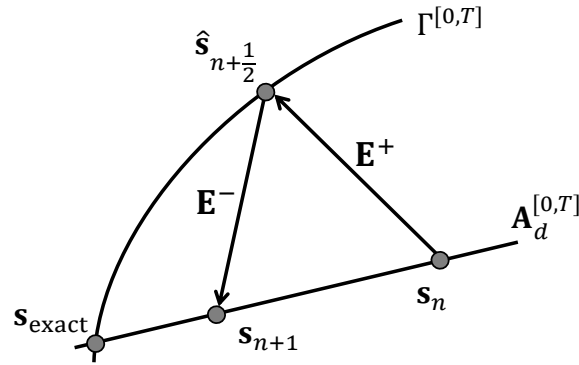


Figure 3.14: Abstract schematic representation of an iteration of the LATIN.

We stress the fact that **the linear and the local stages involve problems solved over the entire space-time domain**, as detailed in the following.

Remark 3.1. An "incremental" version of the LATIN, in which the loop over the LATIN iterations and loop over the time instants are switched, can be adopted when an accurate computation of some propagating front is required at each time instant because it largely influences the solutions at next time instants, as for example delamination fronts [Kerfriden et al., 2009] or fatigue crack propagation fronts [Ribeaucourt et al., 2007]. However in such a way the ability to make use of separated representations in space and time is lost, as well as the informations that can be drawn from a complete space-time view of the solution.

2.3.1 The local stage

The local stage at the current iteration $n + 1$ consists in finding $\hat{\mathbf{s}}_{n+1/2} \in \Gamma^{[0,T]}$, given $\mathbf{s}_n \in \mathbf{A}_d^{[0,T]}$ from the previous iteration, by following the *ascent search direction* \mathbf{E}^+ . For each interface $\Gamma_{EE'}$ the following conditions must be verified, with the subscripts n and $n + 1/2$ omitted to simplify the notations:

Problem 3.2 (local stage). Find $\hat{\mathbf{s}} = \{\hat{\mathbf{s}}_E\}_{E \in \mathbf{E}} \in \Gamma^{[0,T]}$ verifying, $\forall \underline{x} \in \Gamma_{EE'}$ and $\forall t \in [0, T]$,

- the interface constitutive behavior: $\mathbf{b}_{EE'}(\hat{\mathbf{W}}_E, \hat{\mathbf{W}}_{E'}, \hat{\mathbf{F}}_E, \hat{\mathbf{F}}_{E'}) = \mathbf{0}$;

$$- \text{ the search direction } \mathbf{E}^+ : \begin{cases} \widehat{\underline{F}}_E - \underline{F}_E - \mathbf{k}^+(\widehat{\underline{W}}_E - \underline{W}_E) = \underline{0} \\ \widehat{\underline{F}}_{E'} - \underline{F}_{E'} - \mathbf{k}^+(\widehat{\underline{W}}_{E'} - \underline{W}_{E'}) = \underline{0} \end{cases}$$

2.3.2 The linear stage

Given the solution $\hat{\mathbf{s}}_{n+1/2} \in \Gamma^{[0,T]}$ from the local stage, the linear stage at the current iteration $n + 1$ consists in finding $\mathbf{s}_{n+1} \in \mathbf{A}_d^{[0,T]}$ following the *descent search direction* \mathbf{E}^- :

Problem 3.3 (linear stage). Find $\mathbf{s} = \{\mathbf{s}_E\}_{E \in \mathbf{E}} \in \mathbf{A}_d^{[0,T]}$ verifying, $\forall \underline{x} \in \Omega_E$ and $\forall t \in [0, T]$,

- the E -admissibility of \mathbf{s}_E : $\mathbf{s}_E \in \mathbf{S}_E^{[0,T]}$;
- the search direction \mathbf{E}^- : $\underline{F}_E - \widehat{\underline{F}}_E + \mathbf{k}^-(\underline{W}_E - \widehat{\underline{W}}_E) = \underline{0}$.

Taking into account E -admissibility and the search direction \mathbf{E}^- , the following linear problem has to be solved at the linear stage for each substructure Ω_E in the whole space-time domain:

Problem 3.4. Find $(\underline{u}_E, \underline{W}_E) \in \mathbf{E}_{E,ad}^{[0,T]}$ such that, $\forall (\underline{u}^*, \underline{W}^*) \in \mathbf{E}_{E,ad}^{[0,T]}$

$$\int_{\Omega_E \times [0,T]} \boldsymbol{\varepsilon}(\underline{u}_E) : \mathbf{K} : \boldsymbol{\varepsilon}(\underline{u}^*) d\Omega dt + \int_{\partial\Omega_E \times [0,T]} \mathbf{k}^- \underline{W}_E \cdot \underline{W}^* dS dt =$$

$$\int_{\Omega_E \times [0,T]} \underline{f}_{-d|_{\Omega_E}} \cdot \underline{u}^* d\Omega dt + \int_{\partial\Omega_E \times [0,T]} (\widehat{\underline{F}}_E + \mathbf{k}^- \widehat{\underline{W}}_E) \cdot \underline{W}^* dS dt,$$

with $\underline{F}_E = \widehat{\underline{F}}_E + \mathbf{k}^-(\widehat{\underline{W}}_E - \underline{W}_E)$.

The solution of the linear stage problem associated with substructure Ω_E depends solely on the known quantities $\underline{f}_{-d|_{\Omega_E}}$ and $\hat{\mathbf{s}}_E$ on its boundary $\partial\Omega_E$. If \mathbf{K} and \mathbf{k}^- are symmetric positive definite, the **Problem 3.4** has a unique solution [Ladevèze, 1999]. The linear stage problems defined on the different substructures Ω_E are independent and are therefore parallelizable.

2.3.3 On the search directions

In the local stage and linear stage, k^+ and k^- are called search direction operators (or simply search directions). Usually $k^+ = k^- = k$ is adopted and k is taken as $k = kI_d$ [Ladevèze, 1999], with k called search direction parameter.

The search direction parameter k is homogeneous to a stiffness and analogous to the augmentation parameter in an augmented Lagrangian formulation. By looking at **Problem 3.4**, k acts as stiffness penalizing the displacements on the boundary of a substructure, as represented in **Figure 3.15**. Mathematically k acts as a Robin condition on the linear problem on the substructures, which makes the problem well posed as there are no substructure rigid body modes to handle. Physically, it represents a sort of a stiffness related to the surroundings of a substructure.

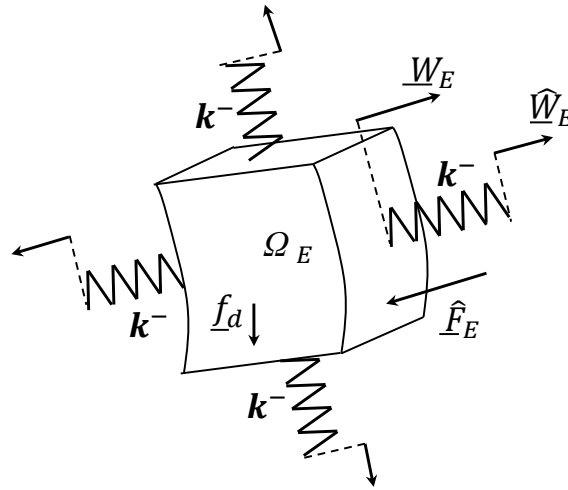


Figure 3.15: Representation of the linear problem on a substructure with the “spring distribution” k^- on the boundary.

Ideally, in linear elasticity and for perfect interfaces, the search direction parameter k would be associated to the first eigenvalue of the primal Schur complement of the stiffness matrix of all the other subdomains condensed on the subdomain boundary. Such value is not affordable in practice to compute and yet with such a choice one would loose the locality of the substructure problems, so simple local low-cost approximations are adopted for the search direction parameter k . Close-to-optimal values for k for perfect interfaces in the monoscale case are commonly given by [Ladevèze, 1999; Champany, 1996; Champany et al., 1999]:

$$k = \frac{E}{L_\Omega}, \quad (3.6)$$

where E is the Young modulus and L_Ω is a characteristic length of the whole structure. The concept of optimality in the sense of **the search direction operator in the LATIN**

strategy concerns the convergence rate of the strategy itself, but not the results at convergence, hence the robustness of the LATIN method. However it is crucial to remind that this close-to-optimal value is good, in general, only for perfect interfaces, and it is taken $\mathbf{k} = k\mathbf{I}_d$ meaning that the same stiffness is adopted in the three directions, which is the simplest choice (normal to the interface and the two tangential directions).

For frictional contact interfaces this reference choice is good in theory only in presence of sticking conditions, so that the behavior of the contact interface is similar to a perfect interface. When opening of the contact occurs ideally one should have $\mathbf{k} = \mathbf{0}$ for the contact interface: in fact when one of the interfaces in [Figure 3.15](#) is an open contact interface, the “spring distribution” \mathbf{k} on it should allow the interface to open freely. Similarly, when an interface is subjected to a large sliding front, the stiffness in the tangential directions should be lower than the stiffness in the normal direction to allow the interfaces to slide more easily. Nevertheless, for a given problem it is not known a priori where and when there will be sliding and opening conditions, so that in practice the value E/L_Ω is adopted also for frictional contact interfaces. The LATIN will converge regardless, however if there is a large number of contact interfaces in opening, and/or large sliding fronts are present, this can severely affect the convergence rate. A simple method to improve from this point of view may be to adopt a different search direction between normal and tangential direction to a contact interface [[Ribeaucourt et al., 2007](#); [Pierres et al., 2010](#); [Giacoma et al., 2014, 2015](#)]:

$$\mathbf{k} = k_n \mathbf{P}_n + k_t \mathbf{P}_t. \quad (3.7)$$

In problems where large sliding fronts are expected, choosing $k_t < k_n$ may benefit the convergence rate.

Remark 3.2. *Nothing prevents one to make use of a different search direction for each side of an interface $\Gamma_{EE'}$, that is a \mathbf{k}_E and a $\mathbf{k}_{E'}$. Such a choice might be for example beneficial in presence of interfaces between elastically dissimilar subdomains.*

2.4 Local stage for different interface behaviors

■ Displacement boundary conditions

For a displacement \underline{U}_d imposed on $\Gamma_{E,1} = \partial\Omega_E \cap \partial_1\Omega$, taking into account the search direction, the following conditions have to be imposed:

$$\begin{cases} \widehat{W}_E = \underline{U}_d \\ \widehat{F}_E = \underline{F}_E + \mathbf{k}^+ (\widehat{W}_E - \underline{W}_E) \end{cases} \quad (3.8)$$

■ Force boundary conditions

For an imposed force \underline{F}_d on $\Gamma_{E,2} = \partial\Omega_E \cap \partial_2\Omega$, taking into account the search direction, the following conditions have to be imposed:

$$\begin{cases} \widehat{\underline{F}}_E = \underline{F}_d \\ \widehat{\underline{W}}_E = \underline{W}_E + \mathbf{k}^+(\widehat{\underline{F}}_E - \underline{F}_E) \end{cases} \quad (3.9)$$

Remark 3.3. *This way of dealing with boundary conditions in the LATIN is not mandatory. It is frequently used in order to not make distinctions between subdomains at boundaries, subdomains at contact interfaces or subdomains with just perfect interfaces and to treat everything in a unified way. One could however apply directly boundary conditions on the subdomains without passing through boundary interfaces, which would make the values of the applied boundary conditions exact at each iteration. One way to enforce this in the classical LATIN treatment of boundary conditions is to heavily penalize the search direction at boundary interfaces with a penalty α , with for example $\alpha = 10^3$ for displacement boundary conditions or $\alpha = 10^{-3}$ for force boundary conditions. The choice of α has an effect mainly on the initialization, not really on the convergence rate in practice. This comes from the fact that boundary conditions are taken into account in the penalty sense at the first iteration and rapidly converge through the LATIN iterations.*

■ Perfect interfaces

For a perfect interface $\Gamma_{EE'}$, displacement continuity $\widehat{\underline{W}}_E = \widehat{\underline{W}}_{E'}$ and force equilibrium $\widehat{\underline{F}}_E + \widehat{\underline{F}}_{E'} = \underline{0}$ have to be verified. By taking into account the search directions, the following explicit expressions are obtained:

$$\begin{cases} \widehat{\underline{W}}_E = \frac{1}{2}(\underline{W}_E + \underline{W}_{E'} - \mathbf{k}^{+^{-1}}(\underline{F}_E + \underline{F}_{E'})) \\ \widehat{\underline{F}}_E = \underline{F}_E + \mathbf{k}^+(\widehat{\underline{W}}_E - \underline{W}_E) \\ \widehat{\underline{W}}_{E'} = \widehat{\underline{W}}_E \\ \widehat{\underline{F}}_{E'} = -\widehat{\underline{F}}_E \end{cases} \quad (3.10)$$

■ Frictional contact interfaces

For frictional contact interfaces, here small displacements are assumed, which greatly simplifies contact pairing as well as the integration of the frictional contact conditions.

In the local stage for frictional contact interfaces we have to find forces and displacements verifying a behavior that is unknown a priori. A classic method consists in assuming a certain contact status (opening or closed contact, sticking or sliding), make a predictive calculation based on these assumptions and then possibly correct it.

The contact conditions are predicted by means of proper *contact indicators* for the normal and tangential status, with the latter expressed here in form of displacement increments as in [Giacoma et al., 2015; Cardoso, 2019]. Normal contact indicator C_n , and tangential sliding indicator C_t for a contact interface $\Gamma_{EE'}$ at space position \underline{x} and time instant t are defined as follows:

$$\begin{aligned}
 C_n(\underline{x}, t) &:= \frac{1}{2} \left(k_n^+ \left[\underline{n} \cdot (\widehat{W}_{E'} - \widehat{W}_E) + g_0 \right] - \underline{n} \cdot (\widehat{F}_{E'} - \widehat{F}_E) \right); \\
 \underline{C}_t(\underline{x}, t) &:= \frac{1}{2} \left(k_t^+ \mathbf{P}_t \left[\delta \widehat{W}_{E'} - \delta \widehat{W}_E \right] - \mathbf{P}_t (\widehat{F}_{E'} - \widehat{F}_E) \right);
 \end{aligned} \tag{3.11}$$

where we make use of the notation $\delta \square = \square(t) - \square(t - \delta t)$ for the increment of tangential gap between two consecutive time instants. We have introduced the contact indicators distinguishing between normal and tangential search direction (3.7) to be more general.

The contact indicators are defined on unknown quantities of the current local stage, and, by making use of the ascent search directions \mathbf{E}^+ , they can be equivalently written in terms of known quantities of the previous linear stage:

$$\begin{aligned}
 C_n(\underline{x}, t) &= \frac{1}{2} \left(k_n^+ \left[\underline{n} \cdot (\underline{W}_{E'} - \underline{W}_E) + g_0 \right] - \underline{n} \cdot (\underline{F}_{E'} - \underline{F}_E) \right) \\
 \underline{C}_t(\underline{x}, t) &= \frac{1}{2} \left(k_t^+ \mathbf{P}_t \left[\underline{W}_{E'}(t) - \widehat{W}_{E'}(t - \delta t) - [\underline{W}_E(t) - \widehat{W}_E(t - \delta t)] \right] - \mathbf{P}_t (\underline{F}_{E'} - \underline{F}_E) \right)
 \end{aligned}$$

In particular it should be noted that the evaluation of the tangential contact indicator at time instant t requires to know the solution of the local stage at time instant $t - \delta t$. For this reason, **the local stage has to be solved incrementally along the time instants**. Once the contact indicators has been evaluated, contact forces \widehat{F}_E and $\widehat{F}_{E'}$ are updated accordingly, as shown in Table 3.2. Subsequently, interface displacements are found explicitly with the search direction equations:

$$\widehat{W}_E = \underline{W}_E + k^{+-1} (\widehat{F}_E - \underline{F}_E) \quad \text{and} \quad \widehat{W}_{E'} = \underline{W}_{E'} + k^{+-1} (\widehat{F}_{E'} - \underline{F}_{E'}) \tag{3.12}$$

The verification of contact conditions in the local stage of the LATIN is therefore straightforward and completely explicit, and it does not require to solve a local non-linear problem. See Appendix A for more details about the local stage for frictional contact interface with a displacement increment formulation.

Normal contact	
■ <i>open contact</i> : $C_n > 0$	■ <i>closed contact</i> : $C_n \leq 0$
$\hat{\underline{F}}_E = \hat{\underline{F}}_{E'} = \underline{0}$	$\hat{\underline{F}}_E \cdot \underline{n} = -\hat{\underline{F}}_{E'} \cdot \underline{n} = C_n$
Tangential contact: if $C_n \leq 0$	
■ <i>sticking</i> : $\ \underline{C}_t\ < f \underline{n} \cdot \hat{\underline{F}}_E $	■ <i>sliding</i> : $\ \underline{C}_t\ \geq f \underline{n} \cdot \hat{\underline{F}}_E $
$\mathbf{P}_t \hat{\underline{F}}_E = -\mathbf{P}_t \hat{\underline{F}}_{E'} = \underline{C}_t$	$\mathbf{P}_t \hat{\underline{F}}_E = -\mathbf{P}_t \hat{\underline{F}}_{E'} = -f C_n \underline{C}_t / \ \underline{C}_t\ $

Table 3.2: Resolution of the local stage for a frictional contact interface.

2.5 Initialization and control of the convergence

The iterative LATIN algorithm is initialized with an admissible solution $\mathbf{s}_0 \in \mathbf{A}_d^{[0,T]}$. A classical choice is the solution obtained assuming $\hat{\mathbf{s}} = \mathbf{0}$ in **Problem 3.4**, that is, for each substructure:

Problem 3.5 (initialization). Find $(\underline{u}_{0,E}, \underline{W}_{0,E}) \in \mathbf{E}_{E,\text{ad}}^{[0,T]}$ such that, $\forall (\underline{u}^*, \underline{W}^*) \in \mathbf{E}_{E,\text{ad}}^{[0,T]}$

$$\int_{\Omega_E \times [0,T]} \boldsymbol{\varepsilon}(\underline{u}_{0,E}) : \mathbf{K} : \boldsymbol{\varepsilon}(\underline{u}^*) d\Omega dt + \int_{\partial\Omega_E \times [0,T]} \mathbf{k}^- \underline{W}_{0,E} \cdot \underline{W}^* dS dt = \int_{\Omega_E \times [0,T]} \underline{f}_d|_{\Omega_E} \cdot \underline{u}^* d\Omega dt,$$

with $\underline{F}_{0,E} = -\mathbf{k}^- \underline{W}_{0,E}$.

For the monoscale strategy, when the search directions are conjugate $\mathbf{k}^+ = \mathbf{k}^-$, and in presence of perfect interfaces or contact interfaces without friction, the quantity $(\mathbf{s}_{n+1} + \mathbf{s}_n)/2$ converges to $\mathbf{s}_{\text{exact}}$ [Ladevèze, 1999]. In order to make \mathbf{s}_n converge to $\mathbf{s}_{\text{exact}}$, as also to ensure practical convergence for other types of interface behaviors such as frictional contact interfaces, a relaxation step is required after the linear stage, which

is classical for fixed-point like algorithms:

$$\mathbf{s}_{n+1} \leftarrow \mu \mathbf{s}_{n+1} + (1 - \mu) \mathbf{s}_n, \quad (3.13)$$

where $\mu \in]0, 1]$ is the relaxation parameter, generally taken to be 0.8 for a large variety of problems [Ladevèze, 1999].

In order to check the convergence of the LATIN algorithm, one can build LATIN convergence indicators based on the distance between two consecutive solutions belonging to each of the two manifolds. The usual convergence indicator adopted, introduced in [Ladevèze, 1999], is the LATIN indicator:

$$\eta = \sqrt{\frac{\sum_E \|\mathbf{s}_E - \hat{\mathbf{s}}_E\|^2}{\frac{1}{2} \sum_E (\|\mathbf{s}_E\|^2 + \|\hat{\mathbf{s}}_E\|^2)}}, \quad \text{with } \|\mathbf{s}_E\|^2 = \int_{\partial\Omega_E \times [0, T]} (\mathbf{k}^- \underline{W}_E^2 + \mathbf{k}^{-1} \underline{F}_E^2) dS dt. \quad (3.14)$$

The LATIN indicator η (schematically represented in Figure 3.16) characterizes the global distance (i.e., in space and time) between the solution of the linear stage and the one belonging to the local stage for both displacements and interface forces along the search directions, and is evaluated accounting for the whole set of interfaces. When the solution converges to $\mathbf{s}_{\text{exact}}$, the two consecutive iterates merge and the indicator tends to zero.

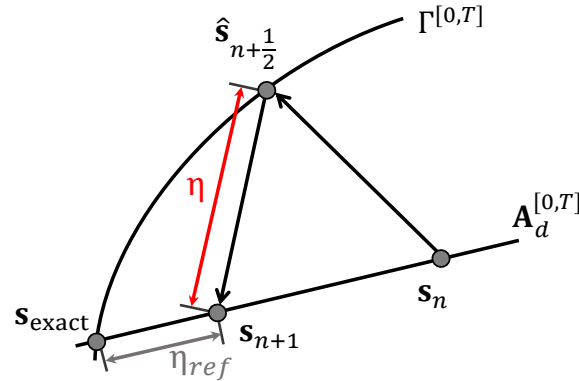


Figure 3.16: Schematic representation of the LATIN indicator η and reference error η_{ref} .

If the exact solution $\mathbf{s}_{\text{exact}}$ of the problem is available, one can compare the evolution of the LATIN indicator η with reference solutions errors η_{ref} (see Figure 3.16) in terms of interface displacements or interface forces, defined as follows:

$$\eta_W = \sqrt{\frac{\sum_E \|\underline{W}_E - \underline{W}_{E,\text{exact}}\|_2^2}{\sum_E \|\underline{W}_{E,\text{exact}}\|_2^2}} \quad \text{and} \quad \eta_F = \sqrt{\frac{\sum_E \|\underline{F}_E - \underline{F}_{E,\text{exact}}\|_2^2}{\sum_E \|\underline{F}_{E,\text{exact}}\|_2^2}}, \quad (3.15)$$

with $\|\square\|_2^2 = \int_{\partial\Omega_E \times [0, T]} \square^2 dS dt$.

The LATIN indicator (3.14) gives an evaluation of the convergence of the problem in a global manner in space and time for all the possible domains and interfaces. It is clear that such a global convergence indicator does not guarantee that the solution has locally converged in space and time. For this reason, one could be also interested in looking for the error at a specific time value t by means of a LATIN time indicator η_t :

$$\eta_t = \sqrt{\frac{\sum_E \|\mathbf{s}_E(t) - \hat{\mathbf{s}}_E(t)\|_{\partial\Omega_E}^2}{\frac{1}{2} \sum_E (\|\mathbf{s}_E(t)\|_{\partial\Omega_E}^2 + \|\hat{\mathbf{s}}_E(t)\|_{\partial\Omega_E}^2)}}, \quad (3.16)$$

with $\|\mathbf{s}_E(t)\|_{\partial\Omega_E}^2 = \int_{\partial\Omega_E} (\mathbf{k}^- \underline{W}_E^2(t) + \mathbf{k}^{-1} \underline{F}_E(t)^2) dS$.

A more strict norm for the LATIN indicator η (3.14) could be used, as for example a sup-norm over all the space-time domain [Ribeaucourt et al., 2007; Giacomini et al., 2015]. However, the previous error indicators are dependent on the search direction \mathbf{k} , and therefore, if \mathbf{k} varies, for a given value of the error the solution may be significantly different. This point is crucial for contact problems where an accurate computation of local contact quantities is required, and it will be discussed and investigated in Chapter 5.

2.6 Application on the 1D test problem

In this section, the monoscale LATIN method presented previously will be applied to the one-dimensional test problem described in Section 1, to highlight strengths of the method and critical points. The benchmark test of Figure 3.1a will be adopted, with the loadcase 1 of Figure 3.1b and the parameters of Table 3.1. Continuous linear shape functions are used for substructure displacement field and piecewise constant shape functions for interface quantities [Ladevèze et al., 2002] (see Appendix B on the discretization of subdomain and interface quantities). We start with the case where only one substructure $\Omega_E = \Omega$, coincident with the space domain, is considered. A reference search direction parameter $k = k_0 = ES/L$ is chosen.

To emphasize the peculiarity of the LATIN to solve the nonlinear problem in a non-incremental manner, the solution obtained for the frictional contact forces, in space and time, along different iterations of the LATIN is shown in Figure 3.17. Already from the first iterations, the algorithm produces a global space-time view of the problem, which is subsequently refined locally along the iterations.

Figure 3.18a shows the evolution of the LATIN indicator η (3.14) along the iterations, compared with the reference errors η_W and η_F (3.15). Displacements and interface forces have roughly the same convergence rate, although, for a fixed number of iterations, the interface forces result less accurate than the displacements, and more critical to make converge. The LATIN indicator, which blends displacements and forces through the search direction \mathbf{k} , presents approximately the same rate of convergence as η_W and

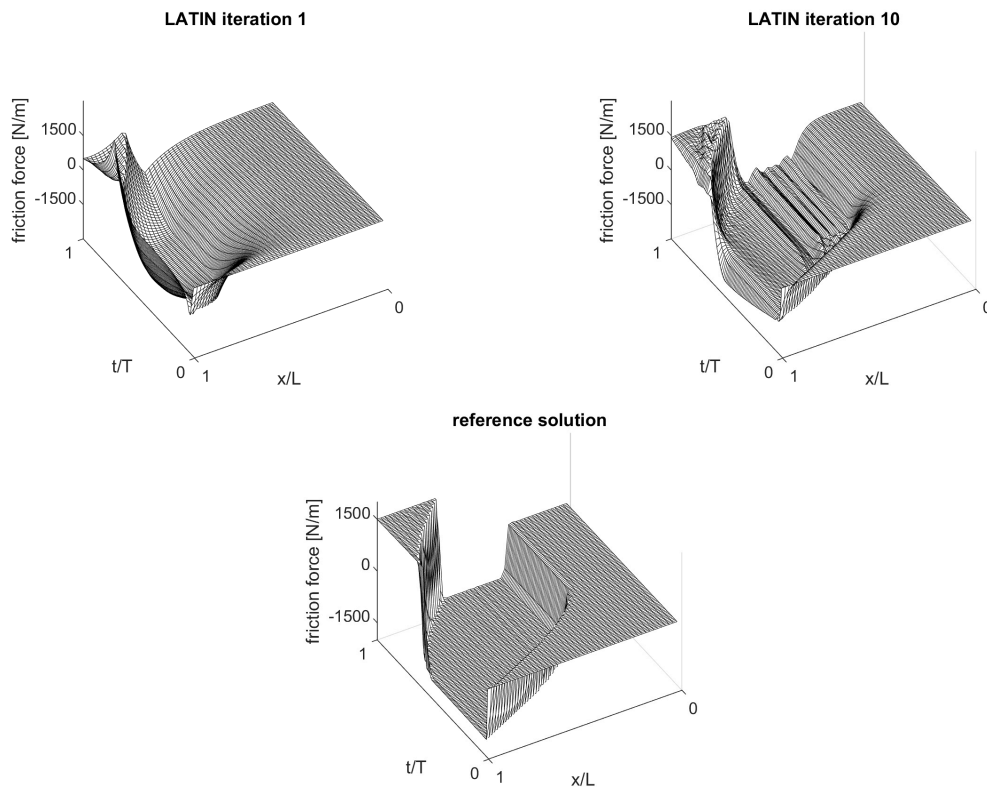


Figure 3.17: Space-time distribution of frictional forces along some LATIN iterations and reference solution.

η_F , and an accuracy for a fixed number of iterations that lies in between the two. In Figure 3.18b is shown the LATIN time indicator η_t (3.16) along the time interval at different iterations. As expected, the error on the different time steps is not uniform.

As mentioned previously, the value of the parameter k that one makes use of in the LATIN algorithm affects the convergence rate of the problem, but not the result at convergence, which renders the method strongly robust for whatever complex loading and any number of frictional contact interfaces. The results in Figure 3.19a show how different values of k affect the convergence rate of the algorithm. The optimal search direction parameter k for frictional contact problems, which guarantees the best convergence rate, is not known a priori since it depends on the particular problem.

It is crucial also to evaluate the influence of the search direction parameter k on the quality of a converged solution. In Figure 3.19b is shown a snapshot of the frictional forces distribution at time $t = 0.5$ s of the problem solved with three different values of the search direction parameter, $k = k_0 = ES/L$, $k = 0.1 k_0$ and $k = 10 k_0$, until reaching a LATIN convergence indicator threshold of $\eta_0 = 10^{-3}$.

A good convergence indicator should provide solutions of comparable quality whatever the value of the search direction adopted, for a fixed value of the convergence threshold. In this case one can notice that for a given convergence threshold η_0 , the

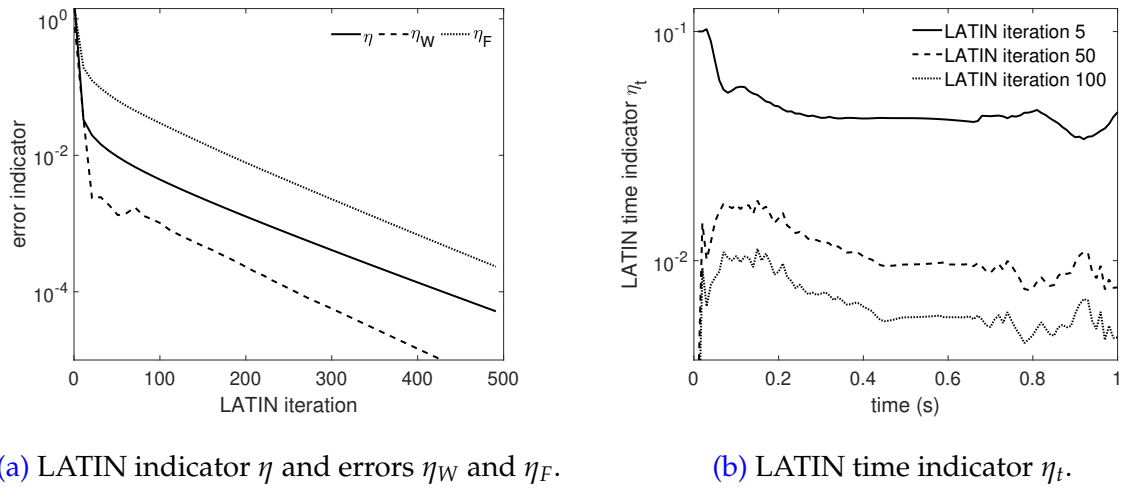


Figure 3.18: LATIN convergence and error indicators.

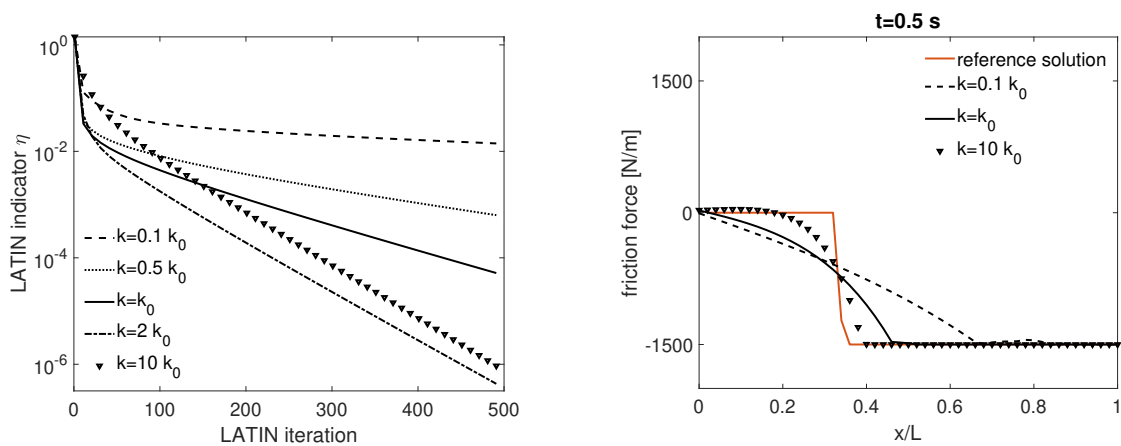


Figure 3.19: Influence of the search direction parameter k .

solutions provided for different values of the search directions are quite different. In particular, **the error concerns mostly the accurate identification of the sticking-sliding transition zones**.

A monostructure case of the problem was considered in previous results. The LATIN, however, naturally leads to a monoscale domain decomposition method. Let us consider how the solution of the original problem, with load case 1, behaves by partitioning it into substructures, as in Figure 3.20. To each substructure is assigned the same spatial discretization of Table 3.1. For this numerical scalability study, the

ratio h/H is kept constant and equal to $1/50$, where h is the element size and H the substructure size. Each substructure is linked to the neighbouring ones through perfect interfaces. Note that by using piecewise constant shape functions for the contact interface quantities, no multiple constraint problem arises at nodes where perfect interfaces are introduced.

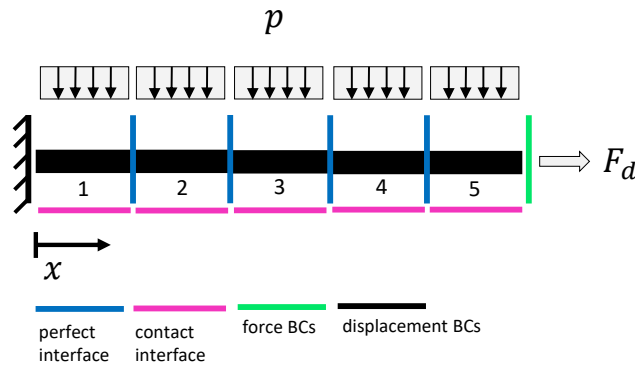
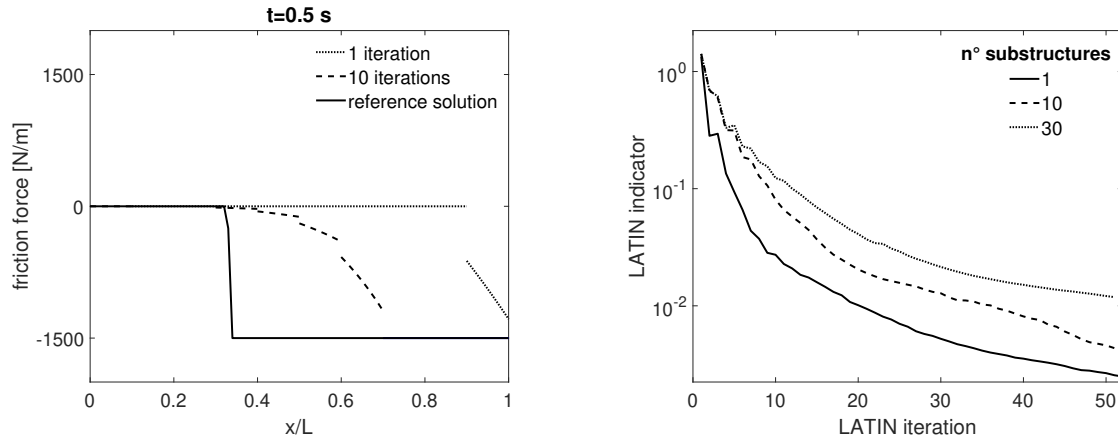


Figure 3.20: Substructured 1D problem into 5 substructures, with respective numbering.

Figure 3.21a shows, in the case of 10 substructures, the frictional forces distribution at time $t = 0.5$ s along some iterations of the LATIN. The monoscale nature of the approach allows the exchange of information only between neighboring substructures. In the first iteration, only the substructure directly subject to the external load (load case 1 here) sees the effect of the loading. The influence of the external load is then slowly propagated to the remaining substructures iteration after iteration, which causes a decrease of the convergence rate with the number of substructures (Figure 3.21b). This domain decomposition strategy is clearly not numerically scalable.



(a) Frictional forces solution at time $t = 0.5$ s with 10 substructures with the monoscale LATIN-DDM. (b) Influence of the number of substructures on the convergence rate of the monoscale LATIN-DDM.

Figure 3.21: Monoscale LATIN-DDM applied to the substructured 1D problem represented in Figure 3.20.

3 Solving linear stage problems with PGD

The linear stage of the LATIN algorithm, as described in Section 2, consists in solving independently, for each substructure Ω_E , a linear problem on the whole space-time domain. For this reason, it is suitable for model-order reduction based on the separation of variables. In particular, a priori model reduction based on the PGD [Nouy, 2010] can be introduced in the linear stage of the LATIN method in order to speed up the computations [Ladevèze, 1999; Ladevèze and Nouy, 2003; Ladevèze et al., 2010].

3.1 Linear stage with corrections

First of all, starting from the initial linear elastic solution \mathbf{s}_0 given by Problem 3.5, let us write the solution \mathbf{s}_{n+1} at the current iteration as a correction with respect to the previous iteration solution, that is

$$\mathbf{s}_{n+1} = \mathbf{s}_n + \Delta \mathbf{s}. \quad (3.17)$$

Given the linearity of the equations pertaining to the manifold $\mathbf{A}_d^{[0,T]}$, the E -admissibility conditions can be equivalently written, for each substructure Ω_E , in terms of corrections:

Definition 3.2 (E-admissibility to zero). $\Delta \mathbf{s}_E = (\Delta \underline{u}_E, \Delta \underline{W}_E, \Delta \underline{\sigma}_E, \Delta \underline{F}_E) \in \mathbf{S}_E^{[0,T]}$ is said to be E-admissible to zero, that is $\Delta \mathbf{s}_E \in \mathbf{S}_{E,ad,0}^{[0,T]}$, if it verifies:

- the kinematic admissibility to zero: $(\Delta \underline{u}_E, \Delta \underline{W}_E) \in \mathbf{E}_{E,ad,0}^{[0,T]} \mid \exists \Delta \underline{u}_E \in \mathcal{U}_E^{[0,T]}$ such that $\Delta \underline{u}_E|_{\partial\Omega_E} = \Delta \underline{W}_E$,
- the static admissibility to zero: $(\Delta \underline{\sigma}_E, \Delta \underline{F}_E) \in \mathbf{F}_{E,ad,0}^{[0,T]} \mid \forall (\underline{u}^*, \underline{W}^*) \in \mathbf{E}_{E,ad,0}^{[0,T]}$

$$\int_{\Omega_E \times [0,T]} \Delta \underline{\sigma}_E : \boldsymbol{\varepsilon}(\underline{u}^*) d\Omega dt = \int_{\partial\Omega_E \times [0,T]} \Delta \underline{F}_E \cdot \underline{W}^* dS dt,$$

- the constitutive relation: $\Delta \underline{\sigma}_E = \mathbf{K} : \boldsymbol{\varepsilon}(\Delta \underline{u}_E)$.

Similarly, the search direction equation \mathbf{E}^- at the current iteration $n + 1$ can be equivalently written as

$$\Delta \underline{F}_E + \mathbf{k}^- \Delta \underline{W}_E - \underline{\delta}_E = \underline{0}, \quad (3.18)$$

with the quantity

$$\underline{\delta}_E = \widehat{\underline{F}}_E + \mathbf{k}^- \widehat{\underline{W}}_E - (\underline{F}_{E,n} + \mathbf{k}^- \underline{W}_{E,n}), \quad (3.19)$$

that we will call *search direction residual*, known at the current iteration, and which depends on the previous local and linear stage.

By taking into account kinematic and static admissibility to zero and the constitutive relation, the equivalent problem in terms of corrections to be solved at the linear stage is the following linear problem:

Problem 3.6 (linear stage with corrections). Find $(\Delta \underline{u}_E, \Delta \underline{W}_E) \in \mathbf{E}_{E,ad}^{[0,T]}$ such that, $\forall (\underline{u}^*, \underline{W}^*) \in \mathbf{E}_{E,ad}^{[0,T]}$

$$\int_{\Omega_E \times [0,T]} \boldsymbol{\varepsilon}(\Delta \underline{u}_E) : \mathbf{K} : \boldsymbol{\varepsilon}(\underline{u}^*) d\Omega dt = \int_{\partial\Omega_E \times [0,T]} \Delta \underline{F}_E \cdot \underline{W}^* dS dt,$$

with $\Delta \underline{F}_E + \mathbf{k}^- \Delta \underline{W}_E - \underline{\delta}_E = \underline{0}$.

Since the search direction is a parameter of the strategy and an exact verification of it is not mandatory for the convergence of the strategy, one can think of solving the previous problem by seeking an admissible solution that verifies the search direction only in weak sense, as follows:

Problem 3.7 (minimization of the error in search direction). Find $(\Delta \underline{u}_E, \Delta \underline{W}_E) \in \mathbf{E}_{E,\text{ad}}^{[0,T]}$ such that, $\forall (\underline{u}^*, \underline{W}^*) \in \mathbf{E}_{E,\text{ad}}^{[0,T]}$,

$$\int_{\Omega_E \times [0,T]} \boldsymbol{\varepsilon}(\Delta \underline{u}_E) : \mathbf{K} : \boldsymbol{\varepsilon}(\underline{u}^*) d\Omega dt = \int_{\partial\Omega_E \times [0,T]} \Delta \underline{F}_E \cdot \underline{W}^* dS dt,$$

with $(\Delta \underline{W}_E, \Delta \underline{F}_E) = \arg \min_{(\Delta \underline{W}_E, \Delta \underline{F}_E) \in \mathbf{S}_{E,\text{ad},0}^{[0,T]}} \|\Delta \underline{F}_E + \mathbf{k}^- \Delta \underline{W}_E - \underline{\delta}_E\|_2^2$.

3.2 Separated representation of the unknowns during the linear stage

A progressive construction of space-time functions for PGD is classically used [Nouy, 2010], and consists in looking for a separated representation solution of Problem 3.7 for the corrections of forces and displacements, that is:

$$\begin{aligned} \Delta \underline{u}_E &= \underline{z}_E(\underline{x}) \lambda_E(t) \quad \text{on } \Omega_E \times [0, T]; \\ \Delta \underline{W}_E &= \underline{Z}_E(\underline{x}) \lambda_E(t) \quad \text{on } \partial\Omega_E \times [0, T]; \\ \Delta \underline{F}_E &= \underline{G}_E(\underline{x}) \psi_E(t) \quad \text{on } \partial\Omega_E \times [0, T]; \end{aligned} \quad (3.20)$$

where $\lambda_E, \psi_E \in \mathcal{J} = \mathcal{L}_{[0,T]}^2$ and time functions of $\Delta \underline{u}_E$ and $\Delta \underline{W}_E$ are taken equal for kinematic admissibility.

By injecting the separated representations (3.20) in Problem 3.7, and by making use of trial functions $\underline{u}^* = \underline{z}_E^* \lambda_E + \underline{z}_E \lambda_E^*$ and $\underline{W}^* = \underline{Z}_E^* \lambda_E + \underline{Z}_E \lambda_E^*$ belonging to $\mathbf{E}_{E,\text{ad},0}^{[0,T]}$, one obtains the following two conditions to be satisfied in order for the separated representations (3.20) to be admissible:

$$\forall \lambda_E^* \in \mathcal{J},$$

$$\int_{[0,T]} \lambda_E \lambda_E^* dt \int_{\Omega_E} \boldsymbol{\varepsilon}(\underline{z}_E) : \mathbf{K} : \boldsymbol{\varepsilon}(\underline{z}_E) d\Omega = \int_{[0,T]} \psi_E \lambda_E^* dt \int_{\partial\Omega_E} \underline{G}_E \cdot \underline{Z}_E dS; \quad (3.21)$$

$$\forall (\underline{z}_E^*, \underline{Z}_E^*) \in \mathbf{E}_{E,\text{ad},0},$$

$$\int_{\Omega_E} \boldsymbol{\varepsilon}(\underline{z}_E) : \mathbf{K} : \boldsymbol{\varepsilon}(\underline{z}_E^*) d\Omega \int_{[0,T]} \lambda_E^2 dt = \int_{\partial\Omega_E} \underline{G}_E \cdot \underline{Z}_E^* dS \int_{[0,T]} \lambda_E \psi_E dt. \quad (3.22)$$

In Eq. (3.22), the space $\mathbf{E}_{E,\text{ad},0}$ is the space of kinematic admissibility to zero for functions not depending on time, such as space modes \underline{z}_E , \underline{Z}_E and \underline{G}_E . Similarly, in the following, $\mathbf{S}_{E,\text{ad},0}$ will indicate the E -admissibility to zero for space modes (see Definition 3.2).

From Eq. (3.21) the arbitrary of λ_E^* enables one to say that, up to a multiplicative constant,

$$\forall t \in [0, T], \quad \psi_E(t) = \lambda_E(t). \quad (3.23)$$

On the other hand, from Eq. (3.22), the following admissibility condition between space modes of forces and displacements holds:

$$\forall (\underline{z}_E^*, \underline{Z}_E^*) \in \mathbf{E}_{E,\text{ad},0}, \quad \int_{\Omega_E} \boldsymbol{\varepsilon}(\underline{z}_E) : \mathbf{K} : \boldsymbol{\varepsilon}(\underline{z}_E^*) d\Omega = \int_{\partial\Omega_E} \underline{G}_E \cdot \underline{Z}_E^* dS. \quad (3.24)$$

The two conditions (3.23) and (3.24) have to be satisfied by the time and space modes of the separated representation of the current linear stage in order for it to belong to the admissible space $\mathbf{A}_d^{[0,T]}$ of the LATIN algorithm. However, with such an admissible separated representation, the search direction equation (3.18), which can be rewritten as $(\underline{G}_E + \mathbf{k}^- \underline{Z}_E) \lambda_E - \underline{\delta}_E = \underline{0}$, **cannot be strictly verified since $\underline{\delta}_E$ is not in a separated format**.

3.3 Finding a new pair of modes

The admissibility conditions (3.23) and (3.24) guarantee that the separated representation lies in the admissible space $\mathbf{A}_d^{[0,T]}$. However, the search direction can be verified only in a weak sense. Since the search direction is a parameter of the strategy, it does not need to be verified accurately, but sufficiently nevertheless, for the strategy to converge:

Problem 3.8 (enrichment stage). Find $(\underline{Z}_E, \underline{G}_E) \in \mathbf{S}_{E,\text{ad},0}$ and $\lambda_E \in \mathcal{J}$ minimizing the error in search direction

$$(\underline{Z}_E, \underline{G}_E, \lambda_E) = \arg \min_{(\underline{G}_E, \underline{Z}_E, \bar{\lambda}_E) \in \mathbf{S}_{E,\text{ad},0} \times \mathcal{J}} \|(\underline{G}_E + \mathbf{k}^- \underline{Z}_E) \bar{\lambda}_E - \underline{\delta}_E\|_2^2. \quad (3.25)$$

In order to solve the above defined problem, an auxiliary mixed space mode, defined on the boundary $\partial\Omega_E$, is introduced [Giacoma et al., 2015]:

$$\underline{L}_E := \underline{G}_E + \mathbf{k}^- \underline{Z}_E. \quad (3.26)$$

Subsequently, the minimization Problem 3.8 is solved for \underline{L}_E and λ_E with a fixed point iterative strategy, shown in Algorithm 5, where we arbitrarily choose to normalize space modes. The first step consists in computing \underline{L}_E knowing λ_E from the previous iteration. Then, the second step consists in updating λ_E knowing \underline{L}_E from the first step. After few iterations (two or three are usually enough), \underline{L}_E and λ_E are no more

significantly updated and the process is stopped [Nouy, 2010]. Then, by making use of admissibility condition (3.24) one can retrieve the admissible \underline{z}_E , \underline{Z}_E and \underline{G}_E space modes from \underline{L}_E .

Algorithm 5: Enrichment stage: new pair of PGD modes

■ **initialization:** $\lambda_E(t) = 1$

for $n = 1$ to n_{\max} **do**

- compute space mode: $\underline{L}_E = \int_{[0,T]} \underline{\delta}_E \lambda_E dt / \int_{[0,T]} \lambda_E^2 dt$
 - compute time mode: $\lambda_E = \int_{\partial\Omega_E} \underline{\delta}_E \cdot \underline{L}_E dS / \int_{\partial\Omega_E} \underline{L}_E^2 dS$
 - normalize space mode: $\underline{L}_E \leftarrow \underline{L}_E / \|\underline{L}_E\|$
 - amplify time mode: $\lambda_E \leftarrow \lambda_E \|\underline{L}_E\|$
-

Therefore $\underline{\delta}_E$ is approximated as

$$\underline{\delta}_E = \widehat{\underline{F}}_E + \mathbf{k}^- \widehat{\underline{W}}_E - (\underline{F}_{0,E} + \mathbf{k}^- \underline{W}_{0,E} + \sum_{k=1}^{p+1} \underline{L}_{E,k} \lambda_{E,k}) \quad (3.27)$$

and solution fields, which are admissible, can be written in a separated representation as:

$$\begin{aligned} \underline{u}_E &= \underline{u}_{0,E} + \sum_{k=1}^{p+1} \underline{z}_{E,k} \lambda_{E,k} \\ \underline{W}_E &= \underline{W}_{0,E} + \sum_{k=1}^{p+1} \underline{Z}_{E,k} \lambda_{E,k} \\ \underline{F}_E &= \underline{F}_{0,E} + \sum_{k=1}^{p+1} \underline{G}_{E,k} \lambda_{E,k} \end{aligned} \quad (3.28)$$

with $p + 1$ being the current PGD basis size after the enrichment stage.

The minimization in **Problem 3.8**, since the substructure is linear and search directions only concern interface quantities, is defined in space on the substructure boundary. When generating new modes the most costly part concerns the generation of space modes due to the admissibility condition (3.24) which requires the resolution of a problem in space of the size of the substructure. For this reason, prior to adding a new pair of modes in the enrichment stage, if a given basis of p modes $\{\underline{L}_{E,k}, \lambda_{E,k}\}_{k=1}^p$ is available a preliminary updating of time modes can be performed by keeping fixed the space modes, as shown in **Problem 3.9**. The updating stage consists in a cheap projection onto the current PGD basis and, since space modes are fixed (i.e., they are already admissible), there is no need to verify admissibility condition for the p space modes.

Problem 3.9 (preliminary updating stage). Find $\Delta\lambda_{E,k} \in \mathcal{J}$, $k = 1, \dots, p$ minimizing the error in search direction

$$\{\Delta\lambda_{E,k}\}_{k=1}^p = \arg \min_{\Delta\bar{\lambda}_{E,k} \in \mathcal{J}} \left\| \sum_{k=1}^p \underline{L}_{E,k} \bar{\lambda}_{E,k} - \underline{\delta}_E \right\|_2^2, \quad (3.29)$$

and subsequently update time modes $\{\lambda_{E,k}\}_{k=1}^p \leftarrow \{\lambda_{E,k}\}_{k=1}^p + \{\Delta\lambda_{E,k}\}_{k=1}^p$.

The updating stage largely improves the quality of the PGD representation [Nouy, 2010]. After the updating stage, if the quality of the representation is not satisfactory, one proceeds to add a new pair (or more) of modes. This step is crucial. In fact for a better efficiency of the method it is necessary to create the minimum amount of modes and to avoid the creation of redundant and unnecessary ones.

Remark 3.4. Since nonlinearities are confined only to interfaces, search directions have been introduced only for interface quantities, resulting into a simple interface residual minimization for the generation of a new mode. For more general nonlinear problems where nonlinearities can also occur within the substructures, search directions have to be introduced for quantities defined on both interfaces and substructures resulting into a more involved formulation. For material nonlinearities interested readers can refer to [Nouy, 2003; Nouy and Ladevèze, 2004; Passieux et al., 2010].

3.4 Controlling the size and quality of the PGD basis

A generally adopted enrichment criterion (e.g., in [Giacoma et al., 2015]) used to decide whether to add or not a new pair of modes is the one based on the LATIN indicator stagnation. Given the LATIN indicator η at the previous iteration, and $\tilde{\eta}$ after the updating stage (Problem 3.9), a new pair of modes is added if the following stagnation criterion is satisfied:

$$\theta = \frac{\eta - \tilde{\eta}}{\eta} < \theta_0. \quad (3.30)$$

However, this indicator is poorly suited for frictional contact problems. In fact, as shown in Figure 3.19a, the convergence rate of the LATIN is mainly driven by the search direction k . Since in the presented formulation admissibility is exactly verified and only the search direction is approximated (see Problem 3.8), after a certain point adding new modes will not improve the convergence rate, which is driven by k , and new useless modes would be consistently added.

A more appropriate criterion is naturally based on the definition of the separated representation itself, according to Problem 3.8. In fact, what one approximates is the quantity $\underline{\delta}_E$ at every iteration (see Eq. (3.25)). For this reason, it is natural to choose

a criterion based on the accuracy of the approximated search direction [Nouy and Ladevèze, 2004]:

$$\zeta = \frac{\|\underline{\delta}_E - \tilde{\underline{\delta}}_E\|_2}{\|\underline{\delta}_E\|_2} > \zeta_0, \quad (3.31)$$

where $\tilde{\underline{\delta}}_E = \hat{\underline{F}}_E + \mathbf{k}^- \hat{\underline{W}}_E - (\underline{F}_{0,E} + \mathbf{k}^- \underline{W}_{0,E} + \sum_{k=1}^p \underline{L}_{E,k} (\lambda_{E,k} + \Delta\lambda_{E,k}))$ is the approximation of the search direction after the updating stage by keeping constant the space basis $\{\underline{L}_{E,k}\}_{k=1}^p$.

In both cases, a threshold of 0.1 is commonly adopted. In the θ -criterion (3.30), this corresponds to a decrease of the LATIN indicator by a factor less than 10%, while, in the ζ -criterion (3.31), it corresponds to an approximation of the search direction with a relative error more than 10%.

A reasonable enrichment criterion is crucial for the PGD basis not to grow uncontrollably in size, loosing effectiveness of the method. For highly non-regular phenomena like frictional contact problems it is challenging to create progressively a ROB of the smallest size possible to ensure a given accuracy, that is to be close to the SVD basis of the final solution. The progressively found PGD modes may be highly redundant even when performing the updating stage and the basis size may increase in size with modes which add little to no contribution to the representation accuracy.

This problem may be reduced for example by performing a Gram–Schmidt orthonormalization for the space modes each time a new couple is found with the enrichment stage and then deciding whether or not to accept the new couple based on the residual norm of the spatial mode after the orthonormalization process. However, even after orthonormalization of space modes, redundancy may still occur on time modes and this approach was proven ineffective to control the basis size in PGD contexts [Alameddine et al., 2019].

A different approach that can be adopted is to perform a full SVD computation of the solution after each enrichment step and taking the most significant modes as basis for the next iteration. Less expansive methods could make use of SVD updating techniques [Bunch and Nielsen, 1978; Brand, 2006] or randomized SVD [Alameddine et al., 2019]. However these methods aim at computing precisely the SVD of the solution throughout the iterations of the LATIN with an effort which may be not worthwhile knowing that the solution may be far from convergence. In [Giacoma et al., 2015], in the context of frictional contact problems with monoscale LATIN, an iterative downsizing algorithm has been proposed to decrease the size of the LATIN-PGD basis throughout the iterations while maintaining the quality of the solution. At convergence the algorithm is equivalent to an SVD, however, since it is not required to compute exactly the SVD, few iterations (1 or 2) of the algorithm at each LATIN iteration are sufficient for the purpose. For more details one can refer to [Giacoma et al., 2015] and [Giacoma et al., 2016].

3.5 Application on the 1D test problem

Here, the LATIN-PGD strategy is applied to the resolution of the benchmark problem illustrated [Figure 3.1a](#), with the loadcase 1 of [Figure 3.1b](#) and the parameters of [Table 3.1](#). The monostructure case $\Omega_E = \Omega$ is considered. The goal is to study deeply the PGD only.

First, the LATIN-PGD algorithm with the θ enrichment criterion (3.30), with $\theta_0 = 0.1$, is considered. A first strategy consists in adding a new pair of modes any time the enrichment criterion (3.30) is satisfied after the updating stage (LATIN-PGD(θ)), without making use of sorting algorithms for the PGD basis. A second strategy consists in performing also a Gram–Schmidt orthonormalization of the space modes any time a new pair of modes is added (LATIN-PGD(θ)+GS), and a third one consists in performing an additional downsizing stage (see [Appendix D](#)) for the PGD basis at each LATIN iteration (LATIN-PGD(θ)+D). In the LATIN-PGD(θ)+D strategy, a single iteration of the downsizing algorithm presented in [[Giacoma et al., 2015](#)] is performed at each LATIN iteration, and a threshold $\epsilon = 10^{-4}$ is chosen for the mode rejection.

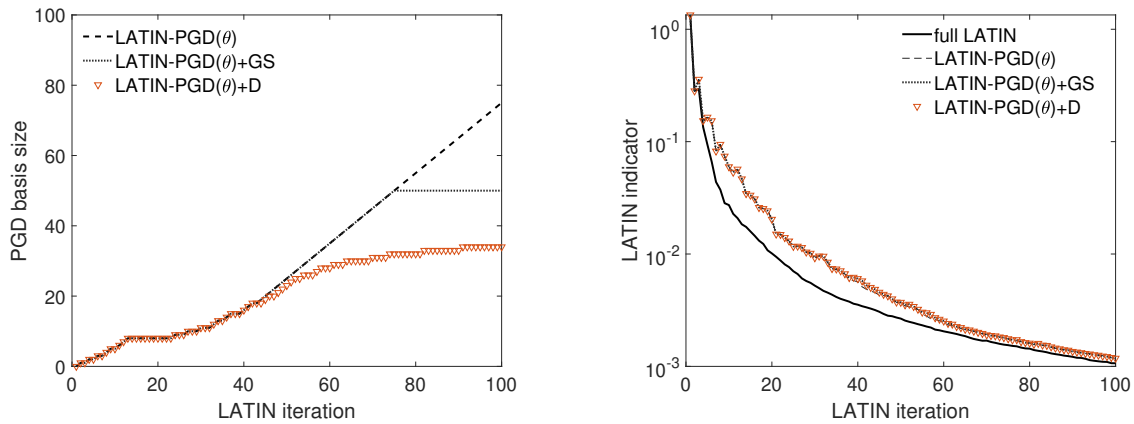
The different strategies investigated throughout the manuscript and their properties are reported in [Table 3.3](#). We consider to add at most one pair of modes after the updating stage. In fact, more pairs of modes can be added at each LATIN iteration, however adding more modes leads to increase the PGD basis with unnecessary modes when far from convergence.

LATIN-PGD strategies			
Strategy	ROB enrichment criterion	ROB sorting algorithm	Comments
full LATIN	-	-	no PGD
LATIN-PGD(θ)	θ -criterion (3.30)	-	no ROB sorting algorithm
LATIN-PGD(θ)+GS	θ -criterion (3.30)	Gram–Schmidt	only space modes are sorted
LATIN-PGD(θ)+D	θ -criterion (3.30)	downsizing (Appendix D)	low-cost SVD algorithm [Giacoma et al., 2015]
LATIN-PGD(ζ)	ζ -criterion (3.31)	-	no ROB sorting algorithm
LATIN-PGD(ζ)+D	ζ -criterion (3.31)	downsizing (Appendix D)	low-cost SVD algorithm [Giacoma et al., 2015]

[Table 3.3](#): Different LATIN-PGD strategies investigated throughout the manuscript.

Figure 3.22a shows the evolution of the PGD basis size along the LATIN iterations by making use of the three different strategies described previously. Regarding the LATIN-PGD(θ), the basis size largely exceeds the original size of the problem (considering the problem size in space variable, a maximum of 50 modes is required for an exact evaluation of the quantities, see Figure 3.10a). Given the particular behavior of the LATIN convergence indicator, with a high rate in the first iterations (almost independent from the search direction parameter k) and a lower rate in the subsequent iterations (controlled by the value of k), the θ -criterion generates less modes in the first part and more modes in the second one. However, since the convergence rate in this second part is driven by the search direction parameter k , most of the generated modes will be useless.

The curve in Figure 3.22a of the LATIN-PGD(θ)+D confirms the previous hypothesis on the useless modes generated. In fact, the downsizing algorithm does not reduce the size of the basis in the first part of the LATIN iterations, while, after a certain point (approximately after iteration 40, where the LATIN indicator curve changes slope), most of the newly added modes are rejected. The final size of the downsized basis lays between 30 and 40 modes, which is the size required for the contact quantities to be accurately represented (see Figure 3.10a). Finally, the LATIN-PGD(θ)+GS shows to be uneffective to control the basis size, as it just limits the basis size not to exceed the size of the problem.



(a) Basis size along the LATIN iterations of the LATIN-PGD(θ), LATIN-PGD(θ)+GS and LATIN-PGD(θ)+D. (b) LATIN convergence indicator for full LATIN, LATIN-PGD(θ), LATIN-PGD(θ)+GS and LATIN-PGD(θ)+D.

Figure 3.22: Convergence curves and PGD basis analysis for the LATIN-PGD(θ) strategies.

Figure 3.22b shows the behaviour of the LATIN indicator for the full LATIN (i.e., without PGD) and the different LATIN-PGD(θ) strategies. The high slope initial convergence is oscillating and not well captured, while the second part of the curve, where

a new mode is generated almost systematically, is more uniform and tends to the full LATIN curve. The convergence curves of the different LATIN-PGD(θ) strategies described are in practice coincident, since the goal of ROB sorting methods is to control the size of the progressively built PGD basis without losing appreciable accuracy.

The relevance of the PGD basis along the LATIN iterations with the LATIN-PGD(θ)+D can be easily visualized by making use of the Modal Assurance Criterion (MAC) diagrams [Pastor et al., 2012] between the PGD modes and the SVD modes. Shortly, given two sets of vectors of the same dimension $\{\mathbf{X}_i\}_{i=1}^p$ and $\{\mathbf{Y}_j\}_{j=1}^p$, the MAC matrix \mathbf{M} is defined as:

$$\mathbf{M}_{ij} = \frac{|\mathbf{X}_i^T \mathbf{Y}_j|^2}{\|\mathbf{X}_i\|^2 \|\mathbf{Y}_j\|^2} \in [0, 1]. \quad (3.32)$$

\mathbf{M}_{ij} measures the correlation between mode \mathbf{X}_i and mode \mathbf{Y}_j . $\mathbf{M}_{ij} = 1$ means that the modes are collinear, that is highly correlated, otherwise $\mathbf{M}_{ij} = 0$ means that the modes are orthogonal, that is highly uncorrelated.

Here the purpose is to evaluate along the iterations of the LATIN how the algorithm is capable of approximating the SVD. To do this, at every LATIN iteration n a full SVD of the linear stage solution \underline{W}_n for the displacements, \underline{E}_n for frictional forces and $\underline{E}_n + \mathbf{k}^{(-)} \underline{W}_n$ for the mixed quantity is computed and compared respectively to downsized PGD modes for displacements $\{\underline{Z}_{E,k}\}$, contact forces $\{\underline{G}_{E,k}\}$ and the auxiliary mixed modes $\{\underline{L}_{E,k}\}$ (see Eq. (3.26) for auxiliary mode definition) by making use of the MAC criterion definition (3.32).

Figure 3.23 displays the MAC diagram for the auxiliary mixed modes, and in Figure 3.24 and Figure 3.25 are displayed the MAC diagrams of displacement and frictional forces modes (that we recall are obtained with a post-processing knowing $\{\underline{L}_{E,k}\}$ from the admissibility condition of Eq. (3.24)). The downsizing algorithm, applied to the auxiliary mixed modes $\{\underline{L}_{E,k}\}$, provides along the iterations a quasi-optimal basis correlated to the SVD (as shown in [Giacoma et al., 2015]). The resultant correlation for space modes $\{\underline{Z}_{E,k}\}$ and $\{\underline{G}_{E,k}\}$ is still good but not as accurate as for $\{\underline{L}_{E,k}\}$.

Nevertheless, the PGD strategy is based on the approximation of the search direction through space modes $\{\underline{L}_{E,k}\}$, from which the admissible space modes $\{\underline{Z}_{E,k}\}$ and $\{\underline{G}_{E,k}\}$ are obtained through the solution of a problem in space at the substructure level. Although applying downsizing to the $\{\underline{L}_{E,k}\}$ basis is cheap, after the process, to compute the downsized space basis $\{\underline{Z}_{E,k}\}$ and $\{\underline{G}_{E,k}\}$ of displacements and frictional forces, Eq. (3.24) must be solved again for all the basis and this step may be expensive. It is therefore clear that the most important thing is to choose a relevant enrichment criterion, and a proper strategy, which enable to generate relevant modes and reduce the generation of redundant and useless ones.

Let us consider now the LATIN-PGD(ξ) strategy by making use of the ξ criterion (3.31), with $\xi_0 = 0.1$ and without resorting to orthonormalization or downsizing.

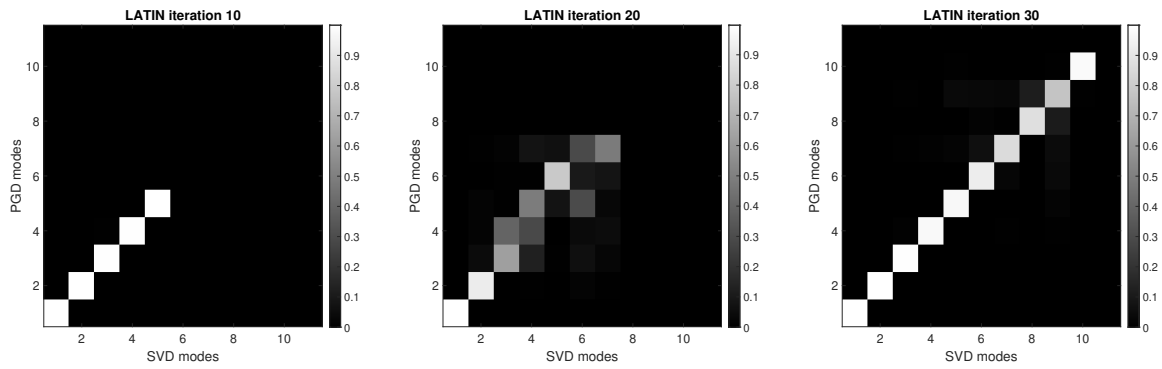


Figure 3.23: MAC diagrams for auxiliary space modes $\{\underline{L}_{E,k}\}$ along the iterations of the LATIN method.

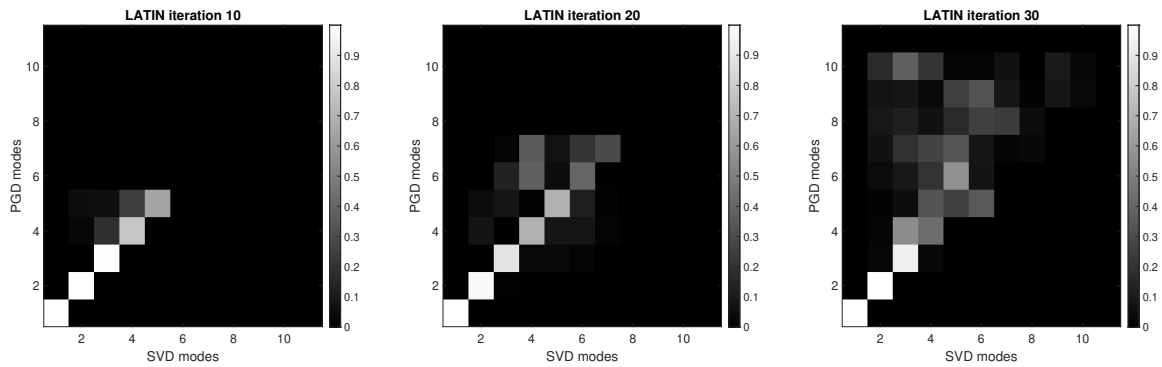


Figure 3.24: MAC diagrams for displacement space modes $\{\underline{Z}_{E,k}\}$ along the iterations of the LATIN method.

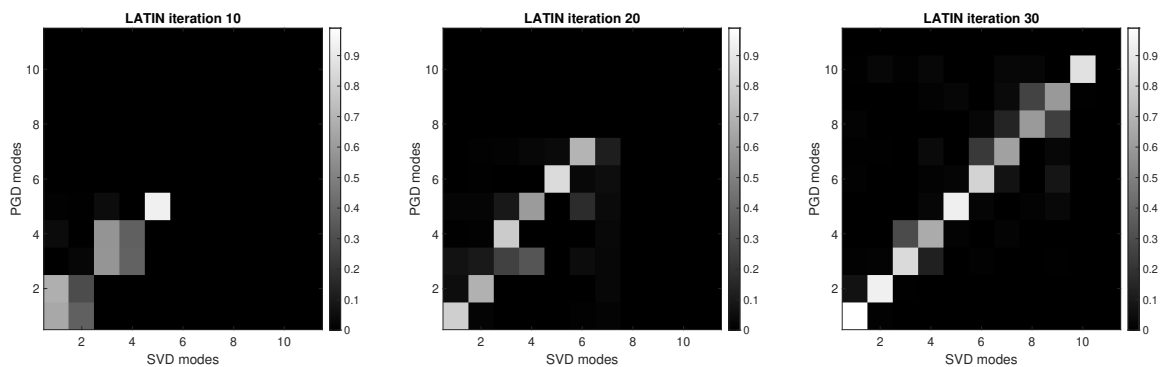


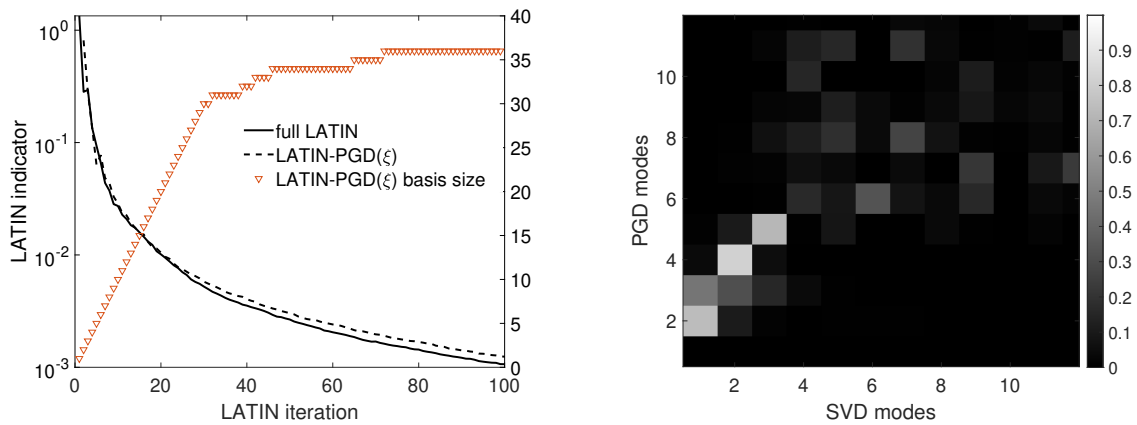
Figure 3.25: MAC diagrams for contact force space modes $\{\underline{G}_{E,k}\}$ along the iterations of the LATIN method.

Figure 3.26a shows the LATIN-PGD(ξ) strategy convergence indicator and basis size along the LATIN iterations. In this case, the evolution of the PGD basis along the iterations is different from the LATIN-PGD(θ). More modes are created in the first

iterations, where the LATIN convergence indicator rate is higher and there is a large variation in the solution from one iteration to another. Afterwards, the contact quantities converge locally slowly and for several LATIN iterations there is no need to enrich the ROB. The LATIN indicator behaves accordingly: a perfect match in the first part of the convergence curve with respect to the full LATIN indicator, and a very good match in the second part. Remarkably, the size of the PGD basis remains limited, and the final size is in the range of the one obtained previously by means of the LATIN-PGD(θ)+D strategy, which corresponds to the range in which the contact forces are accurately approximated (Figure 3.10a).

The progressively built PGD basis, in this case, is not correlated with the SVD, as it can be seen from Figure 3.26b for the auxiliary mixed modes $\{\underline{L}_{E,k}\}$. However, it can be noticed that the very first modes have a good correspondence with the first structural modes of the SVD, while subsequent ones, more related to local corrections, are more dispersed and harder to capture optimally. This is because, in the analyzed case, a monostructure case $\Omega_E = \Omega$ was considered and, as seen in Section 1, higher-order modes carry localized corrections in different areas of the structure according to sticking/sliding conditions.

As suggested in [Giacoma et al., 2015], a multiscale strategy may be useful in this context, with the coarse/macroscale problem quickly capturing the solution at the global scale, and the model-order reduction technique (here PGD) then being able to capture microscopic/local variations in the solution more effectively.



(a) LATIN convergence indicator and the PGD basis size for the LATIN-PGD(ξ) strategy. (b) MAC correlation matrix for auxiliary mixed modes $\{\underline{L}_{E,k}\}$ for the LATIN-PGD(ξ) strategy.

Figure 3.26: Convergence curve and PGD basis analysis for the LATIN-PGD(ξ) strategy.

4 Conclusions

The chapter started with the analysis of a one-dimensional frictional benchmark problem in [Section 1](#). Although significantly much simpler than the real application envisaged, the problem allowed to draw significative insights about the approaches to be used to tackle such problems. The space and time modes of the reference solution of the tested problem showed some similarities with the SVD of a real test case analyzed in [Chapter 2](#), in particular for the space modes that present distinctions between the sticking and sliding zones. For this reason, a domain decomposition method that separates sticking and sliding zones can be efficient in our case. The reducibility confirms that for the target application, consisting in small oscillations around a preloaded state, there is good potential for reducibility since contact conditions do not vary significantly. From this simplified case the lower reducibility of frictional contact forces compared to displacements obtained from the wire rope results in [Chapter 2](#) has also been recovered.

The need to solve frictional contact problems through a reduced model accurately enough for a fatigue analysis led us to consider the LATIN nonlinear solver due to its robustness and flexibility.

The LATIN solver is described in [Section 2](#). When applied to frictional contact problems the LATIN shares similarities with augmented Lagrangian methods, this allows for an accurate computation of contact quantities and a general robustness of the method, i.e., it generally converges to the solution although the speed of convergence depends on the choice of search directions.

The main features of the LATIN method were analyzed through the one-dimensional benchmark contact problem, by selecting a severe load case with long propagation of sticking/sliding front, intended to represent a simplified model of a wire of the wire rope under tension and bending. The fundamental property of LATIN to generate a complete space-time solution at each iteration was highlighted, as well as the importance of the search direction parameter. It has been pointed out that the convergence rate of the problem depends on the search direction, and finding an optimal search direction for evolutionary frictional contact problems is challenging. The search direction also influences the value of the usually adopted LATIN convergence indicator. The global space-time nature of LATIN makes it difficult to accurately control locally the error, as errors can propagate in time, highlighting the **importance of a proper convergence indicator when an accurate identification of sliding fronts is required**.

In addition, the LATIN allows for a simple treatment of domain decomposition even in the presence of friction contact interfaces. It was shown that the “monoscale” treatment of domain decomposition allows an exchange of information only between neighboring subdomains, reducing the efficiency of the method and its scalability according to the number of subdomains. This clearly shows the need to introduce a coarse scale problem in the monoscale strategy, as presented in the next [Chapter 4](#).

Finally, given the peculiarity of LATIN to generate solutions in the entire space

and time domain, the introduction of model reduction based on the PGD is natural in the LATIN scheme and was discussed in [Section 3](#). In this context **it is important to ensure that the progressively built PGD basis does not grow uncontrollably in size, otherwise a general loss of efficiency of the method is expected**. For this reason a particular attention was put on the generation of new modes and the control of the quality and size of the basis. It has been emphasized that the PGD does not drive the convergence rate in the LATIN, as it is mainly by the search direction k . Therefore, to control the quality and size of the PGD basis, the choice of a proper enrichment criterion is crucial. Additional ROB sorting algorithms can be used, and among these the downsizing algorithm is particularly effective in controlling the quality and size of the reduced basis creating along the iterations of the LATIN a reduced basis close to the SVD. However, their cost can be non-negligible, especially when dealing with larger problems and numerous subdomains, as we will see in the next [Chapter 4](#).

The next chapter will discuss a multiscale strategy to model reduction for friction contact problems and its benefits to the different points and limits highlighted in this chapter, that is the loss of scalability when making use of substructuring, the need to control the size of the basis size while still being accurate locally, and the separation of scales at the structural level and the local level of the interfaces.

Chapter 4

A multiscale strategy to model-order reduction for frictional contact problems

This chapter presents the multiscale strategy to model reduction for frictional contact problems, and represents the second part of the article [Zeka et al., 2024a]. Multiscale aspects are introduced in the LATIN framework at the interface level, where a separation of scales between macroquantities and microquantities is operated. This scale separation is intended to put in place a fine description in the frictional contact areas of interest while maintaining a coarser description in the rest of the structure. Thereafter the introduction of PGD in the multiscale framework is described. The coarse scale problem of the multiscale strategy allows to efficiently capture the mechanical behavior at the scale of the structure, then focusing on capturing local contact variations at contact interfaces with local reduced-order bases. The most important features of the approach are shown comprehensively on a 1D benchmark problem introduced in [Chapter 3](#). Then, its robustness and effectiveness are tested on a two-dimensional layered structure with wide frictional contact interfaces with multiple complex loadings.

Contents

1	Introduction of a multiscale strategy at the level of the interfaces	143
1.1	Definition of the macroquantities	144
1.2	Choice of the macrospace	145
1.3	Admissibility of macroquantities	146

2	The multiscale strategy within the LATIN framework	147
2.1	Microproblem on a substructure	149
2.2	The macroproblem over Ω	150
2.3	Search directions in the multiscale strategy	151
2.4	The final algorithm	151
2.5	Resolution of microproblems with PGD	152
3	Application to the 1D benchmark problem	154
4	Application to a layered structure with wide contact interfaces	156
4.1	Problem setting	156
4.2	Analysis of the solution	158
4.3	Introduction of PGD	160
4.4	Analysis of the computational cost	163
5	Conclusions	166

Multiscale methods in mechanics are often based on the resolution of a coarse scale problem on the structure obtained by homogenizing in some manner the underlying microstructure or by means of preconditioning techniques. In this manner the overall behavior of the structure is represented by a reduced number of degrees of freedom and, to represent details at lower scale, local refinements are necessary.

Most multiscale strategies involve the principle of homogenization on Representative Volume Elements (RVE), with a mathematical framework given by the theory of asymptotic homogenization [Sánchez-Palencia, 1980]. Extensions have been also developed in the context of nonlinear problems [Suquet, 1987; Ponte Castañeda, 1996]. One of the most used among these techniques is the concurrent multiscale FE^2 [Feyel and Chaboche, 2000], which has recently gained attention thanks to the acceleration possibilities offered by modern data-driven techniques [Masi and Stefanou, 2022; Rocha et al., 2023].

The described homogenization techniques allow to operate a transition from the microscale to the macroscale from studies at the microscopic scale of the RVE. What we are interested to consists instead in superimposing to the solution of a macroscopic problem a local refinement on the interested zones. Among others one can cite the Arlequin method [Ben Dhia, 1998], the hierarchical Dirichlet projection method [Zohdi et al., 1996; Oden et al., 1999] or multigrid methods [Brandt, 1981].

The domain decomposition methods described in Chapter 1 equipped with a dedicated coarse scale problem also belong to this class of techniques. In primal and dual approaches, a coarse scale solution due to rigid body modes of the subdomains is computed as initialization, and the remaining micropart is sought iteratively through a projected algorithm which ensures that the micropart remains orthogonal to the rigid modes.

In the mixed DDM based on the LATIN the philosophy is a bit different, as the multiscale aspects are introduced at the interface level and not at subdomain level. The coarse scale problem is here built from a reduced set of macroquantities at the interfaces and the construction of a homogenized operator per subdomain. The LATIN macroquantities are endowed with a strong mechanical sense according to de Saint-Venant's principle, as their information is sufficient to express the interaction with sufficiently distant subdomains.

1 Introduction of a multiscale strategy at the level of the interfaces

In this section, the main features of the multiscale strategy of the mixed DDM based on the LATIN are recalled. For further details the interested reader can refer to [Ladevèze et al., 2002; Ladevèze and Nouy, 2003; Ladevèze et al., 2007].

1.1 Definition of the macroquantities

The multiscale strategy is introduced in space at the interface level, in contrast with most of the multiscale approaches. The interface unknowns (interface displacements and forces) are additively split, prior to any discretization, into

$$\mathbf{s} = \mathbf{s}^M + \mathbf{s}^m, \quad (4.1)$$

with \mathbf{s}^M being the set of macroscopic quantities (or macroquantities) and \mathbf{s}^m the complementary set of microscopic ones (or microquantities). The definition of the macroscale is independent of the underlying discretization and is defined by the characteristic length of the interfaces, which is a priori greater than the discretization on the microscale.

Let us consider an interface $\Gamma_{EE'}$. One may freely choose the spaces $\mathcal{F}_{EE'}^{[0,T],M}$ and $\mathcal{W}_{EE'}^{[0,T],M}$ in which the macroforces and macrodisplacements are sought, provided that the work bilinear form

$$\langle \underline{W}, \underline{F} \rangle \mapsto \int_{\Gamma_{EE'} \times [0,T]} \underline{F} \cdot \underline{W} dS dt \quad (4.2)$$

in macroquantities is non-degenerate [Ladevèze and Nouy, 2003]:

Proposition 4.1.

$$\left\{ \underline{F}^M \in \mathcal{F}_{EE'}^{[0,T],M}, \int_{\Gamma_{EE'} \times [0,T]} \underline{F}^M \cdot \underline{W}^{M*} dS dt = 0, \forall \underline{W}^{M*} \in \mathcal{W}_{EE'}^{[0,T],M} \right\} = \{0\}$$

$$\left\{ \underline{W}^M \in \mathcal{W}_{EE'}^{[0,T],M}, \int_{\Gamma_{EE'} \times [0,T]} \underline{W}^M \cdot \underline{F}^{M*} dS dt = 0, \forall \underline{F}^{M*} \in \mathcal{F}_{EE'}^{[0,T],M} \right\} = \{0\}$$

In practice **Proposition 4.1** requires the spaces $\mathcal{W}_{EE'}^{[0,T],M}$ and $\mathcal{F}_{EE'}^{[0,T],M}$ to be of the same size. **The definition of the macroquantities in the LATIN framework follows a strongly physically sound approach: the macroquantities are averages in space of interface forces and displacements.** More specifically, they are determined as the best approximations in the sense of the work bilinear form (4.2) on the interface and thanks to **Proposition 4.1** they are uniquely defined:

Definition 4.1 (macroquantities). The macroquantities $(\underline{W}^M, \underline{F}^M) \in \mathcal{W}_{EE'}^{[0,T],M} \times \mathcal{F}_{EE'}^{[0,T],M}$ of $(\underline{W}, \underline{F}) \in \mathcal{W}_{EE'}^{[0,T]} \times \mathcal{F}_{EE'}^{[0,T]}$ are defined by the following expressions:

$$\underline{W}^M \in \mathcal{W}_{EE'}^{[0,T],M}, \int_{\Gamma_{EE'} \times [0,T]} (\underline{W}^M - \underline{W}) \cdot \underline{F}^{M*} dSdt = 0, \forall \underline{F}^{M*} \in \mathcal{F}_{EE'}^{[0,T],M},$$

$$\underline{F}^M \in \mathcal{F}_{EE'}^{[0,T],M}, \int_{\Gamma_{EE'} \times [0,T]} (\underline{F}^M - \underline{F}) \cdot \underline{W}^{M*} dSdt = 0, \forall \underline{W}^{M*} \in \mathcal{W}_{EE'}^{[0,T],M}.$$

The microquantities are therefore given by:

Definition 4.2 (microquantities). The microquantities $(\underline{W}^m, \underline{F}^m) \in \mathcal{W}_{EE'}^{[0,T],m} \times \mathcal{F}_{EE'}^{[0,T],m}$ of $(\underline{W}, \underline{F}) \in \mathcal{W}_{EE'}^{[0,T]} \times \mathcal{F}_{EE'}^{[0,T]}$ are given by:

$$\underline{W}^m = \underline{W} - \underline{W}^M \text{ and } \underline{F}^m = \underline{F} - \underline{F}^M,$$

and they are consequently uncoupled in the following energetic sense:

$$\int_{\Gamma_{EE'} \times [0,T]} \underline{F} \cdot \underline{W} dSdt = \int_{\Gamma_{EE'} \times [0,T]} \underline{F}^M \cdot \underline{W}^M dSdt + \int_{\Gamma_{EE'} \times [0,T]} \underline{F}^m \cdot \underline{W}^m dSdt. \quad (4.3)$$

We can define the spaces $\mathcal{F}_E^{[0,T],M} = \prod_{E' \in \mathbf{v}_E} \mathcal{F}_{EE'}^{[0,T],M}$ and $\mathcal{W}_E^{[0,T],M} = \prod_{E' \in \mathbf{v}_E} \mathcal{W}_{EE'}^{[0,T],M}$ extended to the set of neighboring interfaces of Ω_E , as well as spaces $\mathcal{F}^{[0,T],M}$ and $\mathcal{W}^{[0,T],M}$ extended to the set of all subdomains. A similar consideration for the microquantities leads to spaces $\mathcal{F}_E^{[0,T],m}$, $\mathcal{W}_E^{[0,T],m}$, $\mathcal{F}^{[0,T],m}$ and $\mathcal{W}^{[0,T],m}$.

1.2 Choice of the macrospace

As seen in [Section 2.6 of Chapter 3](#), the domain decomposition method based on the LATIN without a coarse scale problem is not scalable since the information is only transmitted between neighboring subdomains. To ensure extensibility in the multiscale approach it is necessary that the macrospace $\mathcal{W}_E^{[0,T],M}$ contains at least the rigid body modes of the boundary $\partial\Omega_E$ and that $\mathcal{F}_E^{[0,T],M}$ contains at least the resultants in forces and moments of the loading acting on $\partial\Omega_E$ [[Ladevèze and Dureisseix, 2000](#); [Ladevèze et al., 2001](#); [Loiseau, 2001](#)].

After these considerations, let us denote with $\{e_i^M(\underline{x})\}_{i=1,\dots,n_M}$ a spatial basis on $\Gamma_{EE'}$ of size n_M for the macrospace $\mathcal{W}_{EE'}^{[0,T],M}$ and $\mathcal{F}_{EE'}^{[0,T],M}$, considered to be identical. We can therefore write:

$$\begin{aligned}
 \underline{W}^M &= \mathbf{P}_{\Gamma_{EE'}}^M(\underline{W}) = \sum_{i=1}^{n_M} (\underline{W}, \underline{e}_i^M) \underline{e}_i^M(\underline{x}); \\
 \underline{F}^M &= \mathbf{P}_{\Gamma_{EE'}}^M(\underline{F}) = \sum_{i=1}^{n_M} (\underline{F}, \underline{e}_i^M) \underline{e}_i^M(\underline{x}).
 \end{aligned} \tag{4.4}$$

The macroprojector $\mathbf{P}_{\Gamma_{EE'}}^M$ of an interface $\Gamma_{EE'}$ extracts the rigid body modes of $\Gamma_{EE'}$ as well as the resultant in force and the moments, duals of such kinematics, of the loading acting on $\Gamma_{EE'}$. In practice, in order for the macrobasis to capture at least the rigid body kinematics of an interface, a minimum size $n_M = 6$ for the macrobasis is required in 3D ($n_M = 3$ in 2D). Considering only a rigid body kinematics as macro-scale at the interface level however represents a very poor macroscopic information. What is usually done is to enrich the kinematics of the macrobasis, for example by considering the interface as a deformable body instead of a simple rigid body.

In practice one classically chooses for \underline{F}^M and \underline{W}^M affine functions in space variable over $\Gamma_{EE'}$. A classical choice of affine macrobasis functions $\{\underline{e}_i^M(\underline{x})\}_{i=1,\dots,4}$ is represented in [Figure 4.1](#) for a 2D straight interface, it contains the rigid body motions of the interface (two translations and rotation) and the linear elongation of the interface [[Ladevèze and Dureisseix, 2000](#); [Ladevèze et al., 2001](#)]. These quantities are mean values with regard to space and enable to represent in particular interface rigid body modes and resultants and moments at the interfaces.

Remark 4.1. *An affine macrobasis is usually sufficient for the macroquantities to provide useful information when near-to-interface heterogeneity is low. However, in the presence of strong heterogeneity mismatch between subdomains or crack-type interfaces, such a choice may not optimal. One may consider adding higher order components to the macrobasis or resort to a more efficient "spectrum motivated" macrobasis [[Oumaziz et al., 2021](#)] in the first case or a discontinuous macrobasis in the second case [[Guidault et al., 2008](#)].*

1.3 Admissibility of macroquantities

The key feature of the multiscale strategy is that the equilibrium conditions at the interfaces are required to be verified a priori in a macrosense [[Ladevèze et al., 2001](#); [Ladevèze and Nouy, 2003](#)]. The macroforces must be balanced at the interfaces, including the interfaces with boundary conditions. **This choice is suitable for contact interfaces with or without friction**, as balance of interface forces must be verified for every type of interface behavior. The corresponding space is designated by $\mathcal{F}_{\text{ad}}^{[0,T],M}$ and represents the admissibility of \underline{F}^M :

$$\mathcal{F}_{\text{ad}}^{[0,T],M} := \left\{ \underline{F}^M \in \mathcal{F}^{[0,T],M} \mid \forall E \in \mathbf{E}, \forall E' \in \mathbf{V}_E, \underline{F}_E^M + \underline{F}_{E'}^M = \underline{0} \right\}. \quad (4.5)$$

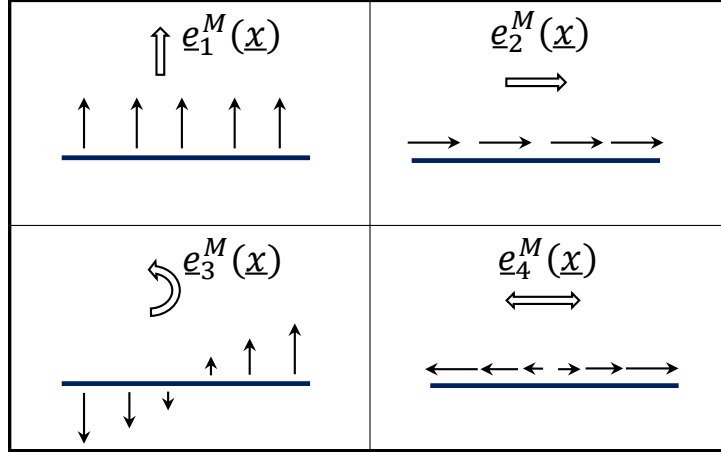


Figure 4.1: Affine macrobasis $\{e_i^M(x)\}_{i=1,\dots,4}$ ($n_M = 4$) for an interface $\Gamma_{EE'}$.

2 The multiscale strategy within the LATIN framework

With reference to the substructured [Problem 3.1](#), the partial verification of the transmission conditions a priori at the interfaces (4.5) leads now to the following partitioning in the LATIN framework:

$$\mathbf{A}_d^{[0,T]}: \left\{ \begin{array}{l} - \text{the } E\text{-admissibility of } \mathbf{s}_E, \forall E \in \mathbf{E} : \mathbf{s}_E \in \mathbf{S}_{E,\text{ad}}^{[0,T]} \text{ (Definition 3.1)} \\ - \text{the admissibility of } \underline{F}^M : \underline{F}^M \in \mathcal{F}_{\text{ad}}^{[0,T],M} \text{ (4.5)} \end{array} \right.$$

$$\Gamma^{[0,T]}: \left\{ - \text{the constitutive behavior of the interfaces (3.3)} \right.$$

The local stage remains unchanged from the one described in [Problem 3.2](#) of [Chapter 3](#). One has to solve a local problem in space for the whole set of interfaces based on known quantities coming from the linear stage. Conversely, in the linear stage, now the a priori balance of the macroforces (4.5) must be also verified. The descent search direction \mathbf{E}^- under a strong form like in [Problem 3.3](#) is not more valid, since \underline{F}_E for each subdomain has to be admissible. These equations for each subdomain are consequently not independent. We therefore write the descent search direction under a weak form under the constraints that the macroforces have to be admissible:

$$\forall \underline{F}^* \in \mathcal{F}^{[0,T],m} \cup \mathcal{F}_{\text{ad}}^{[0,T],M},$$

$$\sum_{E \in \mathbf{E}} \int_{\partial\Omega_E \times [0,T]} \mathbf{k}^{-1} \{ (\underline{F}_E - \widehat{\underline{F}}_E) + (\underline{W}_E - \widehat{\underline{W}}_E) \} \cdot \underline{F}_E^* \, dSdt = 0. \quad (4.6)$$

The constraint (4.5) is enforced at each interface $\Gamma_{EE'}$ through a Lagrange multiplier $\widetilde{W}_{EE'}^M \in \mathcal{W}_{EE'}^{[0,T],M}$. By following [Nouy, 2003], the Lagrange multiplier is then localized at the level of the subdomain, i.e., $\widetilde{W}_E^M \in \mathcal{W}_E^{[0,T],M}$, under the constraint that it is continuous at the interfaces. Therefore the condition (4.6) can be rewritten as follows:

$$\forall \underline{F}^* \in \mathcal{F}^{[0,T]},$$

$$\begin{aligned} \sum_{E \in \mathbf{E}} \int_{\partial\Omega_E \times [0,T]} \{ \mathbf{k}^{-1} (\underline{F}_E - \widehat{\underline{F}}_E) + (\underline{W}_E - \widehat{\underline{W}}_E) \} \cdot \underline{F}_E^* \, dSdt = \\ \sum_{E \in \mathbf{E}} \int_{\partial\Omega_E \times [0,T]} \widetilde{W}_E^M \cdot \underline{F}_E^* \, dSdt, \end{aligned} \quad (4.7)$$

$$\forall \widetilde{W}^{M*} \in \mathcal{W}_{\text{ad},0}^{[0,T],M},$$

$$\sum_{E \in \mathbf{E}} \int_{\partial\Omega_E \times [0,T]} \widetilde{W}_E^{M*} \cdot \underline{F}_E \, dSdt = \sum_{E \in \mathbf{E}} \int_{\partial\Omega_E \cap \partial_2\Omega \times [0,T]} \widetilde{W}_E^{M*} \cdot \underline{F}_d \, dSdt. \quad (4.8)$$

The Lagrange multipliers $\widetilde{W}^M = \{\widetilde{W}_E^M\}_{E \in \mathbf{E}}$ belong to the space $\mathcal{W}_{\text{ad},0}^{[0,T],M}$ of macrodisplacements which are continuous at the interfaces and equal to zero on $\partial_1\Omega$. In the previous equations, (4.7) represents a modified search direction at the interfaces taking into account the admissibility of macroforces, and (4.8) corresponds to the weak form of the macroforce admissibility.

The admissibility of the macroforces (4.8) (or coarse scale problem, macroproblem or reduced interface problem), ensures the propagation of global information throughout the whole set of substructures across the interfaces. The linear stage of the LATIN can then be reformulated as follows:

Problem 4.1 (modified linear stage). Find $\mathbf{s} = \{\mathbf{s}_E\}_{E \in \mathbf{E}} \in \mathbf{A}_d^{[0,T]}$ verifying, $\forall \underline{x} \in \Omega_E$ and $\forall t \in [0, T]$,

- the E -admissibility of \mathbf{s}_E : $\mathbf{s}_E \in \mathbf{S}_{E,\text{ad}}$;
- the modified search direction (4.7);
- the coarse scale problem (4.8).

2.1 Microproblem on a substructure

Taking into account the E -admissibility and the modified search direction (4.7), the following linear problem, called *microproblem*, has now to be solved for each substructure independently:

Problem 4.2 (microproblem on a substructure). Find $(\underline{u}_E, \underline{W}_E) \in \mathbf{E}_{E,ad}^{[0,T]}$ such that, $\forall (\underline{u}^*, \underline{W}^*) \in \mathbf{E}_{E,ad}^{[0,T]}$,

$$\int_{\Omega_E \times [0,T]} \boldsymbol{\varepsilon}(\underline{u}_E) : \mathbf{K} : \boldsymbol{\varepsilon}(\underline{u}^*) d\Omega dt + \int_{\partial\Omega_E \times [0,T]} \mathbf{k}^- \underline{W}_E \cdot \underline{W}^* dS dt =$$

$$\int_{\Omega_E \times [0,T]} \underline{f}_{-d|\Omega_E} \cdot \underline{u}^* d\Omega dt + \int_{\partial\Omega_E \times [0,T]} (\hat{\underline{F}}_E + \mathbf{k}^- \hat{\underline{W}}_E + \mathbf{k}^- \tilde{\underline{W}}_E^M) \cdot \underline{W}^* dS dt,$$

with $\underline{F}_E = \hat{\underline{F}}_E + \mathbf{k}^- (\hat{\underline{W}}_E - \underline{W}_E + \tilde{\underline{W}}_E^M)$.

The solution of **Problem 4.2**, associated with substructure Ω_E , depends only on the known quantities $\underline{f}_{-d|\Omega_E}$, $\hat{\mathbf{s}}_E$ and the unknown Lagrange multiplier $\tilde{\underline{W}}_E^M$ over $\partial\Omega_E$. Since the problem is linear, the following proposition holds:

Proposition 4.2. If \mathbf{K} and \mathbf{k} are symmetric and positive definite, then **Problem 4.2**, defined over Ω_E and its boundary $\partial\Omega_E$, has a unique solution such that

$$\underline{F}_E^M = \mathbf{L}_E^F(\tilde{\underline{W}}_E^M) + \hat{\underline{F}}_{E,d}^M, \quad (4.9)$$

where $\tilde{\underline{W}}_E^M \in \mathcal{W}_E^{[0,T],M}$ and $\hat{\underline{F}}_{E,d}^M$ depends on $\underline{f}_{-d|\Omega_E}$ and $\hat{\mathbf{s}}_E$.

\mathbf{L}_E^F is a linear operator from $\mathcal{W}_E^{[0,T],M}$ onto $\mathcal{F}_E^{[0,T],M}$. It can be interpreted as a homogenized behavior operator over substructure Ω_E which ensures the coupling between the microscale and the macroscale. \mathbf{L}_E^F is in practice evaluated by solving a set of microproblems for a set of loading cases where we take for $\tilde{\underline{W}}_E^M$ the elements of the basis of $\mathcal{W}_E^{[0,T],M}$, with $\underline{f}_{-d|\Omega_E}$ and $\hat{\mathbf{s}}_E$ set to zero [Nouy, 2003; Cremonesi et al., 2013]. If \mathbf{k}^- is constant (and since \mathbf{K} is the constant Hookean operator for linear elasticity), \mathbf{L}_E^F can be precomputed once and for all before starting the iterative process. Since $\tilde{\underline{W}}_E^M$ depends on only a few interface kinematic parameters, the calculation of \mathbf{L}_E^F is obtained at relatively low cost [Ladevèze and Nouy, 2003; Nouy, 2003]. If the Lagrange multiplier $\tilde{\underline{W}}_E^M$ is known, the full solution \mathbf{s}_E can be retrieved. That is to say there exists a localization operator \mathbf{L}_E^s from $\mathcal{W}_E^{[0,T],M}$ onto $\mathcal{S}_E^{[0,T]}$ such that:

$$\mathbf{s}_E = \mathbf{L}_E^s(\tilde{\mathbf{W}}_E^M) + \hat{\mathbf{s}}_{E,d}, \quad (4.10)$$

with $\hat{\mathbf{s}}_{E,d}$ which depends on $f_{-d}|_{\Omega_E}$ and $\hat{\mathbf{s}}_E$.

2.2 The macroproblem over Ω

The Lagrange multiplier $\tilde{\mathbf{W}}^M = \{\tilde{\mathbf{W}}_E^M\}_{E \in \mathbf{E}}$ is found by solving a macroproblem (or coarse scale problem) over all the set of interfaces. The weak form of the static admissibility of macroforces (4.8) and the relation (4.9) lead to the following displacement formulation of the macroproblem in terms of the Lagrange multiplier $\tilde{\mathbf{W}}^M$:

Problem 4.3 (macroproblem). Find $\tilde{\mathbf{W}}^M = \{\tilde{\mathbf{W}}_E^M\}_{E \in \mathbf{E}} \in \mathcal{W}_{\text{ad},0}^{[0,T],M}$ which verifies, $\forall \tilde{\mathbf{W}}^{M*} \in \mathcal{W}_{\text{ad},0}^{[0,T],M}$,

$$\sum_{E \in \mathbf{E}} \int_{\partial\Omega_E \times [0,T]} \tilde{\mathbf{W}}_E^{M*} \cdot (\mathbf{L}_E^F(\tilde{\mathbf{W}}_E^M) + \hat{\mathbf{F}}_{E,d}^M) dS dt = \sum_{E \in \mathbf{E}} \int_{\partial\Omega_E \cup \partial_2\Omega \times [0,T]} \tilde{\mathbf{W}}_E^{M*} \cdot \underline{\mathbf{F}}_d dS dt. \quad (4.11)$$

The problem has a unique solution if $\text{mes}(\partial_1\Omega) \neq 0$ [Nouy, 2003].

The Lagrange multiplier $\tilde{\mathbf{W}}^M$ given by the macroproblem is equal to zero at convergence of the LATIN algorithm when the balance of interface forces is verified. In practice, it tends to zero quickly in the first iterations where the macroquantities are rapidly converged. The macroproblem has a size in space of $\sum_{i=1 \dots n_\Gamma} n_M^{(i)}$, with n_Γ being the total number of interfaces and $n_M^{(i)}$ being the number of macroscopic kinematic unknowns (translations, rotations, extensions) for the interface i . Such kinematics belong to specific classes of continua with affine microstructure [Cosserat and Cosserat, 1909; Eringen, 1966; Mariano, 2002].

Remark 4.2. The macroscale has been introduced only for the space variable, while no macroscale was considered for time variable. When the strategy is multiscale only in space the macroproblem must be solved at each time interval of the fine time partition. When the macroproblem becomes very large this step can become prohibitive in the case of evolution problems with a lot of time steps. Introducing a macroscale in time may then be necessary [Ladevèze and Nouy, 2003], and possibly model-order reduction to solve the macroproblem [Cremonesi et al., 2013].

Remark 4.3. In cases where a large number of interfaces is present and/or the size of the macrobasis is large the macroproblem can become expensive. In this case the

introduction of a third scale (super macroscale) can be beneficial to solve the macroproblem [Loiseau, 2001; Ladevèze and Nouy, 2003; Kerfriden et al., 2009]. In [Loiseau, 2001; Ladevèze and Nouy, 2003] the macroproblem is approximated by introducing a third scale macrokinematics on several third scale macrocells, with the third scale problem which has a smaller size related to the number of macrocells. In [Kerfriden et al., 2009] a BDD solver is used to solve the macroproblem, which has the structure of a primal DDM approach with local homogenized operator per subdomain which plays the role of primal Schur complement of a subdomain. These homogenized operators are gathered/assembled in clusters in order to propose a third scale partitioning.

2.3 Search directions in the multiscale strategy

In the monoscale case, in the context of elastostatics with perfect interfaces, as explained in [Chapter 3](#), the interpretation of k^- , linking interface forces \underline{F}_E to interface displacements \underline{W}_E on $\partial\Omega_E$, is that it corresponds to the stiffness of the complement of Ω_E condensed on $\partial\Omega_E$ (or Schur complement of $\Omega \setminus \Omega_E$). Calculating this optimal operator is costly and in practice, for a homogeneous structure, it is taken $k^- = k^+ = \frac{E}{L_\Omega} \mathbf{I}_d$, with E being the Young modulus and L_Ω being a characteristic length of the structure Ω [[Champaney, 1996](#); [Champaney et al., 1999](#)].

In [[Violeau, 2003](#)] it has been interpreted and optimized the role of the interface search direction parameter k^- , still in the context of elastostatics with perfect interfaces, but in the multiscale case. In the multiscale strategy, since the macrospace contains the resultants and moments of interface forces, by virtue of the de Saint-Venant principle, it was shown that k^- can be calculated by considering only a part of the complementary of Ω_E over a distance of the order of the diameter of Ω_E . Moreover, a rough estimate of this operator approximated by a scalar corresponding to its largest eigenvalue is often sufficient. In practice for each interface it is taken $k^- = k^+ = \frac{E}{L_\Gamma} \mathbf{I}_d$ as a quasi-optimal value, with L_Γ being a characteristic length of the interface.

In the context of evolution problems however, such as for example frictional contact problems, the optimization of this parameter has not yet been addressed. In this case in fact the continuity of displacements at interfaces is not verified, and for problems with opening interfaces or interfaces subjected to wide sliding fronts this reference values may be far from optimal. This point will be investigated in the next [Chapter 5](#).

2.4 The final algorithm

The final algorithm of the LATIN-based multiscale DDM is shown in [Algorithm 6](#). It is an extension of the strategy presented in [Chapter 3](#) for the monoscale case. After the local stage ([Problem 3.2](#)), local stage quantities $\hat{\mathbf{s}}$ are used as boundary loadings to solve a problem at the substructure scale. This is called *microproblem 1*, coincident with the linear stage problem to be solved in the monoscale case ([Problem 3.4](#)). In the multiscale

approach, after solving microproblem 1 for each substructure, the macrocomponent of the interface forces $\widehat{\underline{F}}_{E,d}^M$ are extracted and used to solve the macroproblem (**Problem 4.3**) and to find the Lagrange multiplier $\widetilde{\underline{W}}_E^M$ of each subdomain, which is used as boundary loading to solve the *microproblem 2*. Thus, the linear stage solution is the sum of the solutions of microproblem 1 and microproblem 2.

The resolution of microproblems and the macroproblem at each iteration only involves a reasonable computational cost since the factorization of the linear operator of the microproblems and the assembled homogenized operator can be precomputed before starting the algorithm, especially if these operators are constant.

2.5 Resolution of microproblems with PGD

The introduction of PGD in the multiscale approach to solve the two microproblems is entirely analogous to what was presented in **Section 3 of Chapter 3** for the monoscale case. Starting from an admissible initial solution \mathbf{s}_0 (**Problem 3.5**), the current iteration solution can be expressed as a correction with respect to the previous one: $\mathbf{s}_{n+1} = \mathbf{s}_n + \Delta \mathbf{s}$. Therefore each microproblem of the multiscale strategy can be expressed in terms of corrections as in **Problem 3.6**, as well as the search directions, with

$$\underline{\delta}_{E,1} = \widehat{\underline{F}}_E + \mathbf{k}^- \widehat{\underline{W}}_E - (\underline{F}_{E,n} + \mathbf{k} \underline{W}_{E,n}) \quad (4.12)$$

for microproblem 1, and

$$\underline{\delta}_{E,2} = \mathbf{k}^- \widetilde{\underline{W}}_E^M \quad (4.13)$$

for microproblem 2. The two microproblems share the same PGD basis and the procedure is analogous as the one described in **Section 3 of Chapter 3**, with the only difference that now it is applied to two microproblems.

In microproblem 1, an updating of the time modes is operated with **Problem 3.9** with the given space modes being fixed and, if the ζ enrichment criterion (3.31) is not satisfied, a new pair of modes is added with **Algorithm 5**. Once the first microproblem is solved for each substructure, the macroforces are extracted and the Lagrange multipliers $\widetilde{\underline{W}}^M = \{\widetilde{\underline{W}}_E^M\}_{E \in \mathbb{E}}$ are found through the resolution of the macroproblem (**Problem 4.3**). Then, one proceeds to solve microproblem 2 by updating the current time modes and eventually adding a new pair of modes if the enrichment criterion is not satisfied.

At the start of the multiscale strategy convergence is mainly driven by the macro-quantities, which converge rapidly in the first iterations. Therefore it is reasonable to require the macroquantities to be sufficiently well approximated in the early stages of the iterative process in order to take full advantage of the multiscale strategy. We recall that each microproblem 2 has as a loading the Lagrange multiplier $\widetilde{\underline{W}}_E^M$ on the boundary $\partial\Omega_E$, and that $\widetilde{\underline{W}}_E^M$ belongs to a finite-dimensional space of small size. **Therefore, a**

Algorithm 6: Multiscale LATIN-DDM
■ Preliminary computations
for each substructure Ω_E **do**

 └ – compute homogenized operator \mathbf{L}_E^F and initialize $\mathbf{s}_{0,E}$ ([Problem 3.5](#))

■ LATIN iterations
for $n = 1$ to n_{\max} **do**
■ Local stage: find $\hat{\mathbf{s}}_{n+1/2} \in \Gamma^{[0,T]}$
for each interface $\Gamma_{EE'}$ **do**

 └ – solve interface [Problem 3.2](#) to find $\hat{\mathbf{s}}_E = (\widehat{\mathbf{W}}_E, \widehat{\mathbf{F}}_E)$ (see [2.4](#))

■ Linear stage: find $\mathbf{s}_{n+1} \in \mathbf{A}_d^{[0,T]}$
■ Microproblem 1
for each substructure Ω_E **do**

 – find $(\hat{\mathbf{u}}_{E,d}, \widehat{\mathbf{W}}_{E,d}) \in \mathbf{E}_{E,ad}^{[0,T]}$ such that, $\forall (\underline{\mathbf{u}}^*, \underline{\mathbf{W}}^*) \in \mathbf{E}_{E,ad}^{[0,T]}$,

$$\int_{\Omega_E \times [0,T]} \boldsymbol{\varepsilon}(\hat{\mathbf{u}}_{E,d}) : \mathbf{K} : \boldsymbol{\varepsilon}(\underline{\mathbf{u}}^*) d\Omega dt + \int_{\partial\Omega_E \times [0,T]} \mathbf{k}^- \widehat{\mathbf{W}}_{E,d} \cdot \underline{\mathbf{W}}^* dS dt =$$

$$\int_{\Omega_E \times [0,T]} \underline{\mathbf{f}}_{-d|\Omega_E} \cdot \underline{\mathbf{u}}^* d\Omega dt + \int_{\partial\Omega_E \times [0,T]} (\widehat{\mathbf{F}}_E + \mathbf{k}^- \widehat{\mathbf{W}}_E) \cdot \underline{\mathbf{W}}^* dS dt$$

 – find $\widehat{\mathbf{F}}_{E,d}$ with search direction $\mathbf{E}^-: \widehat{\mathbf{F}}_{E,d} - \widehat{\mathbf{F}}_E + \mathbf{k}^- (\widehat{\mathbf{W}}_{E,d} - \widehat{\mathbf{W}}_E) = \mathbf{0}$

 – compute macroforces $\widehat{\mathbf{F}}_{E,d}^M$
if multiscale **then**
■ Macroproblem:

 – find $\widetilde{\mathbf{W}}^M = \{\widetilde{\mathbf{W}}_E^M\}_{E \in \mathbf{E}} \in \mathcal{W}_{ad,0}^{[0,T],M}$ such that, $\forall \widetilde{\mathbf{W}}^{M*} \in \mathcal{W}_{ad,0}^{[0,T],M}$,

$$\sum_{E \in \mathbf{E}} \int_{\partial\Omega_E \times [0,T]} \widetilde{\mathbf{W}}_E^{M*} \cdot (\mathbf{L}_E^F(\widetilde{\mathbf{W}}_E^M) + \widehat{\mathbf{F}}_{E,d}^M) dS dt = \sum_{E \in \mathbf{E}} \int_{\partial\Omega_E \cup \partial_2\Omega \times [0,T]} \widetilde{\mathbf{W}}_E^{M*} \cdot \underline{\mathbf{F}}_d^M dS dt$$

■ Microproblem 2
for each substructure Ω_E **do**

 – find $(\widetilde{\mathbf{u}}_E, \widetilde{\mathbf{W}}_E) \in \mathbf{E}_{E,ad}^{[0,T]}$ such that, $\forall (\underline{\mathbf{u}}^*, \underline{\mathbf{W}}^*) \in \mathbf{E}_{E,ad}^{[0,T]}$,

$$\int_{\Omega_E \times [0,T]} \boldsymbol{\varepsilon}(\widetilde{\mathbf{u}}_E) : \mathbf{K} : \boldsymbol{\varepsilon}(\underline{\mathbf{u}}^*) d\Omega dt + \int_{\partial\Omega_E \times [0,T]} \mathbf{k}^- \widetilde{\mathbf{W}}_E \cdot \underline{\mathbf{W}}^* dS dt =$$

$$\int_{\partial\Omega_E \times [0,T]} \mathbf{k}^- \widetilde{\mathbf{W}}_E^M \cdot \underline{\mathbf{W}}^* dS dt$$

 – find $\widetilde{\mathbf{F}}_E$ with search direction $\mathbf{E}^-: \widetilde{\mathbf{F}}_E + \mathbf{k}^- (\widetilde{\mathbf{W}}_E - \widetilde{\mathbf{W}}_E^M) = \mathbf{0}$

 – apply relaxation: $\mathbf{s}_{n+1} \leftarrow \mu \mathbf{s}_{n+1} + (1 - \mu) \mathbf{s}_n$

 – compute error indicator η ([3.14](#))

small finite number of modes is sufficient to precisely solve microproblem 2 over all the iterations. For this reason it is reasonable to require a bit more strict enrichment criterion threshold $\zeta_{0,2}$ for microproblem 2 (e.g., $\zeta_{0,2} = 0.01$), and a bit coarser enrichment criterion threshold for microproblem 1 (e.g., $\zeta_{0,1} = 0.1$). Consequently, at the beginning of the iterations, the algorithm tends to generate systematically more modes arising from microproblem 2, so that macroquantities converge quickly and accurately. Thereafter, once a sufficient basis has been formed for the macroquantities, in the following iterations most of the generated modes will be generated from microproblem 1, which converges more slowly and brings more localized corrections.

3 Application to the 1D benchmark problem

The multiscale strategy is applied here to the 1D test problem with load case 1 of [Figure 3.1](#). Substructured cases are considered, as in [Figure 3.20](#), with each substructure assigned the same spatial discretization of [Table 3.1](#).

In [Figure 4.2](#) is shown, for different number of substructures, the behavior of the LATIN indicator η in the monoscale version and in the multiscale one, without resorting to PGD. **The multiscale approach allows for a considerable convergence gain in the first iterations, where macroquantities are rapidly converged. Subsequently, contact quantities are converged to the local microlevel. In this second stage the monoscale and multiscale approach exhibit roughly the same convergence rate since both of them are making converge the quantities at the microlevel, and the convergence rate at the microlevel is mainly driven by the search direction k .**

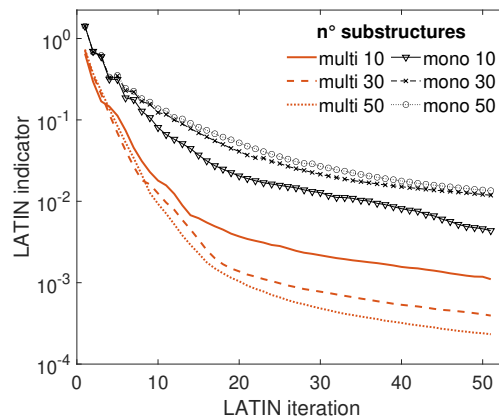


[Figure 4.2](#): Monoscale and multiscale LATIN convergence indicator for different number of substructures.

To highlight the effect of the multiscale strategy on the solution of the problem, in [Figure 4.3](#) is shown, in the case of 10 substructures, the solution for the frictional

forces after 10 iterations of the LATIN method for the monoscale approach and the multiscale one, compared to the reference solution at time $t = 0.5$ s (Figure 4.3a) and $t = 1$ s (Figure 4.3b). Already after few iterations, the multiscale approach succeeds in capturing the global behavior of the problem. Subsequently, further iterations are needed to make converge the microquantities, especially at the sticking-sliding discontinuity zones which need accurate local refinements. The monoscale approach, on the other hand, turns out to be far from the reference solution, with the loading boundary condition still not fully propagated along all the substructures.

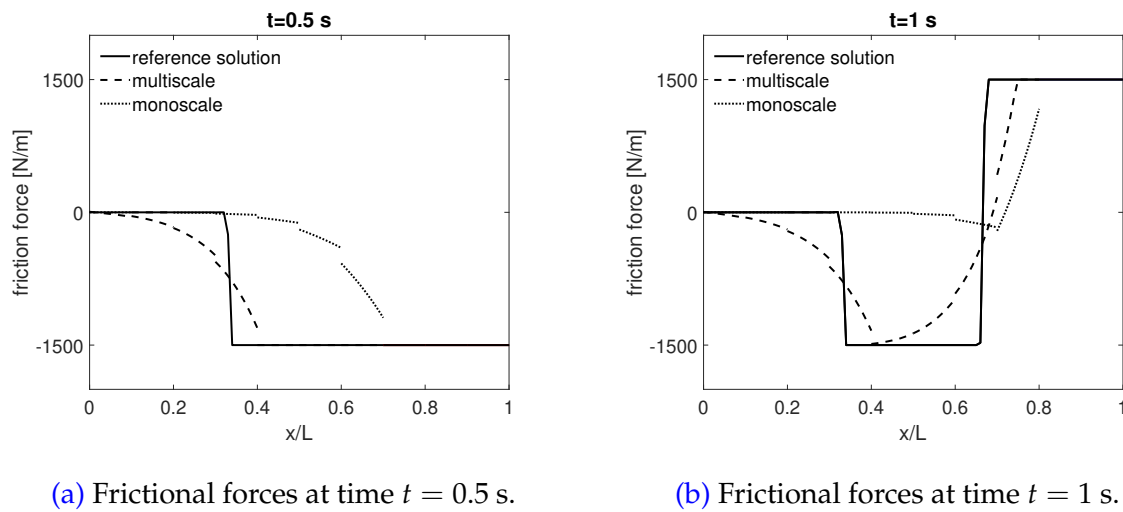
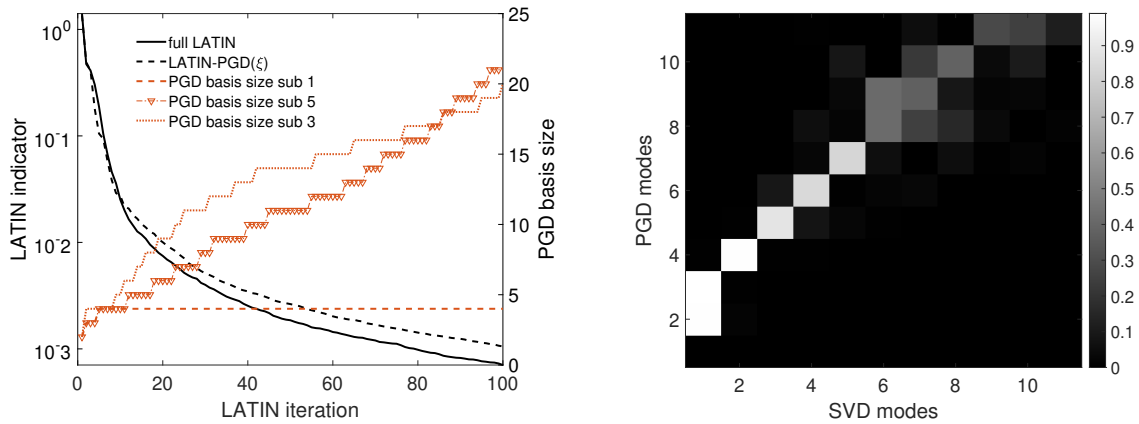


Figure 4.3: Frictional forces distribution after 10 iterations of the full LATIN (without PGD) for the monoscale and the multiscale approach.

The effect of the introduction of the PGD in the multiscale approach is shown in Figure 4.4. By making use of DDM one is able to create local reduced bases per substructure and enrich the basis in the areas with more complex contact conditions, as exemplified in Figure 3.6. In Figure 4.4a, in the case of 5 substructures, is shown the evolution of the PGD basis size for different substructures. An enrichment threshold $\xi_{0,1} = 0.1$ for microproblem 1, and $\xi_{0,2} = 0.01$ for microproblem 2 was adopted as explained in Section 2.5. Different substructures require a different number of modes. For substructure 1, constantly under sticking conditions, the macrobasis is sufficient to capture the solution. Subsequent substructures, on the other hand, require more modes based on the complexity of the sticking-sliding conditions. What is important to remark is that the PGD basis remains in fact limited in size and, in addition, the MAC diagram in Figure 4.4b shows that the first structural modes are roughly well captured by the macroproblem.



(a) LATIN indicator and PGD basis size per substructure. (b) MAC diagram for mixed modes $\{\underline{L}_{Ek}\}$ of substructure 5.

Figure 4.4: Convergence curve and PGD basis analysis for the multiscale LATIN-PGD(ξ) strategy.

4 Application to a layered structure with wide contact interfaces

4.1 Problem setting

In this section, the multiscale strategy is applied to the two-dimensional quasistatic frictional contact problem depicted in Figure 4.5 [Zeka et al., 2024a]. The problem consists of a group of three clamped beams subjected to a constant external pressure p and to time-dependent oscillating traction and shear (which causes bending) loads in correspondence of the free side. Each beam is decomposed internally into 6 substructures, and they are in contact with each other through frictional contact interfaces. The external pressure is constant and equal to 100 MPa, while the external loads evolution in time is represented in Figure 4.6. The parameters of the problem are reported in Table 4.1. Plain strain assumptions are considered, and 8-node quadrilateral elements (QUA8) are adopted for the discretization of the substructures. For the discretization of interface quantities, on the other hand, piecewise constant elements are adopted while satisfying the LBB condition [Ladevèze et al., 2002], with compatible spatial discretizations (see Appendix B).

The test case can be seen as representative of the mechanics of multilayer spiral strand cables, subjected to oscillating traction and bending loads around a preload [Bussolati et al., 2020], with the simplification of neglecting non linear geometry due to bending. We remind that for fretting fatigue the sliding magnitude has a huge effect on the fatigue life expectancy of these structures, with an important decrease around $15 \mu\text{m}$, and then transition between partial sliding in the contact vicinity and large

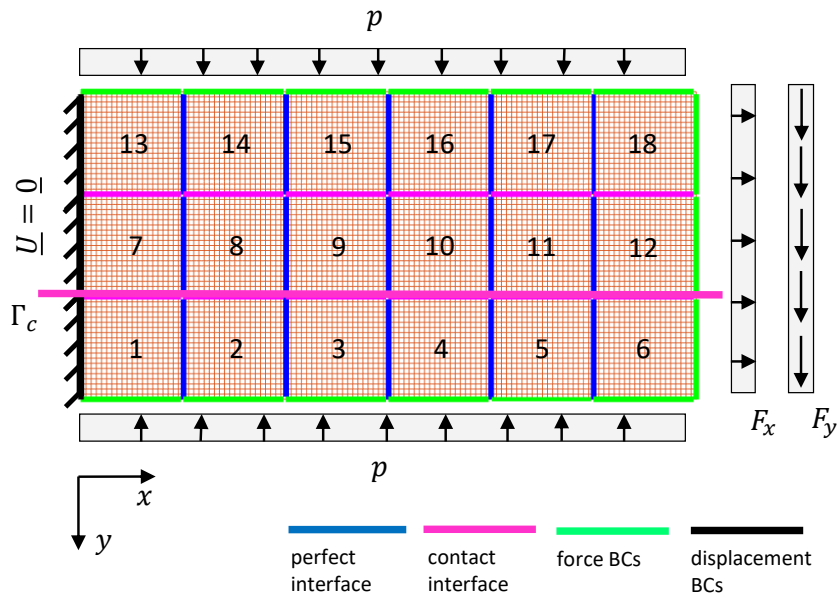


Figure 4.5: Representation of substructures and interfaces, with numbering of the substructures and highlight of the contact interface Γ_c .

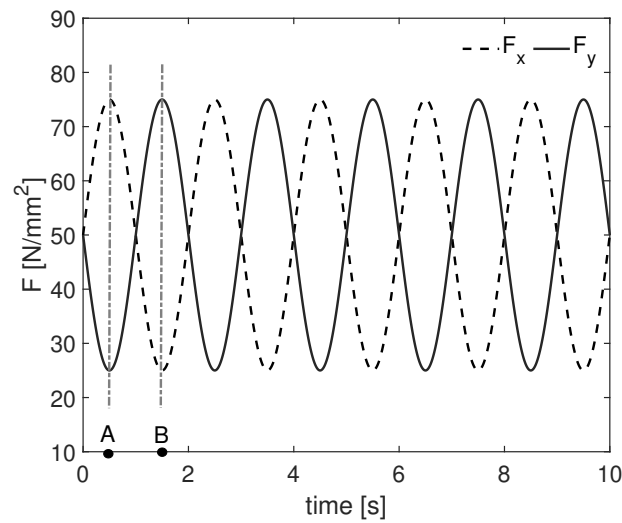


Figure 4.6: Time evolution of prescribed external forces. Highlight of time instants A ($t = 0.5$ s) and B ($t = 1.5$ s).

sliding (wear and increase of life duration) around $150 \mu\text{m}$ [Montalvo et al., 2023]. It is therefore important to accurately compute information located at the interface level.

Parameters of the 2D problem	
Young modulus, E	130 000 MPa
Poisson ratio, ν	0.2
structure size L_x, L_y	180 mm, 90 mm
number of elements per substructure	20×20 QUA8
number of DOFs per substructure, N_x	2562
number of time steps, N_t	1000
time interval, $[0, T]$	$[0, 10 \text{ s}]$
friction coefficient, f	0.3
pressure load, p	100 MPa

Table 4.1: Parameters for the two-dimensional problem.

4.2 Analysis of the solution

The reference solution is here obtained with the full multiscale LATIN method, with a chosen reference search direction $\mathbf{k}^- = \mathbf{k}^+ = \mathbf{k} = \frac{E}{L_\Gamma} \mathbf{I}_d$, with L_Γ being the length of an interface, and for a LATIN convergence indicator threshold of $\eta_0 = 1.5 \cdot 10^{-5}$.

In Figure 4.7 is shown the trend of the tangential frictional forces and their macroscopic part at time instant A ($t = 0.5 \text{ s}$) along the contact interface Γ_c highlighted in Figure 4.5, which goes along the entire length of the structure. As it can be seen, the affine macroscopic part roughly captures the trend of forces on each interface.

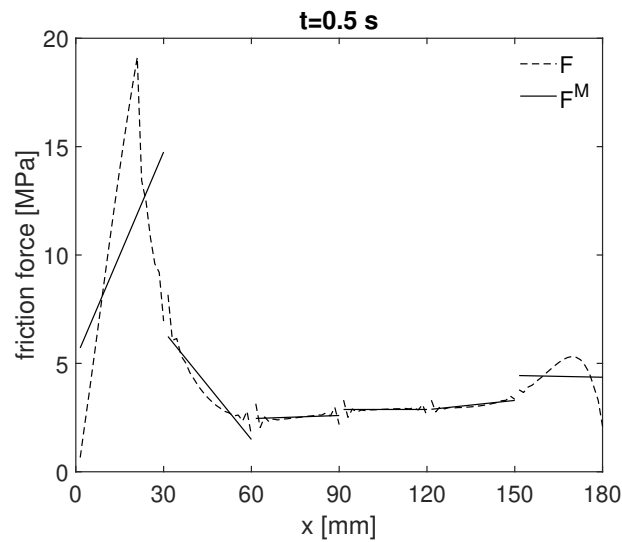


Figure 4.7: Spatial distribution of the frictional forces and their macroscopic part along Γ_c at time instant A.

In Figure 4.8 is shown the relative sliding along Γ_c , at time instants A ($t = 0.5$ s) and B ($t = 1.5$ s). In A, where minimum bending occurs, almost the entire structure results in a sticking state. The sliding is confined near the clamped boundary, between substructures 1 and 7. In B, corresponding to maximum bending, on the other hand, the whole contact interface turns out to be in a sliding state. In this case, the sliding front propagates through the substructures.

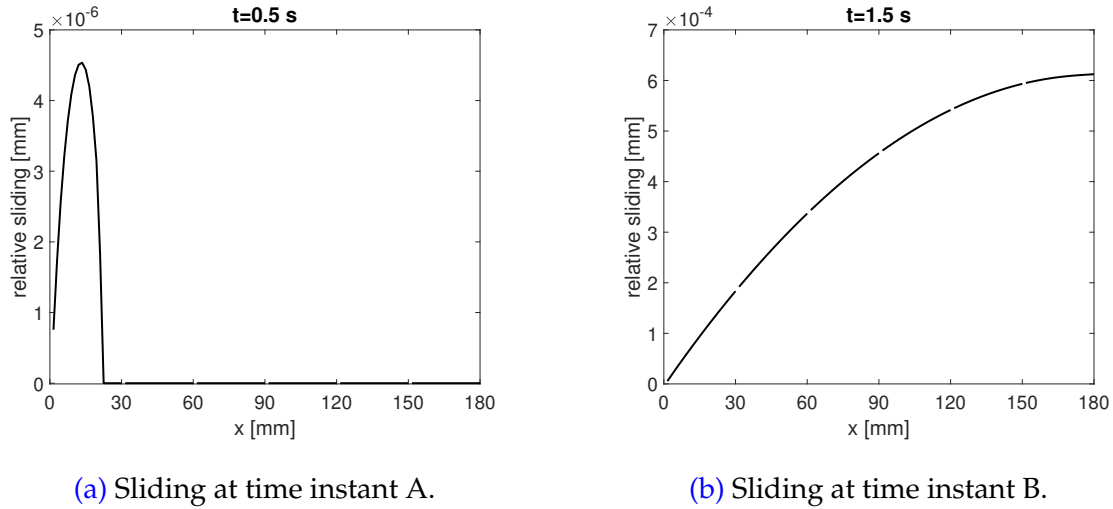


Figure 4.8: Relative sliding along the contact interface Γ_c at time instants A and B.

Discontinuity fronts propagating through all the substructures can affect the relevance of the coarse scale problem [Kerfriden et al., 2009] and slow down the convergence rate. The evolution of the LATIN indicator in Figure 4.12, shows that there is in fact an initial gain in convergence, where boundary conditions and macroquantities are propagated throughout the whole structure. However, thereafter the convergence rate turns out to be comparable to the monoscale one. Since the macroproblem is based on the balance of macroforces, in a problem where a large sliding/discontinuity front propagates through the substructures, the macroproblem after a certain point brings few contribution on the solution of the contact problem locally, and iterating more is necessary (see also [Kerfriden et al., 2009; Saavedra et al., 2012] for the case of propagating delamination fronts).

The convergence state of the contact quantities coming from the linear and local stage (normal and tangential forces and displacements) along the iterations of the multiscale full LATIN, at the contact interface $\Gamma_{c,1-7}$ between substructures 1 and 7, is shown in Figure 4.10 for the time instant A of the loading. After 100 iterations, and a LATIN indicator value of $\eta = 4 \cdot 10^{-4}$, the structure results are far from convergence. Regarding contact forces, the quantities coming from the local stage appear to have already identified the sticking and sliding zones. **This means that the contact status, thanks to the multiscale approach, has converged quickly.** As it can be seen in the next iterations, 500 ($\eta = 8 \cdot 10^{-5}$) and 1000 ($\eta = 1.5 \cdot 10^{-5}$), the forces from the local stage

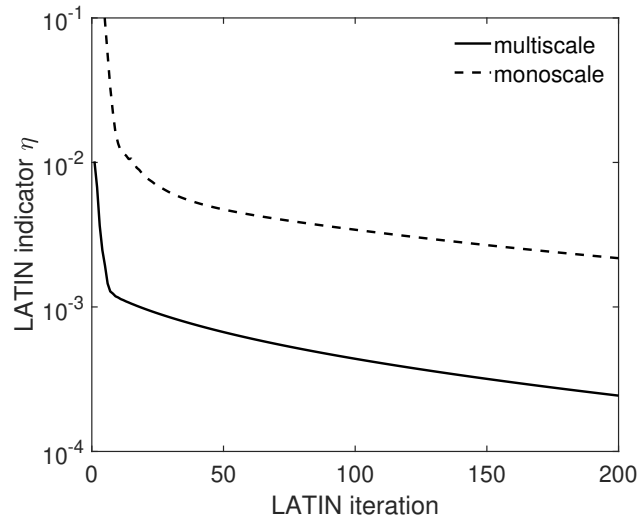


Figure 4.9: LATIN indicator of the multiscale approach compared to the monoscale one for the 2D problem.

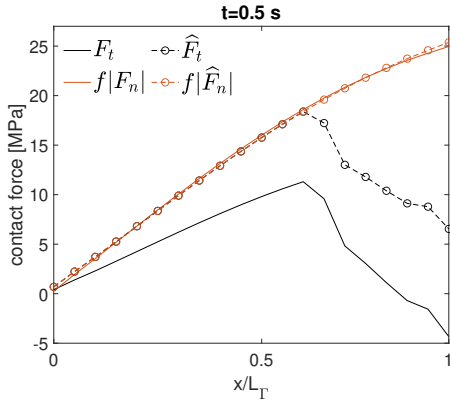
identify roughly the same sticking-sliding transition zones. However, the tangential forces of the linear stage turn out to converge very slowly toward this threshold of sticking-sliding. In contrast, the normal forces result to converge more rapidly. This fact may be due to the choice of search direction parameter k . Tangential contact and normal contact should require different stiffness [Ribeaucourt et al., 2007], especially when wide sliding fronts happen in the tangential direction. In the case of normal contact, under closed gap conditions, the stiffness can be considered as the one of perfect interfaces. In the case of tangential contact, on the other hand, more prone to slippage, the contact stiffness should be lowered. As a result, convergence can be very slow in specific areas where large sliding fronts occur. This point will be investigated in the next Chapter 5.

4.3 Introduction of PGD

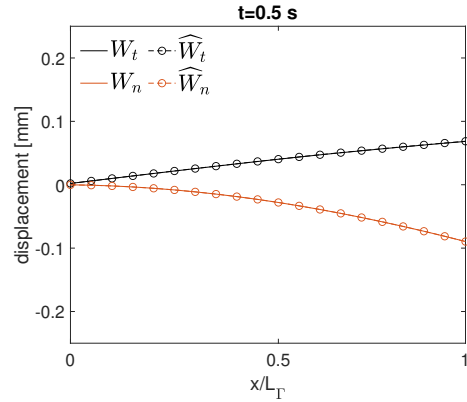
The introduction of PGD is performed at the substructure level, with the enrichment criterion of Eq. (3.31) which takes into account the approximation on the search direction.

Figure 4.11 shows the evolution of the LATIN indicator in the multiscale full LATIN case with the LATIN-PGD(ξ) strategy involving different enrichment thresholds. A very strict enrichment threshold of $\xi_{0,1} = \xi_{0,2} = 10^{-4}$ for both microproblems leads the LATIN-PGD(ξ) convergence curve to coincide with the full LATIN curve, since at each iteration the search direction is approximated with very good accuracy. A very

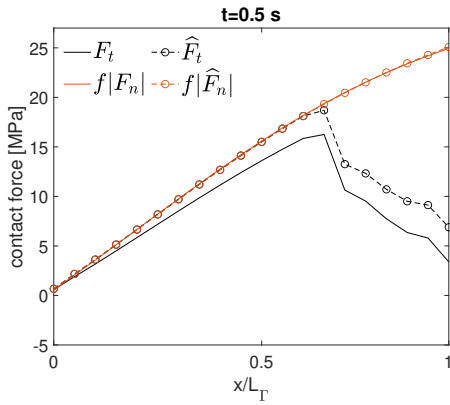
4. Application to a layered structure with wide contact interfaces



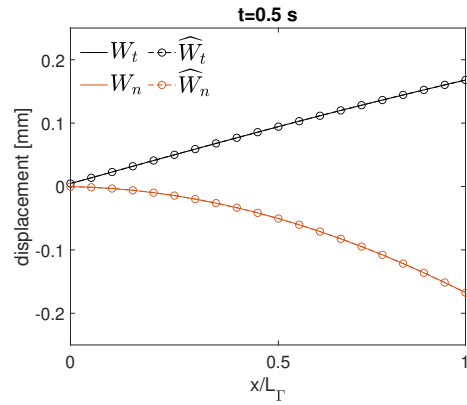
(a) Normal and tangential forces at iteration 100.



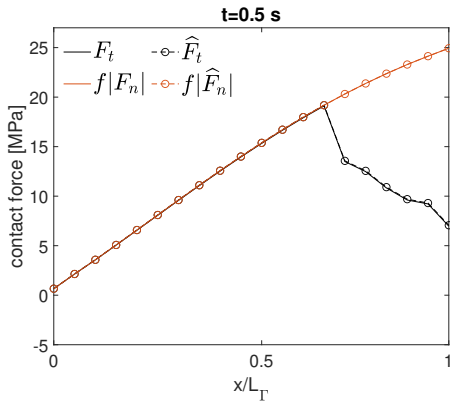
(b) Normal and tangential displacements at iteration 100.



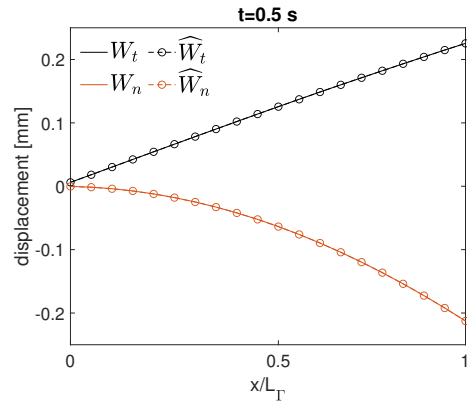
(c) Normal and tangential forces at iteration 500.



(d) Normal and tangential displacements at iteration 500.



(e) Normal and tangential forces at iteration 1000.



(f) Normal and tangential displacements at iteration 1000.

Figure 4.10: Convergence state of normal (in red) and tangential (in black) forces and displacements at time instant A for interface $\Gamma_{c,1-7}$ through the LATIN iterations.

coarse enrichment threshold, such as $\zeta_{0,1} = \zeta_{0,2} = 0.5$ on both microproblems, on the other hand, leads the solution to stagnate and risk diverging. The initial part of the curve is not properly approximated, which leads to affect the convergence in the rest of the iterations. By making use of a different enrichment threshold for the two microproblems, as explained in [Section 2.5](#), that is, a bit more strict for microproblem 2 ($\zeta_{0,2} = 0.01$), and a bit coarser for microproblem 1 ($\zeta_{0,1} = 0.1$), leads to a good approximation of the problem. In fact, **it is not important to correctly approximate the search direction at each iteration, as it is useless when the algorithm is still far from convergence**. The important thing is to approximate the problem sufficiently to stay close to the convergence given by the full LATIN (which, in fact, is the best that can be done with a given search direction k), while trying to generate as few modes as possible.

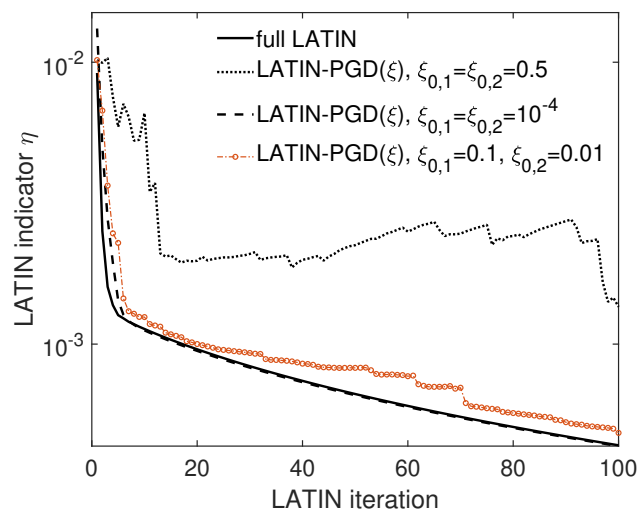


Figure 4.11: LATIN convergence indicator of full LATIN and LATIN-PGD(ξ).

In [Figure 4.12](#) is shown the evolution of the PGD basis size along the LATIN iterations in two different substructures for two choices of the enrichment threshold, that is $\zeta_{0,1} = \zeta_{0,2} = 10^{-4}$ and $\zeta_{0,1} = 0.1, \zeta_{0,2} = 0.01$. The considered substructures are substructure 7 and substructure 12. The former is located in the clamped zone, and presents boundary effects that make the contact conditions more difficult to capture.

Both choices systematically generate two pairs of modes, one from each microproblem, in the first iterations, where the slope of the LATIN curve is higher. Thereafter, in the case with $\zeta_{0,1} = \zeta_{0,2} = 10^{-4}$, only one pair of modes, coming from microproblem 1, is generated systematically at each iteration for both substructures. As exemplified in [Section 2.5](#), we observe that **the PGD basis needs to be enriched more frequently for microproblem 1 than for microproblem 2** after few first iterations, so does the choice of $\zeta_{0,1} = 0.1$ and $\zeta_{0,2} = 0.01$, thus reducing the size of the final basis.

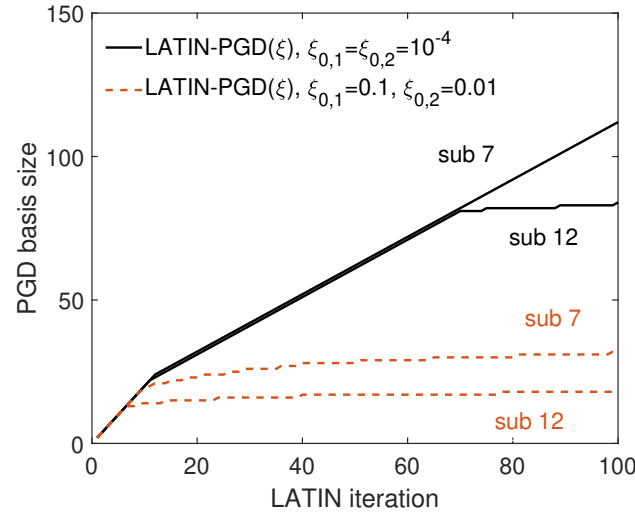


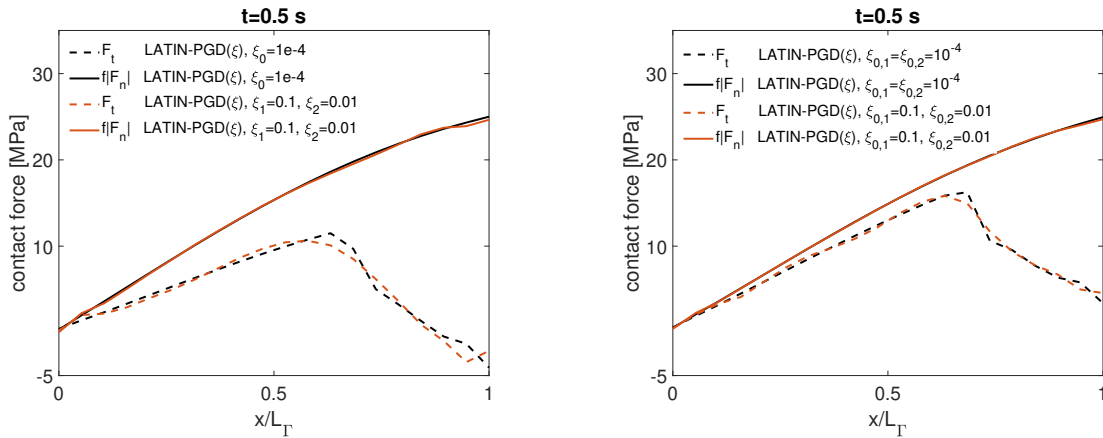
Figure 4.12: PGD basis size along the iterations for the LATIN-PG(ξ) strategy.

The accuracy of the contact quantities for the two enrichment threshold choices described above are shown in Figure 4.13 for the contact forces along interface $\Gamma_{c,1-7}$ at time instant A. When the search direction is well approximated, as in the case of $\xi_{0,1} = \xi_{0,2} = 10^{-4}$, the solution coincides in practice with the full LATIN solution at each iteration, and a large number of modes is required. In the other case, the approximation becomes better as one approaches the converged solution where the two strategies are indistinguishable. Nevertheless, the difference in the size of the PGD basis built by the two strategies per substructure, as it can be seen from Figure 4.12, is of a factor of 4.

4.4 Analysis of the computational cost

It is also crucial to quantify the gain in computational time that adopting PGD brings to the LATIN algorithm, based on the choices of the enrichment criterion threshold and possible algorithms to control the size and quality of the progressively built PGD basis. We remind that the PGD separated representation in the LATIN acts only in the linear stage, while the local stage remains unchanged with or without PGD and is solved with the interface quantities in full field format. Therefore gain in computational time with PGD can only be achieved in the linear stage.

The average computational time (over 100 iterations) of the linear stage of the LATIN-PGD(ξ) and LATIN-PGD(ξ)+D strategies (see Table 3.3), with the two choices of enrichment criteria described previously, is shown in Figure 4.14. Concerning the LATIN-PGD(ξ), undoubtedly a criterion that creates fewer PGD modes is less



(a) Linear stage normal and tangential forces at iteration 100. (b) Linear stage normal and tangential forces at iteration 500.

Figure 4.13: Linear stage normal and tangential forces at time instant A for interface $\Gamma_{c,1-7}$ for the LATIN-PGD(ξ) strategy at two different number of iterations.

expensive, and saves up to 40% of the time in this case. Compared with the full LATIN, the LATIN-PGD(ξ) allows a gain of a factor larger than 10.

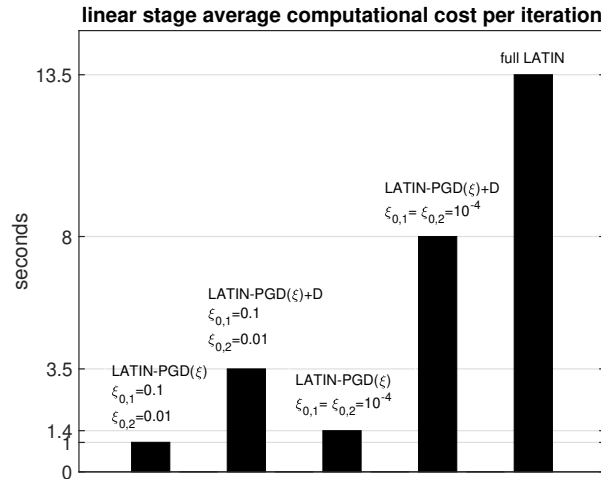


Figure 4.14: Computational cost of the linear stage of the LATIN-PGD(ξ), LATIN-PGD(ξ)+D and full LATIN.

In the LATIN-PGD(ξ)+D strategy with $\xi_{0,1} = \xi_{0,2} = 10^{-4}$, which leads to the generation of a large number of modes (see Figure 4.12), the downsizing stage turns out to be very expensive, with the cost associated with the satisfaction of the admissibility

condition (3.24) for the separated representation of interface quantities each time the downsizing stage is applied. Its overall computational cost becomes therefore comparable with the cost of the full LATIN, leading to a very low gain in computational time. Instead, when in the LATIN-PGD(ξ)+D a more appropriate threshold is chosen ($\xi_{0,1} = 0.1$ and $\xi_{0,2} = 0.01$), performing downsizing becomes less costly, as less modes are generated, yet still the cost is non-negligible. Note that in this cost comparison, all the different strategies produce almost the same LATIN convergence curve, and we can reasonably think that the accuracy of the solution is consequently similar.

The influence of a downsizing stage on the size of the PGD reduced basis is shown in Figure 4.15, where the evolution of the size of the total basis for substructures 7 to 12 of the central beam of Figure 4.5 is plotted. In the LATIN-PGD(ξ) strategy with $\xi_{0,1} = \xi_{0,2} = 10^{-4}$, the size of the progressively built reduced basis is remarkably large. In this case, downsizing significantly reduces the size by sorting and taking out unnecessary modes, however, at a non-negligible computational cost. In the case of LATIN-PGD(ξ) with $\xi_{0,1} = 0.1$ and $\xi_{0,2} = 0.01$, instead, the redundancy of the progressively found modes is minimal, and the effect and the need of of the downsizing stage can be said to be negligible on the final size of the basis.

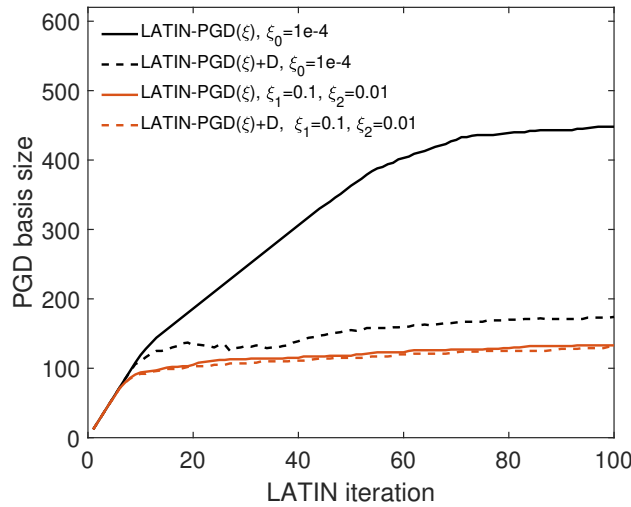


Figure 4.15: PGD basis size of LATIN-PGD(ξ) and LATIN-PGD(ξ)+D for substructures 7 to 12.

5 Conclusions

In this chapter we have described in detail the space multiscale strategy based on the LATIN-based mixed DDM. The strategy involves a separation of scales at the interfaces, with macroquantities representing an average in space of the interface quantities capable of capturing the resulting effect of loads sufficiently far away (based on the de Saint-Venants's principle) and ensuring a **coarse propagation at the structural level of the effect of external loads and the evolving frictional contact conditions**. The introduction of a multiscale strategy is particularly relevant since it is consistent with the physics of contact problems, in which phenomena with different wavelengths interact. Local solutions at contact interfaces presents high gradient effects with a short wavelength compared to the characteristic length of the structure. PGD-based model reduction is naturally introduced in the multiscale strategy, creating and enriching on-the-fly reduced bases per substructure to better represent localized evolving contact conditions. The coarse scale problem of the strategy enables to capture efficiently the behavior of the problem at the structural level, focusing then on capturing the local contact variations at the contact interfaces with an evolving PGD basis.

The most important features and benefits of such a strategy to model reduction for frictional contact problems have been presented on the 1D benchmark problem introduced in [Chapter 3](#):

- the multiscale approach allows for a considerable convergence gain in the first iterations, where macroquantities are rapidly converged. Subsequently, contact quantities are converged to the local microlevel;
- the use of DDM enables one to create local reduced bases per substructure and enrich the basis in the areas with more complex contact conditions;
- the first structural modes of each substructure are roughly well captured by the macroproblem.

The strategy was then tested on a 2D problem with large frictional contact interfaces subjected to multiple multidirectional loads oscillating in time, in order to generate complex contact conditions and wide sliding fronts. In the analyzed 2D problem it was shown how, for a given accuracy, in order to achieve the best efficiency in terms of computational cost reduction it is required to create as few PGD modes as possible. Therefore, the choice of the PGD basis enrichment criterion is crucial. By exploiting the fact that the coarse scale problem brings advantages especially in the first iterations of the LATIN, it is suggested to:

- systematically enrich in the first iterations the ROB due to macroquantities, so as to form a relevant basis for the macroquantities for the rest of the iterations;
- select a more precautionary enrichment criterion threshold for the microquantities, whose convergence is much slower especially in problems with large sliding

fronts across multiple substructures, so as to not add unnecessarily modes when far from convergence.

The sorting and downsizing algorithm proposed in [Giacoma et al., 2015] has been adapted and extended here in the multiscale and DDM version of the LATIN. The algorithm controls the PGD basis size and creates a close-to-optimal basis throughout the computations. However, its computational cost, due to the need to guarantee admissibility between the modes of displacements and forces each time it is applied, may not be negligible, especially when using an inappropriate ROB enrichment criterion which leads to add many modes. It was shown that, by making use of the previous suggestions, the need for downsizing can be avoided thanks to the multiscale aspects and the DDM, since the two microproblems already reflect corrections from different scales. In such a way, an important gain in computational time with respect to the full LATIN solver is achieved, and a ROB of controlled size and good quality is progressively created. Modes due to the macroproblem capture the low frequency modes of each subdomain, while those from the microquantities capture progressively modes that carry more local and refined corrections.

Finally, in the analyzed 2D problem, the large contact interfaces subjected to sliding along the whole set of substructures affect the solution at the global level over the whole structure, and the coarse scale problem, after an initial convergence gain, reduces its effect and at the microlevel still many iterations are needed. **At the microlevel the convergence rate is mainly driven by the search direction k .** A more pertinent choice of the search direction could allow for an improved convergence at the microlevel, however the optimality of the search direction for time-dependent frictional problems with evolving contact conditions is a challenging issue. **Another issue highlighted is the difficulty of the classical LATIN indicator in predicting a good convergence of interface quantities at the microscopic level.**

The next chapter will cover these issues by proposing a more reliable convergence indicator suited to frictional contact problems and a strategy to improve the convergence rate based on the updating of the search directions.

Chapter 5

Control and improvement of the convergence of interface microquantities

In this final chapter, some contributions to the control and improvement of the LATIN convergence for frictional contact problems are proposed. The first part deals with the control of the convergence and quality of the interface contact quantities through the LATIN iterations. The definition of a proper convergence indicator is crucial to ensure the good quality of the solution, especially in a global space-time approach such as LATIN where it is challenging to accurately control the error. In particular, a good convergence indicator should guarantee a level of accuracy in line with a given stopping threshold and should not be dependent on the adopted search direction parameters. Such a convergence indicator is crucial for the second part of the chapter, where a strategy is introduced for the on-the-fly updating of search directions along the LATIN iterations based on the contact status in space and time, in order to improve the convergence rate of the interface quantities.

Contents

1	Control of the convergence of interface quantities	171
1.1	Convergence indicator based on the interface constitutive relation error	172
1.2	Limitations and modifications	175
1.3	Corroboration of the CRE convergence indicator	177

- 2 Improvement of the convergence of interface quantities 187**
 - 2.1 On the relevance of contact conditions on convergence rate . 189
 - 2.1.1 Contact in opening and closing 189
 - 2.1.2 Layered structure with wide sliding propagation front 190
 - 2.2 A strategy based on the contact status indicators 191
 - 2.3 Consequences of a search direction in space and time 193
 - 2.4 Application to the 1D benchmark problem 195
 - 2.5 Application to 2D frictional contact problems 200
- 3 Conclusions 206**

In this chapter we are going to investigate two crucial points for solving frictional contact problems with the LATIN solver, which are:

- the proposition of a relevant convergence indicator in order to stop the solution at a desired quality;
- the improvement of the LATIN convergence rate by appropriate search directions.

Both are crucial to the proposed multiscale model reduction strategy, as the goal is to accurately represent interface contact quantities while seeking maximum computational gain and efficiency.

1 Control of the convergence of interface quantities

Convergence and error control in contact problems with friction is of fundamental importance to ensure a desired quality of contact quantities. In general, simulating contact problems that involve friction necessitates the use of iterative methods and spatial discretization via finite elements. It is then crucial to estimate the errors that result from the numerical approximation and the convergence of the resolution strategy.

For linear problems, the available approaches to estimate some a posteriori errors are numerous, for an overview one may refer to [Ladevèze and Pelle, 2001]:

- approaches based on the constitutive relation error (CRE) [Ladevèze et al., 1991; Ladevèze, 1992];
- approaches based on the residual of the equilibrium equations [Babuvška and Rheinboldt, 1978];
- approaches involving the smoothing of finite element stresses [Zienkiewicz and Zhu, 1987; Boroomand and Zienkiewicz, 1998].

Regarding nonlinear problems, in particular contact problems, the literature is less vast. In the context of contact without friction, a CRE method has been proposed in [Coorevits et al., 1999, 2000], and extended to static frictional contact problems in [Louf et al., 2003]. In this work the authors make use of the bipotential method to formulate the constitutive relation on the contact interface, leading to a straightforward construction of an error in constitutive relation estimator for this kind of problems. For time-dependent problems, the CRE constitutive relation error has been adopted in [Ladevèze and Moës, 1998] to measure the quality of finite element analyses of plastic and viscoplastic structures described by internal variables [Coleman and Gurtin, 1967].

The problem of an appropriate error control is also found in domain decomposition methods. In this case, in addition to the discretization error, it is necessary to account for errors due to the non-verification of continuity and equilibrium at the interfaces

between the different subdomains along the iterations (see for example [Rey, 2015; Rey et al., 2014] in the case of FETI and BBD approach without contact).

Concerning the LATIN strategy, the strongly non-standard nature of the approach (iterative non-incremental mixed strategy in space and time with two alternating search directions) makes it difficult in general to adopt usual methods for error estimation. The admissibility conditions at the interfaces being not verified (force equilibrium or displacement continuity) for a mixed DDM, especially with frictional contact interfaces, makes it difficult to built error indicators with guaranteed bounds at a reasonable cost in the DDM framework.

Error control in the sense of verification is not the issue here, but rather when to stop the iterative process of the solution strategy in order to have converged contact quantities with a reasonable level of accuracy. Also, from a more pragmatic point of view, one might ask whether it is possible to correlate the level of the strategy convergence indicator with a good quality error level, even if this error level is not guaranteed. The classical LATIN convergence indicator η (3.14) measures the distance in space and time along the search direction between two consecutive solutions belonging to $\mathbf{A}_d^{[0,T]}$ and $\Gamma^{[0,T]}$ respectively, as shown in Figure 5.1. This indicator is cheap to compute, however its major drawback is that it depends on the search direction parameter k , even when a strict sup norm is used for the LATIN indicator as in [Ribeaucourt et al., 2007; Giacomini et al., 2015]. The reached level of error is therefore highly dependent on the search directions, which makes it difficult to interpret and in general not a reliable tool for controlling the quality along the iterations when good accuracy of interface quantities is needed.

A more reliable convergence indicator has been proposed in [Passieux, 2008] based in some way on the error in constitutive relation at the interfaces, which does not depend explicitly on the search direction parameter k . A similar indicator was adopted in [Kerfriden, 2008] to quantify the error on cohesive interfaces. However, the robustness and reliability of the CRE convergence indicator introduced in [Passieux, 2008] for frictional contact problems deserved to be studied in greater depth for the purposes of our study. In this section, we will present the CRE indicator by proposing some modifications in order to make it more robust to different possible scenarios, and by testing the indicator's ability to well represent the interface quantities error for several problems with different complex contact conditions.

1.1 Convergence indicator based on the interface constitutive relation error

In the LATIN context, the goal of a convergence indicator is to quantify the distance between one manifold and the solution in the other manifold. The classical LATIN indicator is obtained by measuring the distance between $\mathbf{A}_d^{[0,T]}$ and a solution \hat{s} of $\Gamma^{[0,T]}$. Starting from the proposal in [Passieux, 2008], what can be done is to measure the

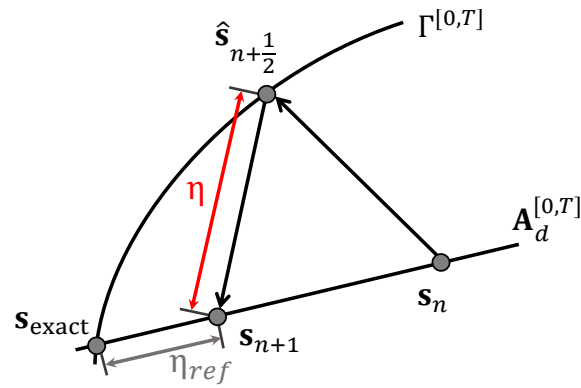


Figure 5.1: Representation of the classical LATIN convergence indicator η and reference error indicator η_{ref} .

distance between $\Gamma^{[0,T]}$ and a solution \mathbf{s} of $\mathbf{A}_d^{[0,T]}$ (see Figure 5.2). Consequently, there is the need to quantify how $\mathbf{s} \in \mathbf{A}_d^{[0,T]}$ does not verify the constitutive behavior of the interfaces.

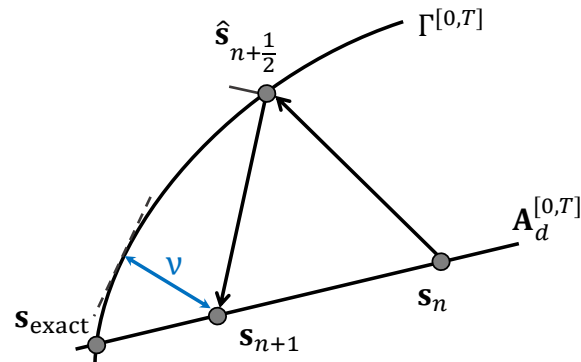


Figure 5.2: Graphical representation of the CRE indicator ν proposed in [Passieux, 2008]. It represents the distance between manifold $\Gamma^{[0,T]}$ and a solution belonging to $\mathbf{A}_d^{[0,T]}$.

Based on the constitutive behavior, formally defined by the equation $\mathbf{b}_{EE'} = \mathbf{0}$, which needs to be verified for each interface at convergence, it is possible to quantify a convergence indicator for the quantities coming from the linear stage taking into account their non-verification of the interface constitutive behavior.

Let us consider that there are N_b different types of interface behaviors $\mathbf{b}_i = \mathbf{0}$, for $i = 1 \dots N_b$, with each i type of interface (displacement boundary condition, force boundary conditions, perfect interface, frictional contact interface...) that needs to satisfy m conditions $\mathbf{b}_{ij} = \mathbf{0}$, for $j = 1 \dots m$. Let Γ_i be the set of interfaces sharing the same behavior $\mathbf{b}_i = \mathbf{0}$, the error in constitutive relation ν is defined as follows:

$$v^2 = \sum_{i=1}^{N_b} \sum_{j=1}^m v_{ij}^2 \quad \text{with} \quad v_{ij}^2 = \frac{\sum_{\Gamma \in \Gamma_i} \int_{\Gamma \times [0, T]} \mathbf{b}_{ij}^2 dS dt}{\frac{1}{2} \sum_{\Gamma \in \Gamma_i} \int_{\Gamma \times [0, T]} \tilde{\mathbf{b}}_{ij}^2 dS dt}. \quad (5.1)$$

The search direction k is not explicitly involved in this indicator, and the terms \mathbf{b}_{ij} and $\tilde{\mathbf{b}}_{ij}$ are evaluated on the different possible interface behaviors as follows:

■ **Perfect interfaces:** $i = 1, m = 2$

$$\begin{aligned} \mathbf{b}_{11} &= \underline{W}_E - \underline{W}_{E'} & \tilde{\mathbf{b}}_{11} &= \underline{W}_E + \underline{W}_{E'} \\ \mathbf{b}_{12} &= \underline{F}_E + \underline{F}_{E'} & \tilde{\mathbf{b}}_{12} &= \underline{F}_E - \underline{F}_{E'} \end{aligned}$$

■ **Frictional contact interfaces:** $i = 2, m = 4$.

Based on the values of the contact indicators C_n and \underline{C}_t from the previous local stage:

– **opening:** $C_n > 0$

$$\mathbf{b}_{21} = \underline{F}_E \quad \tilde{\mathbf{b}}_{21} = \underline{F}_E$$

– **sticking contact:** $C_n \leq 0$ and $\|\underline{C}_t\| < f|C_n|$

$$\begin{aligned} \mathbf{b}_{21} &= \underline{F}_E + \underline{F}_{E'} & \tilde{\mathbf{b}}_{21} &= \underline{F}_E - \underline{F}_{E'} \\ \mathbf{b}_{22} &= \underline{n} \cdot \underline{W}_{E'} - \underline{n} \cdot \underline{W}_E & \tilde{\mathbf{b}}_{22} &= \underline{n} \cdot \underline{W}_{E'} + \underline{n} \cdot \underline{W}_E \\ \mathbf{b}_{23} &= \mathbf{P}_t \delta \underline{W}_{E'} - \mathbf{P}_t \delta \underline{W}_E & \tilde{\mathbf{b}}_{23} &= \mathbf{P}_t \delta \underline{W}_{E'} + \mathbf{P}_t \delta \underline{W}_E \end{aligned}$$

– **sliding contact:** $C_n \leq 0$ and $\|\underline{C}_t\| \geq f|C_n|$

$$\begin{aligned} \mathbf{b}_{21} &= \underline{F}_E + \underline{F}_{E'} & \tilde{\mathbf{b}}_{21} &= \underline{F}_E - \underline{F}_{E'} \\ \mathbf{b}_{22} &= \underline{n} \cdot \underline{W}_{E'} - \underline{n} \cdot \underline{W}_E & \tilde{\mathbf{b}}_{22} &= \underline{n} \cdot \underline{W}_{E'} + \underline{n} \cdot \underline{W}_E \\ \mathbf{b}_{24} &= \|\mathbf{P}_t \underline{F}_E\| - f|\underline{n} \cdot \underline{F}_E| & \tilde{\mathbf{b}}_{24} &= \|\mathbf{P}_t \underline{F}_E\| + f|\underline{n} \cdot \underline{F}_E| \end{aligned}$$

■ **Displacement boundary conditions:** $i = 3, m = 1$

$$\mathbf{b}_{31} = \underline{W}_E - \underline{U}_d \quad \tilde{\mathbf{b}}_{31} = \underline{W}_E + \underline{U}_d$$

■ **Force boundary conditions:** $i = 4, m = 1$

$$\mathbf{b}_{41} = \underline{F}_E - \underline{F}_d \quad \tilde{\mathbf{b}}_{41} = \underline{F}_E + \underline{F}_d$$

Remark 5.1. For the term \mathbf{b}_{23} arising from the non-verification of the tangential sticking conditions, since we make use of a displacement formulation, the condition is expressed in terms of the tangential displacement increment $\mathbf{P}_t \delta \underline{W} = \mathbf{P}_t [\underline{W}(t) - \underline{W}(t - \delta t)]$ between two consecutive time instants, contrary to [Passieux, 2008] where it is expressed in terms of tangential velocities.

Remark 5.2. When material nonlinearities are also present within each subdomain, the CRE indicator can be additively decomposed into a subdomain component and an interface component: $\nu^2 = \nu_\Omega^2 + \nu_\Gamma^2$ [Passieux, 2008]. However, for linear elastic subdomain behaviors, Hooke's law $\sigma_E = \mathbf{K} : \varepsilon_E$ is exactly verified for a solution $\mathbf{s} \in \mathbf{A}_d^{[0,T]}$.

1.2 Limitations and modifications

As originally proposed in [Passieux, 2008], this indicator presents problems when dealing with null boundary conditions $\underline{U}_d = \underline{0}$ ($\underline{F}_d = \underline{0}$). In fact, in this case the terms \mathbf{b}_{31} and $\tilde{\mathbf{b}}_{31}$ (\mathbf{b}_{41} and $\tilde{\mathbf{b}}_{41}$) coincide and lead the error to stagnate on 1. Similarly, when all contact interfaces are open, the contributions \mathbf{b}_{21} and $\tilde{\mathbf{b}}_{21}$ coincide for all the contact interfaces leading the error to stagnate to 1.

To represent this problem we consider the 2D problem depicted in Figure 5.3 together with its reference solution on the right. It consists of a structure with multiple frictional cracks clamped at the bottom and subjected to a traction loading at the top of 50 MPa. The other boundary conditions are set traction free.

Parameters of the 2D problem	
Young modulus, E	130 000 MPa
Poisson ratio	0.2
structure size L_x, L_y	90 mm, 90 mm
number of elements per substructure	6×6 QUA8
friction coefficient, f	1

Table 5.1: Parameters of the problem in Figure 5.3.

From the reference solution in Figure 5.3 it can be noticed that all contact interfaces are open. The evolution of the CRE indicator ν (5.1) and the LATIN indicator (3.14) along the LATIN iterations is shown in Figure 5.4a. As it can be seen, the indicator based on the constitutive relation error ν turns out to be stagnating on the value of 1, not allowing a reliable computation of the error.

To overcome these issues, we propose to aggregate the cases of boundary condition interfaces in displacement and forces among the cases of perfect interfaces, as also

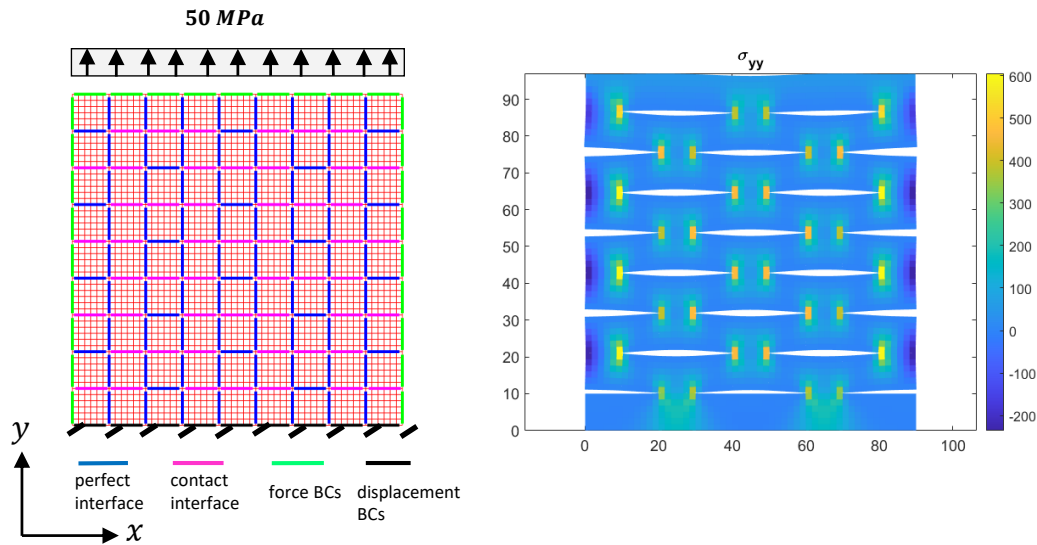
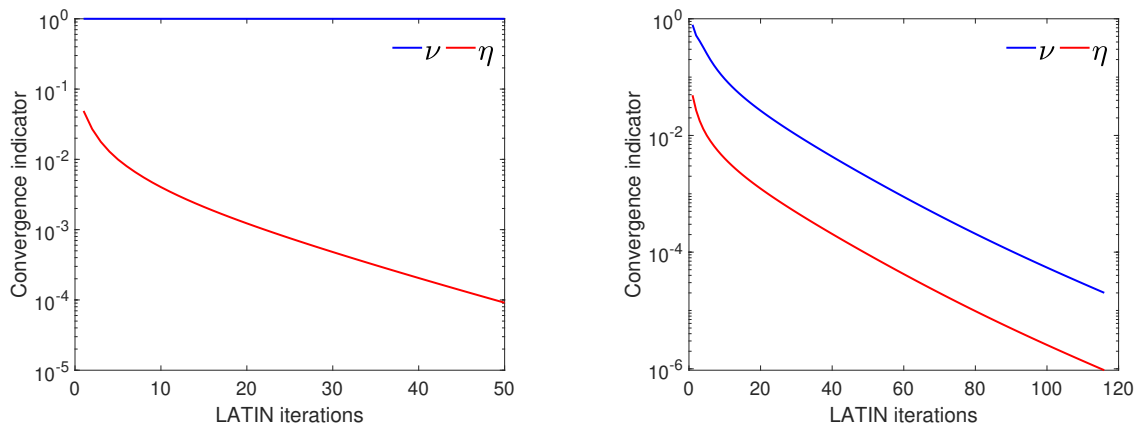


Figure 5.3: 2D test case with opening of frictional cracks.

suggested in [Passieux, 2008]. Moreover, since interface force equilibrium must be verified for any type of interface (as also is verified in a macrosense in the multiscale strategy), we propose to verify all force equilibrium conditions together in the perfect interfaces contributions, as well as the contact interfaces in opening. In this manner both of the described problems vanish, that is null boundary conditions and opening of all contact interfaces. In Figure 5.4b is shown how with these modifications the convergence indicator ν does not have present problems of stagnation.



(a) CRE convergence indicator ν before modifications. (b) CRE convergence indicator ν after modifications.

Figure 5.4: Evolution of the indicators η and ν for the problem in Figure 5.3.

Remark 5.3. *The CRE convergence indicator is still evaluated globally in space and time for all the interfaces, as the LATIN indicator, and thus their computational costs are comparable. There could be situations when a localized error in space and time on a given interface may be larger than the rest of the structure, and this localized error may not be easily captured by the CRE indicator. In this case, more stringent norms could be used, such as a sup norm in space and time used in [Ribeaucourt et al., 2007] for the LATIN indicator. Another alternative could be to propose a "local version" of v [Kerfriden, 2008; Passieux, 2008], which consists in searching for the interface with the worst verification of the interface constitutive behavior, that is to say the highest contribution to the CRE convergence indicator:*

$$v = \max_{i \in [1, N_b]} \max_{\Gamma \in \Gamma_i} \sum_{j=1}^m \frac{\int_{\Gamma \times [0, T]} \mathbf{b}_{ij}^2 dS dt}{\sum_{\Gamma \in \Gamma_i} \int_{\Gamma \times [0, T]} \tilde{\mathbf{b}}_{ij}^2 dS dt}.$$

However, such choices may be too strict and could lead to a very large number of iterations to reach a given threshold v_0 .

1.3 Corroboration of the CRE convergence indicator

We go on here to corroborate the previously introduced CRE convergence indicator with the appropriate modifications. We consider several test cases containing different numbers of contact interfaces under different contact conditions (closed contact, sticking-sliding and opening) and different loading situations in order to get an overview as wide as possible on how the convergence indicator behaves. For each test case the convergence indicator is compared with the classical LATIN indicator (Eq. (3.14) in Section 2.5 of Chapter 3) and the reference solution errors in displacements and forces (Eq. (3.15) in Section 2.5 of Chapter 3). For each test case, the reference solution has been obtained with the multiscale LATIN method without PGD by making use of a constant reference search direction for all the interfaces $\mathbf{k} = \mathbf{k}_0 = \frac{E}{L_\Gamma} \mathbf{I}_d$ and a LATIN indicator threshold $\eta_0 = 10^{-6}$. Finally, for each test case we vary the value of the search direction for the contact interfaces, considering the cases $\mathbf{k} = \mathbf{k}_0$, $\mathbf{k} = 0.1 \mathbf{k}_0$ and $\mathbf{k} = 10 \mathbf{k}_0$ respectively.

■ Open contacts in traction

The first test case is the one described in the previous section in Figure 5.3, where all contact interfaces are in opening.

The evolution of the different convergence indicators for the case with $\mathbf{k} = \mathbf{k}_0 = \frac{E}{L_\Gamma} \mathbf{I}_d$

is shown in Figure 5.5. The convergence indicator based on the error in the constitutive relation ν performs better than the LATIN indicator, presenting a trend closer to the reference errors by one order of magnitude.

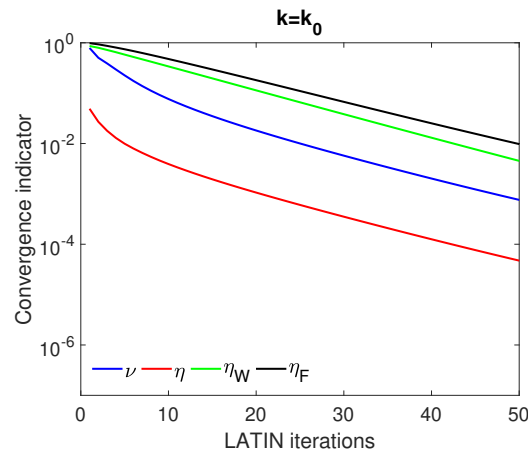


Figure 5.5: Evolution of the indicators η and ν for the problem in Figure 5.3 with $k = k_0$.

Figure 5.6 shows the trends of the convergence indicators for the cases $k = 0.1 k_0$ (Figure 5.6a) and $k = 10 k_0$ (Figure 5.6b). In the case $k = 0.1 k_0$ the problem converges faster, just as in the case $k = 10 k_0$ convergence is very slow. The error in constitutive relation ν manages to account for this very well, resulting in both cases closer to the trend of the reference errors. The LATIN indicator, on the other hand, especially in the case $k = 10 k_0$ is several orders of magnitude far from the reference errors, making it inappropriate to estimate the error in contact quantities.

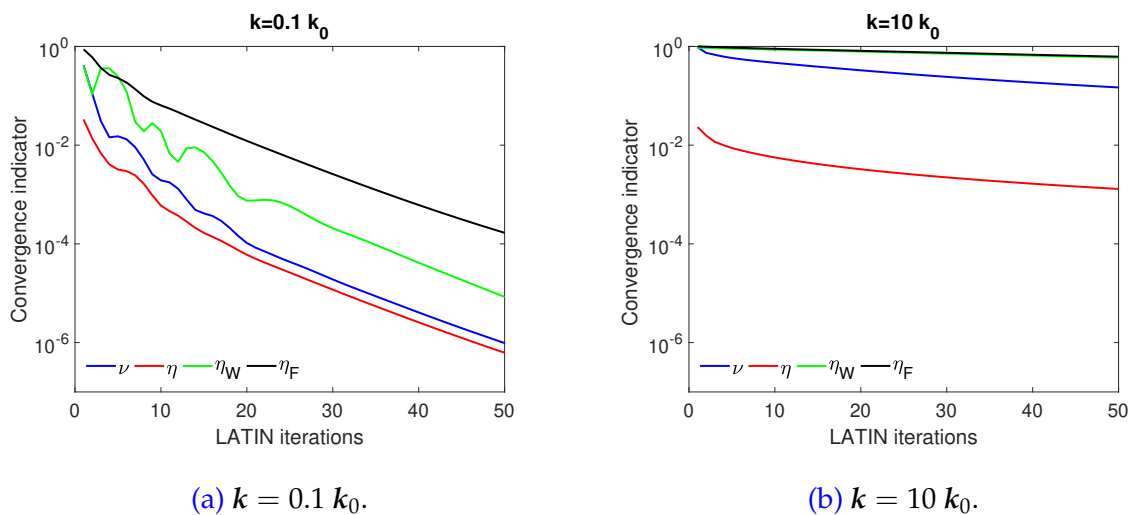


Figure 5.6: Evolution of the indicators η and ν for the problem in Figure 5.3.

■ Open and closed contacts in compression and bending

Similarly to the previous case, we consider here the same structure but now in compression and in bending at the top, as shown in Figure 5.7, with the rest of the boundary set traction-free. The contact interfaces in the compression zone (left-bottom) are closed, whereas those in the traction zone (right-bottom) are open, as it can be seen from the reference solution on the right in Figure 5.7.

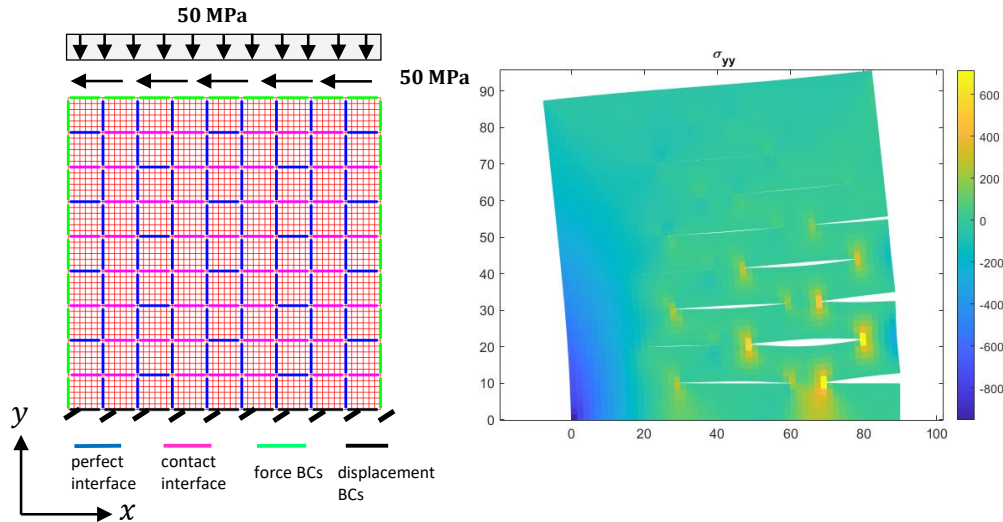


Figure 5.7: Structure with frictional cracks in compression and bending.

Figure 5.8 shows the trends of the different convergence indicators for the considered cases $k = k_0$ (Figure 5.8b), $k = 0.1 k_0$ (Figure 5.8a) and $k = 10 k_0$ (Figure 5.8c). In all three cases the CRE convergence indicator performs very well, with the trend of convergence of the reference errors being very well represented. The LATIN indicator, on the other hand, in all three cases results to be not representative of the actual error committed along the iterations.

■ Structure with a crack under mixed mode loading

Let us consider here the structure in Figure 5.9, presenting a contact interface over four-fifths of its length, clamped at the bottom and subjected to a pressure load of 100 MPa and a tensile load F_x and shear load F_y which vary linearly from zero to a maximum value of 100 MPa and 25 MPa respectively over a 10 s interval discretized in 100 time steps. The contact interfaces have a friction coefficient $f = 0.3$. The rest of the boundary is set traction-free. The structure has dimensions $L_x = 50$ mm and $L_y = 20$ mm, with each subdomain discretized with 15×15 QUA8 elements, the Young modulus is 130 000 MPa and the Poisson ratio is 0.2.

Figure 5.10 shows the reference solution to this problem obtained with a LATIN indicator threshold of $\eta_0 = 10^{-6}$, showing the three possible scenarios of adhesion,

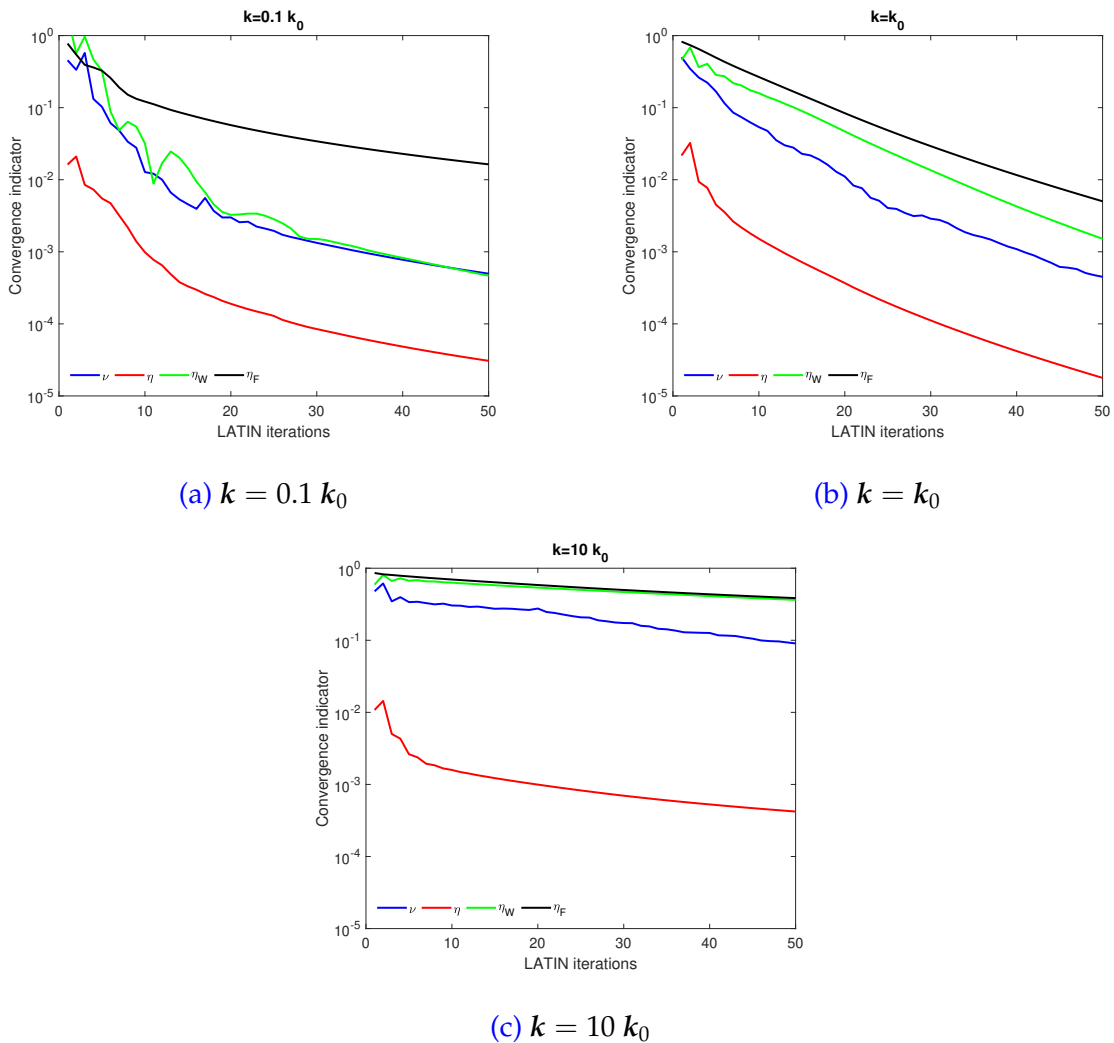


Figure 5.8: Evolution of the indicators η and ν for the problem in Figure 5.7.

sliding and contact opening on the contact interfaces.

Figure 5.11 shows the trend of the different convergence indicators as k varies for the contact interfaces, with $k = k_0$ (Figure 5.11b), $k = 0.1 k_0$ (Figure 5.11a) and $k = 10 k_0$ (Figure 5.11c). In all three cases, the CRE convergence indicator performs better than the LATIN indicator and well represents the convergence trend of the reference error indicators.

In particular, it appears that at the contact interface Γ_{2-7} between substructures 2 and 7 the contact gap is always closed, while in the other contact interfaces the opening front propagates in time with the external loading. Looking in more detail at the frictional contact conditions over time on the different contact interfaces, Figure 5.12 shows, for contact interfaces Γ_{2-7} and Γ_{4-9} , the evolution of the sliding front (Figure 5.12a) and the opening front (Figure 5.12b), respectively for the converged solution. As it can

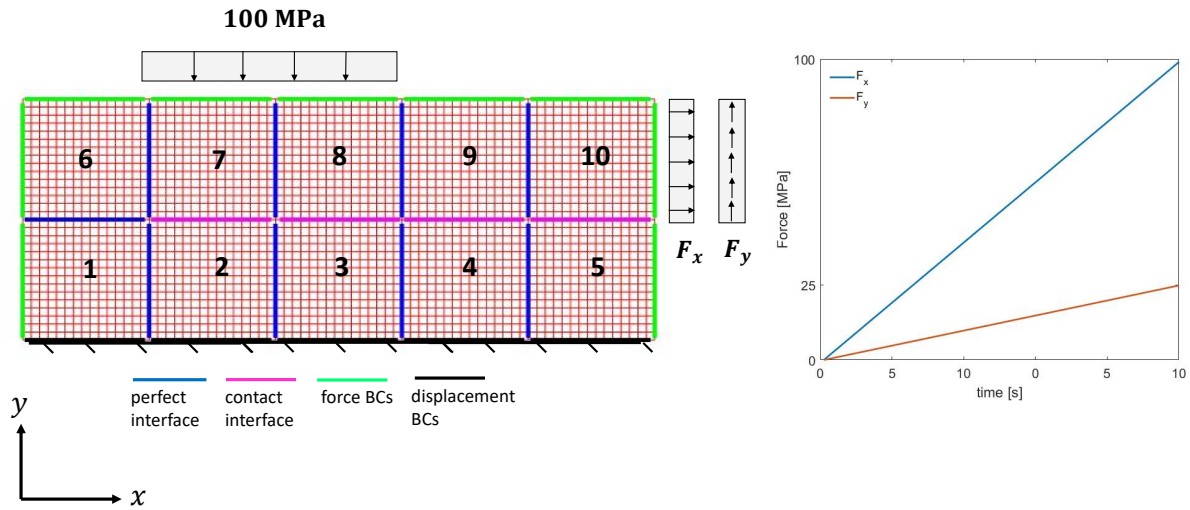


Figure 5.9: 2D structure with a crack under mixed mode loading with numbering of subdomains and prescribed forces.

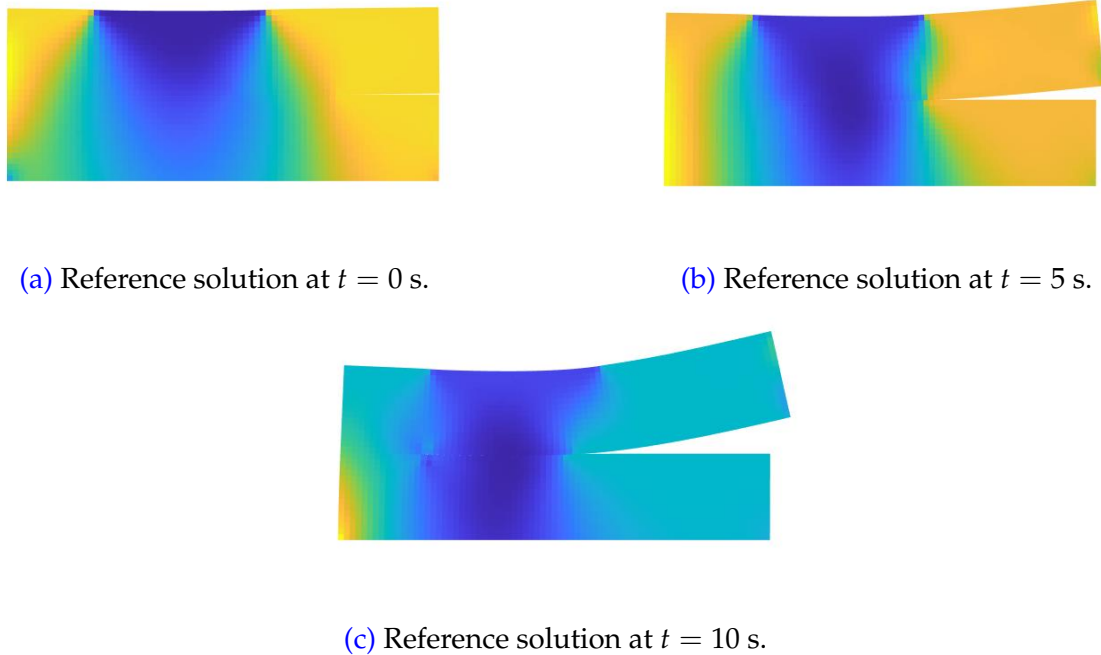


Figure 5.10: Reference solution at different time instants. (a): $t = 0$ s. (b): $t = 5$ s. (c): $t = 10$ s.

be noticed, in this particular test problem the sliding and opening propagation fronts are wide, and it is crucial for a good convergence indicator to well represent these fronts.

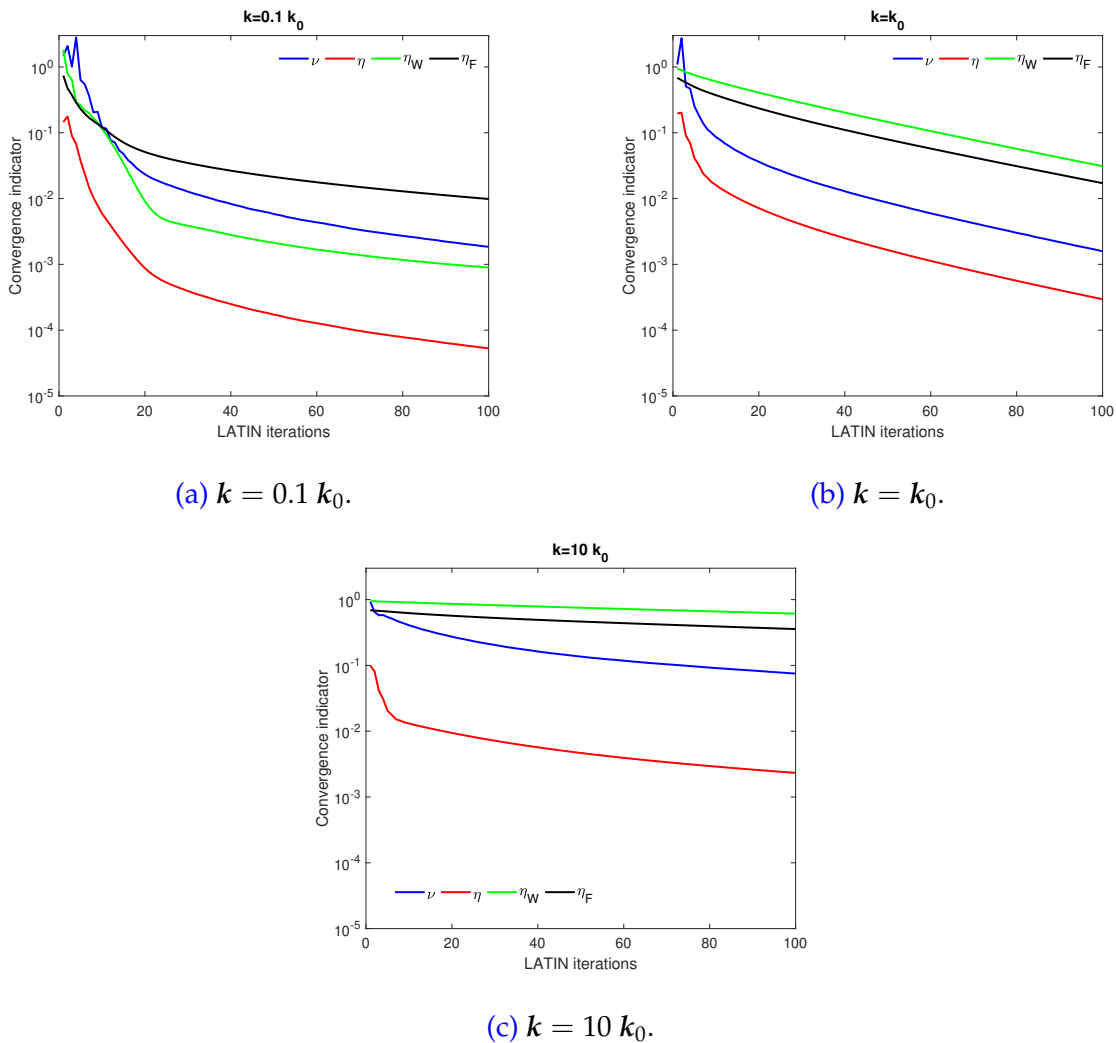


Figure 5.11: Evolution of the convergence and error indicators for the problem in Figure 5.9. (a): For $k = 0.1 k_0$. (b): For $k = k_0$. (c): For $k = 10 k_0$.

In order to assess the ability of the convergence indicators to accurately capture the various sticking and opening fronts, in Figure 5.13, Figure 5.14 and Figure 5.15 are shown the portraits of the sliding and opening fronts of interfaces Γ_{2-7} and Γ_{4-9} represented by the LATIN indicator η and the CRE indicator ν for the 3 different values of k considered previously.

In practice, for the three considered different values of k , the LATIN algorithm was stopped once the threshold value $\eta_0 = 10^{-3}$ for the LATIN indicator, and the threshold value $\nu_0 = 10^{-2}$ for the CRE indicator was reached. A good convergence indicator, for different values of k used in the LATIN strategy, should be able to reproduce solutions of comparable accuracy when using the same stopping threshold, and therefore also

reproduce contact fronts of similar appearance.

As it can be seen from the figures, the proposed CRE indicator behaves very well in this aspect, with the solutions presenting highly similar sliding and opening fronts in line with the reference solution. The LATIN indicator, on the other hand, makes the solution converge to more variable sliding and opening fronts, especially for higher values of k in this case.

It is clear that when the search direction is not optimal and one makes use of a more reliable convergence indicator, this will require a larger number of iterations to reach a given accuracy. This can be clearly seen from Table 5.2, where are compared the number of iterations required to reach a given accuracy for the considered cases with the LATIN indicator and the CRE indicator. However, one will be almost certain that the solution obtained will have a quality comparable to the value of the chosen convergence threshold. This aspect with the classic LATIN indicator is not always guaranteed for frictional contact problems, especially when large fronts of sliding and opening are present.

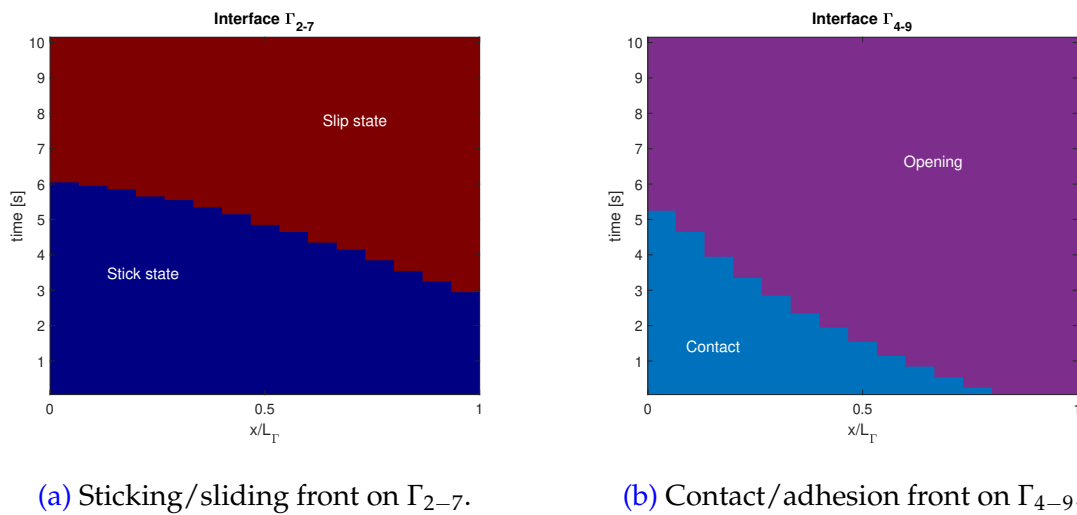
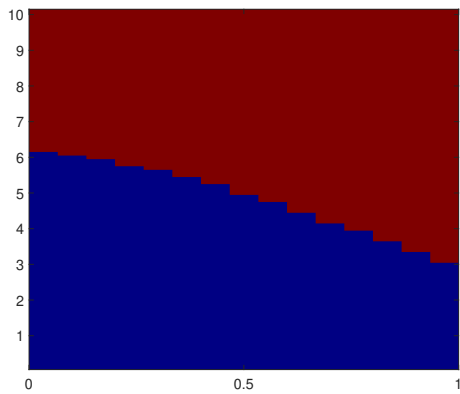


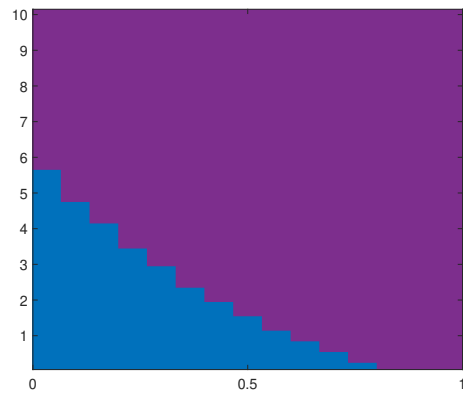
Figure 5.12: Contact status evolution over time for contact interfaces Γ_{2-7} and Γ_{4-9} at convergence. (a): sticking/sliding status of Γ_{2-7} . (b): contact/opening status of Γ_{4-9} .

Search direction	Iterations to convergence	
	$\eta_0 = 10^{-3}$	$\nu_0 = 10^{-2}$
$k = 0.1 k_0$	20	36
$k = k_0$	66	61
$k = 10 k_0$	201	459

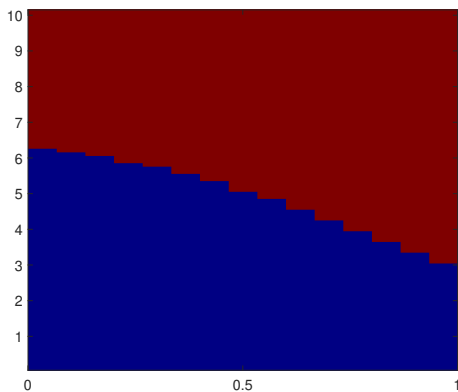
Table 5.2: Number of LATIN iterations to reach a given convergence threshold for η and ν with different values of the search direction parameter k .



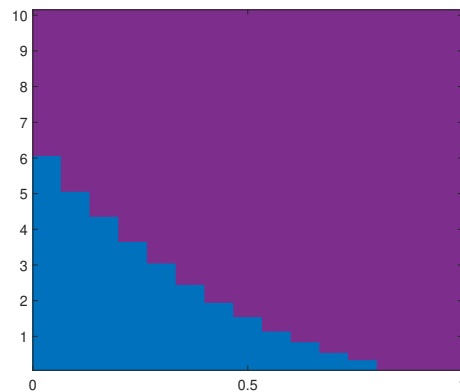
(a) Sliding front for Γ_{2-7} with $\eta_0 = 10^{-3}$.



(b) Opening front for Γ_{4-9} with $\eta_0 = 10^{-3}$.

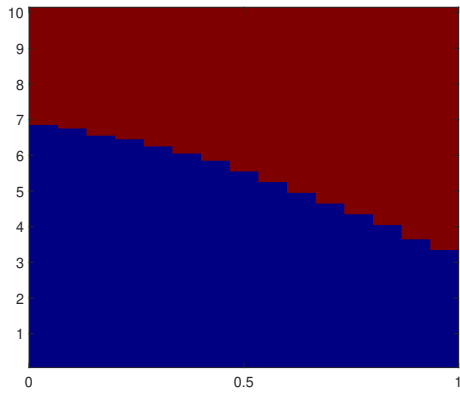


(c) Sliding front for Γ_{2-7} with $\nu_0 = 10^{-2}$.

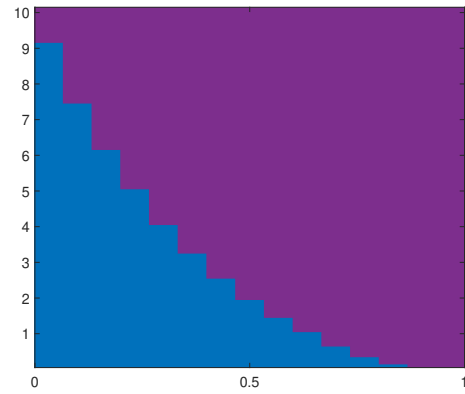


(d) Opening front for Γ_{4-9} with $\nu_0 = 10^{-2}$.

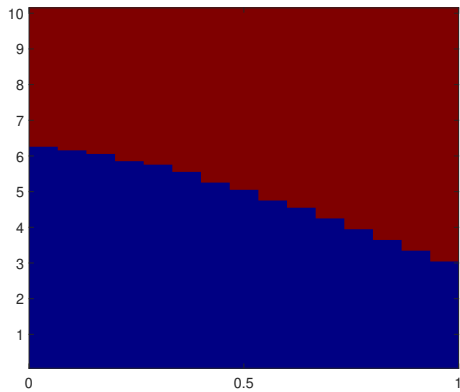
Figure 5.13: Contact front evolution on interfaces Γ_{2-7} and Γ_{4-9} for the solution obtained with $k = k_0$. (a) and (b): convergence threshold $\eta_0 = 10^{-3}$. (c) and (d): convergence threshold $\nu_0 = 10^{-2}$.



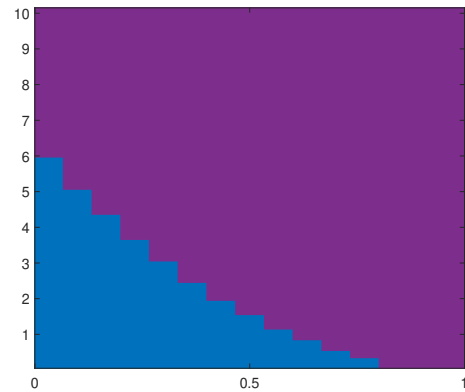
(a) Sliding front for Γ_{2-7} with $\eta_0 = 10^{-3}$.



(b) Opening front for Γ_{4-9} with $\eta_0 = 10^{-3}$.

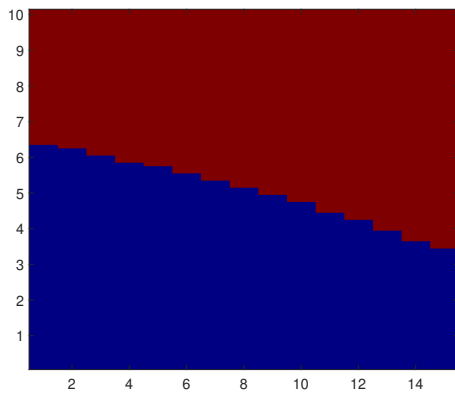


(c) Sliding front for Γ_{2-7} with $\nu_0 = 10^{-2}$.

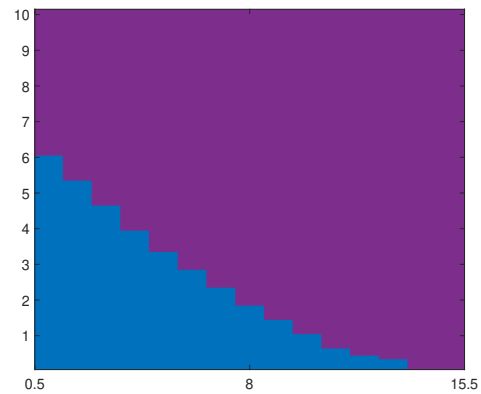


(d) Opening front for Γ_{4-9} with $\nu_0 = 10^{-2}$.

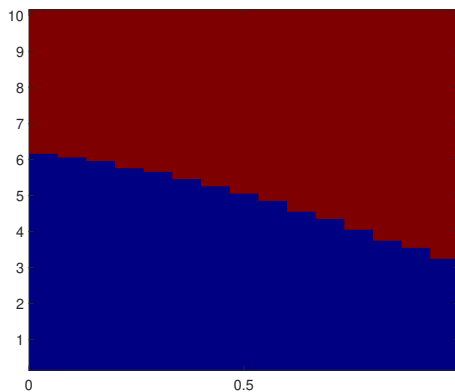
Figure 5.14: Contact front evolution on interfaces Γ_{2-7} and Γ_{4-9} for the solution obtained with $k = 10 k_0$. (a) and (b): convergence threshold $\eta_0 = 10^{-3}$. (c) and (d): convergence threshold $\nu_0 = 10^{-2}$.



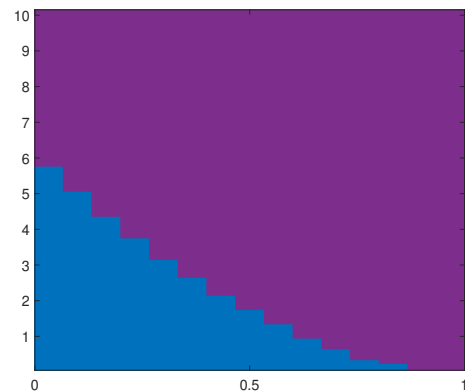
(a) Sliding front for Γ_{2-7} with $\eta_0 = 10^{-3}$.



(b) Opening front for Γ_{4-9} with $\eta_0 = 10^{-3}$.



(c) Sliding front for Γ_{2-7} with $\nu_0 = 10^{-2}$.



(d) Opening front for Γ_{4-9} with $\nu_0 = 10^{-2}$.

Figure 5.15: Contact front evolution on interfaces Γ_{2-7} and Γ_{4-9} for the solution obtained with $k = 0.1 k_0$. (a) and (b): convergence threshold $\eta_0 = 10^{-3}$. (c) and (d): convergence threshold $\nu_0 = 10^{-2}$.

2 Improvement of the convergence of interface quantities

As mentioned extensively throughout this manuscript, the convergence rate of the LATIN is largely determined by the value of the search direction parameters k . This is not surprising since the strategy with which the LATIN method imposes contact constraints, as well as in general all constraints for other types of interfaces, can be traced back to augmented Lagrangian methods in which k plays the role of the augmentation parameter. In the multiscale strategy, in the case of perfect interfaces, it can be shown that the optimal search direction corresponds to a sort of a “microstiffness” of the influence of the immediately neighbouring subdomains on a given subdomain [Violeau, 2003]. However, the computation of this optimal value for each subdomain can be costly, and in practice one often takes, for homogeneous subdomains, the value $k = \frac{E}{L_\Gamma} \mathbf{I}_d$, with L_Γ being a characteristic length of the interface Γ , which can be considered as a close-to-optimal choice for perfect interfaces.

In the case of frictional contact interfaces, a priori optimal values are difficult to determine, since the optimality depends strongly on the contact conditions evolving in space and time and depending on the external loading conditions. Since the contact conditions that occur in space and time for a given problem along the various frictional contact interfaces are not known a priori, it is in fact not possible to give an optimum value to each contact interface. However, the peculiar feature of the LATIN to provide a complete space-time view of the contact status at each iteration allows to have an idea of how the contact conditions evolve already from the very first iterations, and consequently to perform an on-the-fly updating on the search direction to improve convergence rate.

It is well known that augmented Lagrangian methods present a convergence rate which depends on the augmentation factor, and it is generally difficult to select optimally a priori. Various methods to improve the performance of the augmentations are discussed in standard texts on constrained minimization [Luenberger and Ye, 1984; Bertsekas, 1988]. However, the described methods are general and not particularly relevant to contact problems, as shown in [Zavarise and Wriggers, 1999].

The work of [Zavarise and Wriggers, 1999] actually represents the first attempt to improve the performances of the augmentations in augmented Lagrangian strategies for (frictionless) contact problems with a "Lagrangian prediction method". Another attempt is the "adapted augmented Lagrangian method" from [Bussetta et al., 2012] applied to frictional problems.

- *Lagrangian prediction method*

In [Zavarise and Wriggers, 1999] the approach does not involve an optimized choice of the augmentation parameter, but is rather based on a prediction of the contact forces based on datasets of previously converged states. The approach, in order to work, requires some iterations and augmentations with the standard

augmentation method using a reference augmentation parameter. Then, when a sufficient dataset has been constructed, it is used in a sort of "data-driven" approach to predict contact forces without the need for augmentations. To improve the stability of the method the authors show that in predicting the contact force at a given point it is also necessary to take into account the contact status of neighbouring points, introducing a kind of **smoothing of the contact status variability**.

– *Adapted augmented Lagrangian method*

The adapted augmented Lagrangian method [Bussetta et al., 2012], similar to adapted penalty methods [Chamoret et al., 2004], is based on the augmented Lagrangian method equipped with an adaptation of the normal and tangential augmentation parameters. The resolution of the frictional contact problem is the same as for the augmented Lagrangian: the augmentation of the Lagrange multipliers is performed after the convergence of the Newton–Raphson algorithm. However, **the values of the augmentation coefficients are updated during the computations**.

The adaptation of the normal augmentation parameter k_n is performed by considering three cases: at the current iteration i , either the sign of the gap changes ($g_i \times g_{i-1} < 0$), or the absolute value of the gap is more important than a prescribed limit ($|g_i| > g_{max}$), or the absolute value of the gap is less than the maximal limit ($|g_i| < g_{max}$). For the last case, the normal penalty coefficient remains unchanged. For the first case, when $g_i \times g_{i-1}$ is negative, the normal penalty coefficient is adapted so that the absolute value of the gap decreases without changing the sign of the gap. For the second case, when $|g_i|$ is greater than g_{max} , the adaptation of k_n will increase the absolute value of the augmented contribution of the normal stress without changing the sign of the gap. Similar considerations are made for the tangential behavior.

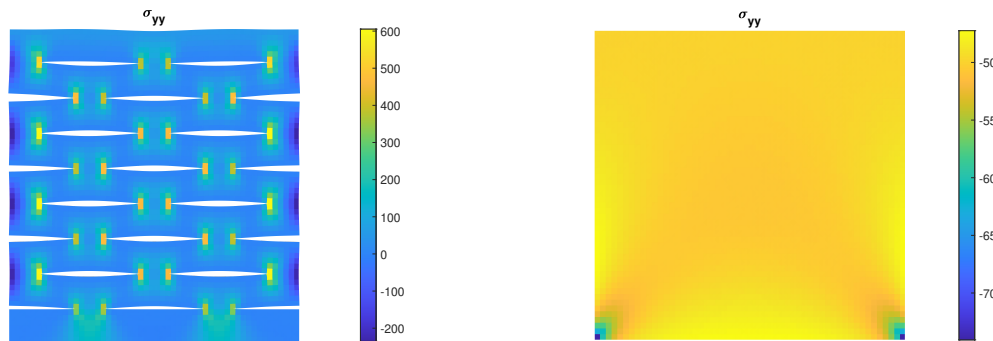
Regarding specifically the LATIN method, an attempt at performing an update of the search direction parameters in the case of frictionless open-closed contacts can be found in [Saavedra et al., 2012], in the context of an "incremental" LATIN method. The authors for a given interface opening, starting from the reference search direction $\mathbf{k}^+ = \mathbf{k}^- = \mathbf{k}_0$, update the search direction after a few iterations by placing $\mathbf{k}^+ = \mathbf{k}^- = \mathbf{0}$ in the whole open contact interface. In that case a contact interface was declared open (respectively closed) if all its integration points have been detected as open (respectively closed) at the local stage. However the large discontinuity between two iterations in the value of the search direction leads the convergence trend to instabilities. Attempts were made also to carry out an independent update on each point of the contact interface, however **instabilities during the iterations were systematically encountered due to oscillations of the contact status**.

2.1 On the relevance of contact conditions on convergence rate

As discussed previously, the reference value $k_0 = \frac{E}{L_T} \mathbf{I}_d$ for the search direction parameter usually adopted in the LATIN strategy is a good candidate when dealing with perfect interfaces. However, in the case of frictional contact problems, depending on the contact conditions that may occur in a given problem due to the external loadings, **this reference value may be far from a good choice leading the strategy to a very poor convergence rate.** We show an example of this in the following for two test cases.

2.1.1 Contact in opening and closing

Here we consider the test case in [Figure 5.3](#). This time, we consider not only the case of the structure loaded with a traction load of 50 MPa, but also the case when the same loading acts in compression. In practice, we consider two cases with loads of opposite direction and make use of the reference value $k_0 = \frac{E}{L_T} \mathbf{I}_d$ for both perfect and contact interfaces. In linear elasticity with only perfect interfaces, the direction of the loading does not affect the LATIN convergence rate. The reference solutions of the problem in the two cases are shown in [Figure 5.16a](#) for the traction case and [Figure 5.16b](#) for the compression case. In the traction case all contact interfaces are open, in the compression case they result closed and the structure behaves similarly to an uncracked one.



(a) Structure in traction.

(b) Structure in compression.

[Figure 5.16](#): Structure with frictional cracks. (a): In traction. (b): In compression.

The convergences of the two problems through the LATIN iterations are shown in [Figure 5.17](#) with both the LATIN indicator η and the CRE indicator ν . As it can be clearly seen, the convergence of the problem in compression ([Figure 5.17b](#)) is several orders of magnitude better than the one in traction ([Figure 5.17a](#)). In particular, in the compression case it can be seen that the LATIN indicator and the CRE indicator are really close. In fact, when the cracks are closed they behave in practice as perfect

interfaces and the reference value k_0 ensures a good convergence rate for perfect interfaces. Instead, when they are open, ideally the interface stiffness should be set to zero, or at least a lower value with respect to the case in contact. In the opening case the LATIN indicator results far from the CRE indicator by more than one order of magnitude.

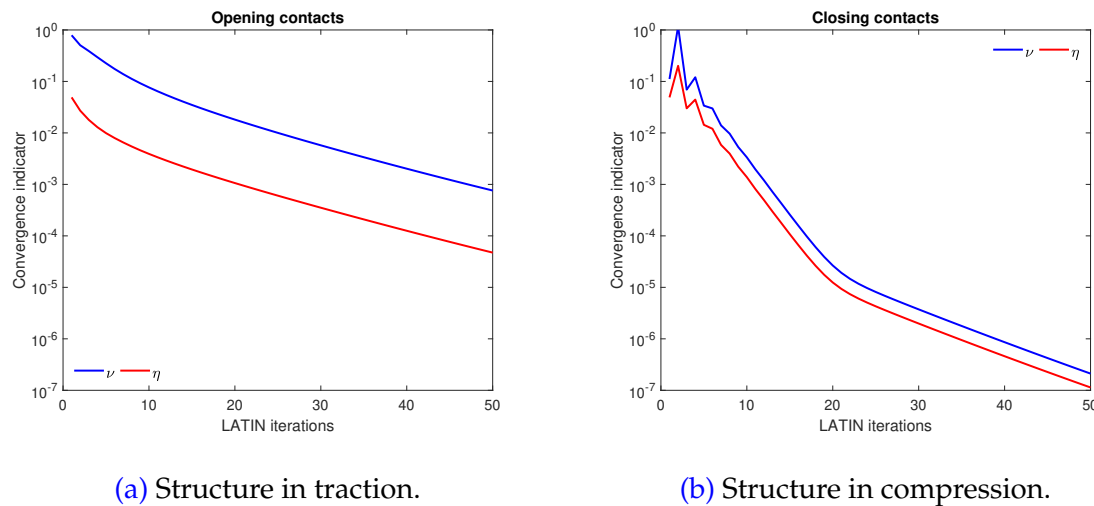


Figure 5.17: LATIN indicator η and CRE indicator ν for the problem in Figure 5.3 with reference search direction $k_0 = \frac{E}{L_T} \mathbf{I}$. (a): Traction case. (b): Compression case.

2.1.2 Layered structure with wide sliding propagation front

Here we consider the problem in Figure 4.5 in Section 4 of Chapter 4. This problem presents large contact interfaces subjected to large sliding propagation fronts over time in the tangential direction to the interface, while in the normal direction the contact always remains closed. Therefore reducing the search direction parameter in the tangential direction k_t (see (3.7) in Section 2.3.3 of Chapter 3) brings benefits as allows sliding to propagate more easily. This can be seen from Figure 5.18, where the cases with $k_t = k_0$ (Figure 5.18b) and $k_t = 0.1 k_0$ are compared.

From these two examples it is clear that the best search direction for frictional contact problems depends on the contact conditions that occur over time at the different interfaces. What we want to propose here is, **starting from a reference value k_0 , to update the search direction parameters for the different contact interfaces based on the contact status of the interfaces themselves (in space and time) along the LATIN iterations.**

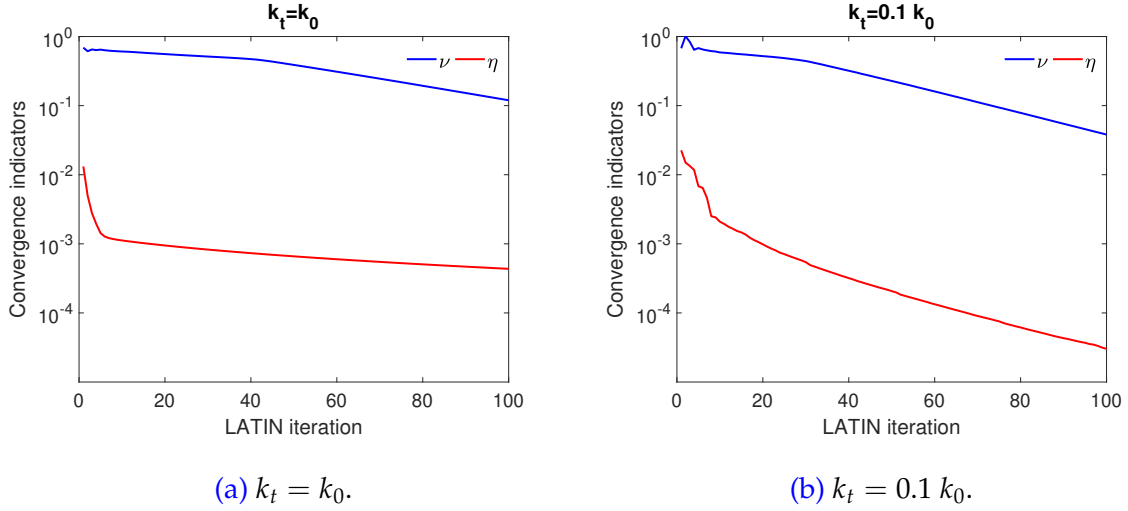


Figure 5.18: LATIN indicator η and CRE indicator ν for the problem in Figure 4.5. (a): $k_t = k_0$. (b): $k_t = 0.1 k_0$.

2.2 A strategy based on the contact status indicators

As seen previously, the reference value for the search direction parameter at interfaces $k_0 = \frac{E}{L_T} \mathbf{I}_d$ is not a good value in the case of opening interfaces and interfaces subject to a large sliding fronts. In the case of interfaces in opening, reducing the contact stiffness significantly increases convergence. Ideally, the contact stiffness in opening should be zero, but this can lead to instabilities in the iterative strategy. Similar considerations can be made for interfaces where the contact gap is closed and there is a large sliding front. In this case, the reduction of the tangential value of the stiffness allows the interfaces to "slide more easily".

These considerations can be taken into account thanks to the contact indicators C_n and C_t used in the resolution of the local stage of the LATIN, the definition of which we report again:

$$\begin{aligned}
 C_n(\underline{x}, t) &= \frac{1}{2} \left(k_n^+ \left[\underline{n} \cdot (\widehat{W}_{E'} - \widehat{W}_E) + g_0 \right] - \underline{n} \cdot (\widehat{F}_{E'} - \widehat{F}_E) \right) \\
 C_t(\underline{x}, t) &= \frac{1}{2} \left(k_t^+ \mathbf{P}_t \left[\delta \widehat{W}_{E'} - \delta \widehat{W}_E \right] - \mathbf{P}_t (\widehat{F}_{E'} - \widehat{F}_E) \right)
 \end{aligned} \tag{5.2}$$

We show now that the indicators are proportional to the tendency of the contact to be closed/open or in sticking/sliding conditions at a specific space-time position (\underline{x}, t) .

– *opening*: $C_n(\underline{x}, t) > 0$

In this case $\widehat{F}_E = \widehat{F}_{E'} = \underline{0}$, and thus we obtain $C_n(\underline{x}, t) = \frac{1}{2} k_n^+ (\underline{n} \cdot (\widehat{W}_{E'} - \widehat{W}_E) + g_0)$

g_0). With g_0 being constant, this means that the tendency to separate at position (\underline{x}, t) is proportional to $C_n(\underline{x}, t)$.

– **closed contact:** $C_n(\underline{x}, t) \leq 0$

In this case $\underline{n} \cdot (\widehat{W}_{E'} - \widehat{W}_E) + g_0 = 0$, and thus we obtain $C_n(\underline{x}, t) = \widehat{F}_E \cdot \underline{n}$. Therefore the contact pressure results proportional to $C_n(\underline{x}, t)$, that is to say the tendency to have contact at position (\underline{x}, t) is proportional to $C_n(\underline{x}, t)$.

– **sliding contact:** $C_n(\underline{x}, t) \leq 0$ and $\|\underline{C}_t(\underline{x}, t)\| - f|\underline{n} \cdot \widehat{F}_E| \geq 0$

In this case we have $\mathbf{P}_t \widehat{F}_E = -\mathbf{P}_t \widehat{F}_{E'} = f|\underline{n} \cdot \widehat{F}_E| \underline{C}_t / \|\underline{C}_t\|$, and therefore we obtain $\underline{C}_t(\underline{x}, t) = \frac{k_t^+}{2} \mathbf{P}_t (\delta \widehat{W}_{E'} - \delta \widehat{W}_E) + f|\underline{n} \cdot \widehat{F}_E| \underline{C}_t / \|\underline{C}_t\|$. Consequently, the tendency to slide at (\underline{x}, t) is proportional to $\|\underline{C}_t(\underline{x}, t)\| - f|\underline{n} \cdot \widehat{F}_E|$.

– **sticking contact:** $C_n(\underline{x}, t) \leq 0$ and $\|\underline{C}_t(\underline{x}, t)\| - f|\underline{n} \cdot \widehat{F}_E| < 0$

In this case we have $\mathbf{P}_t (\delta \widehat{W}_{E'} - \delta \widehat{W}_E) = \underline{0}$, and therefore we obtain $\underline{C}_t(\underline{x}, t) = \mathbf{P}_t \widehat{F}_E$. It is clear that, the closer $\underline{C}_t(\underline{x}, t)$ is to the sliding threshold, the closer is the contact status to incipient sliding. On the contrary, the more far is $\underline{C}_t(\underline{x}, t)$ with respect to the sliding threshold, the more the contact status is far from sliding. Consequently, the tendency to stick at (\underline{x}, t) is proportional to $\|\underline{C}_t(\underline{x}, t)\| - f|\underline{n} \cdot \widehat{F}_E|$.

Therefore, we have identified two scalar indicators in space and time, one for the normal contact and the other for the tangential contact, namely

$$\mathcal{N}(\underline{x}, t) := C_n(\underline{x}, t) \quad \text{and} \quad \mathcal{T}(\underline{x}, t) := \|\underline{C}_t(\underline{x}, t)\| - f|\underline{n} \cdot \widehat{F}_E| \quad (5.3)$$

which inform us on the contact status tendency of a contact point at space position \underline{x} and at time t . Consequently, one can think of the following strategy to update search direction parameters $k^+ = k^- = k$, in the normal and tangential direction, starting from the reference value k_0 :

Definition 5.1 (search directions update). For a contact interface $\Gamma_{EE'}$, the search direction k is updated in the following manner:

– **opening:** $\mathcal{N}(\underline{x}, t) > 0$

$$k_n(\underline{x}, t) = k_t(\underline{x}, t) = k_0 \left(1 - \alpha_n \frac{\mathcal{N}(\underline{x}, t)}{\max_{(\underline{x}, t)} \mathcal{N}(\underline{x}, t)} \right); \quad (5.4)$$

– **closed contact:** $\mathcal{N}(\underline{x}, t) \leq 0$

$$k_n(\underline{x}, t) = k_0 \left(1 + \beta_n \frac{\mathcal{N}(\underline{x}, t)}{\min_{(\underline{x}, t)} \mathcal{N}(\underline{x}, t)} \right); \quad (5.5)$$

– *sliding contact*: $\mathcal{N}(\underline{x}, t) \leq 0$ and $\mathcal{T}(\underline{x}, t) \geq 0$

$$k_t(\underline{x}, t) = k_0 \left(1 - \alpha_t \frac{\mathcal{T}(\underline{x}, t)}{\max_{(\underline{x}, t)} \mathcal{T}(\underline{x}, t)} \right); \quad (5.6)$$

– *sticking contact*: $\mathcal{N}(\underline{x}, t) \leq 0$ and $\mathcal{T}(\underline{x}, t) < 0$

$$k_t(\underline{x}, t) = k_0 \left(1 + \beta_t \frac{\mathcal{T}(\underline{x}, t)}{\min_{(\underline{x}, t)} \mathcal{T}(\underline{x}, t)} \right); \quad (5.7)$$

with $\alpha_n, \alpha_t \in [0, 1]$ and $\beta_n, \beta_t \geq 0$.

In practice, the idea is to update k proportionally to the value of the contact indicators. In the normal contact case, for a given contact interface $\Gamma_{EE'}$, when \mathcal{N} is close to zero (either positive or negative) we are basically in a condition where the contact status is not very certain and subject to possible switches from positive to negative around zero and vice versa. Therefore, it makes sense to require that when the status is uncertain to leave the search direction unchanged, or at least change it very slightly. For this reason when $\mathcal{N} \approx 0$ in Eq. (5.4) and Eq. (5.5) we have $k \approx k_0$. Conversely, when \mathcal{N} increases in absolute value, considering what shown previously about \mathcal{N} indicating the tendency to separate or have closed contact, the larger \mathcal{N} is in absolute value, the more certain we are that separation or contact will occur. In particular, in the maximum value of \mathcal{N} is where it will be more certain that there is opening contact, as well as in the minimum value (in negative) of \mathcal{N} is where it will be more certain that there will be closed contact. Under these conditions the search direction is changed the most, and from Eq. (5.4) and Eq. (5.5) it becomes respectively $k_n = k_t = k_0(1 - \alpha_n)$ and $k_n = k_0(1 + \beta_n)$. For all points, in space and time, with intermediate contact conditions between these two extreme values k varies in an affine manner between k_0 and respectively $k_0(1 - \alpha_n)$ and $k_0(1 + \beta_n)$. The same considerations for the tangential contact.

As for the choice of the coefficients α and β , they should be chosen according to the maximum and minimum value of k to be obtained after the update.

2.3 Consequences of a search direction in space and time

In the LATIN method, search directions are usually defined a priori and are constant for each interface in space and time. This makes it possible to precompute the linear operators of the linear stage of the LATIN for each subdomain and to assemble the homogenized operator, as well as to factorize them so as to be faster during the resolution.

However, let us now consider the strategy of updating search directions described

above. Let us imagine that at a certain LATIN iteration we update the search directions, both ascent and descent ones, i.e.,

$$\mathbf{k}^+ = \mathbf{k}^- = \mathbf{k}(\underline{x}, t). \quad (5.8)$$

This situation involves however certain complications:

- If at a certain LATIN iteration we update the search direction on a given contact interface $\Gamma_{EE'}$, this involves **recomputing the stiffness matrix of the subdomains which share that contact interface, as well as recomputing the homogenized operator**. And this is expensive. Moreover in this case, since $\mathbf{k}(\underline{x}, t)$ would depend on both space and time, It would be not possible to exploit a separation of variables in the integration which would increase even more the cost of computations.
- If PGD is used in the linear stage, since the residual in search direction $\underline{\delta}_E$ depends on \mathbf{k}^- , if at a certain iteration \mathbf{k}^- changes this may lead to a sudden variation of the residual $\underline{\delta}_E$, **reducing the relevance of the ROB previously created**, and may change in general the reducibility of the problem.

For the first problem one could for example make use of a separated representation in space and time, i.e., $\mathbf{k}(\underline{x}, t) = \mathbf{k}_x(\underline{x})\mathbf{k}_t(t)$, obtained by taking for example the first SVD modes of $\mathbf{k}(\underline{x}, t)$. One should expect that since contact indicators $\mathcal{N}(\underline{x}, t)$ and $\mathcal{T}(\underline{x}, t)$ are quite smooth, $\mathbf{k}(\underline{x}, t)$ should present a good reducibility. This could be used to integrate the stiffness matrix more cheaply by exploiting separation of variables during integration. Another approach might be for example to make use of RPM hyperreduction [Capaldo et al., 2017] to integrate the linear operators in space and time. However, this would still require a non-negligible computational cost, especially when numerous contact interfaces are present. And yet the problem with PGD would still remain.

In order to deal with these problems, **one can think of updating only the ascent search direction \mathbf{k}^+** , leaving unchanged \mathbf{k}^- which is used by all operators of the linear stage. The ascent \mathbf{k}^+ search direction is only adopted locally in the local stage for each interface and therefore, by varying it, it does not alter the linear stage resolution. However, one should expect that such an update, in terms of convergence improvement, would be less efficient than updating both search directions. Nevertheless, being the local stage completely local in space and time, **the adoption of a local search direction in space and time for the local stage is completely cost-free** and not expensive, and it may still bring benefits.

One last issue remains when to update and how many times. It is clear that if both \mathbf{k}^+ and \mathbf{k}^- are updated, this update should be done carefully and as few times as possible due to the considerations made previously. If one updates only \mathbf{k}^+ instead the update is cost-free, ideally one could update at each iteration. Since the proposed update of the search directions is based on the contact indicators, it is reasonable to propose to **update the search directions when the contact indicators have converged in some sense**. One can define for exaple, for each contact interface $\Gamma_{EE'}$, a relative

contact status convergence indicator \mathcal{I}_n for the normal contact status and \mathcal{I}_t for the tangential contact status between two consecutive LATIN iterations n and $n - 1$, as follows:

$$\mathcal{I}_n = \frac{\|\mathcal{N}_n - \mathcal{N}_{n-1}\|_{\Gamma_{EE'} \times [0,T]}}{\|\mathcal{N}_{n-1}\|_{\Gamma_{EE'} \times [0,T]}}, \quad \mathcal{I}_t = \frac{\|\mathcal{T}_n - \mathcal{T}_{n-1}\|_{\Gamma_{EE'} \times [0,T]}}{\|\mathcal{T}_{n-1}\|_{\Gamma_{EE'} \times [0,T]}}, \quad (5.9)$$

and to update when both \mathcal{I}_n and \mathcal{I}_t are less than a threshold \mathcal{I}_0 .

2.4 Application to the 1D benchmark problem

Here we go on to test the updating strategy previously described by considering the one-dimensional benchmark problem of [Figure 3.1a](#) described in [Section 1](#) of [Chapter 3](#), with the load case 1 of [Figure 3.1b](#). The parameters used for the problem are the same as in [Table 3.1](#). The case without DDM and PGD in the monoscale version is considered, with a reference search direction parameter (in the tangential direction) $k_0 = ES/L$. In [Figure 5.19](#) is shown the trend of the reference error indicators η_W , η_F and the CRE indicator ν for the considered problem.

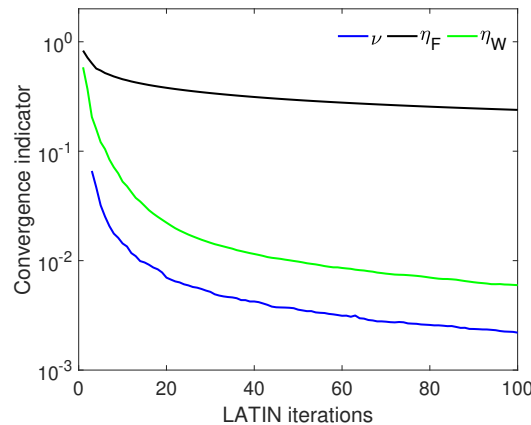


[Figure 5.19](#): Convergence indicators η_W , η_F and ν for the problem in [Figure 3.1a](#).

■ Updating $k^+ = k^-$

Here the updating strategy is tested by updating both ascent and descent search directions k^+ and k^- . We consider a convergence threshold for the (tangential) contact status $\mathcal{I}_0 = 10^{-2}$ and $\alpha_t = \beta_t = 0.9$. We start by considering to update only once when the threshold is reached.

In [Figure 5.20](#) is shown the evolution of the reference error indicators for displacements η_W ([Figure 5.20a](#)) and forces η_F ([Figure 5.20b](#)), as well as the evolution of the CRE

indicator ν (Figure 5.20c) along the LATIN iterations with and without update. It can be clearly seen the moment when the update is performed, with the errors that show an immediate reduction in the next iterations after the update and a gain in convergence rate.

In Figure 5.21 is shown, at the iteration when the updating takes place, the space-time view of the tangential contact indicator $\mathcal{T}(\underline{x}, t) = \|\underline{c}_t(\underline{x}, t)\| - f|\underline{n} \cdot \hat{\underline{F}}_E|$ (Figure 5.21a) and the resulting tangential search direction parameter in space and time $k(\underline{x}, t)$ compared with k_0 (Figure 5.21b). The evolution of $k(\underline{x}, t)$ follows, as per definition, the evolution of the contact status $\mathcal{T}(\underline{x}, t)$. Where the contact status $\mathcal{T}(\underline{x}, t) \approx 0$, the corresponding $k(\underline{x}, t)$ is close to k_0 . The modifications with respect to k_0 are higher in correspondence to the maximum and minimum values of $\mathcal{T}(\underline{x}, t)$. In between these values $k(\underline{x}, t)$ varies smoothly following the tendency to slide or stick.

An important question concerns when to perform the updating, which depends on the given value of the contact status convergence threshold \mathcal{I}_0 . With a high value for \mathcal{I}_0 the updating tends to occur earlier in the iterations, while a low value tends to delay the updating over the iterations. In Figure 5.22 is shown the evolution of the reference error η_F for three different thresholds $\mathcal{I}_0 = 10^{-1}$, $\mathcal{I}_0 = 10^{-2}$ and $\mathcal{I}_0 = 10^{-3}$. It results that updating too late brings less benefits, since with a very low threshold many iterations with k_0 are needed before updating. It results preferable to update sooner. In fact the updating is proportional to the contact indicator, and even from the first iterations we get a rough idea of when and where different contact status conditions will occur. The locations where the contact conditions are uncertain (i.e., in $\mathcal{T}(\underline{x}, t) \approx 0$) do not represent an issue since in that case k does not change significantly to affect the uncertain status in that space-time location. The change in the parameter k is smooth and even updating early should not pose convergence issues. A coarse contact status convergence criterium (e.g., 10% of relative error) should be sufficient for the purpose.

Another question concerns how often to perform the updating of the search direction. From the definition of the updating of k , that is an affine function of the contact status, it can reasonably be said that updating more times brings less benefits compared to the first time the update is performed. In fact in the first update there is a drastic change from k_0 , constant in space and time, to $k(\underline{x}, t)$ which follows the contact status trend and varies between $k_0(1 + \beta_t)$ and $k_0(1 - \alpha_t)$. If the search direction is updated a second time, k would still be varying between $k_0(1 + \beta_t)$ and $k_0(1 - \alpha_t)$ following the contact status trend, but space-time locations where k changes significantly between the two updates will be more localized and it will bring less significant contribution to the convergence gain. One could also think of updating at each iteration, since the variation of k in the update is smooth it should not pose any particular difficulties even in the first iterations where the contact status has not fully converged. In Figure 5.23 is shown the evolution of η_F with constant k_0 and by updating once or twice with an updating threshold of 10^{-2} and by updating at each iterations. The convergence gain from the second update results to be negligible from the first update. By updating at

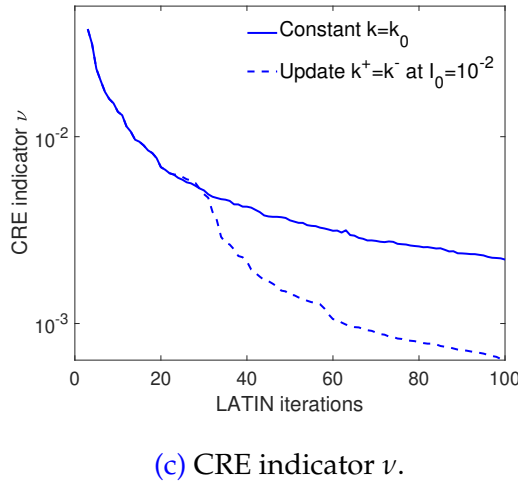
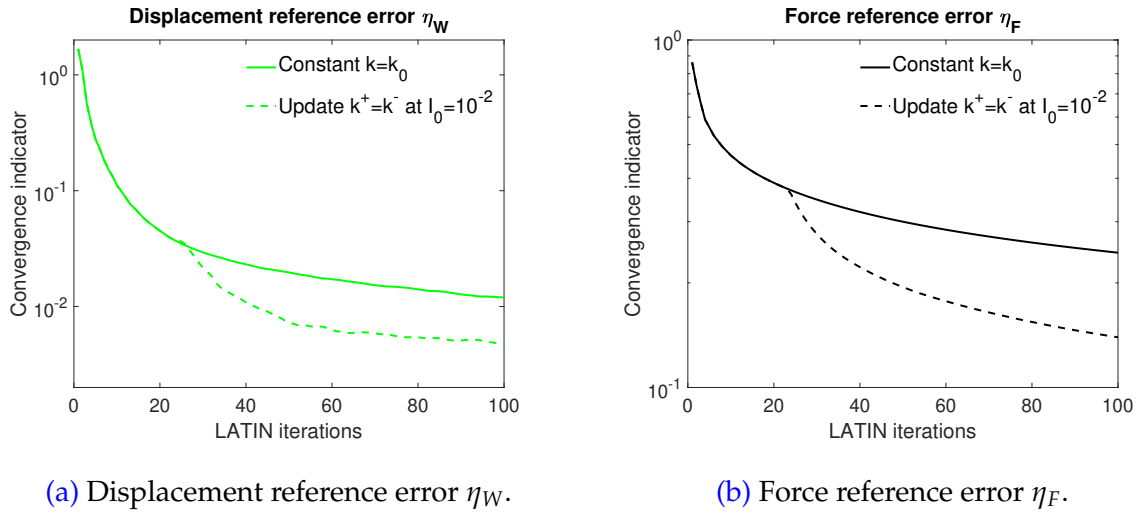
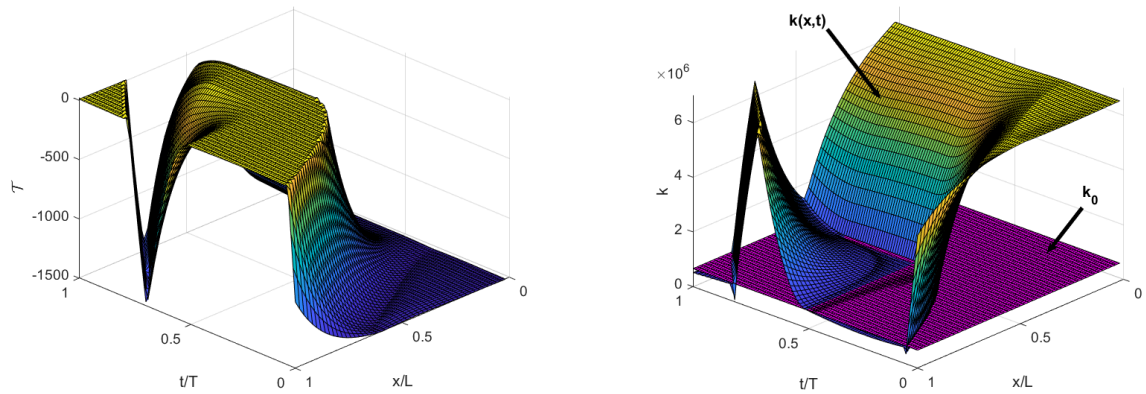


Figure 5.20: Evolution of the indicators η_W , η_F and ν for the problem in Figure 3.1a with constant search direction k_0 and with updating at a threshold $\mathcal{I}_0 = 10^{-2}$.

each iteration we have a gain in the beginning, however at the end the obtained gain is in practice the same as updating once or twice when the contact status has converged.

■ Updating only k^+

The analysis performed previously considered updating both search directions $k^+ = k^-$. However, updating k^- brings some non-trivial consequences and additional computational costs which could nullify the benefits of an update. A good compromise is to update only the ascent search direction k^+ used in the local stage, leaving k^- unchanged. The local stage is in fact local in space and time and a similar choice for k^+ is consistent with this. One expects however that the convergence gain would be lower



(a) Tangential contact status $\mathcal{T}(\underline{x}, t)$ in space and time. (b) Updated search direction $k(\underline{x}, t)$ in space and time compared to k_0 .

Figure 5.21: Tangential contact status and search direction at updating. (a): Tangential contact status $\mathcal{T}(\underline{x}, t)$. (b): Updated search direction $k(\underline{x}, t)$.

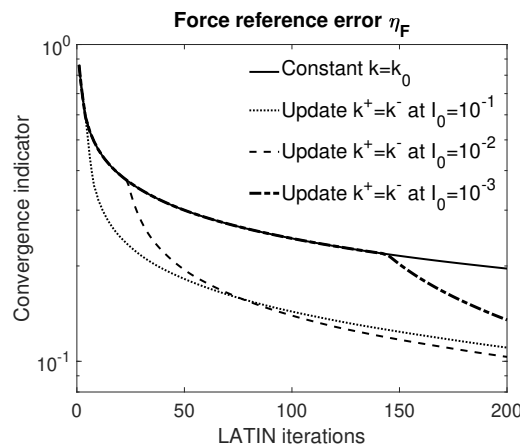


Figure 5.22: Force reference error η_F with constant k_0 and with updating at different thresholds: $\mathcal{I}_0 = 10^{-1}$, $\mathcal{I}_0 = 10^{-2}$ and $\mathcal{I}_0 = 10^{-3}$.

than in the case where both $k^+ = k^-$ are updated. This is shown in [Figure 5.24](#), where is depicted the evolution of the CRE indicator ν is in case when both $k^+ = k^-$ are updated, and in case when only k^+ is updated, with an update threshold $\mathcal{I}_0 = 10^{-2}$. Notice however that in the case when only k^+ was updated, it was necessary to reduce the relaxation parameter to $\mu = 0.5$ to make the strategy converge. Therefore in [Figure 5.24](#) are shown the convergence curves for a relaxation parameter $\mu = 0.5$.

As expected, the convergence gain in the case of only updating k^+ is lower than in the other case. However, the computational cost of the update in this case is completely

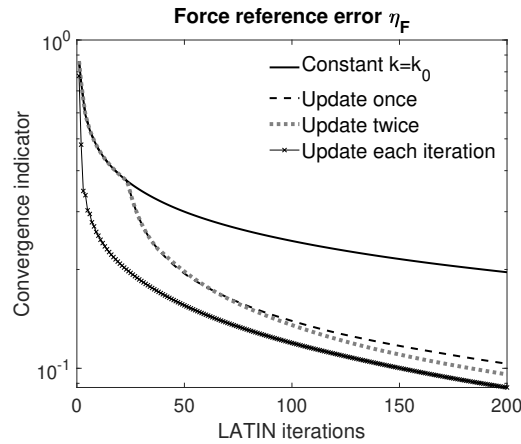


Figure 5.23: Force reference error η_F with constant k_0 and with updating once and twice with $\mathcal{I}_0 = 10^{-2}$ and by updating at each iteration.

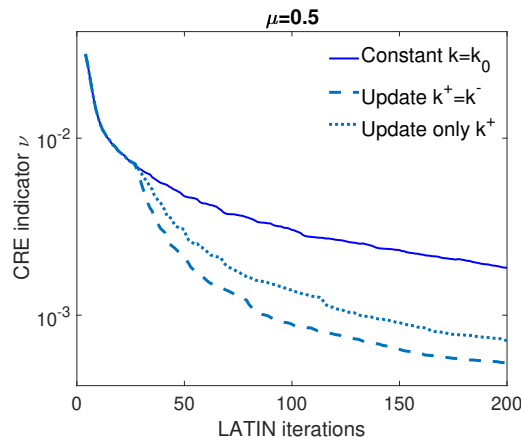


Figure 5.24: CRE indicator ν in the cases of updating both $k^+ = k^-$ and updating only k^- with a threshold $\mathcal{I}_0 = 10^{-2}$ and relaxation parameter $\mu = 0.5$.

negligible, being operated locally on the contact interfaces, and still brings improvement to the convergence of contact quantities. Note also that all the considerations made previously about when to update, how many times to perform the update and on the time-space view of $k(\underline{x}, t)$ are equally valid even in the case where only k^+ is updated. However, compared to the strategy where both $k^+ = k^-$ are updated, in this case the amount we can change k from k_0 is more limited due to convergence issues. We will come back on this point in the next section when the strategy of updating k^+ is applied to different two-dimensional frictional problems.

2.5 Application to 2D frictional contact problems

As noticed previously, the relaxation parameter puts a limitation on the choice of possible variations of the search direction k^+ from k_0 . In practice, with a relaxation parameter of $\mu = 0.8$ usually adopted, for all the different problems considered, the choice of α_n , α_t and β_n , β_t resulted limited in the range of $[0, \frac{1}{3}]$ in order to avoid divergence of the iterative strategy. Reducing the relaxation parameter to $\mu = 0.5$ widens the range to $[0, \frac{2}{3}]$. This inevitably leads to less possible gain in convergence. In Figure 5.25 is shown, for the problem with multiple opening frictional cracks of Figure 5.3, the evolution of the CRE indicator by updating at $I_0 = 0.1$ with relaxation coefficient $\mu = 0.8$ and $\mu = 0.5$ adopting the maximum possible values $\alpha_n = \frac{1}{3}$ in the first case and $\alpha_n = \frac{2}{3}$ in the second case.

As it can be noticed there is a gain, but it remains limited by the range of the possible variation of k^+ from k_0 . We also found that for all the problems considered here the updating of search directions due to β_n and β_t was practically irrelevant under these conditions. This led us to reformulate the updating strategy as follows:

Definition 5.2 (modified search directions update). For a contact interface $\Gamma_{EE'}$, the search direction parameter k^+ is updated in the following manner:

– *opening*: $\mathcal{N}(\underline{x}, t) > 0$

$$k_n^+(\underline{x}, t) = k_t^+(\underline{x}, t) = k_0(1 - \alpha_n); \quad (5.10)$$

– *sliding contact*: $\mathcal{N}(\underline{x}, t) \leq 0$ and $\mathcal{T}(\underline{x}, t) \geq 0$

$$k_t^+(\underline{x}, t) = k_0(1 - \alpha_t); \quad (5.11)$$

with $\alpha_n, \alpha_t \leq 1$ whose maximum value depends on μ .

In fact, since the choice of α_n and α_t is limited, it is not necessary to perform a smooth updating of the search directions proportional to the value of the contact indicators, but one can sharply decrease the value of k^+ at the points in space and time where opening or sliding is detected. The new updating strategy represents a simplification of the original in Definition 5.1 due to the considerations made previously. In practice the limited range of variation of k^+ , and the fact that $k^- = k_0$ is held constant in the linear stage, pose no problems in performing more drastic updating even in areas where the contact state switches between iterations. We go on now to test the new updating strategy of Definition 5.2 compared to the old one of Definition 5.1 for different test cases.

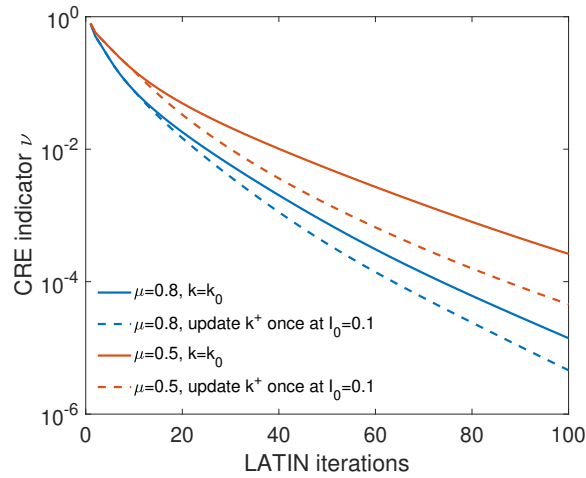


Figure 5.25: CRE indicator with updating of k^+ for the problem in Figure 5.3 with two different relaxation parameters μ .

■ Open contacts in traction

In Figure 5.26 is shown the effect of the new updating strategy for k^+ of Definition 5.2 compared with the old one. The updating for both strategies was performed once when a threshold $I_0 = 0.1$ was reached for the contact status, choosing $\alpha_n = 1/3$ in the case with $\mu = 0.8$ and $\alpha_n = 2/3$ in the case with $\mu = 0.5$.

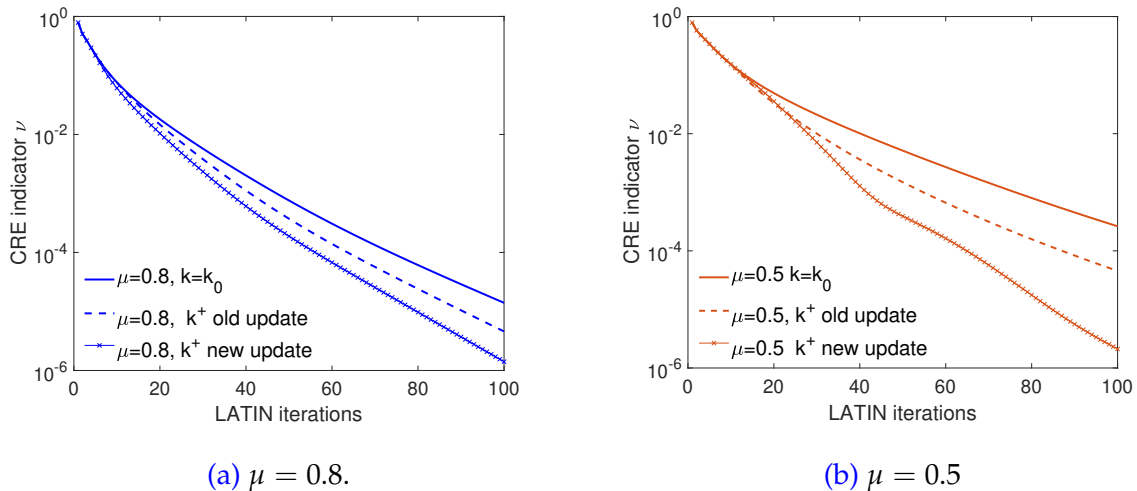


Figure 5.26: New and old updating strategy tested on the problem in Figure 5.3.

The new strategy allows maximizing the possible gain in the limited range of choice of α_n . In the case $\mu = 0.5$, the maximum possible value adoptable for α_n being higher,

there is a larger gain compared to the strategy without updating. However, the lower relaxation coefficient μ dampens this gain and in practice in all cases it has turned out that the gain in the updating for both $\mu = 0.8$ and $\mu = 0.5$ was comparable.

It was also noticed for all the considered test cases that updating, even if done from the first iterations, brings contribution only after the macroquantities have converged, unlike the previous 1D monoscale case where upgrading from the first iterations still brought contribution. In practice, as expected, the strategy of updating only influences the local convergence rate of the microquantities, which is driven by k . In the first iterations the convergence rate is instead driven by the macroproblem.

■ Open and closed contacts in compression and bending

The new updating strategy is applied here to the problem in [Figure 5.7](#), with multiple frictional cracks subjected to bending and compression, which causes the cracks to close on one side and open on the other. The updating strategy was considered with $\mu = 0.8$ and $\alpha_n = \alpha_t = \frac{1}{3}$, by updating once when $I_0 = 0.1$ was reached. As it can be seen from [Figure 5.27](#), similarly to the previous case updating improves the convergence rate of microquantities after the macroquantities have converged. Again, no significant difference was noticed when updating multiple times.

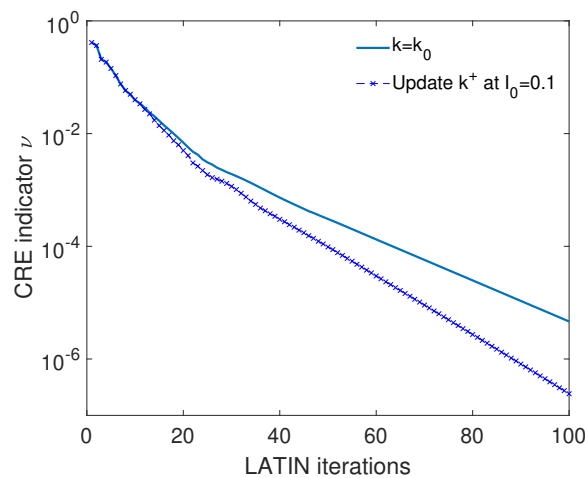


Figure 5.27: Updating strategy for the problem in [Figure 5.7](#).

■ Structure with a crack under mixed mode loading

The same strategy was also applied in the case of the structure with a crack under mixed mode loading in [Figure 5.9](#). The same conclusions as the previous cases hold, as it can be seen from [Figure 5.28](#), with an improvement of the convergence rate of micro-

quantities. Even in this case no significant differences was found by updating different times, with the strategy being robust and showing no signs of possible divergence.

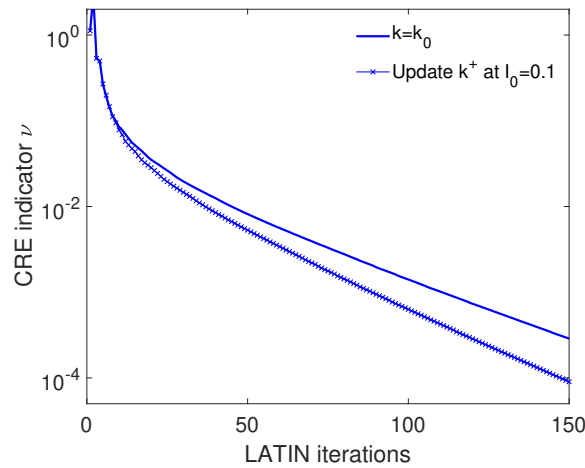


Figure 5.28: Updating strategy for the problem in Figure 5.9.

■ Layered structure with large sliding front propagation

Let us now consider the updating strategy for the type of problems we are most interested in, such as the layered structure presented in Figure 4.5 in Section 4 of Chapter 4.

In Figure 5.29 is shown the trend of the CRE indicator with and without updating. The CRE indicator for this problem results somewhat different from the other problems, with a slow convergence rate at the beginning and a higher convergence rate subsequently. This can be explained by the fact that external loads acting on the structure are oscillating around a considerable preload, and that the friction conditions are evolutionary and therefore dependent on the conditions that are established in the preload. In this case, therefore, in the first initial part at low convergence rate is established since the state of preload is not yet converged, which largely affects the convergence of the rest of the oscillations around it. When more or less the preload state has converged, the rate of convergence of the oscillating part is faster. In the initial part, in addition to the preload, the macroquantities are also made converge. Thus, as we can see, the updating mainly affects the second part, in which oscillating contact microquantities are to be converged locally accurately in space and time. The obtained gain is interesting, considering that the updating strategy is complete cost-free. As it can also be noticed, updating several times after the first updating does not bring any significant benefits. However being totally cost-free one can also think of updating several times without any divergence problems of the contact status or the iterative algorithm.

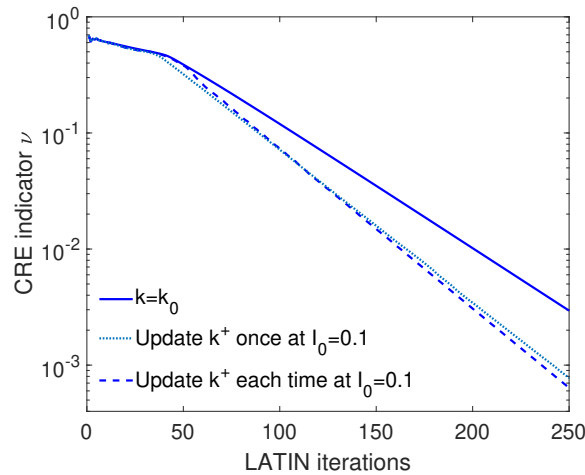
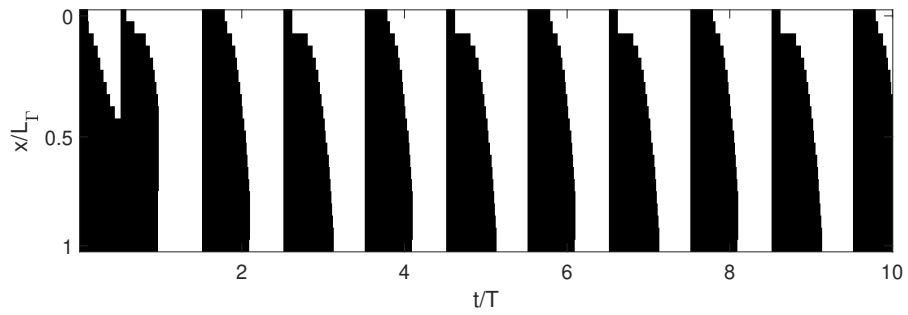


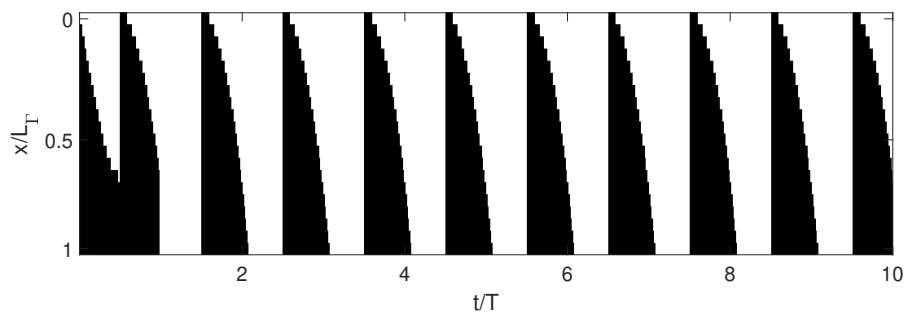
Figure 5.29: Updating strategy for the problem in Figure 4.5.

In Figure 5.30 is shown the tangential contact status over time (white for sliding and black for sticking) for the contact interface $\Gamma_{1,7}$ between substructures 1 and 7, at the moment of the first update (Figure 5.30a), and at convergence (Figure 5.30b). As it can be seen, at the moment when the update is performed, the contact status is roughly well captured, however the sliding front propagation is not accurately detected. The accurate capture of the sliding front concerns local microquantities, which are driven by k . It is in this stage that the update strategy brings contributions by improving the local convergence rate of the sliding front.

We are also especially interested in the effect that this update can have on solving microproblems with PGD. As mentioned above, changing k^+ does not alter the way we solve the linear stage, which depends on k^- . Therefore, using the PGD with the updating strategy does not bring any additional issues. In Figure 5.31 is shown the evolution of the PGD basis for substructures 7 and 12 (the same ones considered in Section 4 of the Chapter 4) along the LATIN iterations with and without the updating strategy. It can be noticed that in the first part driven by the macroproblem, the two strategies coincide and generate the same modes. In the second part, where microquantities are made converge, modes are slowly generated along the LATIN iterations. In the updating strategy it is noticed that there are slightly more modes generated, in fact the convergence rate with the updating is higher and to take this into account the strategy needs to generate modes more frequently. However, the difference is negligible after in comparison to the gain in convergence rate.



(a) Tangential contact status at first update.



(b) Tangential contact status at convergence.

Figure 5.30: Tangential contact status (white for sliding and black for sticking) in space and time for interface $\Gamma_{1,7}$. (a): at first update. (b): at convergence.

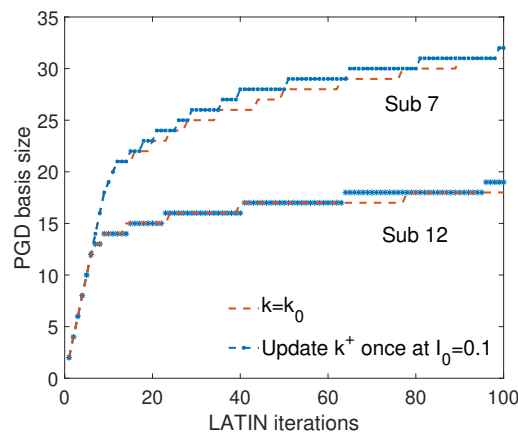


Figure 5.31: PGD basis with and without update.

3 Conclusions

In this last chapter we have dealt with two crucial points for the effectiveness of the multiscale strategy of model reduction for frictional contact problems.

The first one concerned the definition of an appropriate convergence indicator for the iterative strategy in order to stop iterations at a desired level of accuracy. Starting from the definition of a convergence indicator based on the error in constitutive relation at the interfaces introduced in [Passieux, 2008], we have proposed some modifications to make it more robust to different scenarios with different contact states. **The indicator has in all cases proved to be a reliable convergence indicator, performing much better than the classical LATIN indicator especially when the search direction changes.**

In the second part we have dealt with improving the convergence of interface contact quantities at the microscopic level. The latter are dependent solely on the search directions employed in the LATIN method. If the multiscale strategy brings benefits and a gain in convergence in the first iteration by making converge macroscopic quantities, it does not bring benefits at a later point when an accurate convergence of microscopic quantities is necessary. For this case we have introduced a strategy of updating the search directions based on the contact status.

An initial idea was to update both the $k^+ = k^- = k(x, t)$ in space and time in a smooth manner following the value of the contact indicators. However, the introduction of a search direction dependent on space and time in the linear stage involves several complications that may nullify the benefits of an eventual update. Therefore we considered the idea of updating only the ascent search direction k^+ used in the local stage. We have noticed in this case that the maximum value that we can make vary k from the reference value k_0 is limited and depends on the relaxation parameter. This led us to change the initial strategy by proposing a more sharp variation to k^+ in space and time so as to maximize the possible gain in convergence. **The strategy is completely cost-free and requires only the evaluation of contact indicators, which are available from the local stage.** We tested the strategy in several test cases with different loads and different contact states in space-time and **the strategy was robust, leading to an interesting gain in convergence rate of microquantities.**

In particular the strategy has proved to be particularly effective for the type of problem we are interested in, that is, layered structures with wide sliding contact interfaces. The strategy, in the long run allows a gain of an order of magnitude in the accurate computation of interface quantities. In particular, **the adoption of PGD in the updating strategy does not involve any problems as the linear stage remains unchanged.** The introduction of multiscale aspects to capture the behavior at the level of the whole structure, the introduction of PGD to speed up computations at the substructure level and the updating strategy to improve convergence rate at microscopic level at interfaces are therefore a robust, we could say three-level (the structure, substructures and interfaces) strategy to handle such kind of problems.

Part III

Conclusions and perspectives

Conclusions

The context of this work concerned the simulation of the loading on a part of a mooring line of a floating offshore wind turbine in order to accurately predict its fatigue life. Due to their peculiar architecture, tension and bending loadings induce complex frictional phenomena between the wires that make up the mooring lines which may induce fretting fatigue damage. A direct finite element analysis of the wire mechanics in order to predict fatigue life is computationally costly since such kind of problem involves simulating the complex evolution of contact and friction conditions between the wires of the wire rope. Progress in this regard has been made in [Bussolati, 2019] by proposing a less expensive contact algorithm suitable for this type of applications. In this thesis we have been interested in a different but complementary point of view, that is the investigation of the feasibility of model reduction methods, but also domain decomposition methods, to efficiently deal with the multiscale content of a nonlinear problem with large and multiple frictional contact interfaces.

We report here on the investigations, results and proposals made through the various chapters.

- **Chapter 1** of this thesis work consisted of a bibliographical study on the main topics involved. The chapter started with a short focused study on floating offshore wind turbines and their characterization and design, as in fact they represent the ultimate motivation of the thesis. Then we have described the mechanics of spiral strand steel wire ropes which make up their mooring lines, but their geometry and mechanics are also common to power cables or overhead conductors. We have briefly presented some analytical models capable of predicting their main mechanical properties, as well as the most common computational methods. Most of them aim to predict the behavior of spiral strands at a macroscopic level by homogenizing in some way the local interactions between the wires which make up the cables. In this work, however, the aim was to have an accurate representation of the actions between the wires. In this regard numerical models which represent single wires with beam elements guarantee an accurate representation of the contact quantities with a lower computational cost compared to finer models. However, the computational costs of a fatigue analysis on a cable section with different layers subject to complex loads varying over a long period of time are prohibitive for industrial use when general purpose beam-to-beam contact interactions are considered. In this direction small sliding beam-to-beam

contact well represents the mechanics and considerably reduces computational costs. These first two sections of [Chapter 1](#) were also crucial to understand the subsequent [Chapter 2](#), as well as the remaining chapters where simplified models inspired by these mechanics are tested.

An overview of computational contact mechanics and the main numerical strategies was then offered in order to contextualize the way the LATIN treats frictional contact. Similarities and differences of the LATIN with respect to more standard methods were highlighted, in particular concerning the augmented Lagrangian nature of the LATIN and the resolution scheme which shares similarities with alternating direction of multipliers methods and Uzawa algorithms.

The next part was devoted to model reduction, another fundamental aspect of the thesis. The usual differentiation between a posteriori and a priori methods was followed. The classical a posteriori techniques such as POD and Reduced Basis have been introduced, with then particular attention being paid to PGD. The main applications of these techniques have thus been seen in terms of contact mechanics, with or without friction. In particular, it was highlighted that most of the available a posteriori techniques deal with problems for the most parameter-dependent and where the offline part of the strategy is particularly costly. We then emphasized how some of the properties of the LATIN-PGD method, such as the coarse scale problem acting as a very coarse reduced model and then the possibility of enriching locally in the contact zones, can significantly help to handle such kind of problems.

Finally, domain decomposition methods such as the classical primal and dual approaches were shortly reported. The main difference with a mixed approach such as the one based on the LATIN were highlighted, with the latter in particular which allows a simpler and more general way to deal with frictional contact interfaces as well as other complex interface behaviors.

- An important part for the motivation of this work was represented by [Chapter 2](#), where we went on to analyze the evolution of the contact quantities of the target problem and investigate their actual reducibility potential. In particular, we went on to analyze the contact status over time between the different layers, noticing how the contact conditions are particularly critical in the outermost layers where large sliding fronts occur throughout the whole layer interface.

We investigated the potential reducibility in an interesting layer-by-layer view. It has been shown that the complexity of the contact conditions occurring in the various layers strongly influences the reductibility. As a natural consequence, the outermost layers, with more variable contact conditions, have been found to be more critical in terms of reducibility, especially in relation to the reducibility of frictional contact forces. It was investigated also how the various space modes behave, with an accentuated tendency of the modes to bring corrections in the

areas where more complex conditions occur, as for example the angular position of the bending axis from which the sliding initiates and propagates.

In general, the target problem presents a good potential reducibility. This fact is due to the particular loads they are subjected to: in fact, such structures are preloaded and subject to small oscillating loads around this preload. This reduces the formation of strong discontinuity/sliding fronts and reduces their amplitude, especially in the inner layers.

- In [Chapter 3](#) we introduced the strategy based on the LATIN to solve the frictional contact problem and introduce PGD-based model reduction. To do this, the main features of the strategy were first presented when applied to frictional contact problems on a 1D benchmark problem inspired by the mechanics of a single wire of the spiral strand cable. We highlighted the great influence that the external loading has on the problem reducibility and sliding front propagation. In particular, the limit loads we have considered (respectively load case 1 involving significant sliding front propagations, and load case 2 with small variations in sliding fronts) create comparable contact and reducibility conditions respectively to the outermost layers of the cable section analyzed in [Chapter 2](#) where the front propagates over the whole layer interface, and the innermost layers whose front remains located around the bending axis.

We therefore considered the load case 1, and the application of the strategy on the 1D problem allowed to highlight some issues for this type of problems which have not been extensively investigated previously, and for which we made some contributions in [Chapter 5](#). In particular concerning the error control in the iterative solver to accurately capture sticking/sliding discontinuity fronts (as also closed/open contact gaps) and the improvement of convergence through the search directions.

PGD was then introduced in the LATIN strategy. In order to obtain maximum performance in terms of calculation time, the enrichment of the PGD basis is a crucial aspect to accomplish this task. Considering that the addition of new modes is the most costly part of the approach, an optimized choice from this point of view requires first of all to understand what drives the convergence rate of the LATIN. The convergence of microscopic quantities at interfaces is driven by the search direction parameter k , so that even when making use of PGD the convergence rate remains bounded by that of the choice of k , and the addition of new modes at some point does not create benefits from this point of view. As a consequence it is essential to choose an appropriate enrichment criterion, such as the one in error of search direction, so as to avoid the creation of too many modes especially when far from convergence.

We also considered techniques for sorting the reduced basis such as orthonormalization (of space modes) or a downsizing iterative algorithm that progressively creates a basis close to SVD [[Giacoma et al., 2015](#)]. In this case, in the 1D ex-

ample, we did not analyze the cost of the different strategies since the problem is computationally very inexpensive, but only their ability to contain the basis size and control its quality. We have seen that the orthonormalization of space modes is not sufficient to limit and reduce the size of the reduced basis, while downsizing, which in fact operates a double orthogonalization between space modes and time modes, results more effective. However we also showed how the downsizing algorithm, by sorting and projecting the whole basis every time it is applied, requires to re-check the admissibility condition between the space modes, which can be expensive.

- In **Chapter 4** we introduced the multiscale strategy in space based on a separation of scales at interfaces, as well as the introduction of PGD in this case. The crucial aspect first highlighted is the fact that in the strategy the macroscopic quantities tend to converge rapidly in the first iterations of the LATIN iterative solver. Therefore we suggested to enrich the PGD basis due to macroquantities more frequently in the first iterations so as to quickly capture macroscale contributions and to form a relevant basis for the subsequent iterations, then capture the microscale contributions along the iterations. Applied to the 1D problem we showed that it is possible to create reduced bases of different size according to the contact conditions that are established in the various subdomains, with the first modes which well represent the first structural modes of subdomains.

Then a 2D contact problem with friction between three slender bodies subjected to compression, traction and bending alternating over time, representative of the considered application was considered. It was shown that the large sliding front across the different subdomains significantly reduced the convergence rate. The PGD basis behavior follows from what was said above, that is that the basis necessary for macroscopic quantities is created in the first iterations and is sufficient for the remaining ones, instead the basis for microscopic quantities needs to be enriched more along the iterations due to the slower convergence of microquantities. The higher complexity compared to the 1D case has also allowed an analysis of the cost of the LATIN strategy without PGD and with PGD with different sorting techniques. It was shown how the efficiency of PGD depends first of all on the enrichment criterion, as the process of adding a new couple of modes is expensive both at the moment of creation as also when the sorting algorithm operates.

- In the final **Chapter 5**, we have proposed some contributions to the control and improvement of the convergence of interface contact quantities with the LATIN strategy. This point is answering the request to control the accuracy on contact kinematics and forces as input of fretting fatigue laws for the mooring line application [[Montalvo et al., 2023](#)].

Starting from the definition of a convergence indicator based on the error in constitutive relation at the interfaces introduced in [[Passieux, 2008](#)], we have

proposed some modifications to make it more robust to different scenarios with different contact states. The indicator has in all cases proved to be a reliable convergence indicator, performing much better than the classic LATIN indicator especially when the search direction changes. Subsequently we have dealt with improving the convergence rate of interface contact quantities at the microscopic level, which are driven by the search direction parameter k . The idea was to introduce for each contact interface a search direction dependent on space and time $k(\underline{x}, t)$ by updating during the LATIN iterations with respect to the reference value k_0 based on the contact status. However, the introduction of such search direction $k^-(\underline{x}, t)$ in the linear stage involves several complications that may nullify the benefits of an eventual update. Therefore we considered the idea of updating only the ascent search direction k^+ adopted in the local stage. However, due to convergence conditions, the maximum value that we can make vary k from the reference value k_0 along the iterations is limited and depends on the relaxation parameter. Nevertheless, even with these limitations, the strategy resulted robust, leading to an interesting gain in convergence rate of microquantities for several test cases with different loads and different contact states in space and time, while being completely cost-free.

Perspectives

This work can be considered as a first feasibility investigation toward the use of model reduction and domain decomposition methods for an accurate computation of structural problems involving large contact interfaces with large sliding/propagating fronts in time. The strategy has not yet been tested on 3D cases, but this remains the objective under the following perspectives:

- An initial short-term perspective on the motivations of this work concerns the investigations of [Chapter 2](#). The analysis shows that there is a good reducibility potential for the contact quantities of a cable section in tension and bending. It is important however to also show if with a reduced representation of the contact quantities one obtains comparable result to those with full field quantities when applying a fatigue criterion such as Dang Van criterion [[Dang Van, 1999](#)], as discussed in the final section of [[Bussolati, 2019](#)].
- A medium to short term perspective concerns the separated representation of the interface fields involved in the LATIN method. When making use of PGD, a separate representation of the interface quantities is used only in the linear stage of the strategy. In the local stage, however, the contact quantities must be expressed again in full format. Furthermore, when dealing with a large number of frictional contact interfaces and a large number time steps, the local stage can become expensive considering that to solve the local tangential frictional problem one has to proceed incrementally over time. To address this issue one may think of resorting to hyperreduction, in particular hyperreduction for PGD based on the Reference Point Method (RPM) [[Capaldo et al., 2017](#)]. Different questions arise, first of all how to choose reference points in space and time so as to ensure accurate computation of the local contact problem, and how to distribute these reference points among the various interfaces, deciding where and when to enrich. Adaptive selection of these points during the iterations requires the use of a relevant error indicator, computed at a reasonable cost.
- Longer term perspectives are to continue this work, always in the framework of small deformations and sliding at the contacts between wires, but with finite rotations induced by significant cable bending, towards a real 3D application to such structures. This would need to revisit the application of the LATIN method and the PGD for beam elements in small displacements and large rotations [[Boucard,](#)

1996]. First applications in geometrical nonlinear problems have been proposed in the Siemens SAMCEF code [Scanff et al., 2022], with which LMPS has established a strong partnership. It would be interesting to extend the results of this work to IFPEN's target application. More generally, the question of developing these advanced calculation strategies in an effective and recognized research or commercial calculation code is of strategic importance in engineering. Adapting these methods to these development environments in a pragmatic way, without degrading the efficiency and quality of the strategy's results, undoubtedly raises interesting scientific questions.

- Other aspects of interest concern:
 - Choosing appropriate search directions for such slender structures modelled by beam finite elements. For slender structures in which one direction is preponderant over the others, optimal search directions require further optimization [Saavedra et al., 2012].
 - Investigate the effect of the choice of the partitioning in subdomains (layer per layer, section per section...) on the strategy performances. A good partitioning of these type of structures should try to respect its geometric structure as much as possible, in order to take maximum benefit from the different reducibility of the different layer interfaces, as shown in [Chapter 2](#). In particular a good partitioning should allow also the possibility to share the reduced basis between different subdomains with similar contact conditions, in order to maximize the efficiency of the ROM-DDM strategy.
 - An adapted representation of the multiple complex loadings. Loading histories associated with the different sea states undergone by the mooring system of a FOWT being very complex and multiple, another interesting aspect can be the exploitation of model reduction techniques [Rodriguez-Iturra et al., 2021] in order to provide a "compressed" and "adapted" representation of these loading data to the proposed ROM-DDM resolution strategy, and to drastically reduce the costs of the simulation of the fatigue life of a mooring line.

Appendices

Appendix A

Local stage for frictional contact interfaces

Here, only the displacement formulation is presented, where search directions are formulated with a force-displacement relation and the frictional contact law is integrated in sliding displacement increments. For the velocity formulation one can refer to [Nouy, 2003; Passieux, 2008].

Interface contact quantities defined by the local stage iterate denoted by $\hat{\mathbf{s}} \in \Gamma^{[0,T]}$ have to verify the following relations in addition to search directions (on both sides of the interface $\Gamma_{EE'}$):

- action-reaction principle: $\hat{\underline{F}}_E + \hat{\underline{F}}_{E'} = \underline{0}$,
- non penetration: $g_n = \underline{n} \cdot (\hat{\underline{W}}_{E'} - \hat{\underline{W}}_E) + g_0 \geq 0$ and $\underline{n} \cdot \hat{\underline{F}}_E \leq 0$,
- complementarity relation: $g_n (\underline{n} \cdot \hat{\underline{F}}_E) = 0$,
- Coulomb's law:
 - sticking: $\|\mathbf{P}_t \hat{\underline{F}}_E\| < f |\underline{n} \cdot \hat{\underline{F}}_E|$ and $\dot{\underline{g}}_t = \mathbf{P}_t (\hat{\underline{W}}_{E'} - \hat{\underline{W}}_E) = \underline{0}$,
 - sliding: $\dot{\underline{g}}_t \neq \underline{0}$, $\|\mathbf{P}_t \hat{\underline{F}}_E\| = f |\underline{n} \cdot \hat{\underline{F}}_E|$ and $\dot{\underline{g}}_t \cdot \mathbf{P}_t \hat{\underline{F}}_E \geq 0$, with $\mathbf{P}_t \hat{\underline{F}}_E \wedge \dot{\underline{g}}_t = \underline{0}$.

where f is the friction coefficient. The outward normal from Ω_E to $\Omega_{E'}$ at the current point of $\Gamma_{EE'}$ is denoted by \underline{n} . $\mathbf{P}_n = \underline{n} \otimes \underline{n}$ is the projector on the normal, and $\mathbf{P}_t = \mathbf{I}_d - \mathbf{P}_n$ is the associated orthogonal tangential projector. The time derivative of a quantity \square is classically denoted by $\dot{\square}$. The initial normal gap g_0 can be either positive or negative (if a tightening has to be modeled for instance).

By considering the general case where search direction parameters \mathbf{k}_E^+ and $\mathbf{k}_{E'}^+$ are different for each side of the interface, and by denoting with $\mathbf{h} = \mathbf{k}_E^{+^{-1}}$ and $\mathbf{h}' = \mathbf{k}_{E'}^{+^{-1}}$,

the two search directions defined on both sides of interface $\Gamma_{EE'}$ are given by:

$$\mathbf{h} \left(\widehat{\underline{F}}_E - \underline{F}_E \right) - \left(\widehat{\underline{W}}_E - \underline{W}_E \right) = \underline{0} \quad (\text{A.1})$$

$$\mathbf{h}' \left(\widehat{\underline{F}}_{E'} - \underline{F}_{E'} \right) - \left(\widehat{\underline{W}}_{E'} - \underline{W}_{E'} \right) = \underline{0} \quad (\text{A.2})$$

By subtracting these two equations with each other, projecting on the normal \underline{n} and adding the initial gap g_0 on the both sides of the resulting equation, one obtains the definition of scalar quantity C_n as follows:

$$(h_n + h'_n) C_n = \left(\widehat{\underline{W}}_{E'} - \widehat{\underline{W}}_E \right) \cdot \underline{n} + (h_n + h'_n) \left(\widehat{\underline{F}}_E \cdot \underline{n} \right) + g_0 \quad (\text{A.3})$$

$$= g_n + (h_n + h'_n) \widehat{\underline{F}}_E \cdot \underline{n} \quad (\text{A.4})$$

$$= \left(\underline{W}_{E'} - \underline{W}_E \right) \cdot \underline{n} + \left(h_n \underline{F}_E - h'_n \underline{F}_{E'} \right) \cdot \underline{n} + g_0 \quad (\text{A.5})$$

where the decomposition $\mathbf{k} = h_n \mathbf{P}_n + h_t \mathbf{P}_t$ and the action-reaction principle $\widehat{\underline{F}}_E + \widehat{\underline{F}}_{E'} = \underline{0}$ have been used.

Similarly, by projecting onto the tangential plan, it leads to:

$$\mathbf{P}_t \left(\widehat{\underline{W}}_{E'} - \widehat{\underline{W}}_E \right) + (h_t + h'_t) \mathbf{P}_t \left(\widehat{\underline{F}}_E \right) = \mathbf{P}_t \left(\underline{W}_{E'} - \underline{W}_E \right) + \mathbf{P}_t \left(h_t \underline{F}_E - h'_t \underline{F}_{E'} \right)$$

By introducing the displacement increment $\delta \widehat{\underline{W}}_E = \widehat{\underline{W}}_E(t) - \widehat{\underline{W}}_E(t - \delta t)$ and subtracting the value of the tangential displacement jump $\underline{g}_t(t - \delta t) = \mathbf{P}_t \left(\widehat{\underline{W}}_{E'}(t - \delta t) - \widehat{\underline{W}}_E(t - \delta t) \right)$ at the previous time instant on the both sides of the previous equation, one obtains the definition of the vectorial quantity \underline{C}_t :

$$(h_t + h'_t) \underline{C}_t = \mathbf{P}_t \left(\delta \widehat{\underline{W}}_{E'} - \delta \widehat{\underline{W}}_E \right) + (h_t + h'_t) \mathbf{P}_t \left(\widehat{\underline{F}}_E \right) \quad (\text{A.6})$$

$$= \delta \underline{g}_t + (h_t + h'_t) \mathbf{P}_t \left(\widehat{\underline{F}}_E \right) \quad (\text{A.7})$$

$$= \mathbf{P}_t \left(\underline{W}_{E'} - \underline{W}_E \right) + \mathbf{P}_t \left(h_t \underline{F}_E - h'_t \underline{F}_{E'} \right) - \underline{g}_t(t - \delta t) \quad (\text{A.8})$$

Proposition A.1. *Let us consider the previously defined indicators:*

$$C_n = (h_n + h'_n)^{-1} \left[g_n + (h_n + h'_n) \widehat{\underline{F}}_E \cdot \underline{n} \right]$$

$$\underline{C}_t = (h_t + h'_t)^{-1} \left[\delta \underline{g}_t + (h_t + h'_t) \mathbf{P}_t \left(\widehat{\underline{F}}_E \right) \right]$$

■ $C_n > 0 \iff$ separation occurs and: $\widehat{\underline{F}}_E = -\widehat{\underline{F}}_{E'} = \underline{0}$

■ $C_n \leq 0 \iff$ contact occurs and: $\widehat{\underline{F}}_E \cdot \underline{n} = -\widehat{\underline{F}}_{E'} \cdot \underline{n} = C_n$

- $\|\underline{C}_t\| < f |C_n| \iff$ sticking occurs and:

$$\mathbf{P}_t \left(\hat{\underline{F}}_E \right) = -\mathbf{P}_t \left(\hat{\underline{F}}_{E'} \right) = \underline{C}_t$$

- $\|\underline{C}_t\| \geq f |C_n| \iff$ sliding occurs and:

$$\mathbf{P}_t \left(\hat{\underline{F}}_E \right) = -\mathbf{P}_t \left(\hat{\underline{F}}_{E'} \right) = f |C_n| \frac{\underline{C}_t}{\|\underline{C}_t\|}$$

- Interface forces are therefore fully defined as follows:

$$\hat{\underline{F}}_E = -\hat{\underline{F}}_{E'} = \left(\hat{\underline{F}}_E \cdot \underline{n} \right) \underline{n} + \mathbf{P}_t \left(\hat{\underline{F}}_E \right) = C_n \underline{n} + \mathbf{P}_t \left(\hat{\underline{F}}_E \right)$$

- Interface displacement can be finally deduced:

$$\begin{aligned} \hat{\underline{W}}_E &= \underline{W}_E + \mathbf{h} \left(\hat{\underline{F}}_E - \underline{F}_E \right) \\ \hat{\underline{W}}_{E'} &= \underline{W}_{E'} + \mathbf{h}' \left(\hat{\underline{F}}_{E'} - \underline{F}_{E'} \right) \end{aligned}$$

with $\mathbf{h} = h_n \mathbf{P}_n + h_t \mathbf{P}_t$ and $\mathbf{h}' = h'_n \mathbf{P}_n + h'_t \mathbf{P}_t$.

■ Proof:

- If contact occurs, $g_n = 0$, $\hat{F}_n = \hat{\underline{F}}_E \cdot \underline{n} \leq 0$. Consequently, $C_n = \hat{F}_n \leq 0$. Conversely, if $C_n \leq 0$, then contact occurs. In fact let us suppose that $C_n \leq 0$ implies separation, in this case $g_n > 0$ and $\hat{F}_n = 0$, which would imply $C_n > 0$. Therefore $C_n \leq 0$ if and only if contact occurs.
- If separation occurs, $g_n > 0$, $\hat{F}_n = 0$. Consequently, $C_n = (h_n + h'_n)^{-1} g_n > 0$ since $h_n + h'_n > 0$. Conversely, if $C_n > 0$ then separation occurs. In fact let us suppose that $C_n > 0$ implies contact, from what shown previously this is a contradiction, therefore $C_n > 0$ if and only if separation occurs.
- If sticking occurs, $\delta \underline{g}_t = \underline{0}$ and $\|\hat{\underline{F}}_t\| < f |\hat{F}_n| = f |C_n|$ (since contact occurs), with $\hat{\underline{F}}_t = \mathbf{P}_t \left(\hat{\underline{F}}_E \right)$. Consequently, $\underline{C}_t = \hat{\underline{F}}_t$ and $\|\hat{\underline{F}}_t\| = \|\underline{C}_t\| < f |\hat{F}_n| = f |C_n|$. Conversely, if $\|\underline{C}_t\| < f |C_n|$, then sticking occurs. In fact, let us write:

$$\|\underline{C}_t\|^2 = (h_t + h'_t)^{-2} \|\delta \underline{g}_t\|^2 + 2 (h_t + h'_t)^{-1} \delta \underline{g}_t \cdot \hat{\underline{F}}_t + \|\hat{\underline{F}}_t\|^2 \quad (\text{A.9})$$

When sliding occurs, $\|\delta \underline{g}_t\|^2 > 0$, $\delta \underline{g}_t \cdot \hat{\underline{F}}_t \geq 0$ and $\|\hat{\underline{F}}_t\| = f |C_n|$, which would imply $\|\underline{C}_t\| \geq f |C_n|$. Therefore $\|\underline{C}_t\| < f |C_n|$ if and only if sticking occurs.

- If sliding occurs, $\delta \underline{g}_t \neq \underline{0}$ and $\|\widehat{\underline{F}}_t\| = f |\widehat{\underline{F}}_n| = f |C_n|$ (since contact occurs) and $\delta \underline{g}_t \cdot \widehat{\underline{F}}_t \geq 0$. From (A.9) it follows that $\|\underline{C}_t\| \geq f |C_n|$. Moreover if $\|\underline{C}_t\| \geq f |C_n|$, still from (A.9) it implies that sliding occurs and therefore $\|\underline{C}_t\| \geq f |C_n|$ if and only if sliding occurs. From the condition $\delta \underline{g}_t \cdot \widehat{\underline{F}}_t \geq 0$ and in order to satisfy the condition $\mathbf{P}_t \widehat{\underline{F}}_E \wedge \delta \underline{g}_t = \underline{0}$ required from the Coulomb's law, the simplest choice is to take $\widehat{\underline{F}}_t = \rho \delta \underline{g}_t$, with a scalar $\rho \geq 0$. In this case \underline{C}_t results collinear with $\delta \underline{g}_t$ and one has $\widehat{\underline{F}}_t = f |C_n| \frac{\underline{C}_t}{\|\underline{C}_t\|}$. Note that the condition $\mathbf{P}_t \widehat{\underline{F}}_E \wedge \delta \underline{g}_t = \underline{0}$ is not strictly required and other choices are possible [Zmitrowicz, 1989].

Note that the local stage is evaluated at every point of the interface and for every time step at each iteration of the LATIN method. A loop over the time steps is required. Note that the tangential force and sliding direction $\underline{C}_t / \|\underline{C}_t\|$ are explicitly determined by the tangential contact indicator \underline{C}_t . This indicator depends on the previous iteration generated by the global step that verifies the equilibrium of each subdomain and the quantity \underline{g}_t that depends on the solution calculated for the previous time step. Consequently, the tangential contact indicator \underline{C}_t must be determined incrementally, knowing the solution at the previous time step.

The displacement formulation for frictional contact has been used in [Champaney, 1996; Champaney et al., 1999; Ladevèze et al., 2002; Nouy, 2003] in the case of monotonic loadings (term \underline{g}_t is ignored in \underline{C}_t), with an incremental version of the LATIN method (LATIN solver is used at each time step, no global loop over the whole time steps at each LATIN iteration) in [Boucard et al., 2007, 2009] and with the standard approach in [Giacoma et al., 2014, 2015; Cardoso, 2019].

Appendix B

On the discretization of subdomain and interface quantities

Problems on substructures and interfaces are classically solved numerically using standard finite element discretization. Thus, the subdomain displacement field \underline{u}_E usually belongs to $\mathcal{U}_{E,h}$, that is the space of piecewise linear functions in Ω_E . Concerning the discretization of the interface quantities, a priori the interface forces \underline{F}_E belong to $\mathcal{H}^{-1/2}(\partial\Omega_E)$ and they are not necessarily continuous. A natural choice is to take for $\mathcal{F}_{E,h}$ the space of piecewise continuous functions at the interface. In practice also the interface displacements \underline{W}_E are selected in the same space $\mathcal{W}_{E,h} = \mathcal{F}_{E,h}$ of constant piecewise functions. However such a classical discretization of the interface and subdomain quantities does not verify the “inf-sup” stability conditions associated with mixed formulations [Fortin and Brezzi, 1991] and may generate spurious oscillating modes leading to numerical instabilities [Ladevèze et al., 2002; Nouy, 2003]. Ways to avoid this problem include the refinement of the substructure’s mesh (“h-version”) or the use of a higher degree of approximation p for $\mathcal{U}_{E,h}$ (“p-version”) near the boundary, as illustrated in Figure B.1. Other approaches involve boundary bubble functions [Brezzi and Marini, 2001].

Note that when we make use of a different discretization for subdomain displacements $\underline{u}_E \in \mathcal{U}_{E,h}$ and interface displacements $\underline{W}_E \in \mathcal{W}_{E,h}$, the admissibility of \underline{u}_E at the boundary $\partial\Omega_E$ has to be verified in a weak sense:

$$\forall \underline{F}^* \in \mathcal{F}_{E,h}, \int_{\partial\Omega_E} \underline{F}^* \cdot (\underline{u}_E - \underline{W}_E) dS = 0. \quad (\text{B.1})$$

In this work we make use of 8-node order 2 ($p=2$) serendipity quadratic elements in the subdomain for $\mathcal{U}_{E,h}$ (QUA8) and piecewise constant interpolation for interface quantities ($m=0$) so that in the boundary $\partial\Omega_E$ the p-version is satisfied. Note that we could also make use of the h-version by choosing order 1 finite elements (QUA4) within the subdomain and partitioning in triangles the elements located on the boundary (see h-version in Figure B.1).

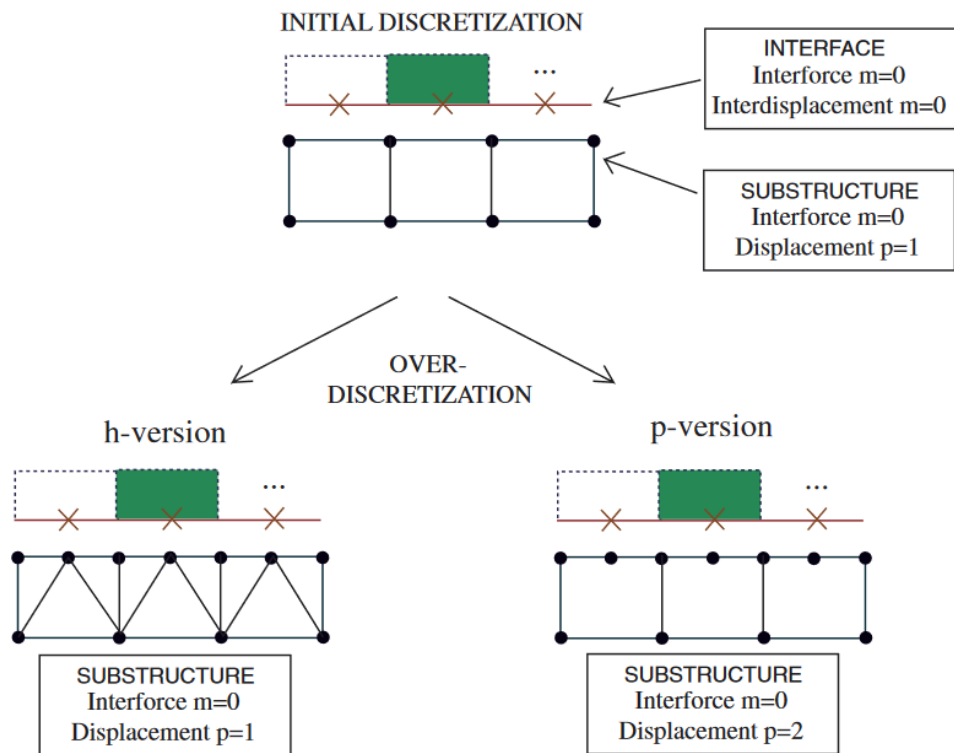


Figure B.1: Modification of the classical approximations of the interface forces (FE approximation of order m) and local displacements along the boundary of a substructure (FE approximation of order p): h-version and p-version [Ladevèze et al., 2002].

Appendix C

Some properties of the homogenized operator

1 Reminder

The microproblem introduced in [Problem 4.2](#), defined on a substructure Ω_E , can be equivalently written in a dual force formulation as [[Nouy, 2003](#)]:

Problem C.1 (*microproblem on a substructure: dual formulation*). Find $(\sigma_E, \underline{F}_E) \in \mathbf{F}_{E,\text{ad}}^{[0,T]}$ such that, $\forall (\sigma^*, \underline{F}^*) \in \mathbf{F}_{E,\text{ad},0}^{[0,T]}$,

$$\int_{\Omega_E \times [0,T]} \sigma_E : \mathbf{K}^{-1} : \sigma^* \, d\Omega dt + \int_{\partial\Omega_E \times [0,T]} \mathbf{h}^- \underline{F}_E \cdot \underline{F}^* \, dS dt = \int_{\partial\Omega_E \times [0,T]} (\mathbf{h}^- \hat{\underline{F}}_E + \hat{\underline{W}}_E + \tilde{\underline{W}}_E^M) \cdot \underline{F}^* \, dS dt,$$

with $\mathbf{h}^- = \mathbf{k}^{-1}$.

From the linearity of the previous problem, the following homogenized (linear) operator has been defined:

$$\underline{F}_E^M = \mathbf{L}_E^F(\tilde{\underline{W}}_E^M) + \hat{\underline{F}}_{E,d}^M, \quad (\text{C.1})$$

with $\tilde{\underline{W}}_E^M \in \mathcal{W}_E^{[0,T],M}$ and $\hat{\underline{F}}_{E,d}^M$ which depends only on $f_{-d|_{\Omega_E}}$ and $\hat{\mathbf{s}}_E$. We remind also that, knowing the Lagrange multiplier $\tilde{\underline{W}}_E^M$, it is possible to solve the microproblem on Ω_E and to determine $\mathbf{s}_E = (\underline{W}_E, \underline{F}_E)$ knowing $\hat{\mathbf{s}}_E$.

There exists also a localization operator \mathbf{L}_E^s from $\mathcal{W}_E^{[0,T],M}$ to $\mathbf{S}_{E,\text{ad}}^{[0,T]}$ such that:

$$\mathbf{s}_E = \mathbf{L}_E^s(\tilde{\mathbf{W}}_E^M) + \hat{\mathbf{s}}_{E,d},$$

with $\hat{\mathbf{s}}_{E,d}$ which depends on $\hat{\mathbf{s}}_E$ and $\underline{f}_{-d}|_{\Omega_E}$.

2 Properties of the homogenized operator

At the linear stage, the distribution \underline{F}_E^M on the boundary $\partial\Omega_E$ is in equilibrium with $\underline{f}_{-d}|_{\Omega_E}$, and it belongs to the space:

$$\overline{\mathcal{F}}_{E,\text{ad}}^{[0,T],M} = \left\{ \underline{F}_E^M \in \mathcal{F}^{[0,T],M} \mid \forall \underline{\alpha}_E \in \mathcal{R}_E^{[0,T]}, \int_{\partial\Omega_E \times [0,T]} \underline{F}_E^M \cdot \underline{\alpha}_E \, dSdt = \int_{\Omega_E \times [0,T]} \underline{f}_{-d} \cdot \underline{\alpha}_E \, d\Omega dt \right\},$$

where $\mathcal{R}_E^{[0,T]} = \left\{ \underline{\alpha}_E \in \mathcal{U}_E^{[0,T]} \mid \varepsilon_E(\underline{\alpha}_E) = \underline{0} \right\}$ represents the space of the infinitesimal rigid body modes of Ω_E . We also designate with $\overline{\mathcal{F}}_{E,\text{ad},0}^{[0,T],M}$ the corresponding space for homogeneous conditions.

■ **Proof:** The solution of the microproblem necessarily verifies:

$$\forall \underline{\alpha}_E \in \mathcal{R}_E^{[0,T]}, \int_{\partial\Omega_E \times [0,T]} \underline{F}_E^M \cdot \underline{\alpha}_E \, dSdt = \int_{\Omega_E \times [0,T]} \underline{f}_{-d} \cdot \underline{\alpha}_E \, d\Omega dt.$$

By definition of the macrospace, it also results that $\mathcal{R}_E^{W,[0,T]} \subset \mathcal{W}_E^{[0,T],M}$, with $\mathcal{R}_E^{W,[0,T]}$ being the trace of the displacements of $\mathcal{R}_E^{[0,T]}$ on the boundary $\partial\Omega_E$. The micro-macro uncoupling property (4.3) enables to write:

$$\forall \underline{\alpha}_E \in \mathcal{R}_E^{[0,T]}, \int_{\partial\Omega_E \times [0,T]} \underline{F}_E \cdot \underline{\alpha}_E \, dSdt = \int_{\partial\Omega_E \times [0,T]} \underline{F}_E^M \cdot \underline{\alpha}_E \, dSdt,$$

which terminates the proof.

Proposition C.1. *The operator \mathbf{L}_E^F :*

- has its image on $\overline{\mathcal{F}}_{E,\text{ad}}^{[0,T],M}$,
- is indefinite and its kernel is $\mathcal{R}_E^{W,[0,T]}$,
- is a bijection between the quotient space $\overline{\mathcal{W}}_E^{M,[0,T]} = \mathcal{W}_E^{[0,T],M} / \mathcal{R}_E^{W,[0,T]}$ and $\overline{\mathcal{F}}_{E,\text{ad},0}^{[0,T],M}$,
- is positive with respect to the work bilinear form on the boundary $\partial\Omega_E$.

■ **Proof:** Let $\mathbf{s}_E = \mathbf{L}_E^s(\tilde{\mathbf{W}}_E^M)$, we have therefore $\mathbf{s}_E \in \mathbf{S}_{E,\text{ad},0}^{[0,T]}$ which verifies the search direction:

$$\forall \underline{F}^* \in \mathcal{F}_E^{[0,T]}, \int_{\partial\Omega_E \times [0,T]} (\mathbf{h}^- \underline{F}_E + \underline{W}_E - \tilde{\mathbf{W}}_E^M) \cdot \underline{F}^* \, dSdt = 0. \quad (\text{C.2})$$

\mathbf{s}_E is solution of the following variational problem: find $(\sigma_E, \underline{F}_E) \in \mathbf{F}_{E,\text{ad}}^{[0,T]}$ which verify, $\forall (\sigma^*, \underline{F}^*) \in \mathbf{F}_{E,\text{ad},0}^{[0,T]}$

$$\int_{\Omega_E \times [0,T]} \sigma_E : \mathbf{K}^{-1} : \sigma^* \, d\Omega dt + \int_{\partial\Omega_E \times [0,T]} \mathbf{h}^- \underline{F}_E \cdot \underline{F}^* \, dSdt = \int_{\partial\Omega_E \times [0,T]} \tilde{\mathbf{W}}_E^M \cdot \underline{F}^* \, dSdt.$$

By injecting \mathbf{s}_E as a virtual field in this formulation and taking into account the micro-macro uncoupling property, we have:

$$\int_{\partial\Omega_E \times [0,T]} (\tilde{\mathbf{W}}_E^M) \cdot \underline{F}_E \, dSdt = \int_{\partial\Omega_E \times [0,T]} (\tilde{\mathbf{W}}_E^M) \cdot \mathbf{L}_E^F(\tilde{\mathbf{W}}_E^M) \, dSdt.$$

Since \mathbf{K} and \mathbf{h}^- are positive definite, as a consequence it results that \mathbf{L}_E^F is positive. Moreover, if $\mathbf{L}_E^F(\tilde{\mathbf{W}}_E^M) = \underline{0}$, then $\sigma_E = \underline{F}_E = \underline{0}$. The constitutive relation $\sigma_E = \mathbf{K} : \varepsilon_E$ implies $\varepsilon_E = \underline{0}$, that is to say $\underline{W}_E \in \mathcal{R}_E^{W,[0,T]}$. The search direction (C.2) gives $\underline{W}_E = \tilde{\mathbf{W}}_E^M$, and consequently $\tilde{\mathbf{W}}_E^M \in \mathcal{R}_E^{W,[0,T]}$. Therefore we have $\text{Ker}(\mathbf{L}_E^F) = \mathcal{R}_E^{W,[0,T]}$. \mathbf{L}_E^F defining an injection of $\overline{\mathcal{W}}_E^{M,[0,T]}$ over $\overline{\mathcal{F}}_{E,\text{ad},0}^{[0,T],M}$, spaces of the same finite dimension, it also realizes a bijection between $\overline{\mathcal{W}}_E^{M,[0,T]}$ and $\overline{\mathcal{F}}_{E,\text{ad},0}^{[0,T],M}$.

Appendix D

Downsizing stage

Algorithm 7: Downsizing stage

for each substructure Ω_E **do**

 ■ **Input:**

- current basis of size p : $\{\underline{L}_{E,k}, \lambda_{E,k}\}_{k=1}^p$
- relative amplitude cut-off: ϵ

 ■ **Output:**

- downsized basis of size $q \leq p$: $\{\underline{L}_{E,m}, \lambda_{E,m}\}_{m=1}^q$

 ■ **Downsizing algorithm** [Giacoma et al., 2015]:

for $n = 1$ to n_{\max} **do**

- sort modes such that $\|\lambda_{E,1}\|_{[0,T]} \geq \dots \geq \|\lambda_{E,p}\|_{[0,T]}$

for $i = p$ down to 2 **do**

for $j = 1$ to $i - 1$ **do**

- project time mode: $\alpha = \langle \lambda_{E,j}, \lambda_{E,i} \rangle_{[0,T]} / \langle \lambda_{E,j}, \lambda_{E,j} \rangle_{[0,T]}$
- update corresponding space mode: $\underline{L}_{E,j} \leftarrow \underline{L}_{E,j} + \alpha \underline{L}_{E,i}$
- subtract projected component: $\lambda_{E,i} \leftarrow \lambda_{E,i} - \alpha \lambda_{E,j}$
- project space mode: $\beta = \langle \underline{L}_{E,j}, \underline{L}_{E,i} \rangle_{\partial\Omega_E} / \langle \underline{L}_{E,j}, \underline{L}_{E,j} \rangle_{\partial\Omega_E}$
- update corresponding time mode: $\lambda_{E,j} \leftarrow \lambda_{E,j} + \beta \lambda_{E,i}$
- subtract projected component: $\underline{L}_{E,i} \leftarrow \underline{L}_{E,i} - \beta \underline{L}_{E,j}$
- normalize $\underline{L}_{E,j} \leftarrow \underline{L}_{E,j} / \|\underline{L}_{E,j}\|_{\partial\Omega_E}$ and update $\lambda_{E,j} \leftarrow \lambda_{E,j} \|\underline{L}_{E,j}\|_{\partial\Omega_E}$

- normalize $\underline{L}_{E,i} \leftarrow \underline{L}_{E,i} / \|\underline{L}_{E,i}\|_{\partial\Omega_E}$ and update $\lambda_{E,i} \leftarrow \lambda_{E,i} \|\underline{L}_{E,i}\|_{\partial\Omega_E}$

for $i = p$ down to 1 **do**

if $\|\lambda_{E,i}\|_{[0,T]} < \epsilon \|\lambda_{E,1}\|_{[0,T]}$ **then**

- eliminate $\underline{L}_{E,i}$ and $\lambda_{E,i}$
- decrease basis size: $p \leftarrow p - 1$

- set $q = p$
-

Appendix E

Extended abstract in french

Dans le contexte des défis posés par la transition énergétique, le développement de l'éolien *offshore* attendu au cours des prochaines années est considérable: de 6,5 GW de capacité installée actuelle à un objectif de 16,5 GW d'ici 2030 [GWEC, 2023]. Parmi les structures *offshore*, les éoliennes offshore flottantes (*Floating Offshore Wind Turbine*, FOWT) présentent l'avantage de pouvoir être installées dans des eaux plus profondes, de capter des vents plus constants et de nécessiter moins de matériel et des processus d'installation plus simples que les structures à fondations fixes [GWEC, 2023]. L'exploitation des FOWT nécessite le développement de concepts combinant des turbines de forte puissance (environ 22 MW en moyenne [IEA, 2023]) avec des systèmes d'ancrage adaptés pour les connecter au fond marin, ainsi que des solutions adaptées pour les connecter au réseau. Parmi les défis à relever pour ces connexions, le contrôle et la prédiction des événements de rupture des lignes d'ancrage ainsi que l'optimisation des chargements sur les systèmes de câbles électriques qui sont soumis aux mouvements du flotteur et aux courants sont cruciaux car les charges sont incertaines et fortement non linéaires.

Une FOWT est essentiellement composée d'une éolienne montée sur une fondation, qui est ancrée au fond marin par des lignes d'ancrage qui limitent ses mouvements et ses rotations. Ce rôle de maintien en position des lignes d'amarrage assure la production opérationnelle de l'éolienne et préserve les câbles électriques et autres éoliennes installées à proximité. Les lignes d'amarrage peuvent être composées de chaînes, de câbles spiralés monotoron en acier ou, plus récemment, de câbles en fibres synthétiques. Malgré leur large application, les chaînes sont à l'origine de nombreuses défaillances, principalement en raison de flexion hors plan et de corrosion. Le comportement à long terme des câbles en fibres pour les applications de lignes d'ancrage permanentes est toujours étudié [Davies et al., 2008; Sørnum et al., 2023] en raison de leur comportement non linéaire complexe impliquant éventuellement des phénomènes de fluage. Dans ce contexte, les câbles spiralés monotoron en acier constituent toujours une solution intéressante et courante de lignes d'ancrage pour les FOWT, comme l'illustre leur utilisation pour le parc éolien Hywind Tampen [ArcelorMittal, 2021].

Malgré les avantages des structures flottantes par rapport aux structures fixes, les

lignes d'ancrage restent un point faible: les défaillances de ces lignes sont un problème important, entraînant des opérations de maintenance et de réparation complexes et coûteuses. En particulier, les défaillances par fatigue des câbles d'acier près des extrémités des embases sont courantes, car ces zones sont soumises à des chargements complexes de tension et de flexion dues au mouvement des vagues au fil du temps, provoquant une fatigue de frottement entre les fils d'acier [Fontaine et al., 2014]. Cependant, leur espérance de vie en fatigue n'est pas clairement établie, en raison d'une approche basée encore aujourd'hui sur des lois empiriques [Rossi, 2005; Maljaars and Misiak, 2021]. La réponse mécanique du câble dépend fortement des interactions de contact par frottement entre les fils, et la fatigue est en grande partie déterminée par les conditions de contact par frottement locales entre deux fils qui se croisent provoquant des phénomènes de *fretting fatigue* [Montalvo et al., 2023]. Comme ces câbles peuvent subir une flexion importante sous l'effet des mouvements du flotteur, les nonlinéarités géométriques doivent également être prises en compte.

Un autre contexte pour lequel une modélisation par éléments finis multi-échelle similaire pourrait également être utile est celui des câbles électriques dynamiques (c'est-à-dire soumis au mouvement des fondations flottantes et aux sollicitations dues aux vagues et aux courants marins) entre les éoliennes flottantes. Les câbles électriques sont généralement triphasés, les trois conducteurs étant des assemblages de fils de cuivre ou d'aluminium, enroulés en hélice autour d'un fil central en toron spiralé. Ils sont entourés d'une couche d'isolant polymère et d'une feuille métallique pour assurer une isolation électrique complète et une étanchéité hydraulique. L'ensemble est entouré de gaines et de couches d'armures métalliques pour reprendre les sollicitations de traction mécanique.

Dans la littérature, la plupart des travaux sur la conception de câbles spiralés monotoron pour les FOWT concernent l'optimisation de la configuration globale d'un câble (sections de masses linéaires différentes et flotteurs), en utilisant des simulations hydrodynamiques avec des solveurs dédiés pour satisfaire certains états limites (conditions extrêmes [Poirette et al., 2017] ou fatigue [Rentschler et al., 2019]). A cette échelle, un modèle de câble homogénéisé est généralement utilisé (voir par exemple [Leroy et al., 2017] ou [Saadat and Durville, 2023]) pour les câbles spiralés basés sur une cinématique de poutre ou de barre. L'objectif de cette conception globale, pour un état environnemental donné, est de rechercher la configuration la moins coûteuse tout en limitant la courbure et l'allongement, et en évitant la compression.

Une limitation majeure de ces approches est que les états limites (seuils maximaux admissibles) sont basés sur les connaissances empiriques des constructeurs (pas forcément représentatives des conditions futures de ferme flottante) et/ou sur des essais expérimentaux difficilement extrapolables. De plus, ces approches ne distinguent pas les états limites pour chaque composant du câble. Pour y remédier, des travaux ont été menés pour proposer des modèles éléments finis simulant le chargement sur les composants du câble, en ayant néanmoins recours à des simplifications appropriées en raison du coût de calcul élevé des simulations requises [Young et al., 2018; Nicholls-Lee et al., 2021].

Proposer un modèle à une échelle de description plus fine, à l'échelle des torons, des fils ou des composants d'un câble, peut être nécessaire mais conduit à des simulations dont les coûts de calcul deviennent rapidement prohibitifs. La complexité vient notamment du fait que les historiques de tension et de flexion d'un câble se traduit par des glissements relatifs entre ses composants, entraînés par des phénomènes de contact et de frottement. Il est donc particulièrement difficile d'établir des règles de conception basées sur des tests expérimentaux simplifiés pour ce type de conditions (contrairement au cas de la tension pure). Cette difficulté est susceptible d'entraîner des taux de défaillance dépassant les limites attendues. Remplacer ces lois empiriques par une modélisation multi-échelle, enrichie par la physique décrivant le comportement de chaque composant du câble, est nécessaire, au moins pour accroître le niveau de compréhension des mécanismes essentiels à prendre en compte pour la conception de telles structures. Un calcul hydrodynamique à l'échelle globale du câble permet d'identifier les zones critiques de traction et de flexion. Il est alors possible d'exploiter un modèle local à plus petite échelle, à l'échelle des composants, torons et fils pour une section d'un câble de longueur métrique. Cependant, un modèle numérique local capable d'estimer correctement ce qui se passe à l'intérieur d'un câble soumis à la tension et à la flexion, dans un compromis entre précision et coût de calcul, fait encore défaut dans l'industrie.

Une avancée dans cette direction a été réalisée dans [Bussolati, 2019; Bussolati et al., 2019; Guidault et al., 2019; Bussolati et al., 2020; Guidault et al., 2021], où un modèle par éléments finis de cette étude de cas a été développé pour simuler efficacement le chargement sur une partie d'une ligne d'ancrage d'une FOWT pour un état de mer donné. Il a été montré qu'en supposant de petits glissements mais de grandes rotations entre les fils du câble (modélisés par des éléments poutre), le modèle proposé permettait de prédire la mécanique des fils avec un coût de calcul réduit par rapport à un algorithme de contact et de frottement en grands glissements (voir aussi [Guiton et al., 2022] pour une comparaison de ce modèle à ceux en grands glissements et leur corrélation avec des résultats expérimentaux).

L'objectif de [Bussolati, 2019] était de proposer un outil qui prenne en compte la tension et la flexion et prédise les dommages de fatigue le long de chaque ligne d'ancrage, en considérant les variations de contraintes locales liées aux interactions de contact entre les fils. Cependant, l'utilisation de ce modèle dans un cadre industriel, prenant en compte le très grand nombre de cas de chargement représentant les différents états de vent et de mer sur une période de plusieurs années, nécessite l'utilisation de stratégies numériques alternatives, efficaces et robustes. Dans cette perspective, l'utilisation de techniques de réduction de modèles pour réduire encore le temps de calcul de ce type de problème peut être une solution intéressante.

Au fil des années, les modèles d'ordre réduit (*Reduced Order Model*, ROM) se sont révélés être des outils fiables pour réduire la complexité de calcul dans le contexte de problèmes linéaires et non linéaires, et consistent à construire une base d'ordre réduit (*Reduced Order Basis*, ROB) dans laquelle sont projetées les équations aux dérivées partielles du problème [Chinesta et al., 2011; Hesthaven et al., 2016]. Ces méthodes

permettent un gain de temps de calcul de plusieurs ordres de grandeur, notamment lorsque la dimension du problème est grande, en espace, en temps ou en paramètres. Néanmoins, l'application de la réduction de modèle pour des problèmes de structure impliquant un grand nombre d'interactions de contact par frottement évolutives et fournissant en sortie des quantités de contact et de frottement avec une précision garantie reste une question largement ouverte [Giacoma et al., 2015; Balajewicz et al., 2016; Fauque et al., 2018; Cardoso et al., 2018; Benaceur et al., 2020].

Les méthodes ROM se distinguent par la manière dont la ROB est construite. Une première famille de techniques, appelées méthodes *a posteriori*, implique une phase d'apprentissage, dite phase *offline*, où le problème d'ordre complet est résolu pour certains instants de temps ou valeurs de paramètres particuliers, générant ce que l'on appelle des *snapshots*. Les *snapshots* sont ensuite utilisés pour créer une ROB sur laquelle projeter les équations d'ordre complet et obtenir un modèle d'ordre réduit. La manière la plus classique d'obtenir une ROB à partir d'un ensemble donné de snapshots est la *Proper Orthogonal Decomposition* (POD) [Chatterjee, 2000]. Néanmoins, la qualité de la ROM est fortement affectée par la représentativité de la ROB, en particulier pour les problèmes fortement non linéaires. Une deuxième famille de techniques ROM consiste à rechercher la solution du problème ciblé dans l'espace d'une ROB cohérente construite progressivement par un algorithme dédié lors de la phase de résolution. Cela représente les méthodes de réduction de modèle *a priori*, où aucune phase d'apprentissage *offline* n'est requise. A cette famille appartient la *Proper Generalized Decomposition* (PGD) [Nouy, 2010; Chinesta et al., 2011].

Une ROB prédéterminée ne permet pas de capturer facilement et efficacement les phénomènes multi-échelles non réguliers et propagatifs qui se produisent aux interfaces de contact : les zones de glissement, d'adhérence et de séparation étant difficiles à suivre. Pour cette raison, une approche *a priori* basée sur la PGD [Nouy, 2010] peut représenter un moyen plus efficace de traiter les problèmes de contact par frottement grâce à un modèle d'ordre réduit qui permet d'enrichir la décomposition généralisée propre au cours du calcul pour tenir compte de l'évolution des conditions de contact par frottement.

De plus, les câbles toronnés présentent une géométrie structurée et présentent naturellement un comportement multi-échelle. A l'échelle macroscopique, leur comportement dépend des variations de tension et de flexion associées aux chargements environnementaux, variant généralement autour de valeurs moyennes (elles sont représentées par des processus gaussiens dans des logiciels multiphysiques dédiés à l'offshore comme DeepLines WindTM [DeepLines, Principia] ou OpenFAST [OpenFAST, NREL]). Ce comportement est caractérisé par une distribution des efforts avec des gradients selon la couche de fils (par exemple, augmentation de la pression de contact de la couche externe au fil central) et selon la position relative par rapport à l'axe de flexion (glissement maximal au niveau de l'axe de flexion et décroissant vers les positions d'arc externe et interne). A l'échelle microscopique, le comportement dépend des phénomènes de frottement entre les fils composant le câble. Une stratégie de calcul multi-échelle de type décomposition de domaine (*Domain Decomposition Method*,

DDM) est donc examinée afin d'améliorer encore les performances. On s'intéresse en particulier à la DDM mixte [Ladevèze and Nouy, 2003; Ladevèze et al., 2007; Ladevèze et al., 2010] basée sur la méthode LATIN [Ladevèze, 1999].

La méthode LATIN présente un traitement robuste des conditions de contact, partageant des similitudes avec les approches de type lagrangien augmenté [Simo and Laursen, 1992], et conduit naturellement à une DDM mixte. De plus, la formulation globale de la méthode en espace-temps permet d'utiliser la réduction de modèle basée sur la PGD pendant les calculs, en créant et en adaptant (c'est-à-dire en ajoutant ou en récupérant certains modes) des bases réduites par sous-structure à la volée pour mieux suivre les fronts de glissement et les phénomènes propagatifs. L'introduction d'une stratégie multi-échelle dans le cadre de la LATIN est cohérente avec la physique des problèmes de contact, dans laquelle des phénomènes de différentes longueurs d'onde interagissent : les solutions locales aux interfaces de contact présentent des effets de gradient élevés avec une longueur d'onde courte par rapport à la longueur caractéristique de la structure [Giacoma et al., 2014; Guidault et al., 2023]. En tirant parti de ce constat, le problème grossier de la DDM permet de capturer efficacement le comportement du problème au niveau de la structure, en se concentrant ensuite sur la capture des variations de contact locales aux interfaces de contact.

L'objectif de cette thèse est de proposer une approche de réduction de modèle adaptée à ce type de problème, réduisant au maximum le temps de calcul tout en représentant fidèlement les informations caractéristiques utiles. Le point crucial de la thèse est que le modèle réduit devra représenter très fidèlement les informations critiques situées sur les interfaces de frottement entre les fils car, en dehors de conditions environnementales particulières comme la corrosion, la fatigue des câbles toronnés est largement déterminée par le phénomène de *fretting fatigue* entre les fils [Montalvo, 2023; Montalvo et al., 2023].

Le développement d'outils de réduction de modèle et de DDM est généralement très intrusif et nécessite l'utilisation d'un code de calcul relativement "ouvert". Les développements récents dans les contextes industriels incluent la réduction de modèles basée sur la technique LATIN-PGD pour les problèmes non linéaires implémentée dans le logiciel Simcenter SAMCEF de Siemens [Scanff et al., 2022], ou la DDM mixte basée sur la méthode LATIN implémentée dans Code_Aster d'EDF R&D [Oumaziz et al., 2017; Oumaziz et al., 2018]. Ici, nous travaillons et développons dans SCoFiEIDD (*Structure Computation by Finite Elements and Domain Decomposition*), un code MATLAB interne, afin d'illustrer la faisabilité de l'approche à travers des exemples simplifiés 2D représentatifs de différentes couches de fils d'un segment de câble d'ancrage en contact frottant les unes avec les autres.

Pour illustrer la faisabilité de la méthode, la première étape consiste à vérifier la possibilité de réduire la solution d'un calcul de tension et de flexion sur une section de câble de longueur métrique avec le modèle développé et décrit dans [Bussolati, 2019; Bussolati et al., 2019; Guidault et al., 2019; Bussolati et al., 2020; Guidault et al., 2021],

pour un état de mer donné. Pour ce calcul local sur une section de câble, les historiques de tension et de courbure imposés sont obtenus à partir d'un calcul global sur une structure éolienne flottante réalisé dans un précédent travail au LMPS en collaboration avec IFP Energies Nouvelles [Bussolati, 2019]. Une analyse SVD *a posteriori* de la solution de calcul locale à différents pas de temps permet d'évaluer sa capacité à être réduite. De plus, la possibilité de séparer les échelles spatiales et temporelles, qui peuvent être exploitées lors de l'approche de réduction du modèle, est étudiée.

Une deuxième étape, qui constitue le cœur de la thèse, est consacrée au développement d'une approche PGD de ce modèle, exploitant la séparation dans le domaine spatial par DDM. On recherche des performances de réduction et une vitesse de convergence maximales, avec une stratégie de calcul multi-échelle de type DDM adaptée au contact, tout en garantissant une évaluation précise des quantités d'interface.

Dans le cadre de l'application visée sur les FOWT, plusieurs défis scientifiques se posent. Tout d'abord, les critères de convergence pour la méthode de résolution non linéaire doivent assurer une bonne convergence pour les quantités de contact locales : un critère de convergence global n'assure pas la convergence locale des quantités d'interface, qui sont cruciales pour la prédiction de la durée de vie en *fretting fatigue*. De plus, le taux de convergence de la méthode LATIN pour les problèmes de contact dépend fortement des directions de recherche, et la mise à jour des directions de recherche est un problème difficile [Sun et al., 2008]. Un autre problème concerne le traitement efficace et la représentation précise du contenu multi-échelle pour les quantités d'interface de contact. De plus, pour les problèmes très irréguliers tels que les problèmes de contact par frottement, le contrôle de la qualité et de la taille de la base réduite construite progressivement par PGD au fil des itérations LATIN est crucial pour l'efficacité de la méthode.

Plan du manuscrit

Le manuscrit est organisé en cinq chapitres.

- **Chapitre 1.** Le travail de ce premier chapitre consiste en une étude bibliographique sur les principaux thèmes abordés dans la thèse. Le chapitre commence par une courte étude ciblée sur les éoliennes *offshore* flottantes, leur caractérisation et leur conception, car elles représentent en fait la motivation ultime de la thèse. Ensuite, nous décrivons la mécanique des câbles spiralés monotoron en acier qui composent leurs lignes d'ancrage. Leur géométrie et leur mécanique sont également communes aux câbles électriques ou aux conducteurs électriques aériens. Nous présentons brièvement quelques modèles analytiques capables de prédire leurs principales propriétés mécaniques, ainsi que les méthodes de calcul les plus courantes. La plupart d'entre eux visent à prédire le comportement des câbles à un niveau macroscopique en homogénéisant d'une certaine manière les interactions locales entre les fils qui les composent. Dans ce travail, cependant, l'objectif est d'avoir une représentation précise des actions entre les fils. À cet

égard, les modèles numériques qui représentent des fils simples avec des éléments de poutre garantissent une représentation précise des quantités de contact avec un coût de calcul inférieur par rapport aux modèles plus fins. Cependant, les coûts de calcul d'une analyse de fatigue sur une section de câble à différentes couches soumise à des chargements complexes variant sur une longue période de temps sont prohibitifs pour une utilisation industrielle lorsque des formulations classiques de contact poutre-poutre sont considérées. A ce titre, un modèle exploitant l'hypothèse de petits glissements au contact poutre-poutre permet de bien représenter la mécanique d'un câble spiralé et réduit considérablement les coûts de calcul. Ces deux premières sections du chapitre 1 sont également cruciales pour comprendre le chapitre 2 suivant, ainsi que les chapitres restants où des modèles simplifiés inspirés de ces mécaniques sont testés.

Un aperçu de la mécanique de contact numérique et des principales stratégies associées est ensuite proposée afin de contextualiser la manière dont la méthode LATIN traite le contact frottant. Les similitudes et différences de la méthode LATIN par rapport aux méthodes plus standards ont été mises en évidence, notamment concernant les liens qu'elle partage avec une formulation du contact de type lagrangien augmenté, les méthodes de direction alternée de multiplicateurs et les algorithmes de type Uzawa.

La partie suivante est consacrée à la réduction de modèle, autre aspect fondamental de la thèse. La différenciation habituelle entre méthodes *a posteriori* et *a priori* est adoptée. Les techniques classiques *a posteriori* telles que la POD et la méthode de base réduite sont introduites, avec ensuite une attention particulière portée à la PGD. Les principales applications de ces techniques sont ainsi vues en termes de mécanique de contact, avec ou sans frottement. En particulier, il est souligné que la plupart des techniques *a posteriori* disponibles traitent de l'analyse de problèmes paramétrés et pour lesquels la partie *offline* est particulièrement coûteuse. Nous soulignons ensuite comment certaines propriétés de la DDM basée sur la LATIN-PGD, comme celles du problème réduit d'interface agissant comme un modèle réduit très grossier ainsi que la possibilité d'enrichir localement la base réduite dans les zones de contact, peuvent aider de manière significative à traiter ce type de problèmes.

Enfin, des méthodes de décomposition de domaine telles que les approches classiques primales et duales sont brièvement présentées. Les principales différences avec une approche mixte telle que celle basée sur la méthode LATIN sont mises en évidence, cette dernière en particulier permettant une manière plus simple et plus générale de traiter les interfaces de contact par frottement ainsi que d'autres comportements complexes d'interface.

– **Chapitre 2.** Une partie importante de la motivation de ce travail est développée dans le chapitre 2, où nous analysons l'évolution des quantités de contact du problème cible et étudions leur potentiel de réductibilité. En particulier, nous analysons l'état de contact au cours du temps entre les différentes couches, en remarquant comment les conditions de contact sont particulièrement critiques dans les couches les plus externes où de grands fronts de glissement se produisent. Nous étudions la réductibilité potentielle dans une analyse intéressante couche par couche. Il est montré que la complexité des conditions de contact se produisant dans les différentes couches influence fortement la réductibilité. En conséquence, les couches les plus externes, avec des conditions de contact plus variables, s'avèrent être plus critiques en termes de réductibilité, en particulier par rapport à la réductibilité des forces de contact de frottement. Nous étudions également le comportement des différents modes spatiaux, avec une tendance accentuée des modes à apporter des corrections dans les zones où des conditions plus complexes se produisent, comme par exemple à la position angulaire de l'axe de flexion à partir duquel le glissement s'initie et se propage. Globalement, le problème cible présente une bonne réductibilité potentielle. Ce fait est dû aux chargements particuliers auxquels les câbles d'ancrage sont soumis : en effet, ces structures sont préchargées et soumises à de petites charges oscillantes autour de cet état. Cela réduit la formation de fortes discontinuités/fronts de glissement et réduit leur amplitude de variations, notamment dans les couches internes.

– **Chapitre 3.** Dans le chapitre 3, nous présentons la stratégie basée sur la méthode LATIN pour résoudre le problème de contact par frottement et introduisons la réduction de modèle basée sur PGD. Pour ce faire, les principales caractéristiques de la stratégie sont d'abord présentées lorsqu'elle est appliquée aux problèmes de contact par frottement sur un problème de référence 1D inspiré de la mécanique d'un seul fil du câble spiralé. Nous mettons en évidence la grande influence que le chargement externe a sur la réductibilité du problème et la propagation du front de glissement. En particulier, les charges limites que nous considérons (respectivement le cas de charge 1 impliquant des propagations de front de glissement importantes, et le cas de charge 2 avec de faibles variations des fronts de glissement) créent des conditions de contact et de réductibilité comparables respectivement aux couches les plus externes de la section de câble analysée au chapitre 2 où le front se propage sur toute la couche, et aux couches les plus internes dont le front reste situé autour de l'axe de flexion.

Nous considérons le cas de charge 1, et l'application de la stratégie sur le problème 1D permet de mettre en évidence certains problèmes pour ce type d'analyse qui n'ont pas été étudiés de manière approfondie auparavant, et pour lesquels nous apportons quelques contributions dans le Chapitre 5. En particulier, on s'intéresse au contrôle d'erreur dans le solveur itératif pour capturer avec précision les fronts de glissement/adhérence (ainsi que le saut de déplacement normal en contact ou séparation) et l'amélioration de la convergence grâce à une mise à jour adaptée

des directions de recherche.

Le PGD est ensuite introduite dans la méthode LATIN. Afin d'obtenir des performances maximales en termes de temps de calcul, l'enrichissement de la base PGD est un aspect crucial pour accomplir cette tâche. Considérant que l'ajout de nouveaux modes est la partie la plus coûteuse de l'approche, un choix optimisé de ce point de vue nécessite tout d'abord de comprendre ce qui pilote le taux de convergence du LATIN. La convergence des quantités microscopiques aux interfaces est pilotée par le paramètre de direction de recherche k , de sorte que même en utilisant la PGD le taux de convergence reste piloté par celui du choix de k , et l'ajout de nouveaux modes à un moment donné ne crée pas d'avantages de gain de ce point de vue. Il est donc essentiel de choisir un critère d'enrichissement approprié, tel que celui de l'erreur de direction de recherche, afin d'éviter de créer trop de modes surtout lorsque le calcul est loin de la convergence.

Nous considérons également des techniques de tri de la base réduite telles que l'orthonormalisation (des modes spatiaux) ou un algorithme itératif de *downsizing* qui crée progressivement une base proche de celle obtenue par SVD [Giacoma et al., 2015]. Dans ce cas, dans l'exemple 1D, nous n'analysons pas le coût des différentes stratégies puisque le problème est très peu coûteux en calcul, mais seulement leur capacité à contenir la taille de la base et à contrôler sa qualité. Nous constatons que l'orthonormalisation des modes spatiaux n'est pas suffisante pour limiter et réduire la taille de la base réduite, alors que le l'algorithme de *downsizing* [Giacoma et al., 2015], qui opère en fait une double orthogonalisation entre les modes spatiaux et les modes temporels, s'avère plus efficace. Cependant, nous montrons également comment l'algorithme de *downsizing*, en triant et en projetant toute la base à chaque fois qu'il est appliqué, nécessite de vérifier la condition d'admissibilité entre les modes spatiaux, ce qui peut être coûteux.

- **Chapitre 4.** Dans le chapitre 4, nous introduisons la DDM multi-échelle en espace basée sur une séparation des échelles aux interfaces, ainsi que l'introduction de la PGD dans ce cas. L'aspect crucial mis en évidence en premier lieu est le fait que dans la stratégie, les quantités macroscopiques ont tendance à converger rapidement dans les premières itérations du solveur itératif LATIN. Par conséquent, nous suggérons d'enrichir la base PGD due aux macroquantités plus fréquemment dans les premières itérations afin de capturer rapidement les contributions à l'échelle macro et de former une base pertinente pour les itérations suivantes, puis de capturer les contributions à l'échelle micro au cours des itérations. Appliqué au problème 1D, nous montrons qu'il est possible de créer des bases réduites par sous-domaine de différentes tailles selon les conditions de contact qui s'établissent dans les différents sous-domaines, avec les premiers modes qui représentent bien les premiers modes structurels des sous-domaines.

Ensuite, un problème de contact 2D avec frottement entre trois corps élançés soumis à une compression, une traction et une flexion alternées au cours du

temps, représentatif de l'application considérée, est considéré. Il est montré qu'une propagation importante du front de glissement à travers les différents sous-domaines réduisait considérablement le taux de convergence. Le comportement de la base PGD découle de ce qui a été dit ci-dessus, c'est-à-dire que la base nécessaire pour représenter les quantités macroscopiques est créée dans les premières itérations et est suffisante pour les itérations suivantes. En revanche, la partie de la base pour représenter les quantités microscopiques doit être enrichie davantage au fil des itérations en raison de la convergence plus lente des micro-quantités. La complexité plus élevée par rapport au cas 1D permet également une analyse du coût de la stratégie LATIN sans PGD et avec PGD avec différentes techniques de tri des bases réduites par sous-domaine. Il est montré comment l'efficacité de la PGD dépend tout d'abord du critère d'enrichissement, car le processus d'ajout d'un nouveau couple de modes est coûteux aussi bien au moment de la création que lorsqu'un algorithme de tri est utilisé.

- **Chapitre 5.** Dans le dernier chapitre 5, nous proposons quelques contributions au contrôle et à l'amélioration de la convergence des quantités de contact d'interface avec la stratégie LATIN. Ce point répond à la demande de contrôle de la précision sur la cinématique de contact et les forces utilisées comme entrées des lois de fatigue de frottement pour l'application de la ligne d'ancrage [Montalvo et al., 2023]. À partir de la définition d'un indicateur de convergence basé sur l'erreur de relation de comportement aux interfaces introduit dans [Passieux, 2008], nous proposons quelques modifications pour le rendre plus robuste à différents scénarios impliquant différents états de contact. L'indicateur s'avère dans tous les cas être un indicateur de convergence fiable, bien plus performant que l'indicateur de convergence LATIN classique notamment lorsque la direction de recherche change. Par la suite, nous nous attachons à améliorer le taux de convergence des quantités de contact d'interface au niveau microscopique, qui sont pilotées par le paramètre de direction de recherche k . L'idée est d'introduire pour chaque interface de contact une direction de recherche dépendant de l'espace et du temps $k(\underline{x}, t)$ basée sur le statut de contact et mise à jour pendant les itérations LATIN en partant d'une valeur de référence k_0 classiquement utilisée pour une interface parfaite. Cependant, l'introduction d'une telle direction de recherche $k^-(\underline{x}, t)$ à l'étape linéaire implique plusieurs complications qui peuvent limiter les avantages d'une éventuelle mise à jour. Par conséquent, nous envisageons l'idée de mettre à jour uniquement la direction de recherche ascendante k^+ de l'étape locale. Cependant, en raison des conditions de convergence, la valeur maximale dont on peut faire varier k par rapport à la valeur de référence k_0 au cours des itérations est limitée et dépend de la valeur du paramètre de relaxation. Néanmoins, même avec ces limitations, la stratégie s'avère être robuste, conduisant à un gain intéressant en taux de convergence des microquantités pour les différents cas de test étudiés impliquant différents chargements et différents états de contact en espace et en temps, et ce pour un coût de calcul très modeste.

Bibliography

- Abel, J. F., & Shephard, M. S. (1979). An algorithm for multipoint constraints in finite element analysis. *International Journal for Numerical Methods in Engineering*, 14(3), 464–467 (cit. on p. 46).
- Alameddin, S., Fau, A., Néron, D., Ladevèze, P., & Nackenhorst, U. (2019). Toward optimality of proper generalised decomposition bases. *Mathematical and Computational Applications*, 24(1), 30 (cit. on p. 133).
- Alart, P. (1997). Méthode de newton généralisée en mécanique du contact. *Journal de mathématiques pures et appliquées*, 76(1), 83–108 (cit. on p. 46).
- Alart, P., & Curnier, A. (1991). A mixed formulation for frictional contact problems prone to newton like solution methods. *Computer methods in applied mechanics and engineering*, 92(3), 353–375 (cit. on pp. 43, 46).
- Alart, P., Iceta, D., & Dureisseix, D. (2012). A nonlinear domain decomposition formulation with application to granular dynamics. *Computer methods in applied mechanics and engineering*, 205, 59–67 (cit. on p. 74).
- Allier, P.-E., Chamoin, L., & Ladevèze, P. (2015). Proper generalized decomposition computational methods on a benchmark problem: Introducing a new strategy based on constitutive relation error minimization. *Advanced Modeling and Simulation in Engineering Sciences*, 2(1), 1–25 (cit. on pp. 63, 107).
- Ammar, K. A., Guidault, P.-A., Boucard, P.-A., Said, J., & Hafid, F. (2023). Wireframe modeling of overhead conductors for life time prediction. *COMPLAS 2023-XVII International Conference on Computational Plasticity* (cit. on p. 32).
- Anand, L. (1993). A constitutive model for interface friction. *Computational Mechanics*, 12(4), 197–213 (cit. on p. 38).
- ArcelorMittal. (2021). *The world's largest floating offshore wind farm built with our ropes*. <https://europe.arcelormittal.com/newsandmedia/europenews/news-2021/Hywind-Tampen>. (Cit. on pp. 2, 233)

- Atwell, J. A., & King, B. B. (2001). Proper orthogonal decomposition for reduced basis feedback controllers for parabolic equations. *Mathematical and computer modelling*, 33(1-3), 1–19 (cit. on p. 54).
- Avery, P., & Farhat, C. (2009). The feti family of domain decomposition methods for inequality-constrained quadratic programming: Application to contact problems with conforming and nonconforming interfaces. *Computer Methods in Applied Mechanics and Engineering*, 198(21-26), 1673–1683 (cit. on p. 74).
- Avery, P., Rebel, G., Lesoinne, M., & Farhat, C. (2004). A numerically scalable dual-primal substructuring method for the solution of contact problems—part i: The frictionless case. *Computer Methods in Applied Mechanics and Engineering*, 193(23-26), 2403–2426 (cit. on p. 74).
- Babuvška, I., & Rheinboldt, W. C. (1978). Error estimates for adaptive finite element computations. *SIAM Journal on Numerical Analysis*, 15(4), 736–754 (cit. on p. 171).
- Bailey, H., Brookes, K. L., & Thompson, P. M. (2014). Assessing environmental impacts of offshore wind farms: Lessons learned and recommendations for the future. *Aquatic biosystems*, 10(1), 1–13 (cit. on p. 16).
- Balajewicz, M., Amsallem, D., & Farhat, C. (2016). Projection-based model reduction for contact problems. *International Journal for Numerical Methods in Engineering*, 106(8), 644–663 (cit. on pp. 4, 63, 236).
- Ballani, J., Huynh, D. P., Knezevic, D. J., Nguyen, L., & Patera, A. T. (2018). A component-based hybrid reduced basis/finite element method for solid mechanics with local nonlinearities. *Computer Methods in Applied Mechanics and Engineering*, 329, 498–531 (cit. on pp. 64, 65).
- Barboteu, M., Alart, P., & Vidrascu, M. (2001). A domain decomposition strategy for non-classical frictional multi-contact problems. *Computer Methods in Applied Mechanics and Engineering*, 190(37-38), 4785–4803 (cit. on p. 74).
- Barboteu, M., Bonaldi, F., Danan, D., & El-Hadri, S. (2023). An improved normal compliance method for dynamic hyperelastic problems with energy conservation property. *Communications in Nonlinear Science and Numerical Simulation*, 123, 107296 (cit. on p. 46).
- Barboteu, M., Bonaldi, F., Dumont, S., & Mahmoud, C. (2024). An energy-consistent discretization of hyper-viscoelastic contact models for soft tissues. *Computer Methods in Applied Mechanics and Engineering*, 421, 116785 (cit. on p. 46).

-
- Barrault, M., Maday, Y., Nguyen, N. C., & Patera, A. T. (2004). An ‘empirical interpolation’ method: Application to efficient reduced-basis discretization of partial differential equations. *Comptes Rendus Mathématique*, 339(9), 667–672 (cit. on p. 63).
- Becker, R., & Hansbo, P. (1999). *A finite element method for domain decomposition with non-matching grids* (Doctoral dissertation). INRIA. (Cit. on p. 44).
- Beltrami, E. (1873). Sulle funzioni bilineari. *Giornale di Matematiche*, 11(2), 98–106 (cit. on pp. 52, 56).
- Ben Dhia, H. (1998). Problèmes mécaniques multi-échelles: La méthode arlequin. *Comptes Rendus de l’Académie des Sciences-Series IIB-Mechanics-Physics-Astronomy*, 326(12), 899–904 (cit. on p. 143).
- Benaceur, A., Ern, A., & Ehrlicher, V. (2020). A reduced basis method for parametrized variational inequalities applied to contact mechanics. *International Journal for Numerical Methods in Engineering*, 121(6), 1170–1197 (cit. on pp. 4, 64, 236).
- Bertails-Descoubes, F., Cadoux, F., Daviet, G., & Acary, V. (2011). A nonsmooth newton solver for capturing exact coulomb friction in fiber assemblies. *ACM Transactions on Graphics (TOG)*, 30(1), 1–14 (cit. on p. 46).
- Bertsekas, D. P. (1988). *Constrained optimization and lagrange multiplier methods*. Academic press. (Cit. on pp. 44, 187).
- Bhattacharyya, M., Fau, A., Nackenhorst, U., Néron, D., & Ladevèze, P. (2018a). A latin-based model reduction approach for the simulation of cycling damage. *Computational Mechanics*, 62, 725–743 (cit. on p. 108).
- Bhattacharyya, M., Fau, A., Nackenhorst, U., Néron, D., & Ladevèze, P. (2018b). A multi-temporal scale model reduction approach for the computation of fatigue damage. *Computer Methods in Applied Mechanics and Engineering*, 340, 630–656 (cit. on p. 108).
- Boisse, P. (1987). *Nouvel algorithme à grand incrément de temps pour le calcul des structures élastoplastiques* (Doctoral dissertation). Paris 6. (Cit. on p. 108).
- Boroomand, B., & Zienkiewicz, O. (1998). Recovery procedures in error estimation and adaptivity: Adaptivity in non-linear problems of elasto-plasticity behaviour. In *Studies in applied mechanics* (pp. 383–410). Elsevier. (Cit. on p. 171).
- Boso, D. P., Lefik, M., & Schrefler, B. A. (2005). A multilevel homogenised model for superconducting strand thermomechanics. *Cryogenics*, 45(4), 259–271 (cit. on p. 30).

- Boucard, P.-A. (1996). *Approche à grand incrément de temps en grandes transformations* (Doctoral dissertation). Cachan, Ecole normale supérieure. (Cit. on pp. 108, 215).
- Boucard, P.-A., Buytet, S., & Guidault, P.-A. (2007). Une stratégie multi-échelle pour l'étude paramétrique de détails géométriques au sein de structures en contacts multiples. *European Journal of Computational Mechanics/Revue Européenne de Mécanique Numérique*, 16(8), 1011–1036 (cit. on p. 224).
- Boucard, P.-A., Buytet, S., & Guidault, P.-A. (2009). A multiscale strategy for structural optimization. *International journal for numerical methods in engineering*, 78(1), 101–126 (cit. on p. 224).
- Brand, M. (2006). Fast low-rank modifications of the thin singular value decomposition. *Linear Algebra and its Applications*, 415(1), 20–30 (cit. on p. 133).
- Brandt, A. (1981). Guide to multigrid development. *Multigrid Methods: Proceedings of the Conference Held at Köln-Porz, November 23–27, 1981*, 220–312 (cit. on p. 143).
- Brezzi, F. (1974). On the existence, uniqueness and approximation of saddle-point problems arising from lagrangian multipliers. *Publications des séminaires de mathématiques et informatique de Rennes*, (S4), 1–26 (cit. on p. 64).
- Brezzi, F., & Marini, D. (2001). Error estimates for the three-field formulation with bubble stabilization. *Mathematics of computation*, 70(235), 911–934 (cit. on p. 225).
- Buannic, N., & Cartraud, P. (2001). Higher-order effective modeling of periodic heterogeneous beams. i. asymptotic expansion method. *International Journal of Solids and Structures*, 38(40-41), 7139–7161 (cit. on p. 30).
- Bunch, J. R., & Nielsen, C. P. (1978). Updating the singular value decomposition. *Numerische Mathematik*, 31(2), 111–129 (cit. on p. 133).
- Bussetta, P., Marceau, D., & Ponthot, J.-P. (2012). The adapted augmented lagrangian method: A new method for the resolution of the mechanical frictional contact problem. *Computational Mechanics*, 49(2), 259–275 (cit. on pp. 187, 188).
- Bussolati, F. (2019). *Modèle multi-échelle de la fatigue des lignes d'ancrage câblées pour l'éolien offshore flottant* (Doctoral dissertation). Université Paris-Saclay (ComUE). (Cit. on pp. 2, 4, 5, 7, 8, 16, 17, 20, 23, 27, 28, 32, 75, 77–80, 84, 94, 101, 209, 215, 235, 237, 238).
- Bussolati, F., Guidault, P.-A., Guiton, M. L. E., Allix, O., & Wriggers, P. (2020). Robust contact and friction model for the fatigue estimate of a wire rope in the mooring line of a floating offshore wind turbine. *Lecture Notes in Application and Computational Mechanics*, 93, 249–270 (cit. on pp. 4, 7, 32, 75, 79, 80, 156, 235, 237).

-
- Bussolati, F., Guiton, M. L., Guidault, P.-A., Poirette, Y., Martinez, M., & Allix, O. (2019). A new fully detailed finite element model of wire rope for fatigue life estimate of a mooring line. *38th International Conference on Ocean, Offshore and Arctic Engineering, OMAE 2019, 1*, OMAE2019–96165 (cit. on pp. [4](#), [7](#), [32](#), [75](#), [80](#), [235](#), [237](#)).
- Caignot, A., Ladèveze, P., Néron, D., & Durand, J.-F. (2010). Virtual testing for the prediction of damping in joints. *Engineering Computations*, *27*(5), 621–644 (cit. on p. [65](#)).
- Capaldo, M., Guidault, P.-A., Néron, D., & Ladevèze, P. (2017). The reference point method, a “hyperreduction” technique: Application to PGD-based nonlinear model reduction. *Computer Methods in Applied Mechanics and Engineering*, *322*, 483–514 (cit. on pp. [55](#), [62](#), [63](#), [194](#), [215](#)).
- Cardoso, A. R. (2019). *Numerical studies on the modeling of fretting fatigue (in french)* (Doctoral dissertation). Université Paris-Saclay. (Cit. on pp. [109](#), [113](#), [119](#), [224](#)).
- Cardoso, R. A., Néron, D., Pommier, S., & Araújo, J. A. (2018). An enrichment-based approach for the simulation of fretting problems. *Computational Mechanics*, *62*(6), 1529–1542 (cit. on pp. [4](#), [64](#), [109](#), [113](#), [236](#)).
- Cartraud, P., & Messenger, T. (2006). Computational homogenization of periodic beam-like structures. *International Journal of Solids and Structures*, *43*(3-4), 686–696 (cit. on pp. [16](#), [30](#)).
- Chamoret, D., Saillard, P., Rassineux, A., & Bergheau, J.-M. (2004). New smoothing procedures in contact mechanics. *Journal of Computational and applied Mathematics*, *168*(1-2), 107–116 (cit. on p. [188](#)).
- Champaney, L. (1996). *Une nouvelle approche modulaire pour l'analyse d'assemblages de structures tridimensionnelles* (Doctoral dissertation). École normale supérieure de Cachan-ENS Cachan. (Cit. on pp. [74](#), [117](#), [151](#), [224](#)).
- Champaney, L., Cognard, J.-Y., Dureisseix, D., & Ladevèze, P. (1997). Large scale applications on parallel computers of a mixed domain decomposition method. *Computational Mechanics*, *19*(4), 253–263 (cit. on p. [74](#)).
- Champaney, L., Cognard, J.-Y., & Ladevèze, P. (1999). Modular analysis of assemblages of three-dimensional structures with unilateral contact conditions. *Computers & Structures*, *73*(1-5), 249–266 (cit. on pp. [49](#), [67](#), [74](#), [109](#), [117](#), [151](#), [224](#)).
- Chatterjee, A. (2000). An introduction to the proper orthogonal decomposition. *Current Science*, 808–817 (cit. on pp. [5](#), [52](#), [54](#), [236](#)).

- Chaturantabut, S., & Sorensen, D. C. (2010). Nonlinear model reduction via discrete empirical interpolation. *SIAM Journal on Scientific Computing*, 32(5), 2737–2764 (cit. on p. 63).
- Chinesta, F., Ladeveze, P., & Cueto, E. (2011). A short review on model order reduction based on proper generalized decomposition. *Archives of Computational Methods in Engineering*, 18(4), 395–404 (cit. on pp. 4, 5, 58, 235, 236).
- Chinesta, F., Ammar, A., & Cueto, E. (2010). Proper generalized decomposition of multiscale models. *International Journal for Numerical Methods in Engineering*, 83(8-9), 1114–1132 (cit. on p. 58).
- Christensen, P. W. (2002). A semi-smooth newton method for elasto-plastic contact problems. *International Journal of Solids and Structures*, 39(8), 2323–2341 (cit. on p. 46).
- Claus, S., & Kerfriden, P. (2018). A stable and optimally convergent latin-cutfem algorithm for multiple unilateral contact problems. *International Journal for Numerical Methods in Engineering*, 113(6), 938–966 (cit. on p. 109).
- Cognard, J.-Y. (1989). *Une nouvelle approche des problèmes de plasticité et de viscoplasticité: La méthode à grand incrément de temps* (Doctoral dissertation). Paris 6. (Cit. on p. 108).
- Coleman, B. D., & Gurtin, M. E. (1967). Thermodynamics with internal state variables. *The journal of chemical physics*, 47(2), 597–613 (cit. on p. 171).
- Coorevits, P., Hild, P., & Pelle, J.-P. (1999). Contrôle et adaptation des calculs éléments finis pour les problèmes de contact unilatéral. *Revue européenne des éléments finis*, 8(1), 7–29 (cit. on p. 171).
- Coorevits, P., Hild, P., & Pelle, J.-P. (2000). A posteriori error estimation for unilateral contact with matching and non-matching meshes. *Computer Methods in Applied Mechanics and Engineering*, 186(1), 65–83 (cit. on p. 171).
- Cosserat, E., & Cosserat, F. (1909). Theories des corps déformables. *Hermann, Paris* (cit. on p. 150).
- Costello, G. A. (2012). *Theory of wire rope*. Springer Science & Business Media. (Cit. on p. 26).
- Coulomb, C. A. (1821). *Théorie des machines simples en ayant égard au frottement de leurs parties et à la roideur des cordages*. Bachelier. (Cit. on p. 35).

-
- Cremonesi, M., Néron, D., Guidault, P.-A., & Ladevèze, P. (2013). A PGD-based homogenization technique for the resolution of nonlinear multiscale problems. *Computer Methods in Applied Mechanics and Engineering*, 267, 275–292 (cit. on pp. 149, 150).
- Curnier, A. (1984). A theory of friction. *International Journal of Solids and Structures*, 20(7), 637–647. [https://doi.org/https://doi.org/10.1016/0020-7683\(84\)90021-0](https://doi.org/https://doi.org/10.1016/0020-7683(84)90021-0) (cit. on p. 37)
- Curnier, A., & Alart, P. (1988). A generalized newton method for contact problems with friction. *Journal de mécanique théorique et appliquée* (cit. on p. 46).
- Curnier, A., He, Q.-C., & Telega, J. (1992). Formulation of unilateral contact between two elastic bodies undergoing finite derformations. *Comptes rendus de l'Académie des sciences. Série 2, Mécanique, Physique, Chimie, Sciences de l'univers, Sciences de la Terre*, 314(1), 1–6 (cit. on p. 45).
- Dang Van, K. (1999). Introduction to fatigue analysis in mechanical design by the multiscale approach. In *High-cycle metal fatigue: From theory to applications* (pp. 57–88). Springer. (Cit. on p. 215).
- Davies, P., Baron, P., Salomon, K., Bideaud, C., Labbé, J.-P., Toumit, S., Francois, M., Grosjean, F., Bunsell, T., & Moysan, A.-G. (2008). Influence of fibre stiffness on deepwater mooring line response. *International Conference on Offshore Mechanics and Arctic Engineering*, 48180, 179–187 (cit. on pp. 2, 233).
- De Saxcé, G., & Bousshine, L. (1998). Limit analysis theorems for implicit standard materials: Application to the unilateral contact with dry friction and the non-associated flow rules in soils and rocks. *International Journal of Mechanical Sciences*, 40(4), 387–398 (cit. on p. 37).
- De Saxcé, G., & Feng, Z.-Q. (1998). The bipotential method: A constructive approach to design the complete contact law with friction and improved numerical algorithms. *Mathematical and computer modelling*, 28(4-8), 225–245 (cit. on pp. 37, 45).
- DeepLines. (Principia). *Deeplines wind*. <https://www.principia-group.com/blog/product/deeplines-wind/>. (Cit. on pp. 6, 236)
- de Jong, B. C. (2015). *Analytical and experimental analysis of the capacity of steel wire ropes subjected to forced bending* (Doctoral dissertation). Thesis. (Cit. on p. 23).
- Di Stasio, J., Dureisseix, D., Georges, G., Gravouil, A., & Homolle, T. (2021). An explicit time-integrator with singular mass for non-smooth dynamics. *Computational Mechanics*, 68(1), 97–112 (cit. on p. 46).

- Dimitrov, N., Natarajan, A., & Mann, J. (2017). Effects of normal and extreme turbulence spectral parameters on wind turbine loads. *Renewable Energy*, 101, 1180–1193 (cit. on p. 19).
- Dostál, Z., & Schöberl, J. (2002). Minimizing quadratic functions over non-negative cone with the rate of convergence and finite termination. *SIAM J. Opt* (cit. on p. 74).
- Dostál, Z., & Horák, D. (2003). Scalability and feti based algorithm for large discretized variational inequalities. *Mathematics and Computers in Simulation*, 61(3-6), 347–357 (cit. on p. 74).
- Dostál, Z., & Horák, D. (2004). Scalable feti with optimal dual penalty for a variational inequality. *Numerical linear algebra with applications*, 11(5-6), 455–472 (cit. on p. 74).
- Dostál, Z., Horák, D., & Kučera, R. (2006). Total feti—an easier implementable variant of the feti method for numerical solution of elliptic pde. *Communications in Numerical Methods in Engineering*, 22(12), 1155–1162 (cit. on p. 70).
- Dostál, Z., Horák, D., & Stefanica, D. (2009). A scalable feti–dp algorithm with non-penetration mortar conditions on contact interface. *Journal of computational and applied mathematics*, 231(2), 577–591 (cit. on p. 74).
- Dostál, Z., Kozubek, T., Brzobohatý, T., Markopoulos, A., & Vlach, O. (2012). Scalable tfeti with optional preconditioning by conjugate projector for transient frictionless contact problems of elasticity. *Computer methods in applied mechanics and engineering*, 247, 37–50 (cit. on p. 74).
- Dostál, Z., Kozubek, T., Sadowská, M., Vondrák, V., Brzobohatý, T., Horak, D., Říha, L., & Vlach, O. (2016). *Scalable algorithms for contact problems* (Vol. 36). Springer. (Cit. on p. 73).
- Dostál, Z., Kozubek, T., Vondrák, V., Brzobohatý, T., & Markopoulos, A. (2010). Scalable tfeti algorithm for the solution of multibody contact problems of elasticity. *International Journal for Numerical Methods in Engineering*, 82(11), 1384–1405 (cit. on p. 74).
- Dureisseix, D., & Farhat, C. (2001). A numerically scalable domain decomposition method for the solution of frictionless contact problems. *International Journal for Numerical Methods in Engineering*, 50(12), 2643–2666 (cit. on p. 74).
- Dureisseix, D., Ladevèze, P., & Schrefler, B. A. (2003). A latin computational strategy for multiphysics problems: Application to poroelasticity. *International Journal for Numerical Methods in Engineering*, 56(10), 1489–1510 (cit. on p. 108).

-
- Durville, D. (2012). Contact-friction modeling within elastic beam assemblies: An application to knot tightening. *Computational Mechanics*, 49(6), 687–707 (cit. on p. 31).
- Duvaut, G. (1980). Equilibre d'un solide élastique avec contact unilatéral et frottement de coulomb. *Comptes Rendus de l'Académie des Sciences*, 263–265. (Cit. on p. 39).
- Duvaut, G. (1972). Les inéquations en mécanique et en physique. *Dunod* (cit. on pp. 33, 39).
- Duvaut, G., & Lions, J. L. (1976). *Inequalities in mechanics and physics* (Vol. 219). Springer Science & Business Media. (Cit. on p. 33).
- Eckart, C., & Young, G. (1936). The approximation of one matrix by another of lower rank. *Psychometrika*, 1(3), 211–218 (cit. on p. 56).
- Eringen, A. C. (1966). Linear theory of micropolar elasticity. *Journal of Mathematics and Mechanics*, 909–923 (cit. on p. 150).
- Fargues, J.-P. (1995). *Modélisation dynamique des risers pétroliers en grands déplacements* (Doctoral dissertation). Ecole Centrale de Paris. (Cit. on p. 78).
- Farhat, C. (1994). Implicit parallel processing in structural mechanics. *Computational Mechanics Advances*, 2, 1–124 (cit. on p. 67).
- Farhat, C., Chen, P.-S., & Roux, F.-X. (1993). The dual Schur complement method with well-posed local Neumann problems: Regularization with a perturbed Lagrangian formulation. *SIAM Journal on Scientific Computing*, 14(3), 752–759 (cit. on p. 67).
- Farhat, C., Mandel, J., & Roux, F. X. (1994). Optimal convergence properties of the FETI domain decomposition method. *Computer Methods in Applied Mechanics and Engineering*, 115(3-4), 365–385 (cit. on p. 68).
- Farhat, C., & Roux, F.-X. (1991). A method of finite element tearing and interconnecting and its parallel solution algorithm. *International Journal for Numerical Methods in Engineering*, 32(6), 1205–1227 (cit. on pp. 67, 68).
- Farhat, C., Chen, P.-S., & Mandel, J. (1995). A scalable lagrange multiplier based domain decomposition method for time-dependent problems. *International Journal for Numerical Methods in Engineering*, 38(22), 3831–3853 (cit. on p. 70).
- Farhat, C., Chen, P.-S., Mandel, J., & Roux, F. X. (1998). The two-level feti method part ii: Extension to shell problems, parallel implementation and performance results.

- Computer methods in applied mechanics and engineering*, 155(1-2), 153–179 (cit. on p. 70).
- Farhat, C., Lesoinne, M., LeTallec, P., Pierson, K., & Rixen, D. (2001). Feti-dp: A dual-primal unified feti method—part i: A faster alternative to the two-level feti method. *International journal for numerical methods in engineering*, 50(7), 1523–1544 (cit. on p. 70).
- Farhat, C., Macedo, A., Lesoinne, M., Roux, F.-X., Magoulés, F., & de La Bourdonnaie, A. (2000a). Two-level domain decomposition methods with lagrange multipliers for the fast iterative solution of acoustic scattering problems. *Computer methods in applied mechanics and engineering*, 184(2-4), 213–239 (cit. on p. 72).
- Farhat, C., Pierson, K., & Lesoinne, M. (2000b). The second generation feti methods and their application to the parallel solution of large-scale linear and geometrically non-linear structural analysis problems. *Computer methods in applied mechanics and engineering*, 184(2-4), 333–374 (cit. on p. 70).
- Fauque, J., Ramière, I., & Ryckelynck, D. (2018). Hybrid hyper-reduced modeling for contact mechanics problems. *International Journal for Numerical Methods in Engineering*, 115(1), 117–139 (cit. on pp. 4, 63–65, 236).
- Feng, Z.-Q. (1995). 2d or 3d frictional contact algorithms and applications in a large deformation context. *Communications in Numerical Methods in Engineering*, 11(5), 409–416 (cit. on p. 45).
- Feng, Z.-Q., Peyraut, F., & Labeled, N. (2003). Solution of large deformation contact problems with friction between blatz–ko hyperelastic bodies. *International Journal of Engineering Science*, 41(19), 2213–2225 (cit. on p. 45).
- Feyel, F., & Chaboche, J.-L. (2000). Fe2 multiscale approach for modelling the elastoviscoplastic behaviour of long fibre sic/ti composite materials. *Computer methods in applied mechanics and engineering*, 183(3-4), 309–330 (cit. on pp. 30, 143).
- Fichera, G. (1973). Boundary value problems of elasticity with unilateral constraints. In *Linear theories of elasticity and thermoelasticity* (pp. 391–424). Springer. (Cit. on pp. 33, 39).
- Fichera, G. (1963). Sul problema elastostatico di signorini con ambigue condizioni al contorno. *Atti Accad. Naz. Lincei, VIII. Ser., Rend., Cl. Sci. Fis. Mat. Nat*, 34, 138–142 (cit. on p. 33).
- Fichera, G. (1964). *Problemi elastostatici con vincoli unilaterali: Il problema di signorini con ambigue condizioni al contorno*. Accademia nazionale dei Lincei. (Cit. on p. 33).

-
- Fontaine, E., Heurtier, J. M., Durville, D., Toumit, S., & Prat, C. (2002). Modeling of riser contact-friction problems. *Offshore Technology Conference* (cit. on p. 78).
- Fontaine, E., Kilner, A., Carra, C., Washington, D., Ma, K. T., Phadke, A., Laskowski, D., & Kusinski, G. (2014). Industry survey of past failures, pre-emptive replacements and reported degradations for mooring systems of floating production units. *Offshore technology conference* (cit. on pp. 2, 234).
- Fortin, M., & Glowinski, R. (2000). *Augmented lagrangian methods: Applications to the numerical solution of boundary-value problems*. Elsevier. (Cit. on pp. 42, 48, 109).
- Fortin, M., & Brezzi, F. (1991). *Mixed and hybrid finite element methods* (Vol. 51). New York: Springer-Verlag. (Cit. on p. 225).
- Fredriksson, B. (1976). Finite element solution of surface nonlinearities in structural mechanics with special emphasis to contact and fracture mechanics problems. *Computers & Structures*, 6(4-5), 281–290 (cit. on p. 45).
- Geers, M. G., Kouznetsova, V. G., & Brekelmans, W. (2010). Multi-scale computational homogenization: Trends and challenges. *Journal of computational and applied mathematics*, 234(7), 2175–2182 (cit. on p. 29).
- Giacoma, A., Dureisseix, D., & Gravouil, A. (2016). An efficient quasi-optimal space-time PGD application to frictional contact mechanics. *Advanced Modeling and Simulation in Engineering Sciences*, 3(1), 1–17 (cit. on pp. 66, 110, 133).
- Giacoma, A., Dureisseix, D., Gravouil, A., & Rochette, M. (2014). A multiscale large time increment/FAS algorithm with time-space model reduction for frictional contact problems. *International Journal for Numerical Methods in Engineering*, 97(3), 207–230 (cit. on pp. 6, 66, 118, 224, 237).
- Giacoma, A., Dureisseix, D., Gravouil, A., & Rochette, M. (2015). Toward an optimal a priori reduced basis strategy for frictional contact problems with LATIN solver. *Computer Methods in Applied Mechanics and Engineering*, 283, 1357–1381 (cit. on pp. 4, 66, 106, 107, 109, 110, 113, 118, 119, 123, 130, 132–134, 136, 138, 167, 172, 211, 224, 231, 236, 241).
- Giannakopoulos, A. (1989). The return mapping method for the integration of friction constitutive relations. *Computers & structures*, 32(1), 157–167 (cit. on pp. 37, 45).
- Giglio, M., & Manes, A. (2003). Bending fatigue tests on a metallic wire rope for aircraft rescue hoists. *Engineering Failure Analysis*, 10(2), 223–235 (cit. on p. 24).

- Glowinski, R. (2015). Augmented lagrangians and alternating direction methods of multipliers. Society for Industrial; Applied Mathematics. (Cit. on pp. [48](#), [108](#)).
- Glowinski, R., & Le Tallec, P. (1984). Finite element analysis in nonlinear incompressible elasticity. *Finite Element*, 5, 67–93 (cit. on pp. [43](#), [44](#)).
- Glowinski, R., & Le Tallec, P. (1989). *Augmented lagrangian and operator-splitting methods in nonlinear mechanics*. SIAM. (Cit. on pp. [48](#), [108](#)).
- Glowinski, R., & Le Tallec, P. (1990). Augmented lagrangian interpretation of the nonoverlapping schwarz alternating method. *Third international symposium on domain decomposition methods for partial differential equations*, 224–231 (cit. on pp. [48](#), [108](#)).
- Glüsmann, P., & Kreuzer, E. (2009). On the application of karhunen–loeve transform to transient dynamic systems. *Journal of Sound and Vibration*, 328(4-5), 507–519 (cit. on p. [56](#)).
- González, D., Masson, F., Poulhaon, F., Leygue, A., Cueto, E., & Chinesta, F. (2012). Proper generalized decomposition based dynamic data driven inverse identification. *Mathematics and Computers in Simulation*, 82(9), 1677–1695 (cit. on p. [58](#)).
- Gosselet, P., & Rey, C. (2006). Non-overlapping domain decomposition methods in structural mechanics. *Archives of Computational Methods in Engineering*, 13(4), 515–572 (cit. on p. [67](#)).
- Grepl, M. A., Maday, Y., Nguyen, N. C., & Patera, A. T. (2007). Efficient reduced-basis treatment of nonaffine and nonlinear partial differential equations. *ESAIM: Mathematical Modelling and Numerical Analysis*, 41(3), 575–605 (cit. on pp. [55](#), [63](#)).
- Guidault, P.-A., Allix, O., Champaney, L., & Cornuault, C. (2008). A multiscale extended finite element method for crack propagation. *Computer Methods in Applied Mechanics and Engineering*, 197(5), 381–399 (cit. on pp. [73](#), [146](#)).
- Guidault, P.-A., Zeka, D., Néron, D., Guiton, M., & Enchéry, G. (2023). Model order reduction for the fatigue life prediction of wire ropes in tension and bending. *7th International Conference on Computational Contact Mechanics* (cit. on pp. [6](#), [95](#), [106](#), [237](#)).
- Guidault, P.-A., Allix, O., Champaney, L., & Navarro, J. (2007). A two-scale approach with homogenization for the computation of cracked structures. *Computers & structures*, 85(17-18), 1360–1371 (cit. on p. [73](#)).

-
- Guidault, P.-A., Bussolati, F., Guiton, M. L., & Allix, O. (2021). A small-sliding beam-to-beam contact formulation for the fatigue estimate of spiral strand wire ropes. *14th World Congress on Computational Mechanics (WCCM) ECCOMAS Congress 2020* (cit. on pp. [4](#), [7](#), [32](#), [75](#), [235](#), [237](#)).
- Guidault, P.-A., Bussolati, F., Guiton, M. L., Allix, O., & Wriggers, P. (2019). A small-sliding node-to-node formulation for beam-to-beam frictional contact with large displacements. *VI. International Conference on Computational Contact Mechanics* (cit. on pp. [4](#), [7](#), [32](#), [75](#), [235](#), [237](#)).
- Guillemin, F., di Domenico, D., Sabiron, G., & Averbuch, D. (2016). Using lidar based control to reduce loads on floating wind turbines and boost performance. *Offshore Technology Conference*, D031S041R003 (cit. on p. [20](#)).
- Guiton, M., Martinez, M., Quideau, T., Heurtier, J.-M., Durville, D., Guidault, P.-A., & Poirette, Y. (2022). Comparaison de modèles fem à un essai de tension-flexion d'un câble d'ancrage offshore. *15ème colloque national en calcul des structures* (cit. on pp. [4](#), [32](#), [235](#)).
- GWEC. (2023). Gwec global offshore wind report 2023. *Global Wind Energy Council* (cit. on pp. [1](#), [233](#)).
- Hall, M. T. J. (2013). *Mooring line modelling and design optimization of floating offshore wind turbines* (Doctoral dissertation). (Cit. on pp. [18](#), [21](#)).
- Hansbo, A., & Hansbo, P. (2002). An unfitted finite element method, based on nitsche's method, for elliptic interface problems. *Computer methods in applied mechanics and engineering*, 191(47-48), 5537–5552 (cit. on p. [109](#)).
- Hertz, H. (1882). Ueber die berührung fester elastischer körper. (cit. on p. [33](#)).
- Hesthaven, J. S., Rozza, G., & Stamm, B. (2016). *Certified reduced basis methods for parametrized partial differential equations* (Vol. 590). Springer. (Cit. on pp. [4](#), [57](#), [235](#)).
- Hobbs, R., & Raoof, M. (1983). Interwire slippage and fatigue prediction in stranded cables for tlp tethers. *Hemisphere Publishing Corp*, 77–99 (cit. on p. [25](#)).
- Hong, K.-J., Der Kiureghian, A., & Sackman, J. L. (2005). Bending behavior of helically wrapped cables. *Journal of engineering mechanics*, 131(5), 500–511 (cit. on p. [25](#)).
- Houle-Paradis, J.-P. (2012). *Modélisation de la flexion libre d'un câble multicouche tenant compte de l'élasticité des contacts*. Library; Archives Canada= Bibliothèque et Archives Canada, Ottawa. (Cit. on p. [29](#)).

- Huang, X., & Vinogradov, O. G. (1996). Extension of a cable in the presence of dry friction. *Structural Engineering and Mechanics*, 4(3), 313–329 (cit. on p. 26).
- Hughes, T. J., Cottrell, J. A., & Bazilevs, Y. (2005). Isogeometric analysis: Cad, finite elements, nurbs, exact geometry and mesh refinement. *Computer methods in applied mechanics and engineering*, 194(39-41), 4135–4195 (cit. on p. 109).
- IEA. (2023). *World Energy Outlook 2023*, IEA, Paris (cit. on pp. 1, 233).
- Joli, P., & Feng, Z.-Q. (2008). Uzawa and newton algorithms to solve frictional contact problems within the bi-potential framework. *International journal for numerical methods in engineering*, 73(3), 317–330 (cit. on p. 45).
- Jolicoeur, C., & Cardou, A. (1996). Semicontinuous mathematical model for bending of multilayered wire strands. *Journal of engineering Mechanics*, 122(7), 643–650 (cit. on pp. 25, 30).
- Jonkman, J., Butterfield, S., Musial, W., & Scott, G. (2009). *Definition of a 5-mw reference wind turbine for offshore system development* (tech. rep.). National Renewable Energy Lab.(NREL), Golden, CO (United States). (Cit. on p. 78).
- Jordan, C. (1874). Mémoire sur les formes bilinéaires. *Journal de Mathématiques Pures et Appliquées*, 19, 35–54 (cit. on p. 52).
- Jourdan, F., Alart, P., & Jean, M. (1998). A gauss-seidel like algorithm to solve frictional contact problems. *Computer methods in applied mechanics and engineering*, 155(1-2), 31–47 (cit. on p. 46).
- Judge, R., Yang, Z., Jones, S., & Beattie, G. (2012). Full 3d finite element modelling of spiral strand cables. *Construction and Building Materials*, 35, 452–459 (cit. on pp. 24, 31).
- Kerfriden, P., Allix, O., & Gosselet, P. (2009). A three-scale domain decomposition method for the 3d analysis of debonding in laminates. *Computational mechanics*, 44(3), 343–362 (cit. on pp. 73, 109, 115, 151, 159).
- Kerfriden, P. (2008). *Stratégie de décomposition de domaine à trois échelles pour la simulation du délaminage dans les stratifiés* (Doctoral dissertation). École normale supérieure de Cachan-ENS Cachan. (Cit. on pp. 73, 172, 177).
- Kerschen, G., Golinval, A. F., J.-C. and Vakakis, & Bergman, L. A. (2005). The method of proper orthogonal decomposition for dynamical characterization and order reduction of mechanical systems: An overview. *Nonlinear dynamics*, 41(1), 147–169 (cit. on p. 54).

-
- Kikuchi, N., & Oden, J. T. (1988). *Contact problems in elasticity: A study of variational inequalities and finite element methods*. SIAM. (Cit. on pp. 39, 40, 42, 43).
- Kinderlehrer, D., & Stampacchia, G. (2000). *An introduction to variational inequalities and their applications*. SIAM. (Cit. on pp. 33, 39).
- Klarbring, A. (1986). A mathematical programming approach to three-dimensional contact problems with friction. *Computer Methods in Applied Mechanics and Engineering*, 58(2), 175–200 (cit. on p. 45).
- Klawonn, A., & Rheinbach, O. (2006). A parallel implementation of dual-primal feti methods for three-dimensional linear elasticity using a transformation of basis. *SIAM Journal on Scientific Computing*, 28(5), 1886–1906 (cit. on p. 70).
- Klawonn, A., & Rheinbach, O. (2010). Highly scalable parallel domain decomposition methods with an application to biomechanics. *ZAMM-Journal of Applied Mathematics and Mechanics/Zeitschrift für Angewandte Mathematik und Mechanik: Applied Mathematics and Mechanics*, 90(1), 5–32 (cit. on p. 70).
- Kmet, S., Stanova, E., Fedorko, G., Fabian, M., & Brodniansky, J. (2013). Experimental investigation and finite element analysis of a four-layered spiral strand bent over a curved support. *Engineering Structures*, 57, 475–483 (cit. on p. 30).
- Knapp, R. (1979). Derivation of a new stiffness matrix for helically armoured cables considering tension and torsion. *International Journal for Numerical Methods in Engineering*, 14(4), 515–529 (cit. on p. 23).
- Kollepara, K. S., Navarro-Jiménez, J. M., Le Guennec, Y., Silva, L., & Aguado, J. V. (2023). On the limitations of low-rank approximations in contact mechanics problems. *International Journal for Numerical Methods in Engineering*, 124(1), 217–234 (cit. on p. 64).
- Konyukhov, A., & Schweizerhof, K. (2010). Geometrically exact covariant approach for contact between curves. *Computer Methods in Applied Mechanics and Engineering*, 199(37-40), 2510–2531 (cit. on p. 31).
- Kozubek, T., Vondrák, V., Menšík, M., Horák, D., Dostál, Z., Hapla, V., Kabelíková, P., & Čermák, M. (2013). Total feti domain decomposition method and its massively parallel implementation. *Advances in Engineering Software*, 60, 14–22 (cit. on p. 70).
- Labeyrie, J. (1990). Stationary and transient states of random seas. *Marine Structures*, 3(1), 43–58 (cit. on p. 17).

- Ladevèze, P. (1999). *Nonlinear Computational Structural Mechanics - new approaches and non-incremental methods of calculation*. Springer New York. (Cit. on pp. [6](#), [48](#), [58](#), [67](#), [72](#), [108](#), [110](#), [116](#), [117](#), [121](#), [122](#), [127](#), [237](#)).
- Ladevèze, P., & Chamoin, L. (2011). On the verification of model reduction methods based on the proper generalized decomposition. *Computer Methods in Applied Mechanics and Engineering*, 200(23-24), 2032–2047 (cit. on p. [58](#)).
- Ladevèze, P., & Dureisseix, D. (2000). A micro/macro approach for parallel computing of heterogeneous structures. *International Journal for Computational Civil and Structural Engineering*, 1, 18–28 (cit. on pp. [49](#), [109](#), [145](#), [146](#)).
- Ladevèze, P., Loiseau, O., & Dureisseix, D. (2001). A micro-macro and parallel computational strategy for highly heterogeneous structures. *International Journal for Numerical Methods in Engineering*, 52(1-2), 121–138 (cit. on pp. [67](#), [73](#), [109](#), [145](#), [146](#)).
- Ladevèze, P., Néron, D., & Gosselet, P. (2007). On a mixed and multiscale domain decomposition method. *Computer Methods in Applied Mechanics and Engineering*, 196(8), 1526–1540 (cit. on pp. [6](#), [65](#), [143](#), [237](#)).
- Ladevèze, P., & Nouy, A. (2002). Une stratégie de calcul multiéchelle avec homogénéisation en espace et en temps. *Comptes Rendus Mécanique*, 330(10), 683–689 (cit. on p. [73](#)).
- Ladevèze, P., & Nouy, A. (2003). On a multiscale computational strategy with time and space homogenization for structural mechanics. *Computer Methods in Applied Mechanics and Engineering*, 192(28-30), 3061–3087 (cit. on pp. [6](#), [49](#), [60](#), [65](#), [109](#), [127](#), [143](#), [144](#), [146](#), [149–151](#), [237](#)).
- Ladevèze, P., Nouy, A., & Loiseau, O. (2002). A multiscale computational approach for contact problems. *Computer Methods in Applied Mechanics and Engineering*, 191(43), 4869–4891 (cit. on pp. [74](#), [109](#), [123](#), [143](#), [156](#), [224–226](#)).
- Ladevèze, P., Passieux, J.-C., & Néron, D. (2010). The LATIN multiscale computational method and the proper generalized decomposition. *Computer Methods in Applied Mechanics and Engineering*, 199(21-22), 1287–1296 (cit. on pp. [6](#), [49](#), [65](#), [127](#), [237](#)).
- Ladevèze, P., Pelle, J.-P., & Rougeot, P. (1991). Error estimation and mesh optimization for classical finite elements. *Engineering Computations*, 8(1), 69–80 (cit. on p. [171](#)).
- Ladevèze, P. (1985). Sur une famille d’algorithmes en mécanique des structures. *Comptes-rendus des séances de l’Académie des sciences. Série 2, Mécanique-physique, chimie, sciences de l’univers, sciences de la terre*, 300(2), 41–44 (cit. on p. [108](#)).

-
- Ladevèze, P. (1992). La maîtrise des modèles en mécanique des structures: Erreurs et améliorations adaptatives. *Revue européenne des éléments finis*, 1(1), 9–30 (cit. on p. 171).
- Ladevèze, P., & Moës, N. (1998). A new a posteriori error estimation for nonlinear time-dependent finite element analysis. *Computer Methods in Applied Mechanics and Engineering*, 157(1-2), 45–68 (cit. on p. 171).
- Ladevèze, P., & Pelle, J.-P. (2001). *La maîtrise du calcul en mécanique linéaire et non linéaire*. Hermes Science Publications. (Cit. on p. 171).
- Lalonde, S., Guilbault, R., & Langlois, S. (2017a). Modeling multilayered wire strands, a strategy based on 3d finite element beam-to-beam contacts-part ii: Application to wind-induced vibration and fatigue analysis of overhead conductors. *International Journal of Mechanical Sciences*, 126, 297–307 (cit. on pp. 31, 32).
- Lalonde, S., Guilbault, R., & Légeron, F. (2017b). Modeling multilayered wire strands, a strategy based on 3d finite element beam-to-beam contacts-part i: Model formulation and validation. *International Journal of Mechanical Sciences*, 126, 281–296 (cit. on pp. 25, 31).
- Lapina, E., Oumaziz, P., & Bouclier, R. (2024). Immersed boundary-conformal isogeometric latin method for multiple non-linear interfaces. *Engineering with Computers*, 1–22 (cit. on p. 109).
- Laursen, T., & Simo, J. (1993). Algorithmic symmetrization of coulomb frictional problems using augmented lagrangians. *Computer methods in applied mechanics and engineering*, 108(1-2), 133–146 (cit. on p. 44).
- Le Tallec, P. (1994). Domain decomposition methods in computational mechnaics. *Computational Mechnaics Advances*, 1, 121–220 (cit. on p. 70).
- Le Tallec, P., De Roeck, Y.-H., & Vidrascu, M. (1991). Domain decomposition methods for large linearly elliptic three-dimensional problems. *Journal of Computational and Applied Mathematics*, 34(1), 93–117 (cit. on p. 67).
- Lee, D. D., & Seung, H. S. (1999). Learning the parts of objects by non-negative matrix factorization. *nature*, 401(6755), 788–791 (cit. on p. 64).
- Leroy, J.-M., Poirette, Y., Brusselle Dupend, N., & Caleyron, F. (2017). Assessing mechanical stresses in dynamic power cables for floating offshore wind farms. *International Conference on Offshore Mechanics and Arctic Engineering*, 57786, V010T09A050 (cit. on pp. 3, 234).

- Li, J., Daviet, G., Narain, R., Bertails-Descoubes, F., Overby, M., Brown, G. E., & Boissieux, L. (2018). An implicit frictional contact solver for adaptive cloth simulation. *ACM Transactions on Graphics (TOG)*, 37(4), 1–15 (cit. on p. 46).
- Litewka, P., & Wriggers, P. (2002). Contact between 3d beams with rectangular cross-sections. *International Journal for Numerical Methods in Engineering*, 53(9), 2019–2041 (cit. on p. 31).
- Loiseau, O. (2001). *Une stratégie de calcul multiéchelle pour les structures hétérogènes* (Doctoral dissertation). Cachan, Ecole normale supérieure. (Cit. on pp. 73, 109, 145, 151).
- Lopez-Olocco, T., González-Gutiérrez, L. M., Calderon-Sanchez, J., Marón Loureiro, A., Saavedra Ynocente, L., Bezunartea Barrio, A., & Vivar Valdés, N. (2022). Experimental and numerical study of the influence of clumped weights on a scaled mooring line. *Journal of Marine Science and Engineering*, 10(5), 676 (cit. on p. 78).
- Louf, F., Combe, J.-P., & Pelle, J.-P. (2003). Constitutive error estimator for the control of contact problems involving friction. *Computers & structures*, 81(18-19), 1759–1772 (cit. on p. 171).
- Luenberger, D. G., & Ye, Y. (1984). *Linear and nonlinear programming* (Vol. 2). Springer. (Cit. on p. 187).
- Maday, Y. (2006). Reduced basis method for the rapid and reliable solution of partial differential equations (cit. on p. 57).
- Magoules, F., & Rixen, D. J. (2007). Domain decomposition methods: Recent advances and new challenges in engineering. *Computer Methods in Applied Mechanics and Engineering*, 196(8) (cit. on p. 67).
- Maljaars, J., & Misiak, T. (2021). Fatigue resistance of steel ropes: Failure criterion: Background to the verification in pren 1993-1-11: 2020. *Steel Construction*, 14(3), 196–204 (cit. on pp. 2, 234).
- Mandel, J. (1993). Balancing domain decomposition. *Communications in Numerical Methods in Engineering*, 9(3), 233–241 (cit. on pp. 67, 70).
- Mandel, J., & Brezina, M. (1996). Balancing domain decomposition for problems with large jumps in coefficients. *Mathematics of Computation*, 65(216), 1387–1401 (cit. on p. 67).

-
- Mandel, J., & Sousedík, B. (2007). Adaptive selection of face coarse degrees of freedom in the bddc and the feti-dp iterative substructuring methods. *Computer methods in applied mechanics and engineering*, 196(8), 1389–1399 (cit. on p. 71).
- Mandel, J., Sousedík, B., & Šístek, J. (2012). Adaptive bddc in three dimensions. *Mathematics and Computers in Simulation*, 82(10), 1812–1831 (cit. on p. 71).
- Mandel, J., & Tezaur, R. (2001). On the convergence of a dual-primal substructuring method. *Numerische Mathematik*, 88(3), 543–558 (cit. on p. 70).
- Mandel, J., Tezaur, R., & Farhat, C. (1999). A scalable substructuring method by lagrange multipliers for plate bending problems. *SIAM Journal on Numerical Analysis*, 36(5), 1370–1391 (cit. on p. 70).
- Mariano, P. M. (2002). Multifield theories in mechanics of solids. *Advances in Applied Mechanics*, 38, 1–93 (cit. on p. 150).
- Masi, F., & Stefanou, I. (2022). Multiscale modeling of inelastic materials with thermodynamics-based artificial neural networks (tann). *Computer Methods in Applied Mechanics and Engineering*, 398, 115190 (cit. on p. 143).
- Meier, C., Grill, M. J., Wall, W. A., & Popp, A. (2018). Geometrically exact beam elements and smooth contact schemes for the modeling of fiber-based materials and structures. *International Journal of Solids and Structures*, 154, 124–146 (cit. on p. 31).
- Meier, C., Wall, W. A., & Popp, A. (2017). A unified approach for beam-to-beam contact. *Computer Methods in Applied Mechanics and Engineering*, 315, 972–1010 (cit. on p. 31).
- Ménard, F., & Cartraud, P. (2021). Solid and 3d beam finite element models for the nonlinear elastic analysis of helical strands within a computational homogenization framework. *Computers & Structures*, 257, 106675 (cit. on p. 30).
- Michalowski, R. (1978). Associated and non-associated sliding rules in contact friction problems. *Archiv. Mech.*, 30, 259–276 (cit. on pp. 37, 45).
- Mlika, R. (2018). *Nitsche method for frictional contact and self-contact: Mathematical and numerical study* (Doctoral dissertation). Université de Lyon. (Cit. on p. 44).
- Mlika, R., Renard, Y., & Chouly, F. (2017). An unbiased nitsche’s formulation of large deformation frictional contact and self-contact. *Computer Methods in Applied Mechanics and Engineering*, 325, 265–288 (cit. on p. 44).

- Moës, N., Dolbow, J., & Belytschko, T. (1999). A finite element method for crack growth without remeshing. *International journal for numerical methods in engineering*, 46(1), 131–150 (cit. on p. 65).
- Montalvo, S., Fouvry, S., & Martinez, M. (2023). A hybrid analytical-FEM 3D approach including wear effects to simulate fretting fatigue endurance: Application to steel wires in crossed contact. *Tribology International*, 108713 (cit. on pp. 2, 6, 16, 24, 80, 88, 157, 212, 234, 237, 242).
- Montalvo, S. (2023). *Étude de l'endommagement par fretting-fatigue de fils de câbles d'ancrage offshore: Influence de la galvanisation, de la graisse et de l'eau de mer* (Doctoral dissertation). Ecole Centrale de Lyon. (Cit. on pp. 6, 24, 88, 237).
- Moreau, J. J. (1999). Numerical aspects of the sweeping process. *Computer methods in applied mechanics and engineering*, 177(3-4), 329–349 (cit. on p. 74).
- Néron, D. (2004). *Sur une stratégie de calcul pour les problèmes multiphysiques* (Doctoral dissertation). École normale supérieure de Cachan-ENS Cachan. (Cit. on p. 108).
- Neto, A. G., Pimenta, P. M., & Wriggers, P. (2016). A master-surface to master-surface formulation for beam to beam contact. part i: Frictionless interaction. *Computer Methods in Applied Mechanics and Engineering*, 303, 400–429 (cit. on p. 31).
- Neto, A. G., Pimenta, P. M., & Wriggers, P. (2017). A master-surface to master-surface formulation for beam to beam contact. part ii: Frictional interaction. *Computer Methods in Applied Mechanics and Engineering*, 319, 146–174 (cit. on p. 31).
- Nguyen, N. C., & Peraire, J. (2008). An efficient reduced-order modeling approach for non-linear parametrized partial differential equations. *International Journal for Numerical Methods in Engineering*, 76(1), 27–55 (cit. on p. 63).
- Niakh, I., Drouet, G., Ehrlacher, V., & Ern, A. (2023). Stable model reduction for linear variational inequalities with parameter-dependent constraints. *ESAIM: Mathematical Modelling and Numerical Analysis*, 57(1), 167–189 (cit. on p. 64).
- Niakh, I., Drouet, G., Ehrlacher, V., & Ern, A. (2024). A reduced basis method for frictional contact problems formulated with nitsche's method. *The SMAI Journal of computational mathematics*, 10, 29–54 (cit. on p. 64).
- Nicholls-Lee, R., Thies, P. R., & Johanning, L. (2021). Coupled modelling for dynamic submarine power cables: Interface sensitivity analysis of global response and local structural engineering models (cit. on pp. 3, 234).

-
- Niroomandi, S., Alfaro, I., González, D., Cueto, E., & Chinesta, F. (2013). Model order reduction in hyperelasticity: A proper generalized decomposition approach. *International Journal for Numerical Methods in Engineering*, 96(3), 129–149 (cit. on p. 58).
- Nitsche, J. (1971). Über ein variationsprinzip zur lösung von dirichlet-problemen bei verwendung von teilräumen, die keinen randbedingungen unterworfen sind. *Abhandlungen aus dem mathematischen Seminar der Universität Hamburg*, 36(1), 9–15 (cit. on p. 44).
- Nouy, A. (2003). *A multiscale strategy with homogenization in space and time for highly heterogeneous structures (in french)* (Doctoral dissertation). École normale supérieure de Cachan. (Cit. on pp. 73, 109, 132, 148–150, 221, 224, 225, 227).
- Nouy, A. (2010). A priori model reduction through proper generalized decomposition for solving time-dependent partial differential equations. *Computer Methods in Applied Mechanics and Engineering*, 199(23-24), 1603–1626 (cit. on pp. 5, 49, 58, 60, 61, 107, 127, 129, 131, 132, 236).
- Nouy, A., & Ladevèze, P. (2004). Multiscale computational strategy with time and space homogenization: A radial-type approximation technique for solving micro-problems. *International Journal for Multiscale Computational Engineering*, 2(4) (cit. on pp. 65, 73, 109, 113, 132, 133).
- Nouy, A. (2009). Recent developments in spectral stochastic methods for the numerical solution of stochastic partial differential equations. *Archives of Computational Methods in Engineering*, 16(3), 251–285 (cit. on p. 58).
- Oden, J. T., Vemaganti, K., & Moës, N. (1999). Hierarchical modeling of heterogeneous solids. *Computer Methods in Applied Mechanics and Engineering*, 172(1-4), 3–25 (cit. on p. 143).
- Oden, J. (1981). Exterior penalty methods for contact problems in elasticity. *Nonlinear Finite Element Analysis in Structural Mechanics: Proceedings of the Europe-US Workshop Ruhr-Universität Bochum, Germany, July 28–31, 1980*, 655–665 (cit. on p. 43).
- Oden, J., & Pires, E. (1984). Algorithms and numerical results for finite element approximations of contact problems with non-classical friction laws. *Computers & Structures*, 19(1-2), 137–147 (cit. on p. 36).
- OpenFAST. (NREL). *Openfast*. <https://github.com/OpenFAST/openfast>. (Cit. on pp. 6, 236)

- Oumaziz, P. (2017). *Une méthode de décomposition de domaine mixte non-intrusive pour le calcul parallèle d'assemblages* (Doctoral dissertation). Université Paris-Saclay (ComUE). (Cit. on p. 109).
- Oumaziz, P., Gosselet, P., Boucard, P.-A., & Guinard, S. (2017). A non-invasive implementation of a mixed domain decomposition method for frictional contact problems. *Computational Mechanics*, 60, 797–812 (cit. on pp. 6, 49, 67, 74, 109, 237).
- Oumaziz, P., Gosselet, P., Saavedra, K., & Tardieu, N. (2021). Analysis, improvement and limits of the multiscale latin method. *Computer Methods in Applied Mechanics and Engineering*, 384, 113955 (cit. on p. 146).
- Oumaziz, P., Gosselet, P., Boucard, P.-A., & Abbas, M. (2018). A parallel noninvasive multiscale strategy for a mixed domain decomposition method with frictional contact. *International Journal for Numerical Methods in Engineering*, 115(8), 893–912 (cit. on pp. 6, 74, 109, 237).
- Pang, J.-S. (1990). Newton's method for b-differentiable equations. *Mathematics of operations research*, 15(2), 311–341 (cit. on pp. 46, 74).
- Papailiou, K. O. (1995). *Bending of helically twisted cables under variable bending stiffness due to internal friction, tensile force and cable curvature* (Doctoral dissertation). ETH, Zurich, Swiss. (Cit. on pp. 25–29, 81).
- Paradis, J.-P. H., & Légeron, F. (2011). Modelling of the free bending behavior of a multilayer cable taking into account the tangential compliance of contact interfaces. *Ninth international symposium on cable dynamics*, 18–20 (cit. on p. 26).
- Passieux, J. .-, Ladevèze, P., & Néron, D. (2010). A scalable time–space multiscale domain decomposition method: Adaptive time scale separation. *Computational Mechanics*, 46(4), 621–633 (cit. on pp. 73, 113, 132).
- Passieux, J.-C. (2008). *Radial approximation and multiscale latin method in space and time (in french)* (Doctoral dissertation). Ecole normale supérieure de Cachan. (Cit. on pp. 73, 172, 173, 175–177, 206, 212, 221, 242).
- Pastor, M., Binda, M., & Harčarik, T. (2012). Modal assurance criterion. *Procedia Engineering*, 48, 543–548 (cit. on p. 136).
- Pierres, E., Baietto, M.-C., & Gravouil, A. (2010). A two-scale extended finite element method for modelling 3d crack growth with interfacial contact. *Computer Methods in Applied Mechanics and Engineering*, 199(17-20), 1165–1177 (cit. on pp. 109, 118).

-
- Pietrzak, G., & Curnier, A. (1999). Large deformation frictional contact mechanics: Continuum formulation and augmented lagrangian treatment. *Computer methods in applied mechanics and engineering*, 177(3-4), 351–381 (cit. on p. 43).
- Poirette, Y., Guiton, M., Huwart, G., Sinoquet, D., & Leroy, J. M. (2017). An optimization method for the configuration of inter array cables for floating offshore wind farm. *International Conference on Offshore Mechanics and Arctic Engineering*, 57786, V010T09A072 (cit. on pp. 3, 234).
- Poirette, Y., Perdrizet, T., Gilloteaux, J. C., Pourtier, A., & Mabile, C. (2014). A new ballasted floating support for offshore wind turbine. *International Conference on Offshore Mechanics and Arctic Engineering*, 45547, V09BT09A052 (cit. on p. 17).
- Ponte Castañeda, P. (1996). Exact second-order estimates for the effective mechanical properties of nonlinear composite materials. *Journal of the Mechanics and Physics of Solids*, 44(6), 827–862 (cit. on p. 143).
- Quarteroni, A., Manzoni, A., & Negri, F. (2015). *Reduced basis methods for partial differential equations: An introduction* (Vol. 92). Springer. (Cit. on p. 57).
- Raouf, M. (1992). Free bending fatigue of axially pre-loaded spiral strands. *The Journal of Strain Analysis for Engineering Design*, 27(3), 127–136 (cit. on p. 16).
- Raouf, M., & Hobbs, R. E. (1988). Torsion tests on large spiral strands. *The Journal of Strain Analysis for Engineering Design*, 23(2), 97–104 (cit. on p. 80).
- Raous, M. (1999). *Quasistatic signorini problem with coulomb friction and coupling to adhesion*. Springer. (Cit. on p. 36).
- Relun, N., Néron, D., & Boucard, P.-A. (2013). A model reduction technique based on the pgd for elastic-viscoplastic computational analysis. *Computational Mechanics*, 51(1), 83–92 (cit. on p. 108).
- Renard, Y. (2013). Generalized newton's methods for the approximation and resolution of frictional contact problems in elasticity. *Computer Methods in Applied Mechanics and Engineering*, 256, 38–55 (cit. on p. 46).
- Rentschler, M. U., Adam, F., & Chainho, P. (2019). Design optimization of dynamic inter-array cable systems for floating offshore wind turbines. *Renewable and Sustainable Energy Reviews*, 111, 622–635 (cit. on pp. 3, 234).
- Rey, V. (2015). *Pilotage de stratégies de calcul par décomposition de domaine par des objectifs de précision sur des quantités d'intérêt* (Doctoral dissertation). Université Paris Saclay (COMUE). (Cit. on p. 172).

- Rey, V., Rey, C., & Gosselet, P. (2014). A strict error bound with separated contributions of the discretization and of the iterative solver in non-overlapping domain decomposition methods. *Computer Methods in Applied Mechanics and Engineering*, 270, 293–303 (cit. on p. 172).
- Ribeaucourt, R., Baietto-Dubourg, M.-C., & Gravouil, A. (2007). A new fatigue frictional contact crack propagation model with the coupled X-FEM/LATIN method. *Computer Methods in Applied Mechanics and Engineering*, 196(33-34), 3230–3247 (cit. on pp. 109, 115, 118, 123, 160, 172, 177).
- Rinker, J. M. (2018). Pyconturb: An open-source constrained turbulence generator. *Journal of Physics: Conference Series*, 1037(6), 062032 (cit. on p. 19).
- Rixen, D. J., & Farhat, C. (1999). A simple and efficient extension of a class of substructure based preconditioners to heterogeneous structural mechanics problems. *International Journal for Numerical Methods in Engineering*, 44(4), 489–516 (cit. on p. 69).
- Řiha, L., Brzobohatý, T., & Markopoulos, A. (2017). Hybrid parallelization of the total feti solver. *Advances in Engineering Software*, 103, 29–37 (cit. on p. 70).
- Řiha, L., Brzobohatý, T., Markopoulos, A., Meca, O., & Kozubek, T. (2016). Massively parallel hybrid total feti (htfeti) solver. *Proceedings of the Platform for Advanced Scientific Computing Conference*, 1–11 (cit. on p. 70).
- Rocha, I. B., Kerfriden, P., & Van Der Meer, F. (2023). Machine learning of evolving physics-based material models for multiscale solid mechanics. *Mechanics of Materials*, 184, 104707 (cit. on p. 143).
- Rodriguez-Iturra, S., Néron, D., Ladevèze, P., Charbonnel, P. E., & Nahas, G. (2021). Latin-pgd multi-scale in time for complex fatigue problems. *14th World Congress on Computational Mechanics (WCCM XIV)-ECCOMAS Congress 2020* (cit. on p. 216).
- Rossi, R. R. (2005). A review of fatigue curves for mooring lines. *International Conference on Offshore Mechanics and Arctic Engineering*, 41952, 1097–1104 (cit. on pp. 2, 234).
- Rozza, G., Huynh, D. B. P., & Patera, A. T. (2008). Reduced basis approximation and a posteriori error estimation for affinely parametrized elliptic coercive partial differential equations. *Archives of Computational Methods in Engineering*, 15(3), 229–275 (cit. on p. 57).
- Rozza, G. (2011). Reduced basis approximation and error bounds for potential flows in parametrized geometries. *Communications in Computational Physics*, 9(1), 1–48 (cit. on p. 57).

-
- Ruda, A. (2023). *Méthode de décomposition de domaine mixte pour la simulation magnétostatique de machines électriques* (Doctoral dissertation). Université Paris-Saclay. (Cit. on p. 73).
- Ruda, A., Louf, F., Boucard, P.-A., Mininger, X., & Verbeke, T. (2024). A parallel implementation of a mixed multiscale domain decomposition method applied to the magnetostatic simulation of 2d electrical machines. *Finite Elements in Analysis and Design*, 235, 104136 (cit. on p. 73).
- Ryckelynck, D. (2005). A priori hyperreduction method: An adaptive approach. *Journal of computational physics*, 202(1), 346–366 (cit. on p. 63).
- Saadat, M. A., & Durville, D. (2023). A mixed stress-strain driven computational homogenization of spiral strands. *Computers & Structures*, 279, 106981 (cit. on pp. 3, 16, 30, 234).
- Saavedra, K., Allix, O., & Gosselet, P. (2012). On a multiscale strategy and its optimization for the simulation of combined delamination and buckling. *International Journal for Numerical Methods in Engineering*, 91(7), 772–798 (cit. on pp. 73, 109, 159, 188, 216).
- Salvadori, A., & Carini, A. (2011). Minimum theorems in incremental linear elastic fracture mechanics. *International journal of solids and structures*, 48(9), 1362–1369 (cit. on p. 38).
- Sánchez-Palencia, E. (1980). Non-homogeneous media and vibration theory. *Lecture Note in Physics*, Springer-Verlag, 320, 57–65 (cit. on p. 143).
- Scanff, R., Nachar, S., Boucard, P.-A., & Néron, D. (2021). A study on the latin-pgd method: Analysis of some variants in the light of the latest developments. *Archives of computational methods in engineering*, 28(5), 3457–3473 (cit. on p. 108).
- Scanff, R., Néron, D., Ladevèze, P., Barabinot, P., Cugnon, F., & Delsemme, J.-P. (2022). Weakly-invasive latin-pgd for solving time-dependent non-linear parametrized problems in solid mechanics. *Computer Methods in Applied Mechanics and Engineering*, 396, 114999 (cit. on pp. 6, 216, 237).
- Schur, J. (1917). Über potenzreihen, die im innern des einheitskreises beschränkt sind. (cit. on p. 67).
- Schwarz, H. (1869). Über einige abbildungseigenschaften. *J. Reine Angew. Numer. Math*, 70, 105–120 (cit. on p. 67).

- Seitz, A., Popp, A., & Wall, W. A. (2015). A semi-smooth newton method for orthotropic plasticity and frictional contact at finite strains. *Computer Methods in Applied Mechanics and Engineering*, 285, 228–254 (cit. on p. 46).
- Seitz, A., Wall, W. A., & Popp, A. (2019). Nitsche's method for finite deformation thermomechanical contact problems. *Computational Mechanics*, 63, 1091–1110 (cit. on p. 44).
- Siegert, D. (1997). *Mécanismes de fatigue de contact dans les câbles de haubanage du génie civil* (Doctoral dissertation). Nantes. (Cit. on pp. 24, 26).
- Signorini, A. (1959). Questioni di elasticità non linearizzata e semilinearizzata. *Rendiconti di Matematica e delle sue Applicazioni*, 18, 95–139 (cit. on pp. 33, 34).
- Simo, J. C., & Laursen, T. (1992). An augmented lagrangian treatment of contact problems involving friction. *Computers and Structures*, 42(1), 97–116 (cit. on pp. 6, 43, 44, 48, 109, 237).
- Simo, J. C., Wriggers, P., & Taylor, R. L. (1985). A perturbed lagrangian formulation for the finite element solution of contact problems. *Computer methods in applied mechanics and engineering*, 50(2), 163–180 (cit. on p. 43).
- Smallwood, R. (1990). Fretting fatigue of steel roping wire in seawater. (cit. on p. 23).
- Sørum, S. H., Fonseca, N., Kent, M., & Faria, R. P. (2023). Modelling of synthetic fibre rope mooring for floating offshore wind turbines. *Journal of Marine Science and Engineering*, 11(1), 193 (cit. on pp. 2, 233).
- Stanova, E., Fedorko, G., Fabian, M., & Kmet, S. (2011). Computer modelling of wire strands and ropes part ii: Finite element-based applications. *Advances in Engineering Software*, 42(6), 322–331 (cit. on p. 31).
- Sun, D., Sun, J., & Zhang, L. (2008). The rate of convergence of the augmented lagrangian method for nonlinear semidefinite programming. *Mathematical Programming*, 114(2), 349–391 (cit. on pp. 7, 44, 238).
- Suquet, P. (1987). Elements of homogenization for inelastic solid mechanics. *Homogenization techniques for composite media*, 272, 193–278 (cit. on p. 143).
- Tiso, P., & Rixen, D. J. (2013). Discrete empirical interpolation method for finite element structural dynamics. *Topics in Nonlinear Dynamics, Volume 1: Proceedings of the 31st IMAC, A Conference on Structural Dynamics, 2013*, 203–212 (cit. on p. 63).

-
- Treysse, F., & Cartraud, P. (2022). A two-dimensional formulation for the homogenization of helical beam-like structures under bending loads. *International Journal of Solids and Structures*, 234, 111270 (cit. on p. 30).
- Usabiaga, H., & Pagalday, J. (2008). Analytical procedure for modelling recursively and wire by wire stranded ropes subjected to traction and torsion loads. *International Journal of Solids and Structures*, 45(21), 5503–5520 (cit. on p. 25).
- Vannes, A., Chicois, J., & Fougères, R. (1973). Restauration des contraintes résiduelles induites par écrouissage, en fonction de la température de chauffage et du temps de maintien. *Mémoires Scientifiques, Métallurgie*, 70, 4 (cit. on p. 23).
- Veroy, K., & Patera, A. T. (2005). Certified real-time solution of the parametrized steady incompressible Navier–Stokes equations: Rigorous reduced-basis a posteriori error bounds. *International Journal for Numerical Methods in Fluids*, 47(8-9), 773–788 (cit. on p. 57).
- Violeau, D. (2003). Sur une amélioration de la stratégie de calcul multiéchelle avec homogénéisation. *Mémoire du DEA TACS, LMT-Cachan* (cit. on pp. 151, 187).
- Violeau, D. (2007). *Une stratégie de calcul pour l'analyse à l'échelle "micro" des endommagements jusqu'à rupture des composites stratifiés* (Doctoral dissertation). École normale supérieure de Cachan-ENS Cachan. (Cit. on p. 73).
- Visse, V., Alart, P., & Dureisseix, D. (2013). High performance computing of discrete nonsmooth contact dynamics with domain decomposition. *International journal for numerical methods in engineering*, 96(9), 584–598 (cit. on pp. 46, 74).
- Vorpahl, F., Schwarze, H., Fischer, T., Seidel, M., & Jonkman, J. (2013). Offshore wind turbine environment, loads, simulation, and design. *Wiley Interdisciplinary Reviews: Energy and Environment*, 2(5), 548–570 (cit. on pp. 16, 19, 20).
- Weeger, O., Narayanan, B., De Lorenzis, L., Kiendl, J., & Dunn, M. L. (2017). An isogeometric collocation method for frictionless contact of Cosserat rods. *Computer Methods in Applied Mechanics and Engineering*, 321, 361–382 (cit. on p. 31).
- Wriggers, P., & Laursen, T. A. (2006). *Computational contact mechanics* (Vol. 2). Springer. (Cit. on pp. 33, 37, 38, 40, 41).
- Wriggers, P., Simo, J., & Taylor, R. (1985). Penalty and augmented Lagrangian formulations for contact problems. *Proceedings of NUMETA Conference, Balkema, Rotterdam* (cit. on pp. 43, 44).

- Wriggers, P., & Zavarise, G. (1997). On contact between three-dimensional beams undergoing large deflections. *Communications in numerical methods in engineering*, 13(6), 429–438 (cit. on p. 31).
- Wriggers, P. (1987). *On consistent tangent matrices for frictional contact problems*. (Cit. on pp. 37, 45).
- Wriggers, P., & Zavarise, G. (2008). A formulation for frictionless contact problems using a weak form introduced by nitsche. *Computational Mechanics*, 41, 407–420 (cit. on p. 44).
- Wu, G. G., Liang, Y. C., Lin, W. Z., Lee, H. P., & Lim, S. P. (2003). A note on equivalence of proper orthogonal decomposition methods. *Journal of Sound and Vibration*, 265(5), 1103–1110 (cit. on p. 56).
- Wurtzer, F., Boucard, P.-A., Ladevèze, P., & Néron, D. (2024). Une approche modulaire basée sur la pgd pour la résolution de problèmes multiphysiques fortement couplés. *16ème Colloque National en Calcul des Structures* (cit. on p. 108).
- Xiang, L., Wang, H., Chen, Y., Guan, Y., Wang, Y., & Dai, L. (2015). Modeling of multi-strand wire ropes subjected to axial tension and torsion loads. *International Journal of Solids and Structures*, 58, 233–246 (cit. on p. 25).
- Xing, Y., Meng, L., Huang, Z., & Gao, Y. (2022). A novel efficient prediction method for microscopic stresses of periodic beam-like structures. *Aerospace*, 9(10), 553 (cit. on p. 30).
- Yastrebov, V. (2011). *Computational contact mechanics: geometry, detection and numerical techniques* (Ph.D. thesis). École Nationale Supérieure des Mines de Paris. (Cit. on pp. 33, 41).
- Yin, Z., Hu, Z., Gao, H., & Lin, G. (2024). A feti b-differentiable equation method for elastic frictional contact problem with nonconforming mesh. *Computational Mechanics*, 1–30 (cit. on p. 74).
- Young, D., Ng, C., Oterkus, S., Li, Q., & Johanning, L. (2018). Assessing the mechanical stresses of dynamic cables for floating offshore wind applications. *Journal of Physics: Conference Series*, 1102(1), 012016 (cit. on pp. 3, 234).
- Zavarise, G., & Wriggers, P. (1999). A superlinear convergent augmented lagrangian procedure for contact problems. *Engineering Computations* (cit. on p. 187).

-
- Zavarise, G., & Wriggers, P. (2000). Contact with friction between beams in 3-d space. *International Journal for Numerical Methods in Engineering*, 49(8), 977–1006 (cit. on p. 31).
- Zavarise, G., Wriggers, P., & Schrefler, B. (1995). On augmented lagrangian algorithms for thermomechanical contact problems with friction. *International Journal for Numerical Methods in Engineering*, 38(17), 2929–2949 (cit. on p. 44).
- Zeka, D., Guidault, P.-A., Néron, D., & Guiton, M. (2024a). On the benefits of a multiscale domain decomposition method to model-order reduction for frictional contact problems. *Computer Methods in Applied Mechanics and Engineering*, 429, 117171 (cit. on pp. 99, 110, 141, 156).
- Zeka, D., Guidault, P.-A., Néron, D., Guiton, M., & Enchery, G. (2023). Model reduction for non-linear structural problems with multiple contact interfaces: Application to the modeling of fowt mooring lines. *MORTech 2023–6th International Workshop on Model Reduction Techniques* (cit. on p. 95).
- Zeka, D., Guidault, P.-A., Néron, D., & Guiton, M. (2024b). A comprehensive study on the benefits of a multiscale approach in model-order reduction for frictional contact problems. *9th European Congress on Computational Methods in Applied Sciences and Engineering-ECCOMAS Congress 2024* (cit. on p. 110).
- Zeka, D., Guidault, P.-A., Néron, D., & Guiton, M. (2024c). On the benefits of a multiscale strategy to model-order reduction for frictional contact problems. *16ème Colloque National en Calcul des Structures* (cit. on p. 110).
- Zeka, D., Guidault, P.-A., Néron, D., Guiton, M., & Enchéry, G. (2022). Preliminary study for the simulation of wire ropes using a model reduction approach suitable for multiple contacts. *25ème Congrès Français de Mécanique* (cit. on p. 101).
- Zeka, D., Guidault, P.-A., Néron, D., Guiton, M., & Enchéry, G. (2024d). A multiscale a priori reduced-order modelling method for problems with multiple frictional contact interfaces. *Contact Mechanics International Symposium CMIS 2024* (cit. on p. 110).
- Zhang, D., & Ostoja-Starzewski, M. (2016). Finite element solutions to the bending stiffness of a single-layered helically wound cable with internal friction. *Journal of Applied Mechanics*, 83(3), 031003 (cit. on p. 31).
- Zheng, Z., Néron, D., & Nackenhorst, U. (2024). A stochastic latin method for stochastic and parameterized elastoplastic analysis. *Computer Methods in Applied Mechanics and Engineering*, 419, 116613 (cit. on p. 108).

- Zienkiewicz, O. C., & Zhu, J. Z. (1987). A simple error estimator and adaptive procedure for practical engineering analysis. *International journal for numerical methods in engineering*, 24(2), 337–357 (cit. on p. 171).
- Zimmermann, R. (2013). Gradient-enhanced surrogate modeling based on proper orthogonal decomposition. *Journal of Computational and Applied Mathematics*, 237(1), 403–418 (cit. on p. 54).
- Zmitrowicz, A. (1989). Mathematical descriptions of anisotropic friction. *International journal of solids and structures*, 25(8), 837–862 (cit. on p. 224).
- Zohdi, T. I., Oden, J. T., & Rodin, G. J. (1996). Hierarchical modeling of heterogeneous bodies. *Computer methods in applied mechanics and engineering*, 138(1-4), 273–298 (cit. on p. 143).